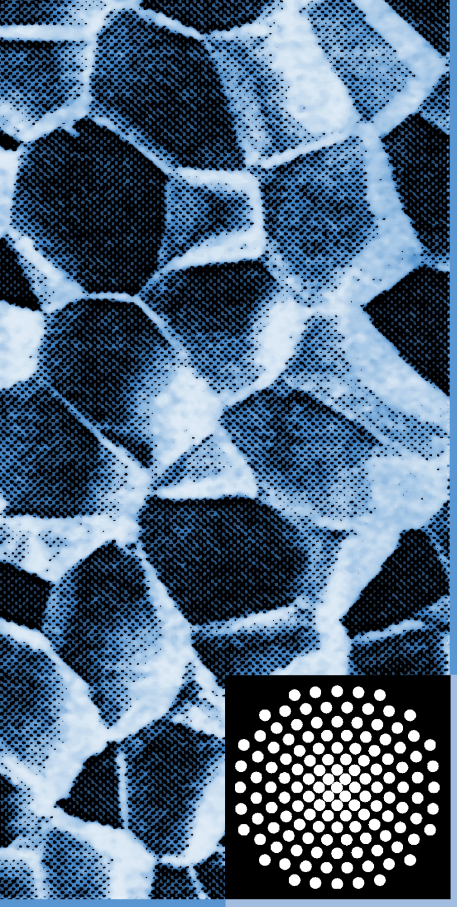

Universität Stuttgart

Institut für Mechanik (Bauwesen)
Lehrstuhl für Kontinuumsmechanik
Prof. Dr.-Ing. Dr. h. c. W. Ehlers

Variational Multiphysics Modeling of Diffusion in Elastic Solids and Hydraulic Fracturing in Porous Media

Steffen Alexander Mauthe

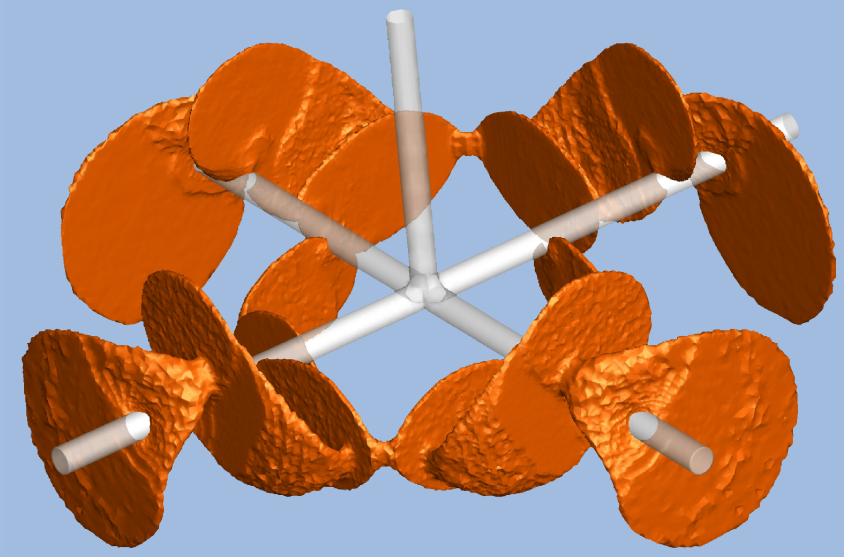

Report No.: II-33 (2017)

Variational Multiphysics Modeling of Diffusion in Elastic Solids and Hydraulic Fracturing in Porous Media

Von der Fakultät Bau- und Umweltingenieurwissenschaften
der Universität Stuttgart und dem Stuttgart Research Centre
for Simulation Technology zur Erlangung der Würde
eines Doktor-Ingenieurs (Dr.-Ing.)
genehmigte Abhandlung

vorgelegt von

Steffen Alexander Mauthe

aus
Obernheim

Hauptberichter:	Prof. Dr.-Ing. Dr. h. c. Wolfgang Ehlers
1. Mitberichter:	Prof. Dr. rer. nat. Klaus Hackl
2. Mitberichter:	Prof. Dr. techn. Günther Meschke

Tag der mündlichen Prüfung: 11. Juli 2017

Institut für Mechanik (Bauwesen) der Universität Stuttgart
Lehrstuhl für Kontinuumsmechanik
Prof. Dr.-Ing. Dr. h. c. W. Ehlers

2017

Report No. II-33
Institut für Mechanik (Bauwesen)
Lehrstuhl für Kontinuumsmechanik
Universität Stuttgart, Germany, 2017

Editor:
Prof. Dr.-Ing. Dr. h. c. W. Ehlers

© Steffen Alexander Mauthe
Institut für Mechanik (Bauwesen)
Lehrstuhl für Kontinuumsmechanik
Universität Stuttgart
Pfaffenwaldring 7
70569 Stuttgart, Germany

ISBN 978 – 3 – 937399 – 33 – 1
(D 93 – Dissertation, Universität Stuttgart)

to Hannes & Denise

Acknowledgements

This work is the result of five interesting, exciting and successfull years at the Institute of Applied Mechanics (Civil Engineering) at the University of Stuttgart. A lot of people contributed to the finalization of this work in many ways. Here I want to take the opportunity to sincerely thank all of them.

First and foremost, I would like to express my deepest appreciation to Prof. Dr.-Ing. Christian Miehe for his imperturbable confidence, inimitable guidance and limitless support in both academic and personal matters. At the institute, his vast knowledge and his everlasting aspiration for excellent research impressed and inspired me every single day. Without our numerous discussions and his help, this work would not have been possible. It was a big pleasure for me working with such a great person.

I would like to thank Prof. Dr.-Ing. Dr. h. c. Wolfgang Ehlers for accepting to take over the main referee position as well as for his valuable support in the final steps of the work. My sincere gratitude goes to Prof. Dr. rer. nat. Klaus Hackl and Prof. Dr. techn. Günther Meschke for their interest in this topic and that they accepted to become co-referees for this doctoral thesis.

Furthermore, I would like to thank all my colleagues from both chairs of the Institute of Applied Mechanics for the fruitful discussions, collaborations and great working atmosphere. Especially, I would like to convey my gratitude to Felix Hildebrand for his fantastic supervision during my time as a student assistant at the institute. He was the one who encouraged and inspired me to join the institute. I was fascinated by his structured way of thinking and his joy in research. Furthermore, I want to thank my officemates Heike Ulmer and Stephan Teichtmeister for their patience, their support and all the fruitful conversations. To Fadi Aldakheel I am truly grateful for the productive collaboration during the first year at the institute. Big thanks go to Daniel Kienle and Felix Göküzüm who provided me with significant support to my dissertation through their master theses. It was a pleasure to supervise their theses.

I want to thank my parents for their unconditional love, their great support during the last 30 years and their firm faith in me. When I needed them, they have been there for me. Without them I would not be the person that I am today.

Finally and most importantly I want to thank my wonderful family: little Hannes for letting my heart shine when smiling whimsically, laughing and simply looking at me; and my beloved wife Denise for her balanced mix of beneficial pressure and limitless support, her understanding, her never-failing confidence and for simply being there. I love you with all my heart.

Stuttgart, July 2017 Steffen Mauthe

Table of Contents

Abstract

The numerical simulation of multiphysics problems is a growing field of research in the computational materials theory. Multiphysics simulations treat models containing multiple different physical phenomena such as for example magneto-mechanical and electro-mechanical coupling, fluid flow coupled to heat transport and chemical reactions or fluid-solid-interaction. The growing research activity can be explained on the one hand by a growing number of applications with materials and construction elements in almost every field of material- and engineering sciences that take advantage of multiphysical coupling phenomena. On the other hand, thanks to the rapid increase of computing power as well as the upgrowth of parallelization techniques, it becomes possible to treat larger and more complex mathematical models numerically. In this context the computational simulation of material failure and complex crack mechanisms plays an increasing role in order to answer safety-relevant questions reliably. This work deals with the computational modeling of multiphysics problems of elastic two-component solids undergoing large strains. The main focus here is on a variational treatment of the coupled problems as well as their efficient numerical exploitation with the finite element method. The work is divided into two parts. The first part introduces the physical and mathematical framework for multicomponent solids. The variational modeling framework is introduced by means of two model problems: The first application deals with fluid-saturated porous materials, the second application is connected to diffusion processes in elastic solids. In the second part of the work the modeling framework is extended to include material failure and crack propagation processes. Main goal in this part is the computational modeling of hydraulically driven fracture in fluid-saturated porous soils.

For the mathematical description of materials containing multiple components two different approaches can be found in the literature. First, there is the so-called *mixture theory* and its extension about the concept of volume fractions, the *theory of porous media*. The mathematical model is derived from a homogenization procedure of overlapping continua that are in interaction with each other. Each of these continua represent one single component of the body. Opposite to this approach is the *macroscopic theory* that treats the multicomponent material as one single continuum. Here no separate physical statements for separate components are made but only for the total multicomponent body. This macroscopic approach is used in the context of the present work. A first step in the direction of a variational formulation is based on the introduction of potentials for energy and dissipation. For multicomponent systems this has been proposed by Biot [28]. However a consistent numerical treatment within the time- and space-time-discrete setting has, to the knowledge of the author, not been considered so far. The variational principle proposed in this work directly leads to a *canonical two-field formulation* with kinematic quantities as primary unknown fields. The model requires as constitutive input only two functions describing the stored energy and the dissipative mechanisms of the material. The variational modeling framework allows to obtain different other (mixed) formulations and to put them into a relationship to one another. For example a Legendre transformation of the dissipation potential function yields the classical saddle-point formulation widely used in the literature. By means of the model problem of *porous media* in Chapter 4 both variational formulations are introduced and compared to each other. To this end, for both formulations suitable finite element designs are proposed. The canonical minimization formulation proves superior as no additional constraints to the interpola-

tion functions of the individual fields have to be fulfilled. Additionally the formulation is computationally more efficient than the saddle-point formulation. Furthermore the introduced variational framework allows for the treatment of gradient-extended problems such as the Cahn-Hilliard theory for the modeling of *phase segregation in diffusion processes* which is demonstrated in Chapter 5. For the treatment of such advanced theories an additional contribution to the energy function has to be added. In particular this is the surface energy accounting for the domain walls between two interfaces. Neglecting this term the modeling framework reduces to potential-driven diffusion processes in elastic solids.

The goal of the second part of the work is the incorporation of material failure in terms of crack initiation and propagation. To this end, the introduced modeling framework of porous media is extended by a diffusive crack phase-field. The phase-field approach is a spatially smooth continuum method for the modeling of fracture mechanics. This method is characterized by an efficient numerical implementation and the possibility to model complex crack topologies in two as well as three dimensions. By introduction of specific constitutive functions the incorporation of this method within the variational formulation is straightforward. Another aspect of multiphysics modeling is comprised by the model problem of *hydraulically induced fracture*. For the modeling of such scenarios the fluid flow in the unbroken bulk as well as within the cracks has to be described. In the bulk porous medium this is done by the Darcy law of fluid flow whereas in the cracks generally a Stokes- or Navier-Stokes flow has to be considered. Assuming moderate crack opening widths the assumption of a Poiseuille-type fluid flow is justified. However this requires an evaluation of the crack opening width, a quantity that usually does not arise in the phase-field fracture approach. Thus an evaluation of the crack opening width based on continuum-mechanical quantities is proposed. In order to raise the computational robustness and efficiency of the method a operator-splitting technique is used. Finally the model capabilities and the performance of the proposed formulation are demonstrated by means of representative numerical examples in two and three dimensions.

Zusammenfassung

Die Simulation multiphysikalischer Fragestellungen nimmt einen stetig wachsenden Anteil der Forschungstätigkeit in der computerorientierten Materialtheorie ein. Multiphysiksimulationen behandeln Modelle, die mehrere verschiedene physikalische Phänomene berücksichtigen. Beispiele sind magento-mechanische und elektro-mechanische Kopplung, Fluidströmung gekoppelt mit Wärmetransport und chemischen Reaktionen oder Fluid-Festkörper-Interaktion. Die steigende Forschungsaktivität liegt einerseits an der wachsenden Verbreitung und Anwendung von Materialien und Bauteilen in nahezu allen Material- und Ingenieurwissenschaften, die gezielt multiphysikalische Kopplungseffekte ausnutzen, andererseits ist es dank der rasant steigenden Rechenleistung von Computern und der Entwicklung von Parallelisierungstechniken möglich geworden, immer größere und kompliziertere mathematische Modelle numerisch zu behandeln. In diesem Zusammenhang spielt auch die numerische Simulation von Materialversagen und Bruchmechanismen eine immer größere Rolle, um sicherheitsrelevante Fragestellungen verlässlich beantworten zu können. Die vorliegende Arbeit beschäftigt sich mit der Modellierung sowie der numerischen Simulation von multiphysikalischen Problemen elastischer Zweikomponentenmaterialien unter Berücksichtigung großer Verzerrungen. Das Hauptaugenmerk liegt hierbei auf einer variationellen Formulierung der gekoppelten Probleme und deren effiziente numerische Behandlung mit der Methode der Finiten Elemente. Die Arbeit ist in zwei Teile gegliedert. Teil Eins befasst sich zunächst mit dem physikalischen und mathematischen Rahmen für mehrkomponentige Materialien. Die variationelle Modellierung wird anhand zweier Modellprobleme diskutiert: Dies sind zum einen fluidgesättigte poröse Materialien und zum anderen Diffusionsprozesse in elastichen Festkörpern. Teil Zwei der Arbeit beschäftigt sich dann mit der Erweiterung des Modellrahmens um Materialversagen und Rissfortschritt. Ziel in diesem Teil der Arbeit ist es, hydraulisch induzierte Rissausbreitungsprozesse in fluidgesättigten, porösen Böden zu simulieren.

Für die mathematische Beschreibung von Materialien mit mehreren Komponenten gibt es zwei grundsätzlich verschiedene Heransgehensweisen. Auf der einen Seite steht die sogenannte *Mischungstheorie* und die um das Konzept der Volumenfraktionen erweiterte *Theorie der porösen Medien*. Das mathematische Modell entsteht hier aus einem Homogenisierungsprozess von sich überlappenden und in Interaktion stehenden Kontinuas, welche die einzelnen Komponenten repräsentieren. Dem gegenüber steht die rein *makroskopische Theorie*, welche das Mehrkomponentenmaterial als Gesamtes betrachtet. Es werden keine physikalischen Aussagen für separate Komponenten konstatiert, sondern ausschließlich für den Gesamtkörper. Diese makroskopische Herangehensweise wird im Rahmen dieser Arbeit verwendet. Ein erster Schritt Richtung variationeller Formulierung basiert auf der Einführung von Potentialen für Energie und Dissipation. Diese Idee wurde erstmals von Biot [28] verfolgt, eine numerische Behandlung im zeit- und raum-zeit-diskreten Fall wurde jedoch nach Kenntnis des Autors nie durchgeführt. Das in dieser Arbeit vorgestellte Variationsprinzip führt auf direktem Wege zu einer *kanonischen Zweifeldformulierung* mit kinematischen Größen als primären Unbekannten. Das Modell benötigt als konstitutiven Input lediglich zwei Funktionen, die die gespeicherte Energie und die dissipativen Effekte des Gesamtmaterials beschreiben. Die variationelle Modellbildung liefert zusätzlich die Möglichkeit, weitere (gemischte) Formulierungen abzuleiten und diese in einen mathematischen Zusammenhang zu bringen. Eine Legendre Transformation des Dissipationspotentials zum Beispiel liefert die in der Literatur klassischerweise

verwendete Sattelpunktformulierung. Anhand des Anwendungsbeispieles *poröser Medien* in Kapitel 4 werden für diese beiden Formulierungen jeweils verschiedene Finite Element Designs vorgestellt und anhand numerischer Beispielen miteinander verglichen. Die kanonische Minimierungsformulierung erweist sich hierbei als vorteilhaft, da keine Nebenbedingungen an die Interpolationsansätze zu berücksichtigen sind. Auch die numerische Effizienz ist besser als bei der klassischen Formulierung. Der vorgestellte variationelle Rahmen ermöglicht zusätzlich die Modellierung von gradientenerweiterten Problemen, wie zum Beispiel Cahn-Hilliard Theorien zur Modellierung von *Phasensegregation in Diffusionprozessen*. Dies wird in Kapitel 5 demonstriert. Für die Modellierung muss lediglich ein zusätzlicher Energieterm eingeführt werden, welcher die Grenzflächenenergie zwischen zwei unterschiedlichen Phasen darstellt. Wird dieser Term vernachlässigt, reduziert sich der Modellrahmen auf potentialgetriebene Diffusionsprozesse in elastischen Medien.

Das Ziel im zweiten Teil der Arbeit ist es *Materialversagen* in Form von Rissentstehung und -ausbreitung mit abzubilden. Hierzu wird das vorgestellte Modell für poröse Medien um ein diffuses Bruch-Phasenfeld erweitert. Die Phasenfeldmethode ist eine kontinuumsmechanische Methode zur Modellierung von Bruchvorgängen, die sich vor allem durch ihre effiziente numerische Implementation und die Möglichkeit komplexe zwei- und dreidimensionale Risstopologien abzubilden auszeichnet. Mit spezifischen konstitutiven Funktionen ist ein Einbau dieser Methode innerhalb des vorgestellten variationellen Rahmens in einfacher Weise möglich. Einen weiteren multiphysikalischen Aspekt birgt der Anwendungsfall von *hydraulisch induziertem Bruch*. Für die Modellierung der Fluidströmung in den fluidgefüllten Rissen ist im Allgemeinen eine Stokes- oder Navier-Stokes-Gleichung zu verwenden, während im ungerissenen Boden meist das Gesetz von Darcy angenommen wird. Bei moderaten Rissöffnungsweiten wird oft das Poiseuille Gesetz zur Bestimmung des Fluidflusses benutzt. Dies erfordert die Auswertung der Rissöffnungweite, welche jedoch bei der Phasenfeldmethode zur diffusen Bruchsimulation nicht explizit auftaucht. Es wird deshalb eine Berechnung der Rissöffnungsweite basierend auf vorhandenen kontinuumsmechanischen Größen vorgestellt. Um die numerische Robustheit und Effizienz der Methode zu steigern, wird eine Operator-Split Technik eingesetzt. Schließlich wird das Potenzial des vorgestellten Modells anhand numerischer Beispiele aufgezeigt.

Chapter 1

Introduction

Multiphysics simulations treat coupled problems with two or more different physical phenomena involved. This includes magneto-mechanical and electro-mechanical coupling effects, fluid flow with heat transfer and chemical reactions or fluid-solid-interactions. An efficient numerical modeling of such multiphysics phenomena in solids are a key to a successful further development and optimization of both technically relevant materials and components. In this respect it is indispensable that a predictive simulation of failure mechanisms and complex crack patterns has to be included in order to provide reliable safety analyses. This work focuses on the modeling and efficient numerical treatment of multiphysics problems in solids at fracture. The main objective is a variational based modeling in terms of two physically motivated constitutive functions related to the free energy storage and the dissipative response of the material.

1.1. Motivation and state of the art

The modeling of multiphysics problems of solids has become a huge area of research within the last decades. Key challenges to deal with are an extended set of coupled partial differential equations as well as an appropriate modeling of multiple physical phenomena that in some extent take place on different scales in time and space. For example slow diffusion processes and very fast chemical reactions in mixtures or fluid flow in both large geothermal reservoirs and thin fractures within this reservoir. To this end, a careful modeling on the one hand as well as an efficient numerical treatment on the other hand are keys to a successful computational treatment of multiphysics problems of solids.

1.1.1. Materials with multiple phases and components

Many engineering materials consist of multiple components of the same or different chemical state of aggregation. This includes for example materials with a *porous microstructure*, the pores of which are filled with gas, fluid or a mixture of both. Examples are rock, soil, timber or human tissue. Since the pioneering works of Terzaghi [255] and Biot [21] research in the field of porous materials has undergone an immense growth and development

due to the huge amount of practical applications in petroleum and geotechnical engineering, civil engineering, continuum biomechanics and medical sciences. For an introduction into the theory of porous solids we refer to Bowen [42], Bedford & Drumheller [19], Truesdell [259], Coussy [66, 67], Detournay & Cheng [83], de Boer [73] and Ehlers [92].

There are other classes of multicomponent materials such as solvents or hydrogels where one usually does not refer to its porous microstructure. In these materials the relative movement of mass of components to each other is denoted as *diffusion process* and can take place in gases, fluids and solids. The first experiments and measurements can be traced back to Graham [116] who studied diffusion of salts in water. Fick [103] established a fundamental law of mass flow in terms of the concentration gradient. For a review on the history of diffusion we refer to Philibert [210]. Typical application in solids is the chemo-mechanical transport of ions and molecules as for example in polymeric hydrogels, where small solvent molecules diffuse through a crosslinked polymer network, see Flory & Rehner [104] or recently Hong et al. [135], or in electrode materials for batteries, where a transport of lithium ions can be observed. A typical feature of hydrogels is the large amount of volumetric swelling that is induced by the diffusion of the molecules or ions, see for example Flory & Rehner [104] or Doyle et al. [90]. Furthermore diffusing species can also cause phase segregation phenomena as for example in Lithium-Ion batteries. The modeling of such effects requires advanced gradient-extended theories, see Anand [6] or Zhao et al. [277].

For the mathematical description of such multiphasic and multicomponent systems two different approaches can be found in the literature. The first class is denoted as *mixture theory* and goes back to Bowen [42] and Truesdell & Toupin [261]. Within this theory, the balance equations are derived from averaging concepts and the multiple components are represented by superimposed and interacting continua, each possessing its own set of balance equations. For the case of porous media the mixture theory is supplemented by the concept of volume fraction yielding the *theory of porous media*, see Bowen [43, 44], de Boer [72, 73], de Boer & Ehlers [75] or Ehlers [92, 94].

In contrast there is the *purely macroscopic theory* that goes back to Biot [21, 24, 28] and was later extended by Biot [33], Coussy [65, 66] and Weitsman [268]. Here the concepts of continuum mechanics are assumed to be still valid on the macroscale, see Coussy et al. [68]. Initially introduced in Biot [21] for nearly fluid saturated soils, this theory is based on a macroscopic free energy potential that provides the stresses in both the solid and the fluid. Coussy et al. [68] showed that one single macroscopic potential exists within the equations of the mixture theory. Hence there is a relation between these two approaches and both can be used equivalently, see Detournay & Cheng [83] and Gajo [109]. In a broad series of publications Biot revealed the generality of the macroscopic approach including compressibility of all constituents, phase transitions, chemical reactions or the extension to the thermodynamical setting, see Biot [24, 26, 27, 28, 29, 33]. The interested reader is referred to these publications as well as the works of Coussy [66, 67]. Applications to diffusion processes can be found for example in Weitsman [268], Dal & Miehe [70] or Miehe et al. [188].

The first steps towards a variational modeling approach can be traced back to Biot [23, 24, 27, 28] who in particular introduced constitutive *potentials* for the energetic and dissipative behavior. The first variational treatment of poro-elasticity was proposed by

Coussy [66]. However the form of this approach is very specific and restricted to the time-discrete setting in the small strain theory. Using Laplace transformed fields and convolutions, saddle-point principles for the linear theory of consolidation can be found in Sandhu & Wilson [231], Sandhu & Pister [230], Booker & Small [36] and Christian [62]. Other works mostly start from a virtual work expression and hence do not account for inherent symmetries, see for example Carter et al. [57, 58], Prévost [214, 216], Borja & Alarcon [39] and Armero [9].

Modeling of these types of problems of solids with the finite element method is still a challenging and actual topic of research in particular concerning numerical stability issues and computational efficiency. An overview of different numerical finite element implementations for the model problem of poro-elasticity can be found in Haga et al. [128]. One source of *numerical stability* issue is that the formulations often possess a saddle-point structure. From a mathematical viewpoint the key for ensuring uniqueness of elliptic saddle-point systems is the satisfaction of the so called Babuška-Brezzi-Ladyzhenskaya condition (shortly BBL or inf-sup condition) as originally developed in Babuška [14] and Brezzi [46]. A substantial difficulty is the fact that the satisfaction of the BBL condition for the continuous time-discrete problem does not imply the space discrete counterpart to be inf-sup stable. Violation of the condition often yields high amplitude spatial oscillations in the primary unknown fields and hence nonphysical results. The discrete BBL condition requires a suitable balance between the interpolations of the primary fields in order to ensure stability. To prove the discrete BBL condition is often quite hard, see Brezzi & Fortin [47]. Thus Chapelle & Bathe [61] proposed a numerical inf-sup test where an equivalent eigenvalue problem has to be solved. From the mathematics as well as from the engineering side a lot of effort was spent in order to construct stable finite element solutions for coupled problems with underlying saddle-point structure, see for example Taylor & Hood [253], Sandhu & Wilson [231], Bouklas et al. [40], Arnold et al. [11], Brezzi & Fortin [47], Pantuso & Bathe [204], Lovadina & Auricchio [165], Papastavrou et al. [205], Zhou et al. [278] or Krischok & Linder [156]. However, in the case of poromechanics both the Taylor-Hood element and the Mini element, each providing an inf-sup stable pairing of approximation spaces, do not always lead to stable solutions, see Murad & Loula [200] and Rodrigo et al. [227]. Other approaches to overcome instability problems of the saddle-point formulation are reduced integration techniques proposed by Reed [219] or stabilized finite elements as performed by Mira et al. [196], Truty & Zimmermann [262], White & Borja [270], Rodrigo et al. [227], Preisig & Prévost [213] and Sun et al. [250]. The idea of the latter is to add stabilization terms in order to get rid of the violation of the BBL condition of low-order elements and can be traced back to Hughes et al. [141], Hughes & Franca [140] and Douglas & Wang [89]. However a considerable disadvantage of these methods lies in the fact that they introduce a stabilization parameter that has to be chosen. This parameter depends on the boundary value problem and is practically not identifiable for complex geometries. Choosing a too high stabilization parameter eliminates the oscillations in the primary fields, however leads to nonphysical over-diffusion. In the case of diffusion-type problems, which are parabolic systems, oscillations in the pressure can also occur additionally due to small time steps. This can be overcome by refining the finite element mesh, see Gresho & Lee [119] and Vermeer & Verruijt [263].

In this context we propose a *new finite strain variational modeling framework* for

solids with two components, see also MIEHE ET AL. [190, 187]. In particular we propose a minimization principle that is a priori stable as it is not constrained by a BBL condition. This gives the freedom of choosing the order of the interpolation spaces for the unknown fields independently of each other. This work is embedded into a multifield variational framework for gradient-extended continuum models proposed by MIEHE [176] that has been successfully applied to different coupled problems, see MIEHE ET AL. [183], MIEHE [178] and HILDEBRAND & MIEHE [133]. Due to the dissipative nature of the problems, the framework is based on rate-type variational principles governing the evolution system. In particular, two model applications are investigated related to (i) fluid-saturated porous media and (ii) diffusion in elastic solids. The main features of the proposed model are:

- *Modeling framework at finite strains*: Due to large swelling and shrinkage deformations in diffusion processes a finite strain theory is inevitable.
- *Variational framework*: Continuous rate-type, time-discrete and space-time-discrete variational principles for multicomponent solids.
- *Physically based potentials*: Modeling based on only two constitutive functions related to the stored free energy of the system and the dissipation.
- *Phase segregation*: The proposed modeling framework allows the incorporation of phase segregation phenomena in diffusion problems.
- *Stable minimization formulation*: Construction of a variational minimization principle, yielding a space-time-discrete formulation that is a priori stable and not restricted to the BBL condition.
- *Connection to classical formulations*: Different variational formulations can be derived from the minimization principle by Legendre transformations, in particular the classical $\{\varphi, \mu\}$ formulation.
- *Symmetric FE solver*: Finite element treatment of the time-discrete variational principles results in symmetric algebraic systems for the monolithic problem.

1.1.2. Fracture mechanics in porous media

The computational modeling of hydraulically driven crack propagation in porous media has achieved increasing research activities in recent years. Predictive simulations are needed to exploit failure mechanisms of materials and structures for numerous practical applications in geotechnical, environmental and petroleum engineering, material science, biomechanics and medical science. Typical examples cover the propagation of magma-driven dikes, fault activation in mining, drying-induced fracture in porous materials and failure of fluid-saturated biological structures. Due to the growing interest of the petroleum industry, major research is currently devoted to the computational modeling of *hydraulic fracturing*, the so-called "fracking".

In literature there are two main guidelines how material failure is modeled: namely damage and fracture mechanics. While the latter directly models the geometrical crack discontinuity, the idea in *damage mechanics* theories is to distribute the discontinuity over a finite width together with a constitutive stress-strain relation with strain-softening

behavior, see for example Chaboche [59, 60], Lemaitre [162], Belytschko et al. [20] and Simo & Ju [240, 241]. To model such a behavior an additional internal variable is introduced, the so-called damage variable denoted as d, that is defined as the ratio between damaged surface to total surface of an underlying microstructure with micro-defects. An evolution of the damage variable that results macroscopically in a strain-softening has a clear mechanical motivation related to the initiation, propagation and nucleation of micro-defects such as micro-voids or micro-cracks. In its final stage, the fully damaged state connected to $d = 1$ represents a macroscopic crack. From the numerical viewpoint however, this strain-softening behavior results in ill-posedness of boundary value problems and mesh-sensitivity. One possible way of tackling this problem is to introduce gradients of the damage variable into the formulation. Such gradient-enhanced damage models can be found for example in Peerlings et al. [206, 207], Comi [64], Dimitrijevic & Hackl [87, 88] and Saczuk et al. [229].

In contrast to damage mechanics, different theoretical foundations for the modeling of crack propagation for *brittle fracture mechanics* in solids has been developed in the last century. The *energetic approach* of Griffith [120, 121] introduces a critical energy release rate. Following this idea a crack propagates if the energy available reaches this critical value that represents the energy needed for the formation of the two new crack surfaces. Thus the energy release rate can be related to a surface energy. In contrast Irwin [142, 143] proposed the concept of *stress intensity factors* describing the intensity of the stresses in the neighborhood of the crack tip. The stress intensity factors are dependent on the loading as well as the crack geometry. Finally the *cohesive zone model* has been proposed by Barenblatt [16] in 1962. Motivated by atomic bonding forces he introduced different crack resistances for the separation of different possible crack surfaces in front of the crack tip. As a consequence of these forces the stress singularity at the crack tip disappears. Different variations of this theory are the *J-integral* of Rice [224] and the material configurational forces of Eshelby [100, 101] and Rice [224]. The interested reader is referred to the book of Freund [108].

The numerical treatment of fracture theories now faces the problem of modeling the geometric discontinuity. Again two different approaches exist in the literature. The first class of methods models the *sharp crack discontinuities*. This requires advanced computational methods to track the crack paths such as the extended finite element method (XFEM) or adaptive remeshing schemes. XFEM formulations for solids are proposed by Moës et al. [198], Moës & Belytschko [197], Dumstorff & Meschke [91] or Sukumar et al. [248, 249]. Formulations with adaptive interface elements are provided for example by Xu & Needleman [274], Pandolfi & Ortiz [203], Camacho & Ortiz [56], Kaliske et al. [146], Gürses & Miehe [123] and Miehe & Gürses [180]. Finite elements with embedded discontinuities that allow for branching are proposed by Armero & Linder [10] and Linder & Armero [164].

However, the above reviewed computational modeling of sharp crack discontinuities suffer in situations with complex crack topologies including branching. This can be overcome by recently developed *phase-field approaches* to fracture, which regularize sharp crack discontinuities within a pure continuum formulation. This *diffusive* crack modeling allows the resolution of complex failure topologies such as crack branching phenomena in dynamic fracture of brittle solids. In contrast to computational models which model sharp cracks, the phase-field approach is a spatially smooth continuum formulation that

avoids the modeling of discontinuities and can be implemented in a straightforward manner. Francfort & Marigo [105] and Bourdin et al. [41] proposed a variational formulation for quasi-static brittle fracture based on a Griffith-type energy minimization. Alternatively, a viscous regularization of the rate-independent crack propagation leads to classical Ginzburg-Landau evolution equations for the crack phase field, see Hakim & Karma [129] and Kuhn & Müller [157]. The phase-field models by Miehe et al. [183] and Borden et al. [38] combine gradient damage theories with ingredients of fracture mechanics by incorporating the regularized crack surface as a central object. For a more detailed review we refer to Miehe et al. [191]. For a comparison between gradient damage theories and phase-field fracture approaches, the mathematical structures of which are very similar, see de Borst & Verhoosel [78].

The treatment of brittle fracture within porous media is an even more challenging task, especially for the case of hydraulically driven cracks. Numerous different coupling effects have to be considered. Being able to model the fluid-solid interaction in the porous bulk medium correctly and efficiently it has to be coupled with a method describing the initiation as well as the propagation of cracks on not a priori known paths. This includes the formulation of a predictive criteria for crack propagation suitable for multicomponent solids. Furthermore another challenge in fluid driven fracture scenarios is the appropriate modeling of the fluid flow along the cracks. Therefore the classical *Poiseuille law* of laminar viscous fluid flow is often applied, see e.g. Adler et al. [3] for a derivation. For the modeling, the permeability in Darcy's law can be made dependent on the crack opening, see Schrefler et al. [233] and Meschke & Grasberger [171]. An approach to directly model Stokes flow within the crack has been proposed recently by Wilson & Landis [271]. Sub-grid scale models for the fluid transport within cracks have been proposed by Réthoré et al. [222, 223] or de Borst [77]. An overview and introduction to hydraulically driven fracture is provided by Rubin [228], Zhang et al. [275], Adachi et al. [2], Bažant et al. [18] and Simoni & Schrefler [243].

Analytical solutions for fracture scenarios in poro-elastic solids are outlined for example by Rice & Clearly [225], Huang & Russell [137, 138], Zhang et al. [275], Savitski & Detournay [232], Garagash & Detournay [112], Bunger et al. [49], Peirce & Detournay [208], Detournay & Peirce [84] and Gordeliy & Detournay [115]. The first numerical model for hydraulic fracture has been proposed by Boone & Ingraffea [37]. They modeled the poro-elastic bulk response by use of the finite element method and added a finite difference method for the modeling of the fluid flow along the crack. Crack propagation was modeled by a cohesive zone model for *predetermined crack paths* that are discretized by *interface elements*. Interface elements for *not a priori known crack paths* using an adaptive remeshing strategy are considered in Schrefler et al. [233] and Secchi & Schrefler [236, 237]. Strong discontinuity methods with crack discontinuities embedded into finite elements are treated in the context of localization analyses by Larsson et al. [159], Steinmann [247], Callari & Armero [54] and Callari et al. [55]. Furthermore the *extended finite element method (XFEM)* for the numerical modeling of fracture in poro-elastic media is used by Meschke et al. [173, 174], Jox et al. [145], de Borst et al. [79] and Rempler et al. [221] in a geometrically linear setting and Irzal et al. [144] and Rempler [220] in a geometrically and physically nonlinear setting. Kraaijeveld et al. [154] applied this method to saturated porous media with coupled ion-diffusion. Further applications of this approach are documented in Réthoré et al. [223] and Mohammadnejad &

Khoei [199]. The *generalized finite element method (GFEM)* which can be interpreted as a generalization of the XFEM has recently been applied to poro-elasticity by Meschke & Leonhart [172]. Approaches to hydraulic fracturing beyond the finite element method are proposed in Gordeliy & Detournay [115] and Grassl et al. [117].

Models for hydraulically driven fracture using a phase-field approach were recently proposed by Chukwudozie et al. [63] in a reduced elastic setting using a prescribed fluid pressure term as well as by Mikelic et al. [192, 195], Wheeler et al. [269] and Lee et al. [161] for a coupling with Biot's geometrically linear theory. A phase-field approach for hydraulic fracturing within the framework of the theory of porous media has recently been proposed by Ehlers & Luo [96]. Large strain formulations of the coupled problems have been proposed by Miehe et al. [190], Miehe & Mauthe [181] and Wilson & Landis [271]. Applications of this approach to coupled problems not related to hydraulic fracturing have been considered in Timothy & Meschke [257], Zhang et al. [276] or Miehe et al. [191, 188].

In this context we propose a *finite strain variational modeling framework* for poro-hydro-elasticity at fracture, see also Miehe et al. [190], Miehe & Mauthe [181] in the finite strain setting or Mauthe & Miehe [169] in the small strain setting. Due to the dissipative nature of the problems the framework is based on rate-type variational principles for the evolution problems. The main features of the proposed model are:

- *Phase-field approach to fracture*: This diffusive approach is a spatially smooth continuum formulation that can be implemented straightforward and is able to model complex crack topologies such as branching.
- *Variational framework*: Continuous rate-type, time-discrete and space-time-discrete variational principles for multiphysics problems of solids at fracture.
- *Stable minimization formulation*: Construction of a minimization principle, yielding a space-time-discrete formulation that is a priori stable and not restricted to the BBL condition.
- *Connection to classical formulations*: Different variational formulations can be derived from the minimization principle by Legendre transformations, in particular the classical $\{\boldsymbol{\varphi}, \mu, d\}$ formulation of poro-elasticity.
- *Crack driving force*: Introduction of different crack driving forces that are suitable for multiphysics problems of solids at finite strains.
- *Symmetric FE solver*: Finite element treatment of the time-discrete variational principles results in symmetric algebraic structures for the monolithic problem.
- *Robust solution strategy*: A robust numerical scheme is obtained by an operator splitting technique combined with a Gauss-Seidel iteration.

1.2. Objectives and overview

The main goal of this work is to develop a variational framework for finite strain multiphysics problems of multicomponent solids at fracture as well as its efficient numerical treatment by use of the finite element method. The major contributions here are:

- *Rate-type potentials*: Construction of rate-type potentials for the evolution problem of multiphysics problems of solids.
- *Time- and space-discretization*: Consistent time- and space-time-discrete counterparts of the potentials that suit for the numerical treatment with the finite element method.
- *Verification of the framework*: The capabilities of the proposed variational approach for modeling of multicomponent solids are illustrated by two model applications related to (i) fluid saturated porous media and (ii) Cahn-Hilliard-type diffusion in elastic solids.
- *Connecting of different formulations*: Different formulations (and especially the classical $\{\boldsymbol{\varphi}, \mu\}$ formulation) are related based on Legendre transformations of the two constitutive functions.
- *Different finite element designs*: For the different variational formulations suitable finite element designs are proposed and tested for numerical stability and computational efficiency.
- *Incorporation of fracture mechanics*: Enhancement of the variational framework to include crack propagation by use of the phase-field approach.
- *Hydraulically driven fracture*: In order to treat fluid driven crack propagation scenarios the additional fluid flow along cracks is modeled by the Poiseuille law.

To this end, the work is divided into two parts. **Part I** deals with the modeling of problems of multicomponent solids without fracture. Chapter 2 introduces the continuum mechanical foundations for single-component materials. In particular the finite strain kinematics and the fundamental physical balance principles are introduced. Chapter 3 enhances these kinematics and physical laws to multiphysics problems of solids containing multiple phases and components. Here we follow the purely macroscopic theory. In addition to the classical thermodynamical approach, the thermodynamical setting proposed by Biot is introduced. In a plenty of publications he showed the applicability of this approach especially in the nonisothermal setting with many components, phase transitions and chemical reactions. In Chapter 4 the framework is applied to the model problem of porous media. The main focus here lies on the construction of rate-type and incremental variational principles and its numerical investigation using the finite element method. In particular a new minimization formulation for the coupled problem is proposed that is shown to be numerically stable and computationally advantageous over the classical $\{\boldsymbol{\varphi}, \mu\}$ saddle-point formulation. Another model problem of diffusion in elastic solids is investigated in Chapter 5. The main goal here is to show the capability of the variational framework to include gradient-enhanced Cahn-Hilliard-type diffusion for the modeling of phase segregation phenomena. Again rate-type and incremental variational principles are stated and used as a basis for the numerical treatment within the finite element method.

Part II of the work extends the framework by including crack propagation in order to model hydraulically driven fracture scenarios. To this end, Chapter 6 introduces the foundations of fracture mechanics. Furthermore the phase-field approach is introduced based on an intuitive geometrical viewpoint. In Chapter 7 the basics of fluid mechanics which

are needed for the description of the fluid flow within opening cracks are reviewed. In particular the kinematics, physical balance principles and the basic constitutive assumptions are introduced. Furthermore we recall the basic idea of the fluid film lubrication theory which performs an order reduction in cases where one space-dimension is small. This idea is applied to the crack geometry. The variational modeling framework for the model problem of hydraulically driven fracture in poro-hydro-elasticity is finally considered in Chapter 8. Rate-type and incremental variational potentials are introduced and the related variational principles are stated. The numerical treatment with the finite element method is shown. Furthermore different crack driving forces are introduced that suit the considered multiphysics problems in solids at large strains. Finally a robust solution strategy is proposed and the capability of the modeling framework is shown by means of numerical simulations of boundary value problems in two and three dimensions.

— Part I —

Variational Modeling of Multiphysics Problems

Chapter 2

Fundamentals of Continuum Thermo-Mechanics

In this Chapter a short introduction to finite strain continuum mechanics is presented. It is the basis to the modeling of large strain macroscopic continuum mechanics and also to macroscopic multicomponent theories presented below. The focus is on a geometric setting of large strain continuum mechanics, where metric tensors appear as natural elements connecting tangent and cotangent spaces. The viewpoint and notation used is based on the lectures Miehe [177, 179] on advanced mechanics held at the Institute of Applied Mechanics at the University of Stuttgart. This chapter has to be viewed as an introduction which by no means is entitled to be complete. For a more comprehensive treatment, the reader is referred to the classical textbooks of Truesdell & Noll [260], Marsden & Hughes [168], Holzapfel [134], Başar & Weichert [15] or Gurtin et al. [124].

2.1. Kinematics of finite deformations

To start with, the basic kinematic quantities necessary for the description of the motion and the deformation of solids undergoing large strains are introduced.

2.1.1. Description of motion

A material body B is a physical object that can mathematically be described by material points $P \in B$ which are mapped in a subset of the Euclidean space $\mathcal{R}^3$ by the placement

$$\boldsymbol{\chi}_t : \begin{cases} B \times T \to \mathcal{B}_t \subset \mathcal{R}^3, \\ (P,t) \mapsto \boldsymbol{x} = \boldsymbol{\chi}_t(P) \ . \end{cases} \tag{2.1}$$

It maps at time t material points P to a position $\boldsymbol{x}$ in the Euclidean space $\mathcal{R}^3$. $\boldsymbol{\chi}_t$ is a one-to-one mapping and thus is invertible and excludes penetration of matter. To identify particles $P \in B$, an arbitrary configuration $\boldsymbol{\chi}_{t_0}(B) = \mathcal{B}$ at time t_0 is chosen as Lagrangian or reference configuration. Within this configuration, a material particle P occupies the Lagrangian or reference coordinate $\boldsymbol{X} := \boldsymbol{\chi}_{t_0}(P) \in \mathcal{B} \subset \mathcal{R}^3$ with respect to a global Cartesian frame $\{\boldsymbol{E}_i\}_{i=1,3}$. Likewise, the Eulerian or spatial configuration at time

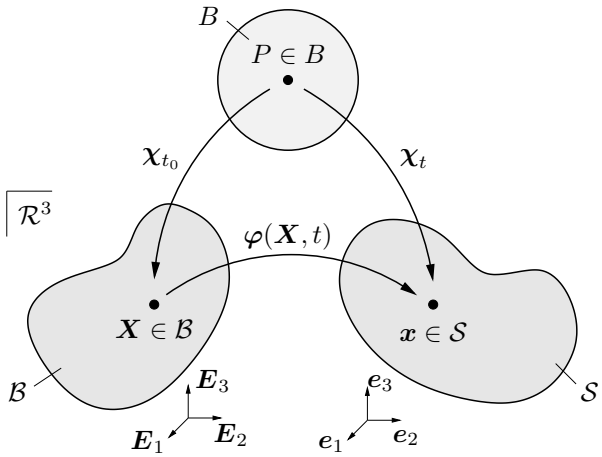

Figure 2.1: *Material body in the Euclidean space* $\mathcal{R}^3$. The material body B in its reference configuration $\mathcal{B}$ and in the spatial configuration $\mathcal{S}$. The material coordinates $\boldsymbol{X}$ are connected to the spatial coordinates $\boldsymbol{x}$ via the deformation map $\boldsymbol{x} = \boldsymbol{\varphi}(\boldsymbol{X}, t)$.

$t \in \mathcal{R}_+$ is henceforth denoted as $\boldsymbol{\chi}_t(B) = \mathcal{S}$. The Eulerian or spatial coordinates are thus $\boldsymbol{x} = \boldsymbol{\chi}_t(P) \in \mathcal{S}$ with respect to the global Cartesian frame $\{\boldsymbol{e}_i\}_{i=1,3}$. The motion of the material body in Euclidean space is now prescribed by the *nonlinear deformation map*

$$\boldsymbol{\varphi} : \begin{cases} \mathcal{B} \times T \to \mathcal{S} \subset \mathcal{R}^3, \\ (\boldsymbol{X}, t) \mapsto \boldsymbol{x} = \boldsymbol{\varphi}(\boldsymbol{X}, t) = \boldsymbol{\chi}_t \circ \boldsymbol{\chi}_{t_0}^{-1} \end{cases} \tag{2.2}$$

that is a point map between Lagrangian and Eulerian configuration, see Figure 2.1 for a visualization of the mapping.

2.1.2. Velocity and acceleration

Having introduced the motion of a material point $\boldsymbol{X}$ in time by the deformation map $\boldsymbol{\varphi}(\boldsymbol{X}, t)$ in (2.2), the *material velocity* and *acceleration* follow as

$$\boldsymbol{V}(\boldsymbol{X}, t) := \frac{d}{dt}\boldsymbol{\varphi}(\boldsymbol{X}, t) = \frac{\partial}{\partial t}\boldsymbol{\varphi}(\boldsymbol{X}, t) \quad \text{and} \quad \boldsymbol{A}(\boldsymbol{X}, t) := \frac{d}{dt}\boldsymbol{V}(\boldsymbol{X}, t) = \frac{\partial^2}{\partial t^2}\boldsymbol{\varphi}(\boldsymbol{X}, t) \ . \tag{2.3}$$

$\boldsymbol{V} \in \mathcal{S}$ and $\boldsymbol{A} \in \mathcal{S}$ are parameterized by material coordinates $\boldsymbol{X}$, however are spatial vector fields. Reparameterization of $(2.3)_1$ in terms of the spatial coordinates $\boldsymbol{x}$ yields the *spatial velocity*

$$\boldsymbol{v}(\boldsymbol{x}, t) := \boldsymbol{V}(\boldsymbol{\varphi}^{-1}(\boldsymbol{x}, t), t) = \boldsymbol{V} \circ \boldsymbol{\varphi}^{-1}(\boldsymbol{x}) \ . \tag{2.4}$$

The *spatial acceleration* is evaluated from (2.4) by using the chain rule as

$$\boldsymbol{a}(\boldsymbol{x}, t) = \dot{\boldsymbol{v}}(\boldsymbol{x}, t) = \frac{\partial}{\partial t}\boldsymbol{v}(\boldsymbol{x}, t) + \nabla_{\boldsymbol{x}}\boldsymbol{v}(\boldsymbol{x}, t) \cdot \boldsymbol{v}(\boldsymbol{x}, t) \ , \tag{2.5}$$

where we introduced the abbreviation $\dot{(\cdot)} = \frac{d}{dt}(\cdot)$ and the spatial gradient operator $\nabla_{\boldsymbol{x}}(\cdot) := \partial_{\boldsymbol{x}}(\cdot)$. The first term in (2.5) is the local part of the acceleration, the second term is the convective part due to the time dependency of $\boldsymbol{x}$.

2.1.3. Basic mappings of finite deformations

In the following the basic mappings of continuum mechanics are introduced. They are connected to the local strain behavior and to local area and volume changes of a deforming body.

Deformation gradient. The most fundamental quantity in the kinematics of finite deformations is the *deformation gradient*, which is defined as the Fréchet derivative of the deformation map

$$\boldsymbol{F}(\boldsymbol{X},t) := D\boldsymbol{\varphi}(\boldsymbol{X},t) = \nabla\boldsymbol{\varphi}(\boldsymbol{X},t) \ . \tag{2.6}$$

Since the deformation map $\boldsymbol{\varphi}$ is a one-to-one mapping, the determinant of $\boldsymbol{F}$ is constrained to $\det[\boldsymbol{F}] \neq 0$. Furthermore, as interpenetration of matter is excluded the determinant has to be non-negative. Consequently

$$J := \det[\boldsymbol{F}] > 0 \tag{2.7}$$

is a fundamental physically based constraint for the deformation map $\boldsymbol{\varphi}$. To provide a geometric interpretation of the deformation map consider a material curve $\hat{C}(\theta) \in \mathcal{B}$, parameterized by a variable $\theta \in \mathcal{R}$. The spatial counterpart of the material curve is $\hat{c}(\theta) = \boldsymbol{\varphi}(\hat{C}(\theta),t) \in \mathcal{S}$. Introducing the material and spatial tangents to these curves $\boldsymbol{T} = d\hat{C}/d\theta \in T_{\boldsymbol{X}}\mathcal{B}$ and $\boldsymbol{t} = d\hat{c}/d\theta \in T_{\boldsymbol{x}}\mathcal{S}$ and using the chain rule yields

$$\boldsymbol{t} = \frac{d\hat{c}(\theta)}{d\theta} = \frac{d\boldsymbol{\varphi}(\hat{C}(\theta))}{d\theta} = \nabla\boldsymbol{\varphi} \cdot \frac{d\hat{C}(\theta)}{d\theta} = \boldsymbol{F}\boldsymbol{T} \ . \tag{2.8}$$

Here we introduced the material and spatial tangent spaces $T_{\boldsymbol{X}}\mathcal{B}$ and $T_{\boldsymbol{x}}\mathcal{S}$. Thus the deformation gradient is a linear mapping from tangent vectors $\boldsymbol{T}$ at material curves onto tangent vectors $\boldsymbol{t}$ at spatial curves

$$\boldsymbol{F} : \begin{cases} T_{\boldsymbol{X}}\mathcal{B} \to T_{\boldsymbol{x}}\mathcal{S}, \\ \boldsymbol{T} \mapsto \boldsymbol{t} = \boldsymbol{F}\boldsymbol{T}. \end{cases} \tag{2.9}$$

Normal and area map. Now consider two material curves $\hat{C}_1(\theta_1)$ and $\hat{C}_2(\theta_2)$ with their spatial counterparts $\hat{c}_1$ and $\hat{c}_2$. At the intersection point the two tangential vectors onto these curves span a material and spatial plane $d\boldsymbol{A} = \boldsymbol{T}_1 \times \boldsymbol{T}_2$ and $d\boldsymbol{a} = \boldsymbol{t}_1 \times \boldsymbol{t}_2$. Recalling the definition of the determinant of a tensor $\boldsymbol{A} \in \mathcal{R}^{3\times3}$

$$(\boldsymbol{A}\boldsymbol{u}) \cdot [(\boldsymbol{A}\boldsymbol{v}) \times (\boldsymbol{A}\boldsymbol{w})] = \det[\boldsymbol{A}]\boldsymbol{u} \cdot [\boldsymbol{v} \times \boldsymbol{w}] \tag{2.10}$$

that can be reformulated to $\boldsymbol{u} \cdot [\boldsymbol{A}^T(\boldsymbol{A}\boldsymbol{v} \times \boldsymbol{A}\boldsymbol{w})] = \boldsymbol{u} \cdot [\det[\boldsymbol{A}](\boldsymbol{v} \times \boldsymbol{w})]$. This has to be valid for arbitrary $\boldsymbol{u} \in \mathcal{R}^3$ yielding $\boldsymbol{A}\boldsymbol{v} \times \boldsymbol{A}\boldsymbol{w} = \det[\boldsymbol{A}]\boldsymbol{A}^{-T}(\boldsymbol{v} \times \boldsymbol{w})$. Using this relation yields the identity

$$d\boldsymbol{a} = \boldsymbol{t}_1 \times \boldsymbol{t}_2 = \boldsymbol{F}\boldsymbol{T}_1 \times \boldsymbol{F}\boldsymbol{T}_2 = J\boldsymbol{F}^{-T}(\boldsymbol{T}_1 \times \boldsymbol{T}_2) = \operatorname{cof}[\boldsymbol{F}]d\boldsymbol{A} \ , \tag{2.11}$$

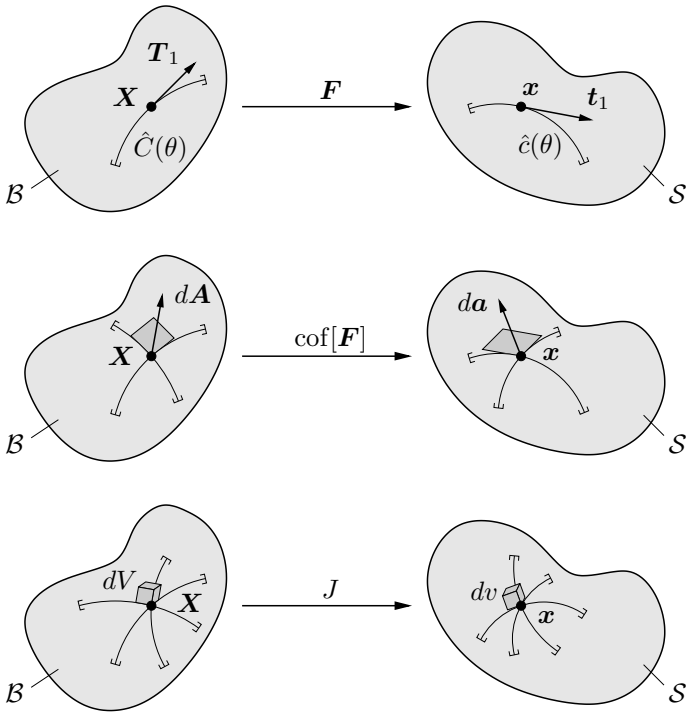

Figure 2.2: *Basic mappings of continuum mechanics.* The tangent map via the deformation gradient $\boldsymbol{t} = \boldsymbol{F}\boldsymbol{T}$, Nanson's formula for the mapping of areas $d\boldsymbol{a} = \mathrm{cof}[\boldsymbol{F}]d\boldsymbol{A}$ and the volume map via the Jacobian $dv = JdV$.

which is known as *Nanson's formula*. It maps material area vectors $d\boldsymbol{A} \in T^*_{\boldsymbol{X}}\mathcal{B}$ of the material co-tangential space $T^*_{\boldsymbol{X}}\mathcal{B}$ onto spatial area vectors $d\boldsymbol{a} \in T^*_{\boldsymbol{x}}\mathcal{S}$ of the spatial co-tangential space $T^*_{\boldsymbol{x}}\mathcal{S}$. Since J is a scalar preserving the change of the deforming area, the map between material and spatial normal vectors can be identified as the quantity

$$\boldsymbol{F}^{-T} : \begin{cases} T^*_{\boldsymbol{X}}\mathcal{B} \to T^*_{\boldsymbol{x}}\mathcal{S}, \\ \boldsymbol{N} \mapsto \boldsymbol{n} = \boldsymbol{F}^{-T}\boldsymbol{N}. \end{cases} \tag{2.12}$$

Volume map. For the deformation of volume elements consider three material curves and at their intersection point their three tangential vectors $\boldsymbol{T}_1$, $\boldsymbol{T}_2$ and $\boldsymbol{T}_3$. The volume of the parallelepiped spanned by these three vectors is hence given as $dV = \boldsymbol{T}_1 \cdot (\boldsymbol{T}_2 \times \boldsymbol{T}_3)$. The spatial counterpart is the deformed parallelepiped with volume $dv = \boldsymbol{t}_1 \cdot (\boldsymbol{t}_2 \times \boldsymbol{t}_3)$, where $\boldsymbol{t}_i = \boldsymbol{F}\boldsymbol{T}_i$ for $i = 1, 2, 3$ are the spatial tangent vectors. Using relation (2.10) yields

$$dv = \boldsymbol{t}_1 \cdot (\boldsymbol{t}_2 \times \boldsymbol{t}_3) = \boldsymbol{F}\boldsymbol{T}_1 \cdot (\boldsymbol{F}\boldsymbol{T}_2 \times \boldsymbol{F}\boldsymbol{T}_3) = JdV \ . \tag{2.13}$$

Hence the Jacobian J is identified to transform material into spatial volume elements. Formally we introduce the Jacobian as the mapping

$$J : \begin{cases} \mathcal{R}_+ \to \mathcal{R}_+, \\ dV \mapsto dv = JdV \ . \end{cases} \tag{2.14}$$

The three basic mappings of continuum mechanics are visualized in Figure 2.2.

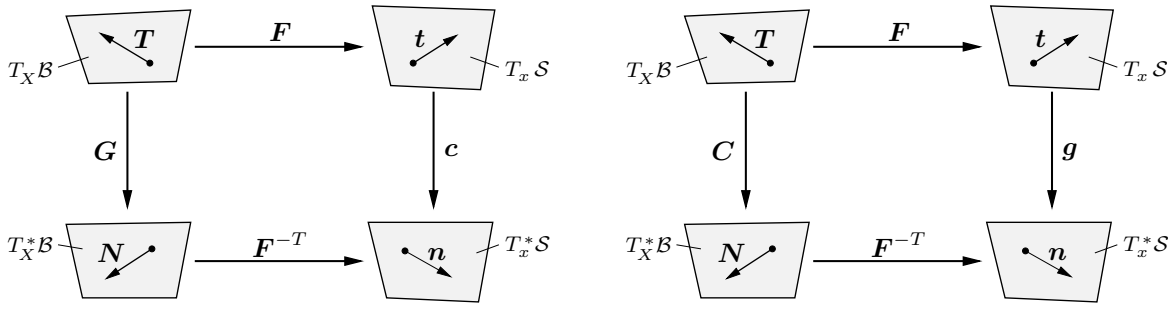

Figure 2.3: *Metric tensors as mappings.* The Lagrangian metric $\boldsymbol{G}$ can be pushed forward in the current configuration yielding the left Cauchy-Green tensor $\boldsymbol{c} = \boldsymbol{\varphi}_*(\boldsymbol{G})$. Analogously the Eulerian metric $\boldsymbol{g}$ has a material representation, which is denoted as the right Cauchy-Green tensor $\boldsymbol{C} = \boldsymbol{\varphi}^*(\boldsymbol{g})$.

2.1.4. Measurement of strains

To be able to measure the deformation at a local point of a body consider a material and a spatial tangential vector $\boldsymbol{T}$ and $\boldsymbol{t} = \boldsymbol{F}\boldsymbol{T}$. The idea is to compare the lengths of the two tangents. They are defined as

$$|\boldsymbol{T}|_{\boldsymbol{G}} = \sqrt{\boldsymbol{T} \cdot (\boldsymbol{G}\boldsymbol{T})} \quad \text{and} \quad |\boldsymbol{t}|_{\boldsymbol{g}} = \sqrt{\boldsymbol{t} \cdot (\boldsymbol{g}\boldsymbol{t})} \,, \tag{2.15}$$

where the material and spatial metric tensors of the Lagrangian and Eulerian Cartesian frames, $\boldsymbol{G} = \delta_{AB}\boldsymbol{E}^A \otimes \boldsymbol{E}^B$ and $\boldsymbol{g} = \delta_{ab}\boldsymbol{e}^a \otimes \boldsymbol{e}^b$, are introduced. There are two possibilities to measure the strain. The first one is to choose the material tangent to have unit length, that is $|\boldsymbol{T}|_{\boldsymbol{G}} = 1$. Then, the stretch λ equals the length of the spatial tangent and follows with (2.8) as

$$\lambda := |\boldsymbol{t}|_{\boldsymbol{g}} = \sqrt{\boldsymbol{t} \cdot (\boldsymbol{g}\boldsymbol{t})} = \sqrt{(\boldsymbol{F}\boldsymbol{T}) \cdot \boldsymbol{g}(\boldsymbol{F}\boldsymbol{T})} = \sqrt{\boldsymbol{T} \cdot \boldsymbol{C}\boldsymbol{T}} = |\boldsymbol{T}|_{\boldsymbol{C}} \,. \tag{2.16}$$

In the same manner, the spatial tangential vector can also be chosen such that $|\boldsymbol{t}|_{\boldsymbol{g}} = 1$. The stretch follows as $1/\lambda = |\boldsymbol{T}|_{\boldsymbol{G}} = \sqrt{\boldsymbol{F}^{-1}\boldsymbol{t} \cdot \boldsymbol{G}\boldsymbol{F}^{-1}\boldsymbol{t}} = |\boldsymbol{t}|_{\boldsymbol{c}}$. Here, the positive definite, symmetric *right* and *left Cauchy-Green tensors* are introduced as

$$\boldsymbol{C} := \boldsymbol{F}^T\boldsymbol{g}\boldsymbol{F} \quad \text{and} \quad \boldsymbol{c} := \boldsymbol{F}^{-T}\boldsymbol{G}\boldsymbol{F}^{-1} \,. \tag{2.17}$$

The right Cauchy-Green tensor $\boldsymbol{C}$ is a material tensor and can also be considered as the pull-back of the Eulerian metric in the Lagrangian configuration. Analogously, the left Cauchy-Green tensor is the push-forward of the Lagrangian metric in the Eulerian configuration. Formally this is written as

$$\boldsymbol{C} = \boldsymbol{\varphi}^*(\boldsymbol{g}) \quad \text{and} \quad \boldsymbol{c} = \boldsymbol{\varphi}_*(\boldsymbol{G}) \,, \tag{2.18}$$

where the pull-back $\boldsymbol{\varphi}^*(\cdot)$ and the push-forward $\boldsymbol{\varphi}_*(\cdot)$ operations are introduced. The basic geometric mappings between tangential and cotangential spaces of the material and spatial configurations are depicted in Figure 2.3.

2.2. Fundamental stress measures and thermal flux

Before stating the physical balance principles, mechanical stress tensors and thermal flux vectors have to be introduced. Consider a part $\mathcal{P}_{\mathcal{S}} \subset \mathcal{S}$ cut out of the deformed solid

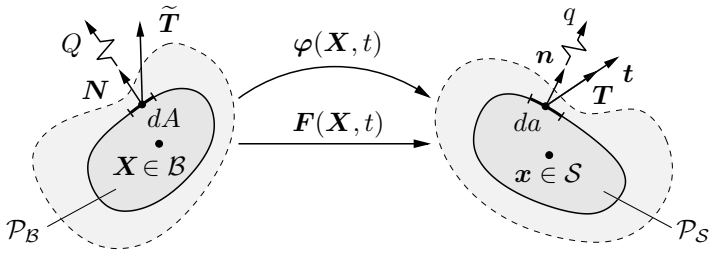

Figure 2.4: *Euler's cut principle.* Lagrangian and Eulerian parts $\mathcal{P}_{\mathcal{B}}$ and $\mathcal{P}_{\mathcal{S}}$ are cut out of $\mathcal{B}$ and $\mathcal{S}$. At a point $\boldsymbol{x} \in \partial\mathcal{P}_{\mathcal{S}}$ on the surface of $\mathcal{P}_{\mathcal{S}}$, the action of the remaining part is replaced by the traction vector $\boldsymbol{t} = \boldsymbol{\sigma}\boldsymbol{n}$ and the heat flux $q = \boldsymbol{q}\boldsymbol{n}$.

$\mathcal{S}$. According to *Euler's cut principle* the mechanical and thermal influences of the cut off part $\mathcal{S} \setminus \mathcal{P}_{\mathcal{S}}$ onto $\mathcal{P}_{\mathcal{S}}$ are accounted for by the introduction of the mechanical surface traction $\boldsymbol{t}(\boldsymbol{x}, t)$ and the thermal heat flux $q(\boldsymbol{x}, t)$. The material counterpart of $\mathcal{P}_{\mathcal{S}}$ is given as $\mathcal{P}_{\mathcal{B}} = \boldsymbol{\varphi}^{-1}(\mathcal{P}_{\mathcal{S}})$. A graphical visualization of this setting is given in Figure 2.4. Here, $\boldsymbol{N}$ and $\boldsymbol{n}$ are the material and spatial outward normal vectors of an area element $dA \subset \mathcal{P}_{\mathcal{B}}$ and $da \subset \mathcal{P}_{\mathcal{S}}$ of the material and spatial surfaces.

2.2.1. Cauchy theorem and stress tensors

The *Cauchy theorem* postulates a linear relationship between the mechanical surface traction $\boldsymbol{t}$ and the spatial normal vector $\boldsymbol{n}$

$$\boldsymbol{t}(\boldsymbol{x}, t; \boldsymbol{n}) := \boldsymbol{\sigma}(\boldsymbol{x}, t)\boldsymbol{n} \ , \tag{2.19}$$

where the *true* or *Cauchy stress tensor* $\boldsymbol{\sigma}$ is introduced. Since it relates the actual force to the deformed area it is the stress tensor with the basic physical meaning. However, as more convenient for the modeling, we introduce further stress tensors. Weighting the stress $\boldsymbol{\sigma}$ by the volume map J yields the *Kirchhoff stress*

$$\boldsymbol{\tau}(\boldsymbol{x}, t) := J\boldsymbol{\sigma}(\boldsymbol{x}, t) \ . \tag{2.20}$$

Both $\boldsymbol{\sigma}$ and $\boldsymbol{\tau}$ are purely Eulerian objects mapping spatial normals onto spatial tangents

$$\boldsymbol{\sigma} : \begin{cases} T^*_{\boldsymbol{x}}\mathcal{S} \to T_{\boldsymbol{x}}\mathcal{S}, \\ \boldsymbol{n} \mapsto \boldsymbol{t} = \boldsymbol{\sigma}\boldsymbol{n} \end{cases} \quad \text{and} \quad \boldsymbol{\tau} : \begin{cases} T^*_{\boldsymbol{x}}\mathcal{S} \to T_{\boldsymbol{x}}\mathcal{S}, \\ \boldsymbol{n} \mapsto J\boldsymbol{t} = \boldsymbol{\tau}\boldsymbol{n} \ . \end{cases} \tag{2.21}$$

Furthermore, a Cauchy-like relation that relates actual force to the reference area gives rise to the introduction of the *1st Piola-Kirchhoff stress* $\widetilde{\boldsymbol{P}}$

$$\boldsymbol{T}(\boldsymbol{X}, t; \boldsymbol{N}) := \widetilde{\boldsymbol{P}}(\boldsymbol{X}, t)\boldsymbol{N} \ . \tag{2.22}$$

This is the conveniently used stress for experimental observations, for instance in tensile tests of metals. Note that $\boldsymbol{T}$ is a spatial object that is related to the actual surface traction via the relation $\boldsymbol{t}da = \boldsymbol{T}dA$. Thus $\widetilde{\boldsymbol{P}}$ is connected to the Cauchy stress by

$$\widetilde{\boldsymbol{P}} = J\boldsymbol{\sigma}\boldsymbol{F}^{-T} \ . \tag{2.23}$$

In contrast to the symmetric one-point Cauchy and Kirchhoff stress tensors the 1st Piola-Kirchhoff stress is unsymmetric and a two-point tensor field which can be written as the

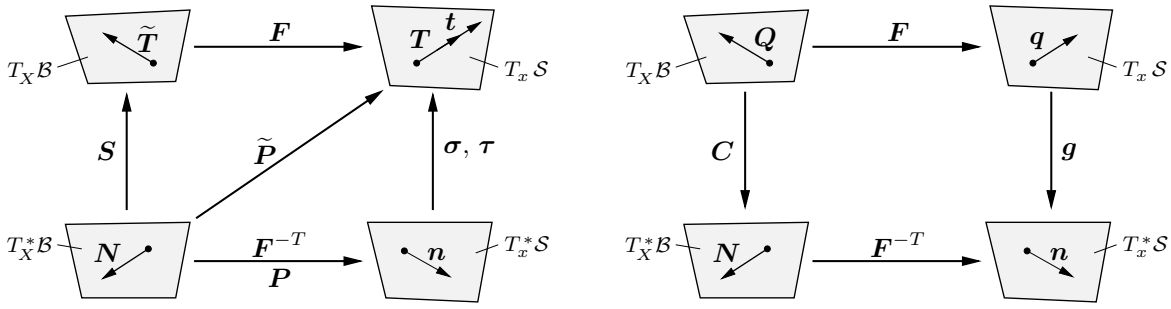

Figure 2.5: *Mapping properties of stress tensors and heat flux vectors.* Purely Eulerian Cauchy and Kirchhoff stress tensors $\boldsymbol{\sigma}$ and $\boldsymbol{\tau}$, two-point 1st Piola-Kirchhoff stress $\widetilde{\boldsymbol{P}}$ and modified 1st P-K. $\boldsymbol{P}$ as well as purely Lagrangian 2nd Piola-Kirchhoff stress $\boldsymbol{S}$. Additionally, Eulerian and Lagrangian heat flux vectors $\boldsymbol{q}$ and $\boldsymbol{Q}$.

mapping

$$\widetilde{\boldsymbol{P}} : \begin{cases} T_{\boldsymbol{X}}^*\mathcal{B} \to T_{\boldsymbol{x}}\mathcal{S}, \\ \boldsymbol{N} \mapsto \boldsymbol{T} = \widetilde{\boldsymbol{P}}\boldsymbol{N} \ . \end{cases} \tag{2.24}$$

Often a modified representation $\boldsymbol{P} := \boldsymbol{g}\widetilde{\boldsymbol{P}}$ of the 1st Piola-Kirchhoff stress $\widetilde{\boldsymbol{P}}$ is used. Since for the case of a Cartesian frame the two representations are identical as $\boldsymbol{g} = \boldsymbol{1}$ we do not distinguish between them in the following and denote the 1st Piola-Kirchhoff stress by $\boldsymbol{P}$. A purely Lagrangian stress tensor is the symmetric *2nd Piola-Kirchhoff stress*. It is obtained by pulling back the spatial tangent $\widetilde{\boldsymbol{T}} = \boldsymbol{\varphi}^*(\boldsymbol{T})$ and constituting a Cauchy-type theorem $\widetilde{\boldsymbol{T}} = \boldsymbol{S}\boldsymbol{N}$. The 2nd Piola-Kirchhoff stress is connected to the 1st Piola-Kirchhoff stress via the relation $\boldsymbol{S} = \boldsymbol{F}^{-1}\boldsymbol{P}$.

2.2.2. Stokes' theorem and heat flux

In analogy to the mechanical Cauchy theorem, the *Stokes' heat flux theorem* postulates a linear relationship between heat flux and spatial normal

$$q(\boldsymbol{x}, t; \boldsymbol{n}) := \boldsymbol{q}(\boldsymbol{x}, t) \cdot \boldsymbol{n} \ , \tag{2.25}$$

where the spatial heat flux vector $\boldsymbol{q}$ is introduced. As for the Cauchy stress $\boldsymbol{\sigma}$ the heat flux $\boldsymbol{q}$ is the *true* heat flux with basic physical meaning. A Lagrangian heat flux vector $\boldsymbol{Q}$ can be introduced by a Stokes-like theorem $Q = \boldsymbol{Q} \cdot \boldsymbol{N}$. Together with the relationship $QdA = qda$ we obtain

$$\boldsymbol{Q} := J\boldsymbol{F}^{-1}\boldsymbol{q} \ . \tag{2.26}$$

The material heat flux vector $\boldsymbol{Q}$ is sometimes called *Piola-Kirchhoff heat flux vector*, see e.g. Šilhavý [266]. The geometric mapping properties of the stress tensors as well as the heat flux vectors are visualized in Figure 2.5.

2.3. Physical balance principles

The objective of this section is the introduction of general physical statements of continuum mechanics. These statements have to hold for every material and do not depend on any material parameters. They result in balance principles for physical quantities such

as mass, linear and angular momentum, energy and entropy and are based on Euler's cut principle. Evaluating these physical quantities in a cut out part $\mathcal{P}_\mathcal{S}$ of the deformed body yields *global statements* of the balance laws. Since the physical statements have to hold for the whole body as well as every arbitrary part of it, the global forms can be localized to *local balance principles* valid at arbitrary positions of the spatial configuration $\boldsymbol{x} \in \mathcal{S}$. Considering the undeformed part $\mathcal{P}_\mathcal{B}$, local statements can alternatively be formulated with respect to arbitrary reference positions $\boldsymbol{X} \in \mathcal{B}$.

2.3.1. Balance of mass

The balance of mass demands that the total mass of the body $\mathcal{P}_\mathcal{S}$ remains constant. This excludes mass production and a flux of mass over the surface $\partial\mathcal{P}_\mathcal{S}$. Defining the total mass $\mathcal{M}_{\mathcal{P}_\mathcal{S}}$ of the part $\mathcal{P}_\mathcal{S}$, the *reference density* $\rho_0(\boldsymbol{X})$ and the *actual mass density* $\rho(\boldsymbol{x}, t)$, the *global mass balance* can be written as

$$\frac{d}{dt}\mathcal{M}_{\mathcal{P}_\mathcal{S}} := \frac{d}{dt}\int_{\mathcal{P}_\mathcal{S}} \rho(\boldsymbol{x}, t)\, dv = \frac{d}{dt}\int_{\mathcal{P}_\mathcal{B}} \rho_0(\boldsymbol{X})\, dV = 0 \ . \tag{2.27}$$

Evaluating the second and third term of (2.27) by using the volume map $dv = J\, dV$ yields the *material* and *spatial local form* of the conservation of mass as

$$J\rho(\boldsymbol{x}, t) = \rho_0(\boldsymbol{X}) \quad \text{and} \quad \dot{\rho} + \rho\, \mathrm{div}[\boldsymbol{v}] = 0 \ , \tag{2.28}$$

where we denote $\mathrm{div}[\,\cdot\,] = (\cdot) \cdot \nabla_{\boldsymbol{x}}$ by the spatial divergence of a quantity $(\cdot)$.

2.3.2. Balance of linear momentum

The balance of linear momentum states that the change of linear momentum $\mathcal{I}_{\mathcal{P}_\mathcal{S}}$ in time is equal to the forces $\mathcal{F}_{\mathcal{P}_\mathcal{S}}$ acting on the body $\mathcal{P}_\mathcal{S}$. Additionally to the surface traction $\boldsymbol{t}(\boldsymbol{x}, t)$ introduced before, a mass specific body force $\boldsymbol{b}(\boldsymbol{x}, t)$ is assumed. The *global form* is given as

$$\frac{d}{dt}\mathcal{I}_{\mathcal{P}_\mathcal{S}} = \frac{d}{dt}\int_{\mathcal{P}_\mathcal{S}} \rho\boldsymbol{v}\, dv = \int_{\mathcal{P}_\mathcal{S}} \rho\boldsymbol{b}\, dv + \int_{\partial\mathcal{P}_\mathcal{S}} \boldsymbol{t}\, da = \mathcal{F}_{\mathcal{P}_\mathcal{S}} \ . \tag{2.29}$$

Together with the Cauchy theorem (2.19) and by use of Stokes' theorem to change the surface integral into a volume integral, we get the *spatial local form* as

$$\rho\dot{\boldsymbol{v}} = \rho\boldsymbol{b} + \mathrm{div}[\boldsymbol{\sigma}] \ . \tag{2.30}$$

Analogously, using (2.22) yields the *material local form* of the balance of linear momentum

$$\rho_0\dot{\boldsymbol{V}} = \rho_0\boldsymbol{b} + \mathrm{Div}[\boldsymbol{P}] \ . \tag{2.31}$$

Here $\mathrm{Div}[\,\cdot\,] = (\cdot) \cdot \nabla$ is denoted by the material divergence of a quantity $(\cdot)$.

2.3.3. Balance of angular momentum

Similar to the statement of the balance of linear momentum, the balance of angular momentum balances the change of angular momentum $\mathcal{D}^{\mathcal{O}}_{\mathcal{P}_\mathcal{S}}$ with respect to a fixed position

in space $\mathcal{O}$ to the resultant moment of the forces $\mathcal{M}^{\mathcal{O}}_{\mathcal{P}_\mathcal{S}}$ acting on the body. The *global form* is given as

$$\frac{d}{dt}\mathcal{D}^{\mathcal{O}}_{\mathcal{P}_\mathcal{S}} = \frac{d}{dt}\int_{\mathcal{P}_\mathcal{S}} \boldsymbol{x} \times \rho \boldsymbol{v}\, dv = \int_{\mathcal{P}_\mathcal{S}} \boldsymbol{x} \times \rho \boldsymbol{b}\, dv + \int_{\partial\mathcal{P}_\mathcal{S}} \boldsymbol{x} \times \boldsymbol{t}\, da = \mathcal{M}^{\mathcal{O}}_{\mathcal{P}_\mathcal{S}} \ . \tag{2.32}$$

Deriving the local forms of the angular momentum balance yield

$$(\boldsymbol{F}\boldsymbol{P}^T)^T = \boldsymbol{F}\boldsymbol{P}^T \quad \text{and} \quad \boldsymbol{\sigma}^T = \boldsymbol{\sigma} \tag{2.33}$$

that is an identity for the 1st Piola-Kirchhoff stress tensor and the symmetry condition for the Cauchy stress tensor.

2.3.4. Balance of energy

The balance of energy describes the change of internal energy in a body. It is often referred to as *first axiom of thermodynamics*. The total energy of a body $\mathcal{P}_\mathcal{S}$ is equal to the kinetic energy $\mathcal{K}_{\mathcal{P}_\mathcal{S}}$ and the internal energy $\mathcal{E}_{\mathcal{P}_\mathcal{S}}$. In particular they are given by

$$\mathcal{K}_{\mathcal{P}_\mathcal{S}} := \int_{\mathcal{P}_\mathcal{S}} \frac{1}{2}\rho \boldsymbol{v}\cdot\boldsymbol{v}\, dv \quad \text{and} \quad \mathcal{E}_{\mathcal{P}_\mathcal{S}} := \int_{\mathcal{P}_\mathcal{S}} e\, dv \ , \tag{2.34}$$

where $e(\boldsymbol{x}, t)$ is the internal energy density per unit volume of the body. Furthermore, the mechanical and thermal external power is introduced as

$$\mathcal{P}_{\mathcal{P}_\mathcal{S}} := \int_{\mathcal{P}_\mathcal{S}} \rho \boldsymbol{b}\cdot\boldsymbol{g}\boldsymbol{v}\, dv + \int_{\partial\mathcal{P}_\mathcal{S}} \boldsymbol{t}\cdot\boldsymbol{g}\boldsymbol{v}\, da \quad \text{and} \quad \mathcal{Q}_{\mathcal{P}_\mathcal{S}} := \int_{\mathcal{P}_\mathcal{S}} \rho r\, dv - \int_{\partial\mathcal{P}_\mathcal{S}} q\, da \tag{2.35}$$

with the heat flux h introduced in (2.25) and a specific heat source per unit mass $r(\boldsymbol{x}, t)$. The *global energy balance* states equality of the change of total energy and the total external power

$$\frac{d}{dt}\left[\mathcal{K}_{\mathcal{P}_\mathcal{S}} + \mathcal{E}_{\mathcal{P}_\mathcal{S}}\right] = \mathcal{P}_{\mathcal{P}_\mathcal{S}} + \mathcal{Q}_{\mathcal{P}_\mathcal{S}} \ . \tag{2.36}$$

Evaluating (2.36) in the same manner as for the other balance equations the *local forms* are obtained as

$$\dot{e}_0 = \boldsymbol{P} : \dot{\boldsymbol{F}} + \rho_0 r - \mathrm{Div}[\boldsymbol{Q}] \quad \text{and} \quad \dot{e} = \boldsymbol{\sigma} : \boldsymbol{g}\boldsymbol{l} + \rho r - \mathrm{div}[\boldsymbol{q}] \ , \tag{2.37}$$

where $e_0(\boldsymbol{X}, t) = Je(\boldsymbol{\varphi}^{-1}(\boldsymbol{x}, t), t)$ is the internal energy density per unit reference volume. Furthermore, $\boldsymbol{l} = \nabla_{\boldsymbol{x}}\boldsymbol{v}$ is denoted as the spatial velocity gradient.

2.3.5. Balance of entropy

The balance of entropy states that the change of entropy $\mathcal{S}_{\mathcal{P}_\mathcal{S}}$ of a body is equal to the entropy power $\mathcal{H}_{\mathcal{P}_\mathcal{S}}$ and an entropy production $\mathcal{G}_{\mathcal{P}_\mathcal{S}}$. Thus the *global form* is

$$\frac{d}{dt}\mathcal{S}_{\mathcal{P}_\mathcal{S}} = \mathcal{G}_{\mathcal{P}_\mathcal{S}} + \mathcal{H}_{\mathcal{P}_\mathcal{S}} \ . \tag{2.38}$$

Here, the specific forms of the three terms in (2.38) are

$$\mathcal{S}_{\mathcal{P}_\mathcal{S}} := \int_{\mathcal{P}_\mathcal{S}} \eta\, dv \ , \quad \mathcal{G}_{\mathcal{P}_\mathcal{S}} := \int_{\mathcal{P}_\mathcal{S}} \frac{\delta}{\theta}\, dv \quad \text{and} \quad \mathcal{H}_{\mathcal{P}_\mathcal{S}} := \int_{\mathcal{P}_\mathcal{S}} \frac{\rho r}{\theta}\, dv - \int_{\partial\mathcal{P}_\mathcal{S}} \frac{q}{\theta}\, da \tag{2.39}$$

with the volume specific entropy $\eta(\boldsymbol{x},t)$, the dissipation δ per unit volume and the absolute temperature $\theta(\boldsymbol{x},t)$. Moreover the specific entropy per unit reference volume is given by $\eta_0(\boldsymbol{X},t) = J\eta(\boldsymbol{\varphi}^{-1}(\boldsymbol{x},t),t)$ and the dissipation per unit reference volume is evaluated as $\delta_0(\boldsymbol{X},t) := J\delta(\boldsymbol{\varphi}^{-1}(\boldsymbol{x},t),t)$. We obtain the *local forms*

$$\begin{aligned} \dot{\eta}_0 &= \frac{\delta_0}{\theta} + \frac{1}{\theta}\left(\rho_0 r - \operatorname{Div}[\boldsymbol{Q}]\right) + \frac{1}{\theta^2}\boldsymbol{Q}\cdot\nabla\theta \ , \\ \dot{\eta} &= \frac{\delta}{\theta} + \frac{1}{\theta}\left(\rho r - \operatorname{div}[\boldsymbol{q}]\right) + \frac{1}{\theta^2}\boldsymbol{q}\cdot\nabla_{\boldsymbol{x}}\theta \ . \end{aligned} \tag{2.40}$$

2.4. Dissipation and second axiom of thermodynamics

The *dissipation postulate* or *second axiom of thermodynamics* provides a major restriction on constitutive equations for elastic and dissipative materials. It states that the dissipation δ has to be always positive, that is in spatial and material form

$$\delta(\boldsymbol{x},t) \geq 0 \quad \text{and} \quad \delta_0(\boldsymbol{X},t) \geq 0 \ . \tag{2.41}$$

Insertion of the balances of entropy (2.40) and energy (2.37) into (2.41) yields in Lagrangian representation

$$\delta_0 = \boldsymbol{P} : \dot{\boldsymbol{F}} - \dot{e}_0 + \dot{\eta}_0\theta - \frac{1}{\theta}\operatorname{Div}[\boldsymbol{Q}]\cdot\nabla\theta \ . \tag{2.42}$$

As it is more convenient for modeling purposes, the *free Helmholtz energy* per unit reference volume $\psi := e_0 - \eta_0\theta$ is introduced. Substitution of the internal energy e_0 by ψ leads to the *Clausius-Duhem inequality*

$$\delta_0 = \boldsymbol{P} : \dot{\boldsymbol{F}} - \eta_0\dot{\theta} - \dot{\psi} - \frac{1}{\theta}\boldsymbol{Q}\cdot\nabla\theta \geq 0 \ . \tag{2.43}$$

This inequality is often splitted into a local and a thermal conductive part, yielding the *Clausius-Planck inequality* and the *Fourier inequality*

$$\delta_0^{\text{loc}} := \boldsymbol{P} : \dot{\boldsymbol{F}} - \eta_0\dot{\theta} - \dot{\psi} \geq 0 \quad \text{and} \quad \delta_0^{\text{th}} := -\frac{1}{\theta}\boldsymbol{Q}\cdot\nabla\theta \geq 0 \ . \tag{2.44}$$

Note that (2.44) gives two separate inequalities that provides sharper restrictions to the constitutive equations than the Clausius-Duhem inequality (2.43).

Chapter 3

Continuum Mechanics of Multicomponent Solids

The continuum-mechanical framework for single-component solids in Chapter 2 is now extended to a macroscopic framework of *large strain continuum mechanics of multicomponent solids*. The general framework presented here is then applied in Chapter 4 and Chapter 5 below to the two model problems of (i) fluid-flow through porous solids and (ii) diffusion processes in elastic materials.

Generally when looking to the literature two different approaches can be found for the mathematical description of multiphasic and multicomponent systems. Namely these are the *mixture theory* and the *macroscopic theory*. The mixture theory goes back to Bowen [42] and Truesdell & Toupin [261]. Within this theory, the balance equations are derived from averaging concepts and the multiple components are represented by superimposed and interacting continua, each possessing its own set of balance equations. For the case of porous media the mixture theory is supplemented by the concept of volume fraction yielding the *theory of porous media*, see Bowen [43, 44], de Boer [72, 73], de Boer & Ehlers [75] or Ehlers [92, 94]. The mathematical framework of this theory is open for a huge spectrum of applications such as diffusion and osmotic problems in multicomponent systems in Wagner [267], Ehlers & Wagner [97], Ehlers et al. [98], drying processes in Kowalski [153], thermo-mechanical coupling in Hassanizadeh [130], non-common temperatures of the components in Ghadiani [114], partially saturated soils in Avci [13], Ehlers & Blome [95] or Gray & Schrefler [118] or mass exchange and mass production in Krause [155], Ehlers et al. [99] or Ricken et al. [226]. An extension of the theory of porous media accounting for electro-mechanical coupling is performed for example in Ehlers [93] and Ehlers et al. [99].

In this work we follow the *macroscopic approach* that goes back to Biot [21] and was extended to the finite strain regime by, among others, Biot [24, 33], Coussy [65, 66] and Weitsman [268]. The generality of this approach, that goes far beyond the original small strain application of Biot [21], has been shown by Biot himself in a broad series of publications where plenty of different applications including thermo-chemo-mechanical coupling, chemical reactions and phase transitions were considered, see Biot [24, 26, 27, 28, 30, 31, 32]. A detailed overview is given in Biot [33]. For a deeper insight into this macroscopic approach to thermodynamics of multiphasic and multicomponent

materials, the reader is referred to these publications as well as to the works of Weitsman [268], Coussy [65, 66, 67] or de Groot & Mazur [80] among others.

In what follows the kinematics of multicomponent systems is shortly introduced in Section 3.1. In this work we restrict the attention to the case of two components. In particular we consider a solid skeleton and one additional component that is referred to as component β in the following. Then in Section 3.2 the original approach proposed by Biot is reviewed. This approach is solely based on thought experiences and the principle of virtual dissipation and is fundamentally different than the classical one. The classical approach to thermodynamics of multicomponent systems bases on physical balance principles and is introduced in Section 3.3. These equations can be seen as an extension of the considerations of Chapter 2 for multiple components. Here we introduce the balance equations in Lagrangian form. They are referred to a *total* elementary volume element dV consisting of all components, but moving with the motion of one "reference" component, which is in this work the solid skeleton. Thus the elementary volume element is *thermodynamically closed* with respect to the solid skeleton but *thermodynamically open* with respect to component β as mass dm of component β can be transferred over the surface. Finally, in Section 3.4 the initial boundary value problem is stated and the constitutive modeling framework is introduced.

3.1. Kinematics of multicomponent solids

Before stating physical balance relations we first introduce the multicomponent solid as well as the basic kinematic fields needed for the subsequent considerations. As stated above, within the macroscopic theory one component (here the solid skeleton) is chosen as reference component. Thus, in order to keep the notation compact, we drop the superscript s for kinematic quantities that refer to the solid skeleton, whereas quantities with a superscript β refer to component β.

3.1.1. Description of motion, velocities, accelerations and particle derivatives

Consider the spatial configuration $\mathcal{S}$ of the multicomponent body at time t. At each spatial position $\boldsymbol{x} \in \mathcal{S}$ both solid particles and particles of component β are present. Although being at the same position $\boldsymbol{x}$ both kind of particles follow their own motion. This is particles of solid and β that are at the same position $\boldsymbol{x} \in \mathcal{S}$ at time t may or may not be at the same position at any other time before and after t.

To this end, we introduce one deformation map $\boldsymbol{\varphi}(\boldsymbol{X}, t)$ describing the motion of the solid as well as a deformation map $\boldsymbol{\varphi}^\beta(\boldsymbol{X}^\beta, t)$ for the motion of component β, that is

$$\boldsymbol{\varphi} : \begin{cases} \mathcal{B} \times T \to \mathcal{S} \subset \mathcal{R}^3, \\ (\boldsymbol{X}, t) \mapsto \boldsymbol{x} = \boldsymbol{\varphi}(\boldsymbol{X}, t) \end{cases} \quad \text{and} \quad \boldsymbol{\varphi}^\beta : \begin{cases} \mathcal{B}^\beta \times T \to \mathcal{S}^\beta \subset \mathcal{R}^3, \\ (\boldsymbol{X}^\beta, t) \mapsto \boldsymbol{x} = \boldsymbol{\varphi}^\beta(\boldsymbol{X}^\beta, t) \ . \end{cases} \tag{3.1}$$

$\boldsymbol{\varphi}$ maps points $\boldsymbol{X} \in \mathcal{B}$ of the material configuration of the solid skeleton to points $\boldsymbol{x} \in \mathcal{S}$ of the spatial configuration of the solid skeleton. In analogy, $\boldsymbol{\varphi}^\beta$ maps points $\boldsymbol{X}^\beta \in \mathcal{B}^\beta$ of the material configuration of component β to points $\boldsymbol{x} \in \mathcal{S}^\beta$ of the spatial configuration of component β. Again note that we dropped the superscript s for kinematic quantities that refer to the solid component. The multicomponent body is defined such that it contains

both components at each spatial position and every point in time. Thus we write $\mathcal{B} \subset \mathcal{B}^\beta$ and $\mathcal{S} \subset \mathcal{S}^\beta$. The material velocity fields of the two components are evaluated from (3.1) as

$$\boldsymbol{V}(\boldsymbol{X},t) = \frac{\partial}{\partial t}\boldsymbol{\varphi}(\boldsymbol{X},t) = \dot{\boldsymbol{\varphi}}(\boldsymbol{X},t) \quad \text{and} \quad \boldsymbol{V}^\beta(\boldsymbol{X}^\beta,t) = \frac{\partial}{\partial t}\boldsymbol{\varphi}^\beta(\boldsymbol{X}^\beta,t) = \dot{\boldsymbol{\varphi}}^\beta(\boldsymbol{X}^\beta,t) \ , \tag{3.2}$$

and the material acceleration fields follow as

$$\boldsymbol{A}(\boldsymbol{X},t) = \frac{\partial^2}{\partial t^2}\boldsymbol{\varphi}(\boldsymbol{X},t) = \ddot{\boldsymbol{\varphi}}(\boldsymbol{X},t) \quad \text{and} \quad \boldsymbol{A}^\beta(\boldsymbol{X}^\beta,t) = \frac{\partial^2}{\partial t^2}\boldsymbol{\varphi}^\beta(\boldsymbol{X}^\beta,t) = \ddot{\boldsymbol{\varphi}}^\beta(\boldsymbol{X}^\beta,t) \ . \tag{3.3}$$

Here we introduce the abbreviation $\dot{F} := \partial_t F$ as the material time derivative of a material field F. According to the considerations of single component bodies in Section 2.1 the spatial velocity fields at a point $\boldsymbol{x} \in \mathcal{S}$ are given by

$$\boldsymbol{v}(\boldsymbol{x},t) = \boldsymbol{V}(\boldsymbol{\varphi}^{-1}(\boldsymbol{x},t),t) \quad \text{and} \quad \boldsymbol{v}^\beta(\boldsymbol{x},t) = \boldsymbol{V}^\beta(\boldsymbol{\varphi}^{\beta\,-1}(\boldsymbol{x},t),t) \ . \tag{3.4}$$

Before evaluating the spatial acceleration fields $\boldsymbol{a}$ and $\boldsymbol{a}^\beta$ we introduce particle derivatives, that is time derivatives of a spatial field $f(\boldsymbol{x},t)$. Following either the motion of the solid or the motion of component β we observe a change in time of the field f of

$$\frac{d^s}{dt}f(\boldsymbol{x},t) := \frac{\partial}{\partial t}f(\boldsymbol{x},t) + \nabla_{\boldsymbol{x}} f(\boldsymbol{x},t)\cdot\boldsymbol{v} \quad \text{or} \quad \frac{d^\beta}{dt}f(\boldsymbol{x},t) := \frac{\partial}{\partial t}f(\boldsymbol{x},t) + \nabla_{\boldsymbol{x}} f(\boldsymbol{x},t)\cdot\boldsymbol{v}^\beta \ . \tag{3.5}$$

As in this work the solid component is chosen as the "reference" we again drop the superscript s and hence define for the subsequent treatment

$$\frac{d^s}{dt}(\cdot) =: \frac{d}{dt}(\cdot) \ . \tag{3.6}$$

Substracting $(3.5)_2$ from $(3.5)_1$ yields a relation between the two particle derivatives

$$\frac{d^\beta}{dt}f(\boldsymbol{x},t) = \frac{d}{dt}f(\boldsymbol{x},t) + \nabla_{\boldsymbol{x}} f(\boldsymbol{x},t)\cdot(\boldsymbol{v}^\beta - \boldsymbol{v}) \ . \tag{3.7}$$

With (3.5) at hand the spatial acceleration fields can be evaluated from (3.4) as

$$\begin{aligned} \boldsymbol{a}(\boldsymbol{x},t) &= \frac{d}{dt}\boldsymbol{v}(\boldsymbol{x},t) &&= \frac{\partial}{\partial t}\boldsymbol{v}(\boldsymbol{x},t) + \nabla_{\boldsymbol{x}}\boldsymbol{v}(\boldsymbol{x},t)\cdot\boldsymbol{v}(\boldsymbol{x},t) \ , \\ \boldsymbol{a}^\beta(\boldsymbol{x},t) &= \frac{d^\beta}{dt}\boldsymbol{v}^\beta(\boldsymbol{x},t) &&= \frac{\partial}{\partial t}\boldsymbol{v}^\beta(\boldsymbol{x},t) + \nabla_{\boldsymbol{x}}\boldsymbol{v}^\beta(\boldsymbol{x},t)\cdot\boldsymbol{v}^\beta(\boldsymbol{x},t) \ . \end{aligned} \tag{3.8}$$

3.1.2. Deformation gradient of solid skeleton

Additionally to the description of the motion for the solid component we introduce the *deformation gradient* of the solid skeleton

$$\boldsymbol{F}(\boldsymbol{X},t) = \nabla\boldsymbol{\varphi}(\boldsymbol{X},t) \ , \tag{3.9}$$

as the most fundamental quantity of finite strain continuum mechanics. Here and henceforward the shortcut $\nabla(\cdot) := \partial_{\boldsymbol{X}}(\cdot)$ is used for the material gradient operator with respect to the solid's reference configuration. Furthermore we introduce the Jacobian of the solid's deformation gradient

$$J(\boldsymbol{X},t) := \det[\boldsymbol{F}(\boldsymbol{X},t)] \ . \tag{3.10}$$

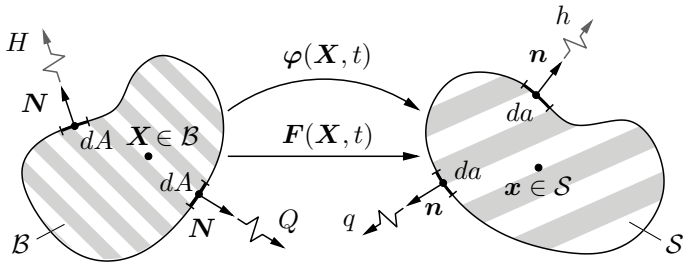

Figure 3.1: *Kinematics of multiphysics problems of solids.* Lagrangian and Eulerian material body $\mathcal{B}$ and $\mathcal{S}$ connected via the deformation map $\boldsymbol{\varphi}(\boldsymbol{X}, t)$ of the solid skeleton. The second component is described by using an open thermodynamic system where a mass flux h is assumed to flow across the spatial boundary $\partial\mathcal{S}$ of the solid skeleton. The relative motion of mass is described by the vector $\mathbb{h}$ with material counterpart $\mathbb{H}$. Furthermore q is the heat flux with material counterpart Q.

3.1.3. Relative mass flux and mass flow vector

As described above, within the macroscopic approach to multicomponent bodies one component (here the solid skeleton) is chosen as "reference" and the motions of all other components (here β) are expressed relative to the motion $\boldsymbol{\varphi}(\boldsymbol{X}, t)$ of this reference. Thus for the description of the motion of β we introduce the *relative spatial mass flux*

$$h := \mathbb{h} \cdot \boldsymbol{n} \quad \text{with} \quad \mathbb{h}(\boldsymbol{x}, t) = m^{\beta}(\boldsymbol{v}^{\beta} - \boldsymbol{v}) \ , \tag{3.11}$$

where $\mathbb{h}$ is denoted as the spatial mass flow vector that can be expressed in terms of the spatial velocity fields of the two components introduced in (3.4) and the actual partial density $m^{\beta}(\boldsymbol{x}, t)$ of component β. Hence $\mathbb{h}$ describes the motion of mass of component β relative to the moving solid.

The mass flow through a surface element da of the deformed boundary $\partial\mathcal{P}_{\mathcal{S}}$ can be evaluated as

$$\int_{\partial\mathcal{P}_{\mathcal{S}}} h \, da = \int_{\partial\mathcal{P}_{\mathcal{S}}} \mathbb{h} \cdot \boldsymbol{n} \, da \ . \tag{3.12}$$

A *material mass flow vector* $\mathbb{H}$ can be introduced by $H = \mathbb{H} \cdot \boldsymbol{N}$, where H is denoted as the relative material mass flux. In analogy to the considerations for the heat flux vector we state

$$\int_{\partial\mathcal{P}_{\mathcal{S}}} h \, da = \int_{\partial\mathcal{P}_{\mathcal{B}}} H \, dA \quad \Rightarrow \quad \mathbb{H} = J\boldsymbol{F}^{-1}\mathbb{h} \ . \tag{3.13}$$

Within the macroscopic Lagrangian treatment of multicomponent solids, the deformation map $\boldsymbol{\varphi}$ of the solid skeleton and the relative fluid mass flow vector $\mathbb{H}$ are the central kinematic quantities. $\mathbb{H}$ as well as its spatial counterpart $\mathbb{h}$ have first been introduced in the finite strain context by Biot [24, 28]. For a visualization of the central kinematic quantities for the subsequent treatment see Figure 3.1.

3.2. Biot's approach to thermodynamics of open systems

In a broad series of publications Biot proposed a macroscopic approach based on the *principle of virtual dissipation*, see Biot [24, 26, 27, 28, 29] and Biot [33]. Within his considerations, Biot reconstructed the thermodynamics of open systems and in particular

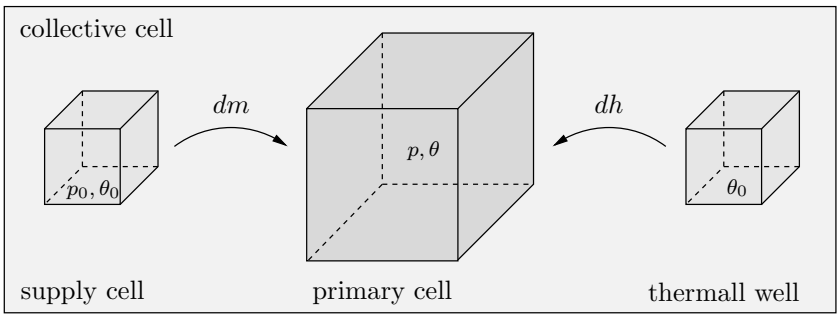

Figure 3.2: *Biot's collective cell.* Thermodynamically closed collective cell consisting of the primary cell, a supply cell and a thermal well. The supply cell and thermal well are used to inject mass dm of component β and heat dh into the primary cell. The supply cell is at constant pressure p_0 and temperature θ_0 no matter how much mass is added or removed. The thermal well is considered as large isothermal reservoir at constant temperature θ_0.

the open system is transferred into a closed system by introduction of supply cells and a thermal well. This leads to new definitions of energy and entropy that circumvents the difficulty of the well-known Gibbs paradox of the classical approach. Within this approach the *convective potential*, that has the advantage of not containing undetermined constants, replaces the chemical potential. All of the considerations of this approach are based on "physical gedankenexperiments". With the thermodynamical quantities defined, the principle of virtual dissipation is stated. The governing equations as well as equations quantifying the heat flux and mass flux of additional components are a direct outcome of this principle. Thus no knowledge of the governing differential equations, that are the physical balance equations, is needed. In what follows the idea of this approach is introduced. For a more detailed introduction into the topic we refer to the comprehensive review Biot [33].

3.2.1. Reconstruction of thermodynamics of open systems

The key idea of this approach is that in contrast to the original thermodynamical open system a closed system is observed. To this end, consider an infinitesimal volume element dV of a multicomponent body. This volume element is denoted as the *primary cell*. The temperature of the primary cell is θ and the pressure of component β inside the primary cell is p. As described above this is a thermodynamically open volume element as heat and mass of component β can be transferred over the surface.

The thermodynamical closed *collective cell* consists in addition to the primary cell of a *supply cell* and a *thermal well*. The supply cell can be viewed as a large reservoir of mass of component β at constant pressure p_0 and temperature θ_0. An increase of mass of β by dm in the primary cell is now achieved by a transfer of mass from the supply cell to the primary cell. The supply cell is assumed to be large enough such that the pressure p_0 is constant no matter how much mass is added or removed from it.

The thermal well is considered as a large isothermal reservoir at constant temperature θ_0. A change in temperature θ of the primary cell is achieved by injecting reversibly by conduction an amount of heat dh from the thermal well into the primary cell. The thermal well is assumed to be large enough such that its temperature θ_0 is constant no matter how much heat is added or removed from it. Thus no mass and heat transfer takes

place over the surface of the collective cell. The collective cell consisting of primary and supply cell as well as thermal well is visualized in Figure 3.2.

One of the key thermodynamical quantities of Biot's approach is the *cell potential* $\mathcal{V}$ defined in terms of the *collective internal energy* $\mathcal{U}$ and *collective entropy increase* $\mathcal{S}$ as

$$\mathcal{V} = \mathcal{U} - \theta_0 \mathcal{S} \ . \tag{3.14}$$

The collective internal energy and entropy increase are all defined based on thought experiments, which is not discussed in detail here. However an important quantity of $\mathcal{V}, \mathcal{U}$ and $\mathcal{S}$ is that in spite of the fact that they refer to the collective cell, they are functions solely of state variables of the primary cell. For the differential we can write

$$d\mathcal{V} = \boldsymbol{P} : d\boldsymbol{F} + \phi \, dm + \vartheta \, d\mathcal{S} \ , \tag{3.15}$$

where ϕ is denoted as the *convective potential* and replaces the chemical potential μ of the classical thermodynamical approach. It is defined as

$$\phi := \psi - \vartheta \bar{s} \quad \text{with} \quad \psi := \int_{p_0,\theta_0}^{p,\theta} \frac{dp}{\rho(p)} + \vartheta d\bar{s} \ , \tag{3.16}$$

where $\vartheta = \theta - \theta_0$ is the increase in temperature of the primary cell and $\bar{s}$ is the relative entropy of component β. A detailed comparison between ϕ and the Gibbs chemical potential μ is provided in Biot [29]. Furthermore in (3.15) we introduced the *total* 1st Piola-Kirchhoff stress tensor $\boldsymbol{P}$.

By introduction of a total entropy displacement vector $\boldsymbol{S} = \boldsymbol{Q}/\theta + \bar{s}\mathbb{H}$ and the produced entropy s^*, the entropy increase $\mathcal{S}$ can be evaluated as

$$\mathcal{S} := s^* + s = s^* - \mathrm{Div}[\boldsymbol{S}] = s^* - \mathrm{Div}[\boldsymbol{Q}/\theta + \bar{s}\mathbb{H}] \ . \tag{3.17}$$

Note that (3.17) is the balance of entropy for $r = 0$, that is for the case where no heat source is considered, see (3.44) below.

From (3.15) we conclude that the convective potential is a function of the deformation gradient, the mass of β and the collective entropy, such that $\mathcal{V} = \hat{\mathcal{V}}(\boldsymbol{F}, m, \mathcal{S})$. Thus (3.15) yields the relations

$$\boldsymbol{P} := \partial_{\boldsymbol{F}} \hat{\mathcal{V}} \ , \quad \phi := \partial_m \hat{\mathcal{V}} \quad \text{and} \quad \vartheta := \partial_{\mathcal{S}} \hat{\mathcal{V}} \ , \tag{3.18}$$

which is in formal accordance to the relations of the classical approach by applying the argumentation of Colemann and Noll.

The quantities $\mathcal{V}, \mathcal{U}$ and $\mathcal{S}$ all have an additive property that allows to define the total cell potential V, the total collective internal energy U and the total collective entropy increase S of a continuous body $\mathcal{B}$ as

$$V = \int_{\mathcal{B}} \mathcal{V} \, dV \ , \quad U = \int_{\mathcal{B}} \mathcal{U} \, dV \quad \text{and} \quad S = \int_{\mathcal{B}} \mathcal{S} \, dV \ . \tag{3.19}$$

3.2.2. The principle of virtual dissipation

With the above defined thermodynamical quantities at hand the principle of virtual dissipation can be stated, which is considered as an extension of d'Alembert's principle to irreversible thermodynamics. The principle of virtual dissipation reads

$$\delta U = \delta W \tag{3.20}$$

and expresses equality of the variation of the total internal energy δU and the variation of the "external energy" δW. By definition the "external energy" includes reversed inertia forces. Thus we write

$$\delta W = -\boldsymbol{I} \cdot \delta \boldsymbol{q} - \delta G + \delta W^{M} + \delta W^{GTH} \tag{3.21}$$

with generalized coordinates $\boldsymbol{q}$ and the potential energy in a gravity field $G = \int_{\mathcal{B}} \mathcal{G}\, dV$ as well as the virtual mechanical work δW^{M} and the virtual work of thermodynamic forces δW^{GTH} at the boundary. The last two are defined as

$$\delta W^{M} = \int_{\partial\mathcal{B}} \bar{\boldsymbol{T}} \cdot \delta \boldsymbol{\varphi}\, dA \quad \text{and} \quad \delta W^{GTH} = -\int_{\partial\mathcal{B}} \left[(\bar{\phi} + \mathcal{G})\delta \mathbb{M} + \bar{\vartheta}\delta \boldsymbol{S}\right] \cdot \boldsymbol{N}\, dA\,. \tag{3.22}$$

In $(3.22)_2$ we introduced the mass fluence $\mathbb{M}$ that is defined via the relation $\dot{\mathbb{M}} = \mathbb{H}$ as well as the prescribed total traction vector $\bar{\boldsymbol{T}}$ acting on the surface $\partial\mathcal{B}$ of the multicomponent body. Using (3.14), (3.17) and (3.21) and due to the fact that there is no heat or mass flux over the boundary of the collective system, the principle of virtual dissipation (3.20) can be rewritten as

$$\boldsymbol{I} \cdot \delta \boldsymbol{q} + \delta V + \delta G + \theta_0 \delta S^{*} = \delta W^{M} + \delta W^{GTH}\,. \tag{3.23}$$

Introducing the reduced variation $\delta_R(\cdot)$ of a quantity $(\cdot)$ excluding its variation with respect to δs^{*} we yield from (3.23)

$$\boldsymbol{I} \cdot \delta \boldsymbol{q} + \delta_R V + \delta G + \int_{\mathcal{B}} \theta \delta s^{*}\, dV = \delta W^{M} + \delta W^{GTH}\,. \tag{3.24}$$

Here $\theta\delta s^{*}$ is the variation of the local rate of intrinsic dissipation. Now consider a local *intrinsic dissipation function* $\mathcal{D} = \hat{\mathcal{D}}(\dot{\boldsymbol{r}})$ in terms of the rates of arbitrary local variables $\dot{\boldsymbol{r}}$. Assuming validity of Onsager's principle, that is assuming only small deviations of local states from the local equilibrium, we write $\theta\delta s^{*} = \partial_{\dot{\boldsymbol{r}}}\mathcal{D} \cdot \delta \boldsymbol{r}$ and thus the principle of virtual dissipation reads

$$\boldsymbol{I} \cdot \delta \boldsymbol{q} + \delta_R V + \delta G + \int_{\mathcal{B}} \partial_{\dot{\boldsymbol{r}}}\mathcal{D} \cdot \delta \boldsymbol{r}\, dV = \delta W^{M} + \delta W^{GTH}\,. \tag{3.25}$$

3.2.3. Model problem of fluid-saturated porous media

In order to get a better insight into the principle of virtual dissipation consider the model problem of fluid-saturated porous solids with heat and mass transfer. We specify

$$\begin{aligned} G &= \int_{\mathcal{B}} (m_0 + m)\bar{\boldsymbol{g}} \cdot \boldsymbol{\varphi}\, dV \\ \boldsymbol{I} \cdot \delta \boldsymbol{q} &= \int_{\mathcal{B}} \left[\left\{\dot{\mathcal{M}} + \mathrm{Div}\left[\left(\boldsymbol{V} + \frac{1}{m_0^{f} + m}\boldsymbol{F}\mathbb{H}\right) \otimes \mathbb{H}\right]\right\} \cdot \delta \boldsymbol{\varphi} + \boldsymbol{F}^{T}\boldsymbol{A}^{f} \cdot \delta \mathbb{M}\right] dV \\ \mathcal{D} &= \frac{1}{2}\mathbb{H} \cdot \widehat{\boldsymbol{K}}^{-1}\mathbb{H} + \mathbb{H} \cdot \boldsymbol{C}^{S}\dot{\boldsymbol{S}} + \frac{\theta}{2}\dot{\boldsymbol{S}} \cdot \boldsymbol{\Lambda}\dot{\boldsymbol{S}} \end{aligned} \tag{3.26}$$

with the initial mass m_0 of the solid-fluid mixture, m_0^f the initial mass of fluid, m the increase of fluid mass, $\bar{g}$ the gravitational force vector, $\widehat{\boldsymbol{K}}^{-1}$ the inverse permeability tensor and $\boldsymbol{\Lambda}$ the thermal resistivity tensor. Furthermore $\boldsymbol{A}^f$ is the acceleration of component β as introduced in $(3.3)_2$. In his original work of 1977, BIOT [28] neglected the part of the acceleration of β relative to the solid skeleton. Thus he identified the acceleration $\boldsymbol{A}^f$ as the acceleration of the solid skeleton, that is $\boldsymbol{A}^f = \dot{\boldsymbol{V}}$. In $(3.26)_3$ the abbreviation $\mathcal{M}$ introduced in (3.38) below has been used. $\boldsymbol{C}^M$ represents a coupling between mass and thermal flow. Evaluation of the principle of virtual dissipation (3.25) by use of (3.18) and (3.26) yields in $\mathcal{B}$ the field equations

$$\begin{aligned} \mathrm{Div}[\boldsymbol{P}] - (m_0+m)\bar{g} &= \dot{\mathcal{M}} + \mathrm{Div}\left[\left(\boldsymbol{V} + \tfrac{1}{m_0^f+m}\boldsymbol{F}\mathbb{H}\right)\otimes\mathbb{H}\right] \,, \\ \nabla[\phi + \bar{g}\cdot\boldsymbol{\varphi}] + \widehat{\boldsymbol{K}}^{-1}\mathbb{H} + \boldsymbol{C}^s\dot{\boldsymbol{S}} &= -\boldsymbol{F}^T\boldsymbol{A}^f \,, \\ \nabla\vartheta + \boldsymbol{C}^{ST}\mathbb{H} + \theta\boldsymbol{\Lambda}\dot{\boldsymbol{S}} &= \boldsymbol{0} \,, \end{aligned} \tag{3.27}$$

along with the Neumann-type boundary conditions

$$\boldsymbol{P}\cdot\boldsymbol{N} = \bar{\boldsymbol{T}} \,, \quad \phi = \bar{\phi} \quad \text{and} \quad \vartheta = \bar{\vartheta} \quad \text{at } \partial\mathcal{B} \,. \tag{3.28}$$

We identify the field equation $(3.27)_1$ as the balance of linear momentum, equation $(3.27)_2$ as the non-isothermal and dynamic extension of the Darcy-type mass flow equation and $(3.27)_3$ as the heat conduction equation.

3.3. Balance equations and dissipation inequality

In contrast to the considerations above, the classical thermodynamical approach to multicomponent systems is reviewed in the following. To this end, the balance equations and the dissipation inequality for materials with one component introduced in Section 2.3 and Section 2.4 are extended to multiple components. Consistent with the macroscopic approach the balance equations of the multicomponent system are expressed in Lagrangian form. They are referred to a *total* elementary volume element dV consisting of all components, but moving with the motion of one "reference" component, which is in this work the solid skeleton. Thus the elementary volume element is *thermodynamically closed* with respect to the solid skeleton but *thermodynamically open* with respect to component β as mass dm of component β can be transferred over the surface. Furthermore, in the macroscopic theory balance equations are stated on the total multicomponent elementary volume element only. Exception is the balance of mass, where the two components are treated separately.

These two points are crucially different when comparing the macroscopic approach to the theory of mixtures and the theory of porous media. In these theories, each component possesses its own set of balance equations in addition to the balance laws for the homogenized total system. Furthermore all these equations are usually expressed in the Eulerian setting. In spite of these differences the macroscopic balance equations correspond to balance equations of the theory of mixtures when a couple of simplifications are met from the beginning: (i) Restriction to two components, (ii) no mass exchange between the two components, (iii) fully saturated conditions, (iv) common temperature fields of the two

components, that is $\theta^s(\boldsymbol{x},t) = \theta^\beta(\boldsymbol{x},t) =: \theta(\boldsymbol{x},t)$ and (v) the stress state of component β contains only a hydrostatic pressure, that is $\boldsymbol{\sigma}^\beta = -p\boldsymbol{1}$. Simplification (v) rules out the possibility of viscous stresses as well as friction forces between the two components.

3.3.1. Balance of mass

The mass conservation is stated separately for each component of the coupled system. As mentioned above, for the solid skeleton a closed thermodynamical system is used for its description and thus the mass of the solid cannot change in time. The global and Lagrangian local forms of the solid's mass conservation can hence be written in analogy to Section 2.3 as

$$\frac{d}{dt}\int_{\mathcal{P}_\mathcal{S}} m^s \, dv = 0 \quad \Rightarrow \quad \int_{\mathcal{P}_\mathcal{S}} m^s \, dv = \int_{\mathcal{P}_\mathcal{B}} m_0^s \, dV \quad \Rightarrow \quad J m^s = m_0^s \; , \tag{3.29}$$

where m_0^s and m^s are denoted as the reference and current partial mass density of the solid. Note that these are not the true mass densities ρ_0^s and ρ^s as introduced in Chapter 2 as the multicomponent elementary volume elements dV and dv contain both solid and β particles. For the case of porous solids, as considered in Chapter 4, both can be connected by the relation $m^s = \rho^s dv^s/dv = \rho^s(1-n)$ in terms of the current porosity n.

Next consider the balance of mass of component β. Within the macroscopic theory the balance equations are expressed in Lagrangian form and refer to a total elementary volume element deforming with the solid's deformation. Thus the considered elementary volume element is thermodynamically open with respect to component β as mass dm of component β can be transferred over the surface. Hence the global form of the mass conservation in the material setting reads

$$\frac{d}{dt}\int_{\mathcal{P}_\mathcal{B}} (m_0^\beta + m) \, dV = -\int_{\partial\mathcal{P}_\mathcal{B}} H \, dA \; , \tag{3.30}$$

where m_0^β and $m(\boldsymbol{X},t)$ are denoted as the initial and the relative change of mass of component β per unit reference volume of the solid. The material local form of the mass balance of component β can then be evaluated as

$$\dot{m} = -\operatorname{Div}[\mathbb{H}] \; . \tag{3.31}$$

The Lagrangian local form (3.31) of mass balance of β can also be gained on an alternative way. When following the motion of component β and excluding mass production (as above) we are dealing with a thermodynamically closed system again. Thus with the partial derivative d^β/dt introduced in $(3.5)_2$ at hand, the mass balance of β can be written in the classical way as

$$\frac{d^\beta}{dt}\int_{\mathcal{P}_\mathcal{S}} m^\beta \, dv = 0 \; , \tag{3.32}$$

where m^β is the partial density of component β. In analogy to the consideration above, for the case of porous solids the partial density can be connected to the true density ρ^β by the relation $m^\beta = \rho^\beta \, dv^\beta/dv = \rho^\beta n$ in terms of the porosity n. Reformulation of (3.32) by use of (3.7) yields

$$\int_{\mathcal{P}_\mathcal{S}} \frac{d}{dt} m^\beta + m^\beta \operatorname{div}[\boldsymbol{v}] + \operatorname{div}\left[m^\beta(\boldsymbol{v}^\beta - \boldsymbol{v})\right] \, dv = 0 \; . \tag{3.33}$$

Here $\boldsymbol{v}$ and $\boldsymbol{v}^\beta$ are the spatial velocities of the solid and of component β as introduced in (3.4). Further manipulations by use of the volume map and Stokes' theorem yield

$$\begin{aligned} &\frac{d}{dt}\int_{\mathcal{P}_\mathcal{B}} m^\beta J\, dV + \int_{\partial\mathcal{P}_\mathcal{S}} \left[m^\beta(\boldsymbol{v}^\beta - \boldsymbol{v})\right]\cdot \boldsymbol{n}\, da \qquad\quad = 0\ , \\ \Leftrightarrow\ &\frac{d}{dt}\int_{\mathcal{P}_\mathcal{B}} m^\beta J\, dV + \int_{\partial\mathcal{P}_\mathcal{B}} \left[J m^\beta \boldsymbol{F}^{-1}(\boldsymbol{v}^\beta - \boldsymbol{V})\right]\cdot \boldsymbol{N}\, dA = 0\ . \end{aligned} \tag{3.34}$$

By comparing (3.30) with (3.34) we identify the relations

$$J m^\beta = m_0^\beta + m \quad , \quad \mathbb{H} = (m_0^\beta + m)\boldsymbol{F}^{-1}(\boldsymbol{v}^\beta - \boldsymbol{V}) \quad \text{and} \quad \mathbb{h} = m^\beta(\boldsymbol{v}^\beta - \boldsymbol{v})\ . \tag{3.35}$$

These relations give a deeper physical understanding of the introduced quantities m, $\mathbb{h}$ and $\mathbb{H}$ based on classical quantities known from the theory of mixture.

In the following we do not make use of the partial porosity m^β of component β as well as the porosity n. Following the considerations of Biot [24, 28] the state of the two-component system is fully characterized by the deformation map $\boldsymbol{\varphi}(\boldsymbol{X}, t)$ of the solid and the relative change of mass $m(\boldsymbol{X}, t)$ of β per unit reference volume of the solid.

3.3.2. Balance of linear momentum

The balance of linear momentum is in the macroscopic theory stated only for a total elementary volume element containing all components. The difference compared to the form (2.29) for solids with only one component is due to an additional momentum of component β. The global form reads

$$\dot{\mathfrak{J}} = \int_{\mathcal{P}_\mathcal{B}} (m_0 + m)\boldsymbol{b}\, dV + \int_{\partial\mathcal{P}_\mathcal{B}} \boldsymbol{T}\, dA\ , \tag{3.36}$$

where $m_0 := m_0^\beta + m_0^s$ is the reference partial density of the two-component system, $\boldsymbol{b}$ is a mass specific body force and $\boldsymbol{T}$ is the total surface traction vector. The change in time of linear momentum is abbreviated by $\dot{\mathfrak{J}}$ and given by

$$\begin{aligned} \dot{\mathfrak{J}} \ &:= \ \frac{d}{dt}\int_{\mathcal{P}_\mathcal{S}} m^s \boldsymbol{v}\, dv + \frac{d^\beta}{dt}\int_{\mathcal{P}_\mathcal{S}} m^\beta \boldsymbol{v}^\beta\, dv \\ &= \ \frac{d}{dt}\int_{\mathcal{P}_\mathcal{B}} (m_0 + m)\boldsymbol{V} + \boldsymbol{F}\mathbb{H}\, dV + \int_{\partial\mathcal{P}_\mathcal{B}} \left(\boldsymbol{V} + \frac{1}{m_0^\beta + m}\boldsymbol{F}\mathbb{H}\right)(\mathbb{H}\cdot\boldsymbol{N})\, dA\ . \end{aligned} \tag{3.37}$$

The local form of the balance of linear momentum can be evaluated from (3.36) as

$$\dot{\mathcal{M}} + \mathrm{Div}\left[\left(\boldsymbol{V} + \frac{1}{m_0^\beta + m}\boldsymbol{F}\mathbb{H}\right)\otimes\mathbb{H}\right] = (m_0 + m)\boldsymbol{b} + \mathrm{Div}[\boldsymbol{P}]\ , \tag{3.38}$$

with the momentum per unit undeformed volume $\mathcal{M} := (m_0 + m)\boldsymbol{V} + \boldsymbol{F}\mathbb{H}$ and where m_0 is the initial mass density of the total system. The second term is due to the rate of momentum of β that is gained by convection. This form can be equivalently found in Coussy [67], Biot [28, 33] and Gajo & Denzer [111] and is also in line with the corresponding expression in the theory of mixtures, see e.g. Bowen [42] or Ehlers [92]. Note that in Biot [28] the term with the square of the relative mass flow vector $\mathbb{H}\otimes\mathbb{H}$ is neglected.

3.3.3. Balance of angular momentum

The global form of the angular momentum balance can in accordance to the balance of linear momentum (3.36) be given by

$$\frac{d}{dt}\int_{\mathcal{P}_\mathcal{S}} \boldsymbol{x}\times m^s\boldsymbol{v}\,dv + \frac{d^\beta}{dt}\int_{\mathcal{P}_\mathcal{S}} \boldsymbol{x}\times m^\beta\boldsymbol{v}^\beta\,dv = \int_{\mathcal{P}_\mathcal{B}} \boldsymbol{x}\times(m_0+m)\boldsymbol{b}\,dV + \int_{\partial\mathcal{P}_\mathcal{B}} \boldsymbol{x}\times\boldsymbol{T}dA\ . \tag{3.39}$$

Evaluation of the local forms yield the known relations for the total stress tensors

$$(\boldsymbol{F}\boldsymbol{P}^T)^T = \boldsymbol{F}\boldsymbol{P}^T \quad \text{and} \quad \boldsymbol{\sigma}^T = \boldsymbol{\sigma}\ . \tag{3.40}$$

3.3.4. Balance of energy

Within the macroscopic theory the components are assumed to have a common temperature field, that is $\theta^s(\boldsymbol{x},t) = \theta^\beta(\boldsymbol{x},t) =: \theta(\boldsymbol{x},t)$. Furthermore we assume that the stress state of component β contains only a hydrostatic pressure, that is $\boldsymbol{\sigma}^\beta = -p\boldsymbol{1}$. This rules out the possibility of viscous stresses as well as friction forces between the two components. With these simplifications, the global form of the energy balance in the reference configuration reads

$$\begin{aligned}\frac{d}{dt}\int_{\mathcal{P}_\mathcal{B}} e_0\,dV + \int_{\mathcal{P}_\mathcal{B}} \boldsymbol{a}^\beta\cdot\boldsymbol{F}\mathbb{H}\,dV \;=\; &\int_{\partial\mathcal{P}_\mathcal{B}} \boldsymbol{T}\cdot\boldsymbol{V}\,dA \\ &+ \int_{\mathcal{P}_\mathcal{B}} (m_0+m)r\,dV - \int_{\partial\mathcal{P}_\mathcal{B}} Q\,dA \\ &+ \int_{\mathcal{P}_\mathcal{B}} \boldsymbol{b}\cdot\boldsymbol{F}\mathbb{H}\,dV - \int_{\partial\mathcal{P}_\mathcal{B}} h^\beta H\,dA\ .\end{aligned} \tag{3.41}$$

In comparison to (2.36) the second term on the left hand side and the last two terms on the right hand side are additional. Here h^β is the free enthalpy of component β. Furthermore $\boldsymbol{a}^\beta(\boldsymbol{x}=\boldsymbol{\varphi}(\boldsymbol{X},t))$ is the spatial acceleration of component β as introduced in $(3.8)_2$ and evaluated at the spatial point $\boldsymbol{x}=\boldsymbol{\varphi}(\boldsymbol{X},t)$. Localization of (3.41) yields the material local form

$$\dot{e}_0 = \boldsymbol{P}:\dot{\boldsymbol{F}} + (m_0+m)r - \mathrm{Div}[\boldsymbol{Q}] + (\boldsymbol{b}-\boldsymbol{a}^\beta)\cdot\boldsymbol{F}\mathbb{H} - \mathrm{Div}[h^\beta\mathbb{H}]\ . \tag{3.42}$$

For a detailed derivation of (3.42) the interested reader is referred to Coussy [67].

3.3.5. Balance of entropy

The balance of entropy (2.38) has to be extended to the entropy flux of component β over the boundary $\partial\mathcal{P}_\mathcal{B}$. Hence the material global form can be written as

$$\frac{d}{dt}\int_{\mathcal{P}_\mathcal{B}} \eta_0\,dV = \int_{\mathcal{P}_\mathcal{B}} \frac{\delta_0}{\theta}\,dV + \int_{\mathcal{P}_\mathcal{B}} \frac{(m_0+m)r}{\theta}\,dV - \int_{\partial\mathcal{P}_\mathcal{B}} \frac{Q}{\theta}\,dA + \int_{\partial\mathcal{P}_\mathcal{B}} \eta^\beta H\,dA\ , \tag{3.43}$$

where η^β is the entropy of component β. The local form of the balance of entropy can be evaluated from (3.43) as

$$\dot{\eta}_0 = \frac{\delta_0}{\theta} + \frac{1}{\theta}\big((m_0+m)r - \mathrm{Div}[\boldsymbol{Q}]\big) + \frac{1}{\theta^2}\boldsymbol{Q}\cdot\nabla\theta - \mathrm{Div}[\eta^\beta\mathbb{H}]\ . \tag{3.44}$$

3.3.6. Dissipation inequality

In analogy to Section 2.4 the dissipation inequality for multicomponent systems is achieved by combining the balance of energy and the balance of entropy. With (3.42) and (3.44) we get

$$\delta_0 = \boldsymbol{P} : \dot{\boldsymbol{F}} - \eta_0 \dot{\theta} + \mu \dot{m} - \dot{\psi} + \left[-\nabla\mu - \eta^\beta \nabla\theta + \boldsymbol{F}^T(\boldsymbol{b} - \boldsymbol{a}^\beta)\right] \cdot \mathbb{H} - \frac{1}{\theta}\boldsymbol{Q} \cdot \nabla\theta \geq 0 \ , \tag{3.45}$$

where $\mu := h^\beta - \theta\eta^\beta$ is the *chemical potential* of component β. In line with Coussy [67], (3.45) is split into a local, a thermal conductive and a convective part

$$\begin{aligned} \delta_0^{\text{loc}} &:= \boldsymbol{P} : \dot{\boldsymbol{F}} - \eta_0 \dot{\theta} + \mu \dot{m} - \dot{\psi} && \geq 0 \ , \\ \delta_0^{\text{th}} &:= -\frac{1}{\theta}\boldsymbol{Q} \cdot \nabla\theta && \geq 0 \ , \\ \delta_0^{\text{con}} &:= \left[-\nabla\mu - \eta^\beta \nabla\theta + \boldsymbol{F}^T(\boldsymbol{b} - \boldsymbol{a}^\beta)\right] \cdot \mathbb{H} && \geq 0 \ , \end{aligned} \tag{3.46}$$

which gives three separate inequalities that provide sharper restrictions to the constitutive equations than (3.45).

3.3.7. Restriction to the isothermal case

Within this work the attention is restricted to the isothermal setting. This implies the assumptions that (i) the surrounding has a constant temperature θ_0 and (ii) heat conduction within the body is much faster and heat production much slower than all other relevant processes. Then it is adequate to assume

$$\theta = \theta_0 \quad \Rightarrow \quad \dot{\theta} = 0 \quad \text{and} \quad \nabla\theta = \boldsymbol{0} \quad \text{in } \mathcal{B} \ . \tag{3.47}$$

With the assumptions (3.47) at hand the dissipation inequality (3.45) reduces to

$$\delta_0 = \boldsymbol{P} : \dot{\boldsymbol{F}} + \mu \dot{m} - \dot{\psi} + \left[-\nabla\mu + \boldsymbol{F}^T(\boldsymbol{b} - \boldsymbol{a}^\beta)\right] \cdot \mathbb{H} \geq 0 \ . \tag{3.48}$$

Again this inequality is split into two parts yielding sharper restrictions to the constitutive equations. By introducing the driving force $\mathbb{B} := -\nabla\mu + \boldsymbol{F}^T(\boldsymbol{b} - \boldsymbol{a}^\beta)$ dual to the mass flow vector $\mathbb{H}$ we get

$$\delta_0^{\text{loc}} := \boldsymbol{P} : \dot{\boldsymbol{F}} + \mu \dot{m} - \dot{\psi} \geq 0 \quad \text{and} \quad \delta_0^{\text{con}} := \mathbb{B} \cdot \mathbb{H} \geq 0 \ . \tag{3.49}$$

3.4. Constitutive modeling framework

In this section the constitutive modeling framework for multicomponent solids is introduced. First, the coupled initial boundary value problem is recalled and the necessity of constitutive relations is shown. Then, general relations are specified by use of assumptions and constitutive principles.

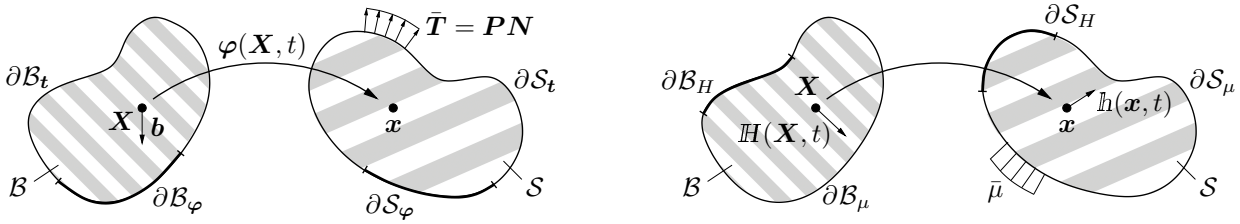

Figure 3.3: *Initial boundary value problem.* The IBVP is given by the balance equations together with initial and boundary conditions. The boundary of the material and spatial configuration is decomposed into Dirichlet and Neumann parts for the two fields $\boldsymbol{\varphi}$ and $\mathbb{H}$, that is the solid's deformation field and the relative mass flow vector field of component β.

3.4.1. Initial boundary value problem

Having introduced the kinematics and physical balance principles, the coupled initial boundary value problem can be stated. To this end, consider a body $\mathcal{B}$ and a deformation map $\boldsymbol{\varphi}(\boldsymbol{X}, t)$ that maps material points $\boldsymbol{X}$ of the reference configuration $\mathcal{B}$ of solid skeleton onto material points $\boldsymbol{x}$ in the spatial configuration $\mathcal{S}$. The material mass flow of component β relative to the solid skeleton at a material point $\boldsymbol{X} \in \mathcal{B}$ is denoted as $\mathbb{H}$. The material out-flux of mass is given by $H = \mathbb{H} \cdot \boldsymbol{N}$. The body under consideration is subject to boundary conditions. The material surface is split into *Dirichlet boundaries*, where the deformation and the mass flow vector is prescribed, and *Neumann boundaries*, where the mechanical traction and the chemical potential μ is prescribed,

$$\begin{aligned} \boldsymbol{\varphi}(\boldsymbol{X}, t) &= \bar{\boldsymbol{\varphi}}(\boldsymbol{X}, t) \text{ on } \partial\mathcal{B}_{\boldsymbol{\varphi}} , \quad \boldsymbol{T}(\boldsymbol{X}, t) = \bar{\boldsymbol{T}}(\boldsymbol{X}, t) \text{ on } \partial\mathcal{B}_{\boldsymbol{T}} = \partial\mathcal{B} \setminus \partial\mathcal{B}_{\boldsymbol{\varphi}} , \\ \mathbb{H}(\boldsymbol{X}, t) &= \bar{\mathbb{H}}(\boldsymbol{X}, t) \text{ on } \partial\mathcal{B}_H , \quad \mu(\boldsymbol{X}, t) = \bar{\mu}(\boldsymbol{X}, t) \text{ on } \partial\mathcal{B}_\mu = \partial\mathcal{B} \setminus \partial\mathcal{B}_H . \end{aligned} \tag{3.50}$$

Furthermore initial conditions are imposed onto the body for the solid's deformation and velocity as well as for the relative mass and the mass flow vector of component β

$$\begin{aligned} \boldsymbol{\varphi}(\boldsymbol{X}, t_0) &= \bar{\boldsymbol{\varphi}}_0(\boldsymbol{X}) \quad \text{in } \mathcal{B} , \\ \boldsymbol{V}(\boldsymbol{X}, t_0) &= \bar{\boldsymbol{V}}_0(\boldsymbol{X}) \quad \text{in } \mathcal{B} , \\ m(\boldsymbol{X}, t_0) &= 0 \quad \text{in } \mathcal{B} , \\ \mathbb{H}(\boldsymbol{X}, t_0) &= \bar{\mathbb{H}}_0(\boldsymbol{X}) \quad \text{in } \mathcal{B} . \end{aligned} \tag{3.51}$$

The *initial boundary value problem* depicted in Figure 3.3 is now to find the deformation and the mass flow vector

$$\boldsymbol{\varphi} : \begin{cases} \mathcal{B} \times T \to \mathcal{S} \subset \mathcal{R}^3, \\ (\boldsymbol{X}, t) \mapsto \boldsymbol{x} = \boldsymbol{\varphi}(\boldsymbol{X}, t) , \end{cases} \quad \mathbb{H} : \begin{cases} \mathcal{B} \times T \to \mathcal{R}^3, \\ (\boldsymbol{X}, t) \mapsto \mathbb{H} = \mathbb{H}(\boldsymbol{X}, t) , \end{cases} \tag{3.52}$$

that satisfy the boundary conditions (3.50), the initial conditions (3.51) and the balance equations for a given material. Note that we restrict ourselves to the isothermal case, that means $\theta = \theta_0 = const.$, see (3.47).

3.4.2. Necessity of constitutive relations

For the solution of the initial boundary value problem stated above a number of equations introduced in the previous sections are available. These equations are

$$\begin{aligned}
&(3.29): \quad Jm^s = m_0^s \\
&(3.31): \quad \dot{m} = -\operatorname{Div}[\mathbb{H}] \\
&(3.38): \quad \dot{\mathfrak{M}} + \operatorname{Div}\left[\left(\boldsymbol{V} + \tfrac{1}{m_0^\beta + m}\boldsymbol{F}\mathbb{H}\right) \otimes \mathbb{H}\right] = (m_0 + m)\boldsymbol{b} + \operatorname{Div}[\boldsymbol{P}] \\
&(3.40): \quad \boldsymbol{F}\boldsymbol{P}^T = \boldsymbol{P}\boldsymbol{F}^T \\
&(3.46): \quad \mathbb{B} = -\nabla\mu + \boldsymbol{F}^T(\boldsymbol{b} - \boldsymbol{a}^\beta)
\end{aligned} \tag{3.53}$$

that is in total $1 + 1 + 3 + 3 + 3 = 11$ scalar equations. On the other hand, counting the number of unknowns that appear in these equations yields

mass density of solid	m^s
relative mass of β	m
deformation map	$\boldsymbol{\varphi}$
1st Piola-Kirchhoff stress	$\boldsymbol{P}$
relative mass flow vector	$\mathbb{H}$
chemical potential of β	μ
driving force	$\mathbb{B}$

(3.54)

that is 21 scalar unknowns. Hence, $21 - 11 = 10$ equations are missing to solve the initial boundary value problem of Subsection 3.4.1. These equations are provided by *constitutive relations* for the 1st Piola-Kirchhoff stress tensor $\boldsymbol{P}$, the chemical potential μ and the force $\mathbb{B}$ dual to the relative mass flow vector. Here, the stress $\boldsymbol{P}$ is constitutively constructed such that it fulfills the balance of angular momentum a priorily. Furthermore note, that in (3.53) the dissipation inequality is missing. In the dissipation inequality (3.49) a further unknown, namely the free energy ψ appears. The idea is to relate the constitutive functions ψ, $\boldsymbol{P}$ and μ such that a priori inequality $(3.49)_1$ is satisfied and to construct the constitutive relation for $\mathbb{B}$ such that a priori inequality $(3.49)_2$ is satisfied. Such material relations are denoted as *thermodynamically consistent*.

3.4.3. Constitutive framework

The goal is now to provide a general form of constitutive relations for the fields specified above based on assumptions and constitutive principles. In the following these assumptions and principles are only written for the free energy function ψ but apply in the same manner also to the fields $\boldsymbol{P}$ and μ. Analogously to the procedure in classical thermomechanics for the constitutive relation of the heat flux, a constitutive relation for the driving force $\mathbb{B}$ is stated by evaluation of the convective part of the dissipation inequality.

Principle of determinism. The first assumption is provided by the *principle of determinism*, stating that $\psi(\boldsymbol{X}, t)$ at a material point $\boldsymbol{X}$ at time t is fully determined by the deformation map $\boldsymbol{\varphi}(\boldsymbol{Y}, t)$ of the solid skeleton and relative mass $m(\boldsymbol{Y}, t)$ of component β

at all material points $\boldsymbol{Y} \in \mathcal{B}$ and at all instants of time in the past $\tau = [0, t]$. We write this in the form

$$\psi(\boldsymbol{X}, t) = \hat{\psi}\big(\boldsymbol{\varphi}(\boldsymbol{Y} \in \mathcal{B}, \tau \in [0, t]), m(\boldsymbol{Y} \in \mathcal{B}, \tau \in [0, t])\big) \ . \tag{3.55}$$

The principle of determinism is a very general constitutive relations however rules out stochastic processes in the material model.

Concept of internal variables. The idea of this concept is to reduce relation (3.55) by the dependency of all instants of time to a dependency on $\boldsymbol{\varphi}$ and m only at the considered time t. This is possible by introducing a set of *internal variables* $\mathfrak{q}(\boldsymbol{X}, t)$. We then get

$$\psi(\boldsymbol{X}, t) = \hat{\psi}\big(\boldsymbol{\varphi}(\boldsymbol{Y} \in \mathcal{B}, t), m(\boldsymbol{Y} \in \mathcal{B}, t), \mathfrak{q}(\boldsymbol{Y} \in \mathcal{B}, t)\big) \ . \tag{3.56}$$

The set of internal variables $\mathfrak{q}$ contains unknown fields of tensorial nature for which constitutive relations have to be specified. This is done in the same manner for the evolution of the internal variables, that is

$$\dot{\mathfrak{q}}(\boldsymbol{X}, t) = \hat{\dot{\mathfrak{q}}}\big(\boldsymbol{\varphi}(\boldsymbol{Y} \in \mathcal{B}, t), m(\boldsymbol{Y} \in \mathcal{B}, t), \mathfrak{q}(\boldsymbol{Y} \in \mathcal{B}, t)\big) \tag{3.57}$$

together with appropriate initial conditions $\mathfrak{q}(\boldsymbol{X}, t_0) = \bar{\mathfrak{q}}_0(\boldsymbol{X})$ in $\mathcal{B}$.

Principle of local action. The next assumption done is the so-called *principle of local action*. It states that the constitutive response at a material point $\boldsymbol{X}$ does not depend on all material points $\boldsymbol{Y} \in \mathcal{B}$ but is solely dependent on material points $\boldsymbol{Y}$ in a small neighborhood $\mathcal{N}_{\boldsymbol{X}}$ around $\boldsymbol{X}$. Approximating the deformation map $\boldsymbol{\varphi}(\boldsymbol{Y}, t)$, the relative mass $m(\boldsymbol{Y}, t)$ and the set of internal variables $\mathfrak{q}(\boldsymbol{Y}, t)$ in the neighborhood $\mathcal{N}_{\boldsymbol{X}}$ by a Taylor series expansion gives

$$\begin{aligned} \boldsymbol{\varphi}(\boldsymbol{Y}, t) &\approx \boldsymbol{\varphi}(\boldsymbol{X}, t) + \nabla\boldsymbol{\varphi}(\boldsymbol{X}, t)\,[\boldsymbol{Y} - \boldsymbol{X}] \ , \\ m(\boldsymbol{Y}, t) &\approx m(\boldsymbol{X}, t) + \nabla m(\boldsymbol{X}, t)[\boldsymbol{Y} - \boldsymbol{X}] \ , \\ \mathfrak{q}(\boldsymbol{Y}, t) &\approx \mathfrak{q}(\boldsymbol{X}, t) + \nabla\mathfrak{q}(\boldsymbol{X}, t)\,[\boldsymbol{Y} - \boldsymbol{X}] \ , \end{aligned} \tag{3.58}$$

for $\boldsymbol{Y} \in \mathcal{N}_{\boldsymbol{X}}$. Considering the Taylor series up to the first order as done in (3.58) yields a so-called *theory of grade one*. Recalling the definition of the deformation gradient $\boldsymbol{F} = \nabla\boldsymbol{\varphi}$, we obtain the basic structure

$$\begin{aligned} \psi(\boldsymbol{X}, t) &= \hat{\psi}\big(\boldsymbol{\varphi}, \boldsymbol{F}, m, \nabla m, \mathfrak{q}, \nabla\mathfrak{q}\big) \ , \\ \dot{\mathfrak{q}}(\boldsymbol{X}, t) &= \hat{\dot{\mathfrak{q}}}\big(\boldsymbol{\varphi}, \boldsymbol{F}, m, \nabla m, \mathfrak{q}, \nabla\mathfrak{q}\big) \ , \end{aligned} \tag{3.59}$$

with all arguments $\{\boldsymbol{\varphi}, \boldsymbol{F}, m, \nabla m, \mathfrak{q}, \nabla\mathfrak{q}\}$ evaluated solely at the material point $\boldsymbol{X}$ and at time t.

Principle of material objectivity. The *principle of material objectivity* is a fundamental principle that has to be fulfilled at all times. It was first introduced by Truesdell & Noll [260]. There are two ways to formulate the principle: The *passive version* states that constitutive relations should be invariant with respect to a change of frame, that is

independent of the observer. The *active version* requires invariance with respect to rigid body motions superimposed onto the current configuration. Consider a rigid body motion consisting of a translation $\boldsymbol{c}(t) \in \mathcal{R}^3$ and a rotation $\boldsymbol{Q}(t) \in \mathcal{SO}(3)$ superimposed onto the deformation $\boldsymbol{\varphi}$. The total deformation map $\boldsymbol{\varphi}^*$ with deformation gradient $\boldsymbol{F}^*$ can be evaluated as

$$\boldsymbol{\varphi}^*(\boldsymbol{X},t) = \boldsymbol{Q}(t)\boldsymbol{\varphi}(\boldsymbol{X},t) + \boldsymbol{c}(t) \quad \text{and} \quad \boldsymbol{F}^*(\boldsymbol{X},t) = \boldsymbol{Q}(t)\boldsymbol{F}(\boldsymbol{X},t) \ . \tag{3.60}$$

Then, the active version of the principle of material objectivity requires that

$$\begin{aligned} \hat{\psi}^*(\boldsymbol{\varphi}^*, \boldsymbol{F}^*, m, \nabla m, \mathfrak{q}^*, \nabla \mathfrak{q}^*) &= \hat{\psi}(\boldsymbol{\varphi}, \boldsymbol{F}, m, \nabla m, \mathfrak{q}, \nabla \mathfrak{q}) \ , \\ \hat{\mathfrak{q}}^*(\boldsymbol{\varphi}^*, \boldsymbol{F}^*, m, \nabla m, \mathfrak{q}^*, \nabla \mathfrak{q}^*) &= \hat{\mathfrak{q}}(\boldsymbol{\varphi}, \boldsymbol{F}, m, \nabla m, \mathfrak{q}, \nabla \mathfrak{q}) \ . \end{aligned} \tag{3.61}$$

A direct consequence is that $\hat{\psi}$ and $\hat{\mathfrak{q}}$ cannot be functions of the deformation map $\boldsymbol{\varphi}$ as (3.61) has to hold for arbitrary translations $\boldsymbol{c}(t) \in \mathcal{R}^3$. The statement then reduces to

$$\begin{aligned} \hat{\psi}(\boldsymbol{Q}\boldsymbol{F}, m, \nabla m, \mathfrak{q}, \nabla \mathfrak{q}) &= \hat{\psi}(\boldsymbol{F}, m, \nabla m, \mathfrak{q}, \nabla \mathfrak{q}) \ , \\ \hat{\mathfrak{q}}(\boldsymbol{Q}\boldsymbol{F}, m, \nabla m, \mathfrak{q}, \nabla \mathfrak{q}) &= \hat{\mathfrak{q}}(\boldsymbol{F}, m, \nabla m, \mathfrak{q}, \nabla \mathfrak{q}) \ , \end{aligned} \tag{3.62}$$

that has to hold for all $\boldsymbol{Q} \in \mathcal{SO}(3)$.

Principle of material symmetry. Many materials possess certain symmetry properties due to their microstructure. Examples could be orthotropic anisotropy in metals with fcc crystalline structure, transverse isotropy in fibre-reinforced composites or full isotropy. This symmetry of a material can be described by a set of rotations $\mathcal{G} \subseteq \mathcal{SO}(3)$ that leave the microstructure of the material unchanged. The *principle of material symmetry* states that constitutive functions should be invariant with respect to all rotations in $\mathcal{G}$ superimposed onto the reference configuration

$$\begin{aligned} \hat{\psi}(\boldsymbol{F}\boldsymbol{Q}, m, \nabla m, \mathfrak{q}, \nabla \mathfrak{q}) &= \hat{\psi}(\boldsymbol{F}, m, \nabla m, \mathfrak{q}, \nabla \mathfrak{q}) \ , \\ \hat{\mathfrak{q}}(\boldsymbol{F}\boldsymbol{Q}, m, \nabla m, \mathfrak{q}, \nabla \mathfrak{q}) &= \hat{\mathfrak{q}}(\boldsymbol{F}, m, \nabla m, \mathfrak{q}, \nabla \mathfrak{q}) \ , \end{aligned} \tag{3.63}$$

that has to hold for all $\boldsymbol{Q} \in \mathcal{G} \subseteq \mathcal{SO}(3)$.

Evaluation of local dissipation inequality for gradient-extended behavior. Considering gradient-extended dissipative solids such as for example in Miehe [176, 178], Hildebrand [132] or Miehe et al. [186] or of Cahn-Hilliard-type models such as for example in Gurtin [125], Anand [6] or Miehe et al. [187] requires an evaluation of the local dissipation inequality in a global form. To this end, by integrating δ_0^{loc} over the specimen $\mathcal{B}$ and by using integration by parts yields the global dissipation inequality constraint

$$\begin{aligned} \int_{\mathcal{B}} \delta_0^{\text{loc}} \, dV \ = & \int_{\mathcal{B}} \big(\boldsymbol{P} - \partial_{\boldsymbol{F}}\hat{\psi}\big) : \dot{\boldsymbol{F}} \, dV + \int_{\mathcal{B}} \big(- \partial_{\mathfrak{q}}\hat{\psi} + \text{Div}[\partial_{\nabla \mathfrak{q}}\hat{\psi}]\big) \cdot \dot{\mathfrak{q}} \, dV \\ & + \int_{\mathcal{B}} \big(\mu - \partial_m \hat{\psi} + \text{Div}[\partial_{\nabla m}\hat{\psi}]\big)\dot{m} \, dV \\ & - \int_{\partial\mathcal{B}} \big(\partial_{\nabla m}\hat{\psi}\big) \cdot \boldsymbol{N}\dot{m} \, dA - \int_{\partial\mathcal{B}} \big(\partial_{\nabla \mathfrak{q}}\hat{\psi}\big) \cdot \boldsymbol{N} \cdot \dot{\mathfrak{q}} \, dA \qquad \geq 0 \ . \end{aligned} \tag{3.64}$$

This equation can be fulfilled by the three conditions

$$\begin{aligned}\big(\boldsymbol{P}-\partial_{\boldsymbol{F}}\hat{\psi}\big):\dot{\boldsymbol{F}}+\big(\mu-\partial_m\hat{\psi}+\mathrm{Div}[\partial_{\nabla m}\hat{\psi}]\big)\dot{m}-\big(\partial_{\mathfrak{q}}\hat{\psi}-\mathrm{Div}[\partial_{\nabla\mathfrak{q}}\hat{\psi}]\big)\cdot\dot{\mathfrak{q}}\geq 0 \text{ in } \mathcal{B}\ ,\\ \big(\partial_{\nabla m}\hat{\psi}\big)\cdot\boldsymbol{N}\dot{m}\geq 0 \text{ on } \partial\mathcal{B}\ ,\\ \big(\partial_{\nabla\mathfrak{q}}\hat{\psi}\big)\cdot\boldsymbol{N}\cdot\dot{\mathfrak{q}}\geq 0 \text{ on } \partial\mathcal{B}\ .\end{aligned}\tag{3.65}$$

Using a reasoning often denoted as *Coleman-Noll argument*, the constraint $(3.65)_1$ can only be fulfilled if the terms within the first two brackets vanish. Thus we obtain the relations

$$\partial_{\boldsymbol{F}}\hat{\psi}=\hat{\boldsymbol{P}}\quad\text{and}\quad\partial_m\hat{\psi}-\mathrm{Div}[\partial_{\nabla m}\hat{\psi}]=\hat{\mu}\ .\tag{3.66}$$

Hence the general structure of the constitutive relation for free energy is given by

$$\psi(\boldsymbol{X},t)=\hat{\psi}\big(\boldsymbol{F},m,\nabla m,\mathfrak{q},\nabla\mathfrak{q}\big)\ .\tag{3.67}$$

Note that the constitutive equations have to fulfill the principle of material objectivity and the principle of material symmetry. The reduced local dissipation postulate reads

$$\begin{aligned}\tilde{\delta}_0^{\mathrm{loc}}:=\quad&\big(-\partial_{\mathfrak{q}}\hat{\psi}+\mathrm{Div}[\partial_{\nabla\mathfrak{q}}\hat{\psi}]\big)\cdot\dot{\mathfrak{q}}\geq 0 \text{ in } \mathcal{B}\ ,\\ &\big(\partial_{\nabla m}\hat{\psi}\big)\cdot\boldsymbol{N}\dot{m}\geq 0 \text{ on } \partial\mathcal{B}\ ,\\ &\big(\partial_{\nabla\mathfrak{q}}\hat{\psi}\big)\cdot\boldsymbol{N}\cdot\dot{\mathfrak{q}}\geq 0 \text{ on } \partial\mathcal{B}\ .\end{aligned}\tag{3.68}$$

Equation $(3.68)_1$ is a restriction to the constitutive relation for the evolution of the internal variables. In order to fulfill $(3.68)_1$ a priorily we introduce *dissipation potentials*. The constraints $(3.68)_2$ and $(3.68)_3$ will be fulfilled by setting appropriate boundary conditions and not via constitutive relations.

Evaluation of local dissipation inequality for local material behavior. Precluding gradient-extended dissipative solids the local dissipation inequality $\delta_0^{\mathrm{loc}}\geq 0$ can also be fulfilled pointwise at all $\boldsymbol{X}\in\mathcal{B}$. For such local material models the gradients $\nabla\mathfrak{q}$ and ∇m are assumed to be not arguments of the constitutive functions, such that $\psi=\hat{\psi}(\boldsymbol{F},m,\mathfrak{q})$. Then, evaluating the local dissipation inequality $(3.49)_1$ yields

$$\delta_0^{\mathrm{loc}}=\big(\boldsymbol{P}-\partial_{\boldsymbol{F}}\hat{\psi}\big):\dot{\boldsymbol{F}}+\big(\mu-\partial_m\hat{\psi}\big)\dot{m}-\partial_{\mathfrak{q}}\hat{\psi}\cdot\dot{\mathfrak{q}}\geq 0\ .\tag{3.69}$$

Using again the Colemann-Noll argument, the constraint (3.69) can only be fulfilled if the first two terms vanish separately. Thus we obtain the relations

$$\partial_{\boldsymbol{F}}\hat{\psi}=\hat{\boldsymbol{P}}\quad\text{and}\quad\partial_m\hat{\psi}=\hat{\mu}\ .\tag{3.70}$$

Thus the structure of the constitutive relation for the free energy reduces to

$$\psi(\boldsymbol{X},t)=\hat{\psi}\big(\boldsymbol{F},m,\mathfrak{q}\big)\tag{3.71}$$

and in addition has to fulfill the principle of material objectivity and the principle of material symmetry. The reduced local dissipation postulate (3.69) reads

$$\delta_0^{\mathrm{loc}}=-\partial_{\mathfrak{q}}\hat{\psi}\cdot\dot{\mathfrak{q}}\geq 0\ ,\tag{3.72}$$

which is a restriction to the constitutive relations for the evolution of the internal variables. In order to fulfill (3.72) a priori for all processes $\dot{\mathfrak{q}}$ we introduce *dissipation potentials*.

Concept of dissipation potentials. The concept of dissipation potentials goes back to Biot [23], Ziegler & Wehrli [279] and Nguyen [202], see also Miehe [175]. It is based on the introduction of a *dissipation potential* ϕ in terms of the rate $\dot{\mathbf{q}}$ of the internal variables. The dissipation potential is used for an implicit definition of the evolution of the internal variables by

$$-\delta_{\mathbf{q}}\hat{\psi}(\boldsymbol{F}, m, \nabla m, \mathbf{q}, \nabla \mathbf{q}) \in \partial_{\dot{\mathbf{q}}}\phi(\dot{\mathbf{q}}) \ , \tag{3.73}$$

where we introduced the functional derivative $\delta_{\mathbf{q}}(\cdot) = \partial_{\mathbf{q}}(\cdot) - \mathrm{Div}[\partial_{\nabla \mathbf{q}}(\cdot)]$. The derivative $\partial_{\dot{\mathbf{q}}}\phi(\dot{\mathbf{q}})$ is generalized to the subdifferential for non-smooth continuous potentials ϕ. At a point of non-differentiability $-\delta_{\mathbf{q}}\hat{\psi}$ has to be an element of the subdifferential $\partial_{\dot{\mathbf{q}}}\phi$. Evolution equations of the form (3.73) a priori satisfy the reduced dissipation inequality (3.72) or $(3.68)_1$ if $\phi(\dot{\mathbf{q}})$ is (i) convex in $\dot{\mathbf{q}}$, (ii) positive $\phi \geq 0$ for all $\dot{\mathbf{q}}$ and (iii) normalized, that is $\phi(\boldsymbol{0}) = 0$.

Evaluation of convective dissipation inequality. Finally the convective part of the dissipation inequality $\delta_0^{\mathrm{con}} \geq 0$ is to be fulfilled a priori. Recalling $(3.49)_2$ we have

$$\delta_0^{\mathrm{con}} = \mathbb{B} \cdot \mathbb{H} \geq 0 \ . \tag{3.74}$$

In order to fulfill this condition we proceed as above and introduce a *convective dissipation potential* $\phi_{\mathrm{con}}(\mathbb{H})$ in terms of the mass flow vector $\mathbb{H}$. The constitutive equation for $\mathbb{B}$ is thus written as

$$\mathbb{B} \in \frac{\partial \phi_{\mathrm{con}}(\mathbb{H})}{\partial \mathbb{H}} \ . \tag{3.75}$$

Constitutive functions of this form a priori satisfy the dissipation inequality (3.74) if ϕ_{con} is (i) convex, (ii) positive $\phi_{\mathrm{con}} \geq 0$ for all $\mathbb{H}$ and (iii) normalized, that is $\phi_{\mathrm{con}}(\boldsymbol{0}) = 0$. As an example consider the quadratic form

$$\hat{\phi}_{\mathrm{con}}(\mathbb{H}) = \frac{1}{2}\widehat{\boldsymbol{K}}^{-1} : (\mathbb{H} \otimes \mathbb{H}) \quad \Rightarrow \quad \mathbb{B} = \widehat{\boldsymbol{K}}^{-1}\mathbb{H} \tag{3.76}$$

which fulfills (3.74) for a positive definite inverse permeability tensor $\widehat{\boldsymbol{K}}^{-1}$. For the special case of isotropic mass flow, the second-order tensor $\widehat{\boldsymbol{K}}$ takes the special form $\widehat{\boldsymbol{K}} = \hat{k} J \boldsymbol{C}^{-1}$ with $\hat{k} > 0$. The idea of introducing a dissipation potential in the context of coupled multicomponent problems first occurs in Biot [28].

The concept of dissipation potentials is not the only possible way of constructing thermodynamically consistent constitutive equations. Another approach is based on the principle of maximum dissipation, well known from the modeling of rate-independent plasticity. For this approach in the context of multicomponent problems we refer to Svoboda et al. [251, 252] or Hackl et al. [127]. A study on the relation of these two approaches for single-component inelastic materials is considered in Hackl & Fischer [126]. A further possibility is provided by the principle of virtual dissipation that goes back to Biot [22]. Using this approach the flow equation is obtained as a direct outcome of the principle.

Chapter 4

Variational Modeling of Poro-Elasticity

The first application of the introduced macroscopic multicomponent framework problems of solids deals with *fluid-saturated porous media*. In analogy to Miehe et al. [190] we propose a variational formulation for the poro-elastic solid that governs the evolution of the two basic kinematic fields, that is the rate of solid deformation $\dot{\boldsymbol{\varphi}}$ and the fluid mass flow vector $\mathbb{H}$

$$\{\dot{\boldsymbol{\varphi}}, \mathbb{H}\} = \arg \left\{ \inf_{\dot{\boldsymbol{\varphi}} \in \mathcal{W}_{\dot{\boldsymbol{\varphi}}}} \inf_{\mathbb{H} \in \mathcal{W}_{\mathbb{H}}} \Pi(\dot{\boldsymbol{\varphi}}, \mathbb{H}) \right\} . \tag{4.1}$$

The formulation is based on the rate potential Π that depends on only two constitutive functions connected to the energy storage and the dissipative behavior. The framework (4.1) provides a *canonical minimization principle* for the evolution problem, the Euler equations of which are the total linear momentum balance and Darcy's law of fluid flow. Using a Legendre transformation of the dissipation potential function, (4.1) can be transformed into a *saddle-point variational formulation* for the evolution problem based on a dual rate potential Π^*

$$\{\dot{\boldsymbol{\varphi}}, \dot{m}, \mu\} = \arg \left\{ \inf_{\dot{\boldsymbol{\varphi}} \in \mathcal{W}_{\dot{\boldsymbol{\varphi}}}} \inf_{\dot{m} \in \mathcal{W}_{\dot{m}}} \sup_{\mu \in \mathcal{W}_{\mu}} \tilde{\Pi}^*(\dot{\boldsymbol{\varphi}}, \dot{m}, \mu) \right\} . \tag{4.2}$$

The numerical treatment of poro-elasticity with the finite element method still is a challenging and actual topic of research in particular concerning numerical stability issues and computational efficiency. An overview of different numerical finite element implementations can be found in Haga et al. [128]. One source of *numerical stability* issue is the saddle-point structure of the underlying problem for the stability of which the BBL condition has to be satisfied. From this point of view the proposed *minimization formulation* is advantageous over the saddle-point formulations, as the numerical treatment of which is a priori not affected by the BBL condition. Uniqueness of the solution for the minimization formulation is ensured for the bilinear form of the linearized time-discrete problem being elliptic. This allows a much bigger freedom since any conforming batch of finite element ansatz spaces will provide a stable solution. The minimizer is shown to be prone to a locking phenomena which however can be avoided, for example by selective reduced integration techniques.

Other formulations, however without a pure minimization structure, are the three-field formulation in deformation, fluid pressure and fluid velocity, see PHILLIPS & WHEELER [211] and the four-field formulation in deformation, fluid pressure, fluid velocity and solid pressure, see KORSAWE & STARKE [151] and TCHONKOVA ET AL. [254].

Section 4.1 starts with a summary of the initial boundary value problem for the poro-elastic solid. Furthermore the stored energy and load functionals as well as the load potential is introduced. The chosen constitutive functions complete the section. The canonical two-field rate-type variational formulation (4.1) is then stated in Section 4.2. It is shown that the Euler equations of this formulation are the total linear momentum balance together with Darcy's flow law. A Legendre transformation of the dissipation function yields a three-field saddle-point formulation that can be condensed to the reduced three-field saddle-point formulation introduced in (4.2). For a numerical investigation of the different formulations first a time-discretization is performed in Section 4.3 yielding time-discrete counterparts of the minimization and saddle-point variational formulations. The incremental problems are then discretized in space by use of the finite element method in Section 4.4. Beside stating the time-space discrete variational formulations of the problem of poro-elasticity different finite element approximations are introduced. A validation of the modeling approach as well as a comparative study of minimization and saddle-point formulation regarding numerical stability and computational efficiency is performed in Section 4.5.

4.1. Initial boundary value problem of coupled poro-elasticity

This section provides an introduction to the modeling framework of fluid-saturated porous media. It is based on the general considerations of the macroscopic theory presented in Chapter 3. Modifications of the general theory are due to the specific modeling assumptions and simplifications presumed.

4.1.1. Modeling assumptions

For the model problem of poro-elasticity the second component is a fluid, wherefore we specify $\beta =: f$. Furthermore the following simplifications are assumed:

- Isothermal conditions, such that $\dot{\theta} = 0$ and $\nabla\theta = \boldsymbol{0}$,
- elastic solid behavior, such that $\mathfrak{q} = \emptyset$,
- quasi-static conditions, such that $|\ddot{\boldsymbol{\varphi}}| \approx 0$ and $|\boldsymbol{A}^f| \approx 0$,
- body force is associated with gravitational force, such that $\boldsymbol{b} = \bar{g}$,
- no gradient-enhanced model is considered, such that $\psi = \hat{\psi}(\boldsymbol{F}, m)$.

For the assumption that $\hat{\psi}$ is not a function of the gradient of the relative fluid mass m the local dissipation inequality constraint is fulfilled pointwise, that is (3.72) has to hold.

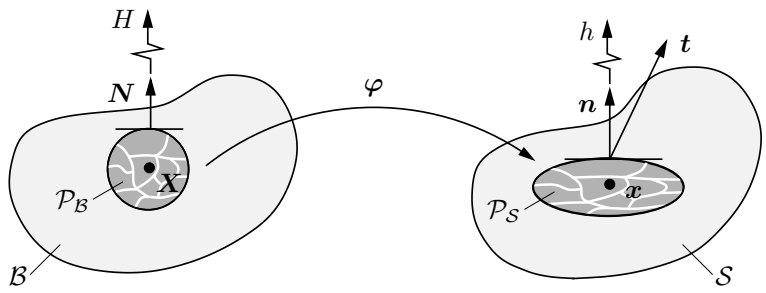

Figure 4.1: *Phenomenological quantities in finite poro-elasticity.* The total traction vector $\boldsymbol{t}$ represents the action of contact forces on surfaces of the cut-out part $\partial\mathcal{P}_\mathcal{S}$. The material and spatial fluid transports H and h characterize the fluid out-flux with respect to the areas $\partial\mathcal{P}_\mathcal{B}$ and $\partial\mathcal{P}_\mathcal{S}$.

Since $\mathfrak{q} = \emptyset$ we directly conclude $\delta_0^{\text{loc}} = 0$. With these modeling assumptions at hand, the balance equations and constitutive functions under consideration are summarized as:

$$\boxed{\begin{aligned}
&\textit{Balance of fluid mass} && \dot{m} = -\operatorname{Div}[\mathbb{H}] \\
&\textit{Balance of linear momentum} && \boldsymbol{0} = \operatorname{Div}[\boldsymbol{P}] + (m_0 + m)\bar{g} \\
&\textit{Definition of driving force} && \mathbb{B} = -\nabla[\mu - \bar{g} \cdot \boldsymbol{\varphi}] \\
&\textit{Constitutive stress} && \boldsymbol{P} = \partial_{\boldsymbol{F}}\hat{\psi} \\
&\textit{Constitutive chemical potential} && \mu = \partial_m \hat{\psi} \\
&\textit{Constitutive driving force} && \hat{\mathbb{B}} = \partial_{\mathbb{H}}\hat{\phi}_{\text{con}}
\end{aligned}} \tag{4.3}$$

4.1.2. Initial boundary value problem

We now recall the coupled initial boundary value problem introduced in Subsection 3.4.1 for the considered model problem of poro-elasticity. The unknown kinematic fields of the coupled problem are the deformation map and the fluid mass flow vector

$$\boldsymbol{\varphi} : \begin{cases} \mathcal{B} \times T \to \mathcal{S} \subset \mathcal{R}^3, \\ (\boldsymbol{X}, t) \mapsto \boldsymbol{\varphi}(\boldsymbol{X}, t) \end{cases} \quad \text{and} \quad \mathbb{H} : \begin{cases} \mathcal{B} \times T \to \mathcal{R}^3, \\ (\boldsymbol{X}, t) \mapsto \mathbb{H}(\boldsymbol{X}, t) \ . \end{cases} \tag{4.4}$$

The fluid mass flow vector $\mathbb{H}$ and the relative fluid mass m that appear as state variables in the constitutive functions are connected via the mass balance equation $(4.3)_1$. For the two global fields boundary values have to be prescribed. Therefor the boundary of $\mathcal{B}$ is decomposed into *Dirichlet boundaries*, where the deformation map and the fluid flux is prescribed and *Neumann boundaries*, where the mechanical traction and the chemical potential is prescribed. Thus

$$\begin{aligned}
&\boldsymbol{\varphi}(\boldsymbol{X}, t) = \bar{\boldsymbol{\varphi}}(\boldsymbol{X}, t) \text{ on } \partial\mathcal{B}_{\boldsymbol{\varphi}} \ , \quad \boldsymbol{T}(\boldsymbol{X}, t) = \bar{\boldsymbol{T}}(\boldsymbol{X}, t) \text{ on } \partial\mathcal{B}_{\boldsymbol{T}} = \partial\mathcal{B} \setminus \partial\mathcal{B}_{\boldsymbol{\varphi}} \ , \\
&H(\boldsymbol{X}, t) = \bar{H}(\boldsymbol{X}, t) \text{ on } \partial\mathcal{B}_H \ , \quad \mu(\boldsymbol{X}, t) = \bar{\mu}(\boldsymbol{X}, t) \text{ on } \partial\mathcal{B}_\mu = \partial\mathcal{B} \setminus \partial\mathcal{B}_H \ .
\end{aligned} \tag{4.5}$$

Furthermore initial conditions have to be prescribed for the two kinematic fields $\boldsymbol{\varphi}$ and $\mathbb{H}$ as well as for the relative fluid mass field m

$$\boldsymbol{\varphi}(\boldsymbol{X}, t_0) = \bar{\boldsymbol{\varphi}}_0(\boldsymbol{X}) \ , \ \mathbb{H}(\boldsymbol{X}, t_0) = \bar{\mathbb{H}}_0(\boldsymbol{X}) \ , \ m(\boldsymbol{X}, t_0) = 0 \ . \tag{4.6}$$

As we are restricting ourselves to the quasi-static case initial conditions for the solid skeleton's velocity $\boldsymbol{V}$ are not needed. The initial boundary value problem is now to find the deformation $\boldsymbol{\varphi}$ and the fluid mass flow vector $\mathbb{H}$ that satisfy the boundary conditions (4.5), the initial conditions (4.6) and the balance equations (4.3). In this initial boundary value problem the two unknown fields $\boldsymbol{\varphi}$ and $\mathbb{H}$ are the kinematic variables of the two-phase material. Therefor we denote this as the *canonical form* of initial boundary value problem.

Alternatively, different *mixed formulations* can be deduced from the canonical form by means of Legendre transformations of the constitutive functions ψ and ϕ. For example the classical $\{\boldsymbol{\varphi}, \mu\}$-formulation (or $\{\boldsymbol{\varphi}, p\}$-formulation) of coupled poro-elasticity is achieved by using the dual convective dissipation potential function ϕ^* instead of ϕ. This formulation is widely used in the literature, see for example Prévost [214, 216], Armero [9], Haga et al. [128], Murad & Loula [200] or Carter et al. [57, 58].

4.1.3. Stored energy, dissipation potential and load functionals

In the following we introduce three functionals needed to state the variational principle. They are related to the energy storage, the convective dissipative mechanism and the external loading. The first two are based on two constitutive functions, namely the free energy function and the convective dissipation potential.

Rate of energy functional. The *stored energy functional* depends on the deformation field $\boldsymbol{\varphi}$ and the relative fluid mass field m

$$E(\boldsymbol{\varphi}, m) := \int_{\mathcal{B}} \hat{\psi}(\boldsymbol{F}, m)\, dV \tag{4.7}$$

and characterizes the poro-mechanical energy stored in the solid-fluid mixture. It is governed by the constitutive energy function $\hat{\psi}$. The rate of energy is evaluated as

$$\frac{d}{dt} E(\dot{\boldsymbol{\varphi}}, \dot{m}) = \int_{\mathcal{B}} \{\, \partial_{\boldsymbol{F}} \hat{\psi} : \nabla \dot{\boldsymbol{\varphi}} + \partial_m \hat{\psi} \dot{m} \}\, dV \tag{4.8}$$

and can be considered as a functional of the rates $\{\dot{\boldsymbol{\varphi}}, \dot{m}\}$ at given state $\{\boldsymbol{\varphi}, m\}$.

Dissipation potential functional. The *canonical dissipation potential functional* depends on the species flow vector $\mathbb{H}$ and is assumed to have the form

$$D(\mathbb{H}) := \int_{\mathcal{B}} \hat{\phi}_{\text{con}}(\mathbb{H}; \boldsymbol{F}, m)\, dV \tag{4.9}$$

in terms of the convective dissipation potential function $\hat{\phi}_{\text{con}}$, which is a function of $\mathbb{H}$, see (3.75), and evaluated at a given state $\{\boldsymbol{F}, m\}$ of deformation and fluid mass. Alternatively to the representation (4.9) the dissipation potential functional can be expressed in terms of the dual convective dissipation potential function $\hat{\phi}^*_{\text{con}}$. Recalling the definition of the Legendre transformation we have

$$\hat{\phi}_{\text{con}}(\mathbb{H}) = \sup_{\mathbb{B}} \left[\mathbb{B} \cdot \mathbb{H} - \hat{\phi}^*_{\text{con}}(\mathbb{B}; \boldsymbol{F}, m) \right] \tag{4.10}$$

in terms of the force $\mathbb{B}$ dual to $\mathbb{H}$. Insertion of (4.10) into (4.9) suggests the introduction of an *extended dissipation potential functional* $D^*(\mathbb{H}, \mathbb{B})$ defined as

$$D^*(\mathbb{H}, \mathbb{B}) = \int_{\mathcal{B}} \left[\mathbb{B} \cdot \mathbb{H} - \hat{\phi}^*_{\text{con}}(\mathbb{B}; \boldsymbol{F}, m) \right] dV \ . \tag{4.11}$$

The extended dissipation functional (4.11) is connected to the dissipation potential functional (4.9) by the relationship

$$D(\mathbb{H}) = \sup_{\mathbb{B}} \left[D^*(\mathbb{H}, \mathbb{B}) \right] \ . \tag{4.12}$$

External load functional. The external load functional decomposes into mechanical and fluid contributions

$$P_{\text{ext}}(\dot{\boldsymbol{\varphi}}, \mathbb{H}) = P^{g,\boldsymbol{T}}_{\text{ext}}(\dot{\boldsymbol{\varphi}}) + P^{g,\mu}_{\text{ext}}(\mathbb{H}) \, . \tag{4.13}$$

The mechanical part again decomposes into a volume contribution due to the gravitational acceleration $\bar{g}$ and a surface contribution due to the dead surface load $\bar{\boldsymbol{T}}$. We write

$$P^{g,\boldsymbol{T}}_{\text{ext}}(\dot{\boldsymbol{\varphi}}) := \int_{\mathcal{B}} (m_0 + m) \bar{g} \cdot \dot{\boldsymbol{\varphi}} \, dV + \int_{\partial \mathcal{B}_{\boldsymbol{T}}} \bar{\boldsymbol{T}} \cdot \dot{\boldsymbol{\varphi}} \, dA \ . \tag{4.14}$$

The functional $P^{g,\boldsymbol{T}}_{\text{ext}}$ is assumed to be a functional of the rate $\dot{\boldsymbol{\varphi}}$ at given state m of relative fluid content. The fluid contribution takes the form

$$P^{g,\mu}_{\text{ext}}(\mathbb{H}) = \int_{\mathcal{B}} \bar{g} \cdot (\boldsymbol{F}\mathbb{H}) \, dV - \int_{\partial \mathcal{B}_\mu} \bar{\mu} H \, dA \ . \tag{4.15}$$

$P^{g,\mu}_{\text{ext}}$ is considered to be a functional of $\mathbb{H}$ at given state $\boldsymbol{\varphi}$ of solid deformation.

4.1.4. Constitutive functions for the model problem

Before stating the variational principle of coupled poro-elasticity the two constitutive functions are specified. These are the free energy function ψ and the convective dissipation potential ϕ_{con}.

The first attempts to the modeling of macroscopic poro-elasticity at small strains goes back to Biot [21]. Later Biot & Willis [34] and Detournay & Cheng [83] constituted a macroscopic free energy function for small strains based on microscopic considerations. Biot extended his theory to the finite strain regime and to thermo-poro-mechanical coupling, see Biot [24, 28]. However in these works he gave no answer on how to get the macroscopic potential for the finite strain setting based on physical knowledge of the solid and fluid constituents. Gajo [109] recently stated that in the large strain regime the macroscopic potential is not simply the sum of individual fluid and solid potentials. In 1973, Biot [25] evaluated the macroscopic free energy for the case of *semilinearity* where the constituents show a "partial linear behavior with respect to their compressibility". Other examples of large strain formulations are provided by Armero [9], Carter et al. [57] or Borja & Alarcon [39]. Recently, Gajo [109, 110] and Gajo & Denzer [111] presented a macroscopic free energy for the completely nonlinear setting with compressibility of both constituents.

Restriction to the case of semilinearity. In the following we restrict our attention to a partial linear behavior of the fluid with respect to its compressibilty. This simplification goes back to Biot [25] and is proposed in many other modeling frameworks such as for example in De Boer & Bluhm [74] and Advani et al. [4]. To this end we introduce the constant fluid bulk modulus

$$\kappa^f = \frac{dp}{dv^f} = const. \tag{4.16}$$

With the relation $dv^f = 1/d\rho^f$ between the differentials of the fluid volume dv^f and the fluid density $d\rho^f$ equation (4.16) can be integrated to

$$p = -\kappa^f \ln[J^f] \quad \text{with} \quad J^f := \frac{\rho_0^f}{\rho^f} \ . \tag{4.17}$$

This yields a linear relationship between the fluid pressure p and the logarithm of the fluid volume ratio $dv^f/dV^f = \rho_0^f/\rho^f$ of fluid volume in the current configuration dv^f to fluid volume in the initial configuration dV^f. Differentiating equation $(4.17)_1$ as well as the definition of the chemical potential with respect to time yields

$$\dot{p} = -\frac{\kappa^f}{J^f}\dot{J}^f \quad \text{and} \quad \dot{\mu} = \frac{\dot{p}}{\rho^f} = -\frac{\kappa^f}{\rho_0^f}\dot{J}^f \ . \tag{4.18}$$

Note that $(4.18)_2$ assumes isothermal conditions, that is $\dot{\theta} = 0$. Integration of (4.18) in $\tau \in (t_0, t)$ gives the fluid's chemical potential μ as

$$\mu = \int_{t_0}^{t} -\frac{\kappa^f}{\rho_0^f}\dot{J}^f \, dt = \frac{\kappa^f}{\rho_0^f}(1 - J^f) \ , \tag{4.19}$$

where the initial potential μ_0 at time t_0 is chosen to be $\mu(t_0) = \mu_0 = 0$. Now consider a split of the current fluid density in $\rho^f = \rho_0^f + \Delta\rho^f$ in initial density and an increment. For the ratio J^f we get $J^f = 1 + \rho_0^f/\Delta\rho^f = 1 + e^f$ where the volumetric fluid strain $e^f := \Delta v^f/V^f = \rho_0^f/\Delta\rho^f$ is introduced. The fluid pressure p and the chemical potential μ in (4.17) and (4.19) can be rewritten as

$$p = -\kappa^f \ln[1 + e^f] \quad \text{and} \quad \mu = -\frac{\kappa^f}{\rho_0^f}e^f. \tag{4.20}$$

Assuming *slightly compressible fluids* such that $e^f \ll 1$ we can approximate the fluid pressure $(4.20)_1$ in a Taylor series which results in the simple expression

$$p = -\kappa^f e^f \ . \tag{4.21}$$

Thus for the assumption of semilinearity, comparison of $(4.20)_2$ and (4.21) yields the simplifications

$$\mu = \frac{p}{\rho_0^f} \quad \text{and} \quad \rho^f = \frac{\rho_0^f}{1 + e^f} \approx \rho_0^f \ . \tag{4.22}$$

Equation (4.22) is in analogy to equation (66) in Biot [25]. The evaluation performed above is presented in a slightly different way in Gajo [109].

Free energy function. We assume the free energy function $\hat{\psi}$ to be split into two contributions associated with the solid skeleton and the pore fluid behavior, such that

$$\hat{\psi}(\boldsymbol{F}, m) = \hat{\psi}_{\text{eff}}(\boldsymbol{F}) + \hat{\psi}_{\text{fluid}}(\boldsymbol{F}, m) \ . \tag{4.23}$$

We choose a compressible form of neo-Hookean material model for the solid skeleton contribution

$$\hat{\psi}_{\text{eff}}(\boldsymbol{F}) = \frac{\gamma}{2}[\ (\boldsymbol{F} : \boldsymbol{F} - 3) + \frac{2}{\beta}(J^{-\beta} - 1)\ ] \ . \tag{4.24}$$

Here, $\gamma > 0$ is the shear modulus of the skeleton and $\beta > 0$ a parameter describing its volumetric compressibility. It is possible to link β to the classical Poisson number of linear elasticity via the relation $\beta = 2\nu/(1-2\nu)$. For the fluid contribution $\hat{\psi}_{\text{fluid}}$ we choose the quadratic form

$$\hat{\psi}_{\text{fluid}}(\boldsymbol{F}, m) = \frac{M}{2}\big[b(J-1) - (m/\rho^f)\big]^2 \ , \tag{4.25}$$

where b and M are denoted as Biot's coefficient and Biot's modulus.

Dissipation potential function. The *canonical convective dissipation potential* is assumed to be of quadratic form in terms of the mass flow vector $\mathbb{H}$

$$\hat{\phi}_{\text{con}}(\mathbb{H}; \boldsymbol{F}) = \frac{1}{2}\widehat{\boldsymbol{K}}^{-1} : (\mathbb{H} \otimes \mathbb{H}) \quad \text{with} \quad \widehat{\boldsymbol{K}} = (\rho^f)^2 K J \boldsymbol{C}^{-1} \ , \tag{4.26}$$

at given state $\boldsymbol{F}$ and where $\widehat{\boldsymbol{K}}$ is denoted as the spatial permeability tensor in terms of the spatial permeability K, the Jacobian $J = \det[\boldsymbol{F}]$ and the right Cauchy-Green tensor $\boldsymbol{C}$. K can be connected to Darcy's hydraulic conductivity K_h by the relation $K = K_h/(\rho^f g)$ with the gravitational acceleration $g = |\bar{\boldsymbol{g}}|$. From (4.26) the dual convective dissipation potential ϕ^*_{con} can be computed as the Legendre transformation yielding

$$\hat{\phi}^*_{\text{con}}(\mathbb{B}; \boldsymbol{F}) = \frac{1}{2}\widehat{\boldsymbol{K}} : (\mathbb{B} \otimes \mathbb{B}) \ . \tag{4.27}$$

Constitutive total stress tensor. The local dissipation inequality leads us to the constitutive equation for the total stresses in terms of the free energy function as $\boldsymbol{P} = \partial_{\boldsymbol{F}}\hat{\psi}$, see (3.70). With (4.23) at hand we obtain

$$\boldsymbol{P} = \partial_{\boldsymbol{F}}\hat{\psi} = \boldsymbol{P}_{\text{eff}} - b\rho^f \mu J \boldsymbol{F}^{-T} \quad \text{with} \quad \boldsymbol{P}_{\text{eff}} = \partial_{\boldsymbol{F}}\hat{\psi}_{\text{eff}} = \gamma\big[\boldsymbol{F} - J^{-\beta}\boldsymbol{F}^{-T}\big] \ . \tag{4.28}$$

The fluid contribution $\hat{\psi}_{\text{fluid}}(\boldsymbol{F}, m)$ is constructed such that the chemical potential (and hence the fluid pressure) is independent of the energy contribution $\hat{\psi}_{\text{eff}}$. Using the relations (2.23) and (4.22), the Cauchy stress is evaluated as

$$\boldsymbol{\sigma} = \boldsymbol{\sigma}_{\text{eff}} - bp\boldsymbol{1} \quad \text{with} \quad \boldsymbol{\sigma}_{\text{eff}} = \frac{\gamma}{J}\big[\boldsymbol{F}\boldsymbol{F}^T - J^{-\beta}\boldsymbol{1}\big] \ , \tag{4.29}$$

yielding for $b = 1$ the classical definition of Terzaghi's effective stress, see Terzaghi [255, 256] or de Boer & Ehlers [76].

Constitutive chemical potential. The local dissipation inequality leads us to the constitutive equation for the chemical potential in terms of the free energy function as $\mu = \partial_m \hat{\psi}$, see (3.70). From (4.23) we obtain

$$\mu = \partial_m \hat{\psi} = \frac{M}{\rho^f} \left[\frac{m}{\rho^f} - b(J-1) \right] . \tag{4.30}$$

Constitutive fluid flow. Using the constitutive relation $(4.3)_6$ the driving force dual to the fluid flow vector is obtained as $\mathbb{B} = \partial_{\mathbb{H}} \hat{\phi}_{\text{con}}$. Evaluation of the dissipation potential function (4.26) we have $\hat{\mathbb{B}} = \widehat{\boldsymbol{K}}^{-1} \mathbb{H}$. Together with the definition of the driving force $(4.3)_3$ we can evaluate the fluid flow law as

$$\mathbb{H} = -\widehat{\boldsymbol{K}} \nabla [\mu - \bar{g} \cdot \boldsymbol{\varphi}] . \tag{4.31}$$

Furthermore using the Gibbs relation $\nabla \mu = (1/\rho^f) \nabla p - \eta^f \nabla \theta$ as well as the relationships $\mathbb{H} = J \boldsymbol{F}^{-1} \mathbb{h}$ and $\nabla(\cdot) = \boldsymbol{F}^T \nabla_{\boldsymbol{x}}(\cdot)$ yield the fluid flow vector per unit deformed area for the isothermal setting as

$$\mathbb{h} = -\rho^f K \boldsymbol{g} \cdot \nabla_{\boldsymbol{x}} [p - \rho^f \bar{g} \cdot \boldsymbol{\varphi}] . \tag{4.32}$$

Equation (4.32) can be identified as Darcy's isotropic filter law, see Darcy [71]. Hence the choice of the quadratic form (4.26) for $\hat{\phi}_{\text{con}}$ models a Darcy-type fluid flow.

4.2. Variational principles for the evolution problem

With the functionals introduced above three variational principles for the coupled problem of poro-elasticity are stated. The first variational principle has a *minimization structure* whereas the other two principles are of mixed type and have a *saddle-point structure*. The last one is shown to be equivalent to the classical $\{\boldsymbol{\varphi}, \mu\}$ formulation widely used in the literature, whereas the first principle leads to a type of modeling for poro-elasticity which is due to its minimization structure advantageous from the numerical viewpoint.

4.2.1. Rate-type variational potential

Based on the energy E introduced in (4.7), the dissipation potential functional D in (4.9) and the external load functional P_{ext} in (4.13) the *two-field rate potential* is defined as

$$\underbrace{\Pi(\dot{\boldsymbol{\varphi}}, \mathbb{H})}_{\text{rate potential}} := \underbrace{\frac{d}{dt} E(\boldsymbol{\varphi}, \mathbb{H})}_{\text{rate of energy}} + \underbrace{D(\mathbb{H})}_{\text{dissipation}} - \underbrace{P_{\text{ext}}(\dot{\boldsymbol{\varphi}}, \mathbb{H})}_{\text{external power}} \tag{4.33}$$

at a given state $\{\boldsymbol{\varphi}, m\}$. Evaluation of the rate potential by use of (4.8), (4.9), (4.14) and (4.15) yields

$$\begin{aligned} \Pi(\dot{\boldsymbol{\varphi}}, \mathbb{H}) = & \int_{\mathcal{B}} \left\{ \frac{\partial \hat{\psi}(\boldsymbol{F}, m)}{\partial \boldsymbol{F}} : \dot{\boldsymbol{F}} - \frac{\partial \hat{\psi}(\boldsymbol{F}, m)}{\partial m} \operatorname{Div}[\mathbb{H}] + \hat{\phi}_{\text{con}}(\mathbb{H}; \boldsymbol{F}) \right\} dV \\ & - \int_{\mathcal{B}} (m_0 + m) \bar{g} \cdot \dot{\boldsymbol{\varphi}} \, dV - \int_{\partial \mathcal{B}_{\boldsymbol{T}}} \bar{\boldsymbol{T}} \cdot \dot{\boldsymbol{\varphi}} \, dA \\ & - \int_{\mathcal{B}} \bar{g} \cdot \boldsymbol{F} \mathbb{H} \, dV + \int_{\partial \mathcal{B}_{\mu}} \bar{\mu} H \, dA , \end{aligned} \tag{4.34}$$

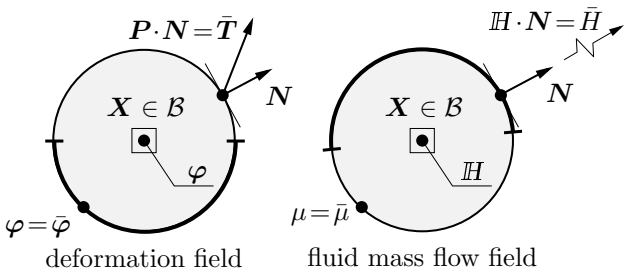

Figure 4.2: *Two-field problem of finite poro-elasticity.* The boundary $\partial\mathcal{B}$ of the solid's reference configuration $\mathcal{B}$ is decomposed into Dirichlet and Neumann parts $\partial\mathcal{B}_{\boldsymbol{\varphi}}\cup\partial\mathcal{B}_T$ for the deformation field and $\partial\mathcal{B}_H\cup\partial\mathcal{B}_\mu$ for the fluid mass flow field.

where in the first integral the balance of fluid mass $\dot{m}=-\operatorname{Div}[\mathbb{H}]$ is used. Note that the potential Π is *linear* with respect to the rate $\dot{\boldsymbol{F}}$ and *convex* with respect to the fluid mass flow vector $\mathbb{H}$. The latter is due to the dissipation potential function $\hat{\phi}_{\text{con}}$, the convexity of which ensures a thermodynamically consistent formulation, see Subsection 3.4.3.

4.2.2. Rate-type variational minimization principle

With the rate potential (4.33) at hand we can state the *two-field variational principle*

$$\{\dot{\boldsymbol{\varphi}},\mathbb{H}\}=\arg\left\{\inf_{\dot{\boldsymbol{\varphi}}\in\mathcal{W}_{\dot{\boldsymbol{\varphi}}}}\inf_{\mathbb{H}\in\mathcal{W}_{\mathbb{H}}}\Pi(\dot{\boldsymbol{\varphi}},\mathbb{H})\right\}\ , \tag{4.35}$$

which defines at the given state $\{\boldsymbol{\varphi},m\}$ at time t the rate $\dot{\boldsymbol{\varphi}}$ of the deformation fields and the fluid mass flow field $\mathbb{H}$. The admissible spaces for the rate of deformation $\dot{\boldsymbol{\varphi}}$ and the mass flux $\mathbb{H}$ are given by

$$\begin{aligned}\mathcal{W}_{\dot{\boldsymbol{\varphi}}}&:=\{\dot{\boldsymbol{\varphi}}\in H^1(\mathcal{B})|\ \dot{\boldsymbol{\varphi}}=\bar{\dot{\boldsymbol{\varphi}}}\ \text{on}\ \partial\mathcal{B}_{\boldsymbol{\varphi}}\}\ ,\\ \mathcal{W}_{\mathbb{H}}&:=\{\mathbb{H}\in H(\operatorname{Div},\mathcal{B})|\ \mathbb{H}\cdot\boldsymbol{N}=\bar{H}\ \text{on}\ \partial\mathcal{B}_H\}\ .\end{aligned} \tag{4.36}$$

The necessary condition of the variational principle (4.35) is that its variation vanishes. Taking the variation of the potential (4.34) the Euler equations of the variational principle are obtained as

$$\begin{aligned}&\textit{Balance of linear momentum} && -\operatorname{Div}[\partial_{\boldsymbol{F}}\hat{\psi}]-(m_0+m)\bar{g}=\boldsymbol{0} && \text{in}\ \mathcal{B}\\ &\textit{Fluid flow equation} && \nabla[\partial_m\hat{\psi}-\bar{g}\cdot\boldsymbol{\varphi}]+\partial_{\mathbb{H}}\hat{\phi}_{\text{con}}=\boldsymbol{0} && \text{in}\ \mathcal{B}\\ &\textit{Traction boundary condition} && \partial_{\boldsymbol{F}}\hat{\psi}\cdot\boldsymbol{N}=\bar{\boldsymbol{T}} && \text{on}\ \partial\mathcal{B}_{\boldsymbol{T}}\\ &\textit{Potential boundary condition} && \partial_m\hat{\psi}=\bar{\mu} && \text{on}\ \partial\mathcal{B}_\mu\end{aligned} \tag{4.37}$$

and turn out to be the linear momentum balance $(4.3)_2$ and the Darcy fluid flow equation in inverse form as a combination of $(4.3)_3$ and $(4.3)_6$, along with the Neumann boundary conditions (4.5). Note that the balance of fluid mass $(4.3)_1$ was used in (4.34) in order to express the rate of relative fluid content $\dot{m}$ by the fluid flow vector $\mathbb{H}$. Hence the fluid mass balance is fulfilled strongly.

4.2.3. Rate-type mixed variational potential

A mixed variational principle is obtained by exchanging the dissipation potential functional $D(\mathbb{H})$ in (4.33) by the *extended* dissipation potential function $D^*(\mathbb{H},\mathbb{B})$ introduced

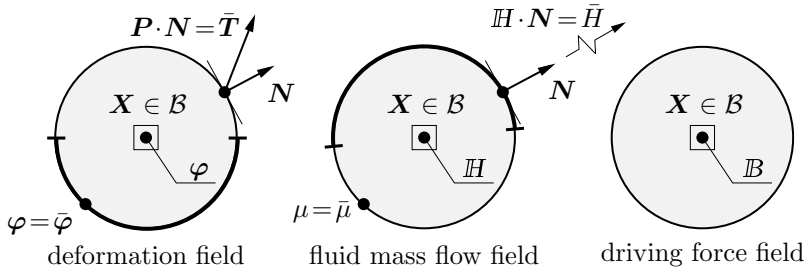

Figure 4.3: *Three-field saddle-point problem of finite poro-elasticity.* The boundary $\partial\mathcal{B}$ of the solid's reference configuration $\mathcal{B}$ is decomposed into Dirichlet and Neumann parts $\partial\mathcal{B}_{\boldsymbol{\varphi}} \cup \partial\mathcal{B}_T$ for the deformation field and $\partial\mathcal{B}_H \cup \partial\mathcal{B}_\mu$ for the fluid mass flow field.

in (4.11). The *mixed three-field potential* is hence defined as

$$\underbrace{\Pi^*(\dot{\boldsymbol{\varphi}}, \mathbb{H}, \mathbb{B})}_{\text{rate potential}} := \underbrace{\frac{d}{dt}E(\boldsymbol{\varphi}, \mathbb{H})}_{\text{rate of energy}} + \underbrace{D^*(\mathbb{H}, \mathbb{B})}_{\text{dissipation}} - \underbrace{P_{\text{ext}}(\dot{\boldsymbol{\varphi}}, \mathbb{H})}_{\text{external power}} \tag{4.38}$$

at a given state $\{\boldsymbol{\varphi}, m\}$. Evaluation of this mixed rate potential by use of (4.8), (4.11), (4.14) and (4.15) yields

$$\begin{aligned}\Pi^*(\dot{\boldsymbol{\varphi}}, \mathbb{H}, \mathbb{B}) = & \int_{\mathcal{B}} \left\{ \frac{\partial\hat{\psi}(\boldsymbol{F}, m)}{\partial \boldsymbol{F}} : \dot{\boldsymbol{F}} - \frac{\partial\hat{\psi}(\boldsymbol{F}, m)}{\partial m} \operatorname{Div}[\mathbb{H}] \right\} dV \\ & + \int_{\mathcal{B}} \left\{ \mathbb{H}\cdot\mathbb{B} - \hat{\phi}^*_{\text{con}}(\mathbb{B}; \boldsymbol{F}, m) \right\} dV \\ & - \int_{\mathcal{B}} (m_0 + m)\bar{\boldsymbol{g}}\cdot\dot{\boldsymbol{\varphi}}\, dV - \int_{\partial\mathcal{B}_{\boldsymbol{T}}} \bar{\boldsymbol{T}}\cdot\dot{\boldsymbol{\varphi}}\, dA \\ & - \int_{\mathcal{B}} \bar{\boldsymbol{g}}\cdot(\boldsymbol{F}\mathbb{H})\, dV + \int_{\partial\mathcal{B}_\mu} \bar{\mu} H\, dA\ ,\end{aligned} \tag{4.39}$$

where in the first integral the balance of fluid mass $\dot{m} = -\operatorname{Div}[\mathbb{H}]$ is used. The potential Π^* is *linear* with respect to the rate of deformation gradient $\dot{\boldsymbol{F}}$ and the fluid mass flow vector $\mathbb{H}$ and *concave* with respect to the driving force vector $\mathbb{B}$. The latter is due to the dual dissipation potential function $\hat{\phi}^*_{\text{con}}$ the convexity of which is implied by the convexity of $\hat{\phi}_{\text{con}}$.

4.2.4. Rate-type variational saddle-point principle

With the potential (4.38) at hand we can state the *mixed three-field variational principle*

$$\{\dot{\boldsymbol{\varphi}}, \mathbb{H}, \mathbb{B}\} = \arg\left\{ \inf_{\dot{\boldsymbol{\varphi}}\in\mathcal{W}_{\dot{\boldsymbol{\varphi}}}} \inf_{\mathbb{H}\in\mathcal{W}_{\mathbb{H}}} \sup_{\mathbb{B}\in\mathcal{W}_{\mathbb{B}}} \Pi^*(\dot{\boldsymbol{\varphi}}, \mathbb{H}, \mathbb{B}) \right\}\ , \tag{4.40}$$

which defines at the given state $\{\boldsymbol{\varphi}, m\}$ at time t the rate $\dot{\boldsymbol{\varphi}}$ of the deformation fields, the fluid mass flow field $\mathbb{H}$ and the dual driving force field $\mathbb{B}$. Note that due to the concavity of (4.39) with respect to $\mathbb{B}$ this variational principle has a *saddle-point structure*. The admissible spaces for $\dot{\boldsymbol{\varphi}}$, $\mathbb{H}$ and $\mathbb{B}$ are given by

$$\begin{aligned}\mathcal{W}_{\dot{\boldsymbol{\varphi}}} &:= \{\dot{\boldsymbol{\varphi}} \in H^1(\mathcal{B}) |\ \dot{\boldsymbol{\varphi}} = \dot{\bar{\boldsymbol{\varphi}}} \text{ on } \partial\mathcal{B}_{\boldsymbol{\varphi}}\}\ , \\ \mathcal{W}_{\mathbb{H}} &:= \{\mathbb{H} \in H(\operatorname{Div}, \mathcal{B}) |\ \mathbb{H}\cdot\boldsymbol{N} = \bar{H} \text{ on } \partial\mathcal{B}_H\}\ , \\ \mathcal{W}_{\mathbb{B}} &:= \{\mathbb{B} \in L^2\}\ .\end{aligned} \tag{4.41}$$

The necessary condition of the variational principle (4.40) is that its variation vanishes. Taking the variation of the potential (4.39) the Euler equations of the variational principle are obtained as

$$\begin{aligned}
&\textit{Balance of linear momentum} && -\operatorname{Div}[\partial_{\boldsymbol{F}}\hat{\psi}] - (m_0+m)\bar{\boldsymbol{g}} = \boldsymbol{0} && \text{in } \mathcal{B}\\
&\textit{Constitutive driving force} && \nabla[\partial_m\hat{\psi} - \bar{\boldsymbol{g}}\cdot\boldsymbol{\varphi}] + \mathbb{B} = \boldsymbol{0} && \text{in } \mathcal{B}\\
&\textit{Fluid flow equation} && \mathbb{H} - \partial_{\mathbb{B}}\hat{\phi}^*_{\text{con}} = \boldsymbol{0} && \text{in } \mathcal{B}\\
&\textit{Traction boundary condition} && \partial_{\boldsymbol{F}}\hat{\psi}\cdot\boldsymbol{N} = \bar{\boldsymbol{T}} && \text{on } \partial\mathcal{B}_{\boldsymbol{T}}\\
&\textit{Potential boundary condition} && \partial_m\hat{\psi} = \bar{\mu} && \text{on } \partial\mathcal{B}_{\mu}
\end{aligned} \tag{4.42}$$

and turn out to be the governing equations $(4.3)_2$, $(4.3)_3$ and the Darcy fluid flow equation, along with the Neumann boundary conditions (4.5). Note that the balance of fluid mass $(4.3)_1$ was used in (4.39) in order to express the rate of relative fluid content $\dot{m}$ by the fluid flow vector $\mathbb{H}$. Hence the fluid mass balance is fulfilled strongly.

4.2.5. Reduced rate-type mixed variational potential

The mixed variational principle (4.40) is an initial boundary value problem containing nine scalar unknown fields $\{\dot{\boldsymbol{\varphi}}, \mathbb{H}, \mathbb{B}\}$. Based on the knowledge of the Euler equation $(4.42)_3$ the unknown fields can be reduced to five. To this end we introduce the chemical potential field $\mu = \partial_m\hat{\psi}$, see (3.70) and rewrite $(4.42)_2$ as

$$\mathbb{B} = -\nabla[\mu - \bar{\boldsymbol{g}}\cdot\boldsymbol{\varphi}] \text{ in } \mathcal{B}\ . \tag{4.43}$$

By reinsertion of the fluid mass balance and by use of (4.43) a *reduced mixed three-field potential* can be obtained from (4.39) as

$$\begin{aligned}
\tilde{\Pi}^*(\dot{\boldsymbol{\varphi}}, \dot{m}, \mu) = &\int_{\mathcal{B}} \Big\{ \frac{\partial\hat{\psi}(\boldsymbol{F}, m)}{\partial \boldsymbol{F}} : \dot{\boldsymbol{F}} + \frac{\partial\hat{\psi}(\boldsymbol{F}, m)}{\partial m}\dot{m} - \mu\dot{m} - \hat{\phi}^*_{\text{con}}(\mathbb{B}; \boldsymbol{F}, m) \Big\}\, dV\\
&- \int_{\mathcal{B}} (m_0+m)\bar{\boldsymbol{g}}\cdot\dot{\boldsymbol{\varphi}}\, dV - \int_{\partial\mathcal{B}_{\boldsymbol{T}}} \bar{\boldsymbol{T}}\cdot\dot{\boldsymbol{\varphi}}\, dA - \int_{\partial\mathcal{B}_H} \mu\bar{H}\, dA\ .
\end{aligned} \tag{4.44}$$

Note that in order to obtain (4.44) the boundary conditions $(4.5)_2$ have to be evaluated. The potential $\tilde{\Pi}^*$ is *linear* with respect to the rates $\dot{\boldsymbol{F}}$ and $\dot{m}$ and *concave* with respect to the chemical potential field μ. The latter is due to the dual dissipation potential function $\hat{\phi}^*_{\text{con}}$ the convexity of which is implied by the convexity of $\hat{\phi}_{\text{con}}$.

4.2.6. Reduced rate-type variational saddle-point principle

With the reduced rate-type potential (4.44) at hand we can state a *reduced mixed three-field variational principle*

$$\{\dot{\boldsymbol{\varphi}}, \dot{m}, \mu\} = \arg\left\{ \inf_{\dot{\boldsymbol{\varphi}}\in\mathcal{W}_{\dot{\boldsymbol{\varphi}}}} \inf_{\dot{m}\in\mathcal{W}_{\dot{m}}} \sup_{\mu\in\mathcal{W}_{\mu}} \tilde{\Pi}^*(\dot{\boldsymbol{\varphi}}, \dot{m}, \mu) \right\} \tag{4.45}$$

which defines the rates of deformation $\dot{\boldsymbol{\varphi}}$ and relative fluid mass content $\dot{m}$ as well as the chemical potential μ at the given state $\{\boldsymbol{\varphi}, m\}$ at time t. Due to the concavity of the

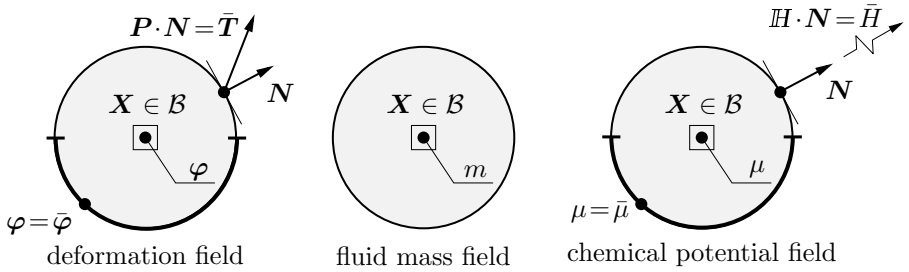

Figure 4.4: *Three-field reduced saddle-point problem of finite poro-elasticity.* The boundary $\partial\mathcal{B}$ of the solid's reference configuration $\mathcal{B}$ is decomposed into Dirichlet and Neumann parts $\partial\mathcal{B}_{\boldsymbol{\varphi}} \cup \partial\mathcal{B}_T$ for the deformation field and $\partial\mathcal{B}_\mu \cup \partial\mathcal{B}_H$ for the chemical potential field.

potential $\tilde{\Pi}$ with respect to μ the principle has saddle-point structure. The admissible spaces for $\dot{\boldsymbol{\varphi}}$, $\dot{m}$ and μ are given by

$$\begin{aligned} \mathcal{W}_{\dot{\boldsymbol{\varphi}}} &:= \{\dot{\boldsymbol{\varphi}} \in H^1(\mathcal{B}) |\ \dot{\boldsymbol{\varphi}} = \dot{\bar{\boldsymbol{\varphi}}} \text{ on } \partial\mathcal{B}_{\boldsymbol{\varphi}}\} \ , \\ \mathcal{W}_{\dot{m}} &:= \{\dot{m} \in L^2\} \ , \\ \mathcal{W}_{\mu} &:= \{\mu \in H^1(\mathcal{B}) |\ \mu = \bar{\mu} \text{ on } \partial\mathcal{B}_{\mu}\} \ . \end{aligned} \tag{4.46}$$

The necessary condition of the variational principle (4.45) is that its variation vanishes. Taking the variation of the potential (4.44) the Euler equations of the variational principle are obtained as

$$\begin{aligned} &\textit{Balance of linear momentum} && -\operatorname{Div}[\partial_{\boldsymbol{F}}\hat{\psi}] - (m_0 + m)\bar{\boldsymbol{g}} = \boldsymbol{0} && \text{in } \mathcal{B} \\ &\textit{Constitutive chemical potential} && \partial_m \hat{\psi} - \mu = \boldsymbol{0} && \text{in } \mathcal{B} \\ &\textit{Balance of fluid mass} && -\dot{m} - \operatorname{Div}[\partial_{\mathbb{B}}\hat{\phi}^*_{\text{con}}] = \boldsymbol{0} && \text{in } \mathcal{B} \\ &\textit{Traction boundary condition} && \partial_{\boldsymbol{F}}\hat{\psi}\cdot\boldsymbol{N} = \bar{\boldsymbol{T}} && \text{on } \partial\mathcal{B}_{\boldsymbol{T}} \\ &\textit{Flux boundary condition} && \partial_{\mathbb{B}}\hat{\phi}^*_{\text{con}}\cdot\boldsymbol{N} = \bar{H} && \text{on } \partial\mathcal{B}_H \end{aligned} \tag{4.47}$$

and turn out to be the governing equations $(4.3)_1$, $(4.3)_2$ and the definition of the chemical potential μ, along with the Neumann boundary conditions (4.5). Note that in contrast to the variational principles in Subsection 4.2.2 and Subsection 4.2.4, $\partial\mathcal{B}_H$ is the Neumann boundary and $\partial\mathcal{B}_\mu$ is the Dirichlet boundary.

4.3. Incremental variational principle for the update problem

We now perform a time-discretization of the rate-type variational principles introduced above. The procedure closely follows the considerations of Miehe [176]. In the following we restrict the attention to the minimization principle of Subsection 4.2.2 and the reduced mixed saddle-point principle introduced in Subsection 4.2.6.

4.3.1. Time-discretization and incremental variational potentials

Consider discrete points in time $[t_0, ..., t_n, t_{n+1}, ..., t_\infty]$ of the process time $[t_0, t_\infty]$. Here $\tau := t_{n+1} - t_n$ is the time step size. The objective is now to determine the unknown fields at time t_{n+1}, whereas all fields at time t_n are assumed to be known. The rate of a quantity $\dot{q}(t)$ is considered to be constant within a time step τ and can hence be written as

$\dot{q}_{n+1}(t_{n+1}) = (q_{n+1} - q_n)/\tau$. For sake of a compact notation in the further considerations all subscripts $n+1$ are dropped, such that all variables without index are associated with time t_{n+1}.

Canonical two-field potential. The time-discrete counterpart of the variational functional Π given in (4.34) within the time step $[t_n, t]$ under consideration is obtained by an algorithmic integration scheme. With the above stated assumption of *constant* rates of field quantities within a time step the incremental potential is considered of the form

$$\begin{aligned}\Pi^\tau(\boldsymbol{\varphi}, \mathbb{H}) = & \int_{\mathcal{B}} \left\{ \hat{\psi}(\boldsymbol{F}, m) - \hat{\psi}_n + \tau \hat{\phi}_{\text{con}}(\mathbb{H}; \boldsymbol{F}_n, m_n) \right\} dV \\ & - \int_{\mathcal{B}} (m_0 + m_n) \bar{\boldsymbol{g}} \cdot [\boldsymbol{\varphi} - \boldsymbol{\varphi}_n] \, dV - \int_{\partial \mathcal{B}_{\boldsymbol{T}}} \bar{\boldsymbol{T}} \cdot [\boldsymbol{\varphi} - \boldsymbol{\varphi}_n] \, dA \\ & - \int_{\mathcal{B}} \tau \bar{\boldsymbol{g}} \cdot \boldsymbol{F}_n \mathbb{H} \, dV + \int_{\partial \mathcal{B}_\mu} \tau \bar{\mu} H \, dA \, ,\end{aligned} \tag{4.48}$$

where we introduced $\hat{\psi}_n = \hat{\psi}(\boldsymbol{F}_n, m_n)$. Note that the convective dissipation potential $\hat{\phi}_{\text{con}}(\mathbb{H}; \boldsymbol{F}_n, m_n)$ is evaluated at frozen state $\{\boldsymbol{F}_n, m_n\}$ of deformation gradient and relative fluid mass at time t_n. Furthermore m_n in the mechanical power as well as $\boldsymbol{F}_n$ in the fluid power are evaluated at time t_n.

Reduced mixed three-field potential. The incremental counterpart of the reduced mixed variational functional $\tilde{\Pi}^\tau$ given in (4.44) within the time step $[t_n, t]$ under consideration is again obtained by an algorithmic integration. Assuming *constant* rates of field quantities within a time step the incremental potential is considered of the form

$$\begin{aligned}\tilde{\Pi}^{*\tau}(\boldsymbol{\varphi}, m, \mu) = & \int_{\mathcal{B}} \left\{ \hat{\psi}(\boldsymbol{F}, m) - \hat{\psi}_n - \mu(m - m_n) - \tau \hat{\phi}^*_{\text{con}}(\mathbb{B}; \boldsymbol{F}_n, m_n) \right\} dV \\ & - \int_{\mathcal{B}} (m_0 + m_n) \bar{\boldsymbol{g}} \cdot [\boldsymbol{\varphi} - \boldsymbol{\varphi}_n] \, dV - \int_{\partial \mathcal{B}_{\boldsymbol{T}}} \bar{\boldsymbol{T}} \cdot [\boldsymbol{\varphi} - \boldsymbol{\varphi}_n] \, dA \\ & - \int_{\partial \mathcal{B}_H} \tau \mu \bar{H} \, dA \, .\end{aligned} \tag{4.49}$$

Note that the dual convective dissipation potential $\hat{\phi}^*_{\text{con}}(\mathbb{B}; \boldsymbol{F}_n, m_n)$ as well as the mechanical volume power is evaluated at frozen state $\{\boldsymbol{F}_n, m_n\}$ of deformation gradient and relative fluid mass at time t_n.

4.3.2. Incremental canonical variational minimization principle

With the incremental potential (4.48) at hand, the time-discrete counterpart of the *canonical two-field variational principle* (4.35) for the problem of coupled poro-elasticity can be stated as

$$\{\boldsymbol{\varphi}, \mathbb{H}\} = \arg \left\{ \inf_{\boldsymbol{\varphi} \in \mathcal{W}_{\boldsymbol{\varphi}}} \inf_{\mathbb{H} \in \mathcal{W}_{\mathbb{H}}} \Pi^\tau(\boldsymbol{\varphi}, \mathbb{H}) \right\} \, . \tag{4.50}$$

The variational principle determines the fields $\{\boldsymbol{\varphi}, \mathbb{H}\}$ at current time t as a *minimum* of the time-discrete potential Π^τ. The admissible spaces for the fields are

$$\begin{aligned} \mathcal{W}_{\boldsymbol{\varphi}} &:= \{\boldsymbol{\varphi} \in H^1(\mathcal{B}) |\ \boldsymbol{\varphi} = \bar{\boldsymbol{\varphi}} \text{ on } \partial\mathcal{B}_{\boldsymbol{\varphi}}\} \ , \\ \mathcal{W}_{\mathbb{H}} &:= \{\mathbb{H} \in H(\mathrm{Div}, \mathcal{B}) |\ \mathbb{H} \cdot \boldsymbol{N} = \bar{H} \text{ on } \partial\mathcal{B}_H\} \ . \end{aligned} \tag{4.51}$$

The necessary condition of the variational principle (4.50) is that its variation vanishes. Taking the variation of the potential (4.48) the Euler equations of the variational principle are obtained as

$$\begin{aligned} &\textit{Balance of linear momentum} && -\mathrm{Div}[\partial_{\boldsymbol{F}}\hat{\psi}] - (m_0 + m_n)\bar{g} = \boldsymbol{0} && \text{in } \mathcal{B} \\ &\textit{Fluid flow equation} && \tau\nabla[\partial_m\hat{\psi} - \bar{g}\cdot\boldsymbol{\varphi}_n] + \tau\partial_{\mathbb{H}}\hat{\phi}_{\mathrm{con}} = 0 && \text{in } \mathcal{B} \\ &\textit{Traction boundary condition} && \partial_{\boldsymbol{F}}\hat{\psi}\cdot\boldsymbol{N} = \bar{\boldsymbol{T}} && \text{on } \partial\mathcal{B}_{\boldsymbol{T}} \\ &\textit{Potential boundary condition} && \partial_m\hat{\psi} = \bar{\mu} && \text{on } \partial\mathcal{B}_\mu \end{aligned} \tag{4.52}$$

These are consistent algorithmic counterparts of the Euler equations (4.37) representing the linear momentum balance $(4.3)_2$ and the Darcy fluid flow equation in inverse form, along with the Neumann boundary conditions. Here the algorithmic balance of fluid mass

$$m = m_n + \tau\,\mathrm{Div}[\mathbb{H}] \tag{4.53}$$

is used in (4.52) in order to express the relative fluid content m in terms of the fluid flow vector $\mathbb{H}$. The fluid mass balance is hence fulfilled strongly.

4.3.3. Incremental reduced mixed variational saddle-point principle

With the incremental potential (4.49) at hand the time-discrete counterpart of the *mixed three-field variational principle* (4.45) is given by

$$\{\boldsymbol{\varphi}, m, \mu\} = \arg\left\{ \inf_{\boldsymbol{\varphi}\in\mathcal{W}_{\boldsymbol{\varphi}}} \inf_{m\in\mathcal{W}_m} \sup_{\mu\in\mathcal{W}_\mu} \tilde{\Pi}^{*\tau}(\boldsymbol{\varphi}, m, \mu) \right\} \ . \tag{4.54}$$

It determines the fields $\{\boldsymbol{\varphi}, m, \mu\}$ at current time t as a *saddle-point* of the time-discrete potential $\tilde{\Pi}^{*\tau}$. The admissible spaces for the fields are

$$\begin{aligned} \mathcal{W}_{\boldsymbol{\varphi}} &:= \{\boldsymbol{\varphi} \in H^1(\mathcal{B}) |\ \boldsymbol{\varphi} = \bar{\boldsymbol{\varphi}} \text{ on } \partial\mathcal{B}_{\boldsymbol{\varphi}}\} \ , \\ \mathcal{W}_m &:= \{m \in L^2\} \ , \\ \mathcal{W}_\mu &:= \{\mu \in H^1(\mathcal{B}) |\ \mu = \bar{\mu} \text{ on } \partial\mathcal{B}_\mu\} \ . \end{aligned} \tag{4.55}$$

The necessary condition of the variational principle (4.54) is that its variation vanishes. Taking the variation of the potential (4.49) the Euler equations of the variational principle are obtained as

$$\begin{aligned} &\textit{Balance of linear momentum} && -\mathrm{Div}[\partial_{\boldsymbol{F}}\hat{\psi}] - (m_0 + m_n)\bar{g} = \boldsymbol{0} && \text{in } \mathcal{B} \\ &\textit{Constitutive chemical potential} && \partial_m\hat{\psi} - \mu = \boldsymbol{0} && \text{in } \mathcal{B} \\ &\textit{Balance of fluid mass} && -[m - m_n] - \tau\,\mathrm{Div}[\partial_{\mathbb{B}}\hat{\phi}^*_{\mathrm{con}}] = \boldsymbol{0} && \text{in } \mathcal{B} \\ &\textit{Traction boundary conditons} && \partial_{\boldsymbol{F}}\hat{\psi}\cdot\boldsymbol{N} = \bar{\boldsymbol{T}} && \text{on } \partial\mathcal{B}_{\boldsymbol{T}} \\ &\textit{Flux boundary conditons} && \tau\partial_{\mathbb{B}}\hat{\phi}^*_{\mathrm{con}}\cdot\boldsymbol{N} = \tau\bar{H} && \text{on } \partial\mathcal{B}_H \end{aligned} \tag{4.56}$$

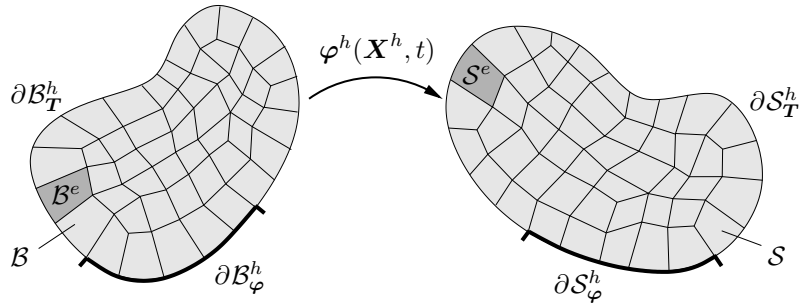

Figure 4.5: *Finite element discretization.* The material body $\mathcal{B}$ is approximated by the discrete body $\mathcal{B}^h \approx \mathcal{B}$. The discretization $\mathcal{B}^h$ is the union of n_e finite elements $\mathcal{B}^e$. The deformation field $\boldsymbol{\varphi}$ and all other unknown fields are approximated based on discrete values at interpolation points and so-called shape functions.

Again we obtain the consistent algorithmic counterparts of the Euler equations (4.42) representing the linear momentum balance $(4.3)_2$, the constitutive definition of the chemical potential and the time-discrete fluid mass balance $(4.3)_1$, along with the Neumann boundary conditions. Note that in contrast to the variational minimization principle $\partial\mathcal{B}_H$ is the Neumann boundary and $\partial\mathcal{B}_\mu$ is the Dirichlet boundary.

4.4. Space-discrete incremental variational principles

In what follows the time-discrete variational principles (4.50) and (4.54) are discretized in space by use of the finite element method. To this end the finite element approximation of the geometry and the fields of unknowns are introduced in Subsection 4.4.1. Then the space-time-discrete variational principles are stated and different finite element designs for the two formulations are proposed. For a deeper insight into the method the interested reader is referred to the classical textbooks Zienkiewicz et al. [280], Hughes [139], Braess [45] and Wriggers [273].

4.4.1. Finite element approximation

The finite element method is based on an approximation of the domain $\mathcal{B} \approx \mathcal{B}^h$ that consists of the union of n_e non-overlapping finite elements $\mathcal{B}^e$

$$\mathcal{B} \approx \mathcal{B}^h = \bigcup_{e=1}^{n_e} \mathcal{B}^e \ , \tag{4.57}$$

see Figure 4.5 for a visualization. Here h describes a typical element size. The idea of the finite element method is to make an ansatz for the continuous fields, here $\boldsymbol{\varphi}(\boldsymbol{X})$, $\mathbb{H}(\boldsymbol{X})$ and $\mu(\boldsymbol{X})$, *within a finite element* $\mathcal{B}^e$ based on discrete values at discrete interpolation points and so-called shape functions associated to these discrete points

$$\boldsymbol{\varphi}^e(\boldsymbol{X}) = \sum_{i=1}^{m_{\boldsymbol{\varphi}}} \check{N}_{\boldsymbol{\varphi}}^{e,i}(\boldsymbol{X})\boldsymbol{\varphi}^i \ , \ \mathbb{H}^e(\boldsymbol{X}) = \sum_{i=1}^{m_{\mathbb{H}}} \check{N}_{\mathbb{H}}^{e,i}(\boldsymbol{X})\mathbb{H}^i \ , \ \mu^e(\boldsymbol{X}) = \sum_{i=1}^{m_\mu} \check{N}_{\mu}^{e,i}(\boldsymbol{X})\mu^i \ . \tag{4.58}$$

Here, $\boldsymbol{\varphi}^i$, $\mathbb{H}^i$ and μ^i are discrete values of deformation, flow vector and chemical potential at the $m_{\boldsymbol{\varphi}}$, $m_{\mathbb{H}}$ and m_μ discrete interpolation points $\boldsymbol{X}_{e,\boldsymbol{\varphi}}^{h,i}$, $\boldsymbol{X}_{e,\mathbb{H}}^{h,i}$ and $\boldsymbol{X}_{e,\mu}^{h,i}$ of the element

e. Furthermore $\check{N}^{e,i}_{\boldsymbol{\varphi}}(\boldsymbol{X})$, $\check{N}^{e,i}_{\mathbb{H}}(\boldsymbol{X})$ and $\check{N}^{e,i}_{\mu}(\boldsymbol{X})$ are the shape functions associated to the interpolation points $\boldsymbol{X}^{h,i}_{e,\boldsymbol{\varphi}}$, $\boldsymbol{X}^{h,i}_{e,\mathbb{H}}$ and $\boldsymbol{X}^{h,i}_{e,\mu}$ and associated to element e. Within the context of *isoparametric finite elements* the approximation with shape functions is not only used for the global fields of unknown but also for the description of the geometry $\boldsymbol{X}^e$ of an element. That is, by introduction of a parent element $\mathcal{A}$ with local element's coordinates $\boldsymbol{\xi}$, the geometry of an element $\mathcal{B}^e$ is approximated based on discrete coordinates $\boldsymbol{X}^i$ at $m_{\boldsymbol{X}}$ discrete interpolation points and associated shape functions $\hat{N}^i_{\boldsymbol{X}}(\boldsymbol{\xi})$ as

$$\boldsymbol{X}^e(\boldsymbol{\xi}) = \sum_{i=1}^{m_{\boldsymbol{X}}} \hat{N}^i_{\boldsymbol{X}}(\boldsymbol{\xi}) \boldsymbol{X}^i \ . \tag{4.59}$$

The relation (4.59) provides an invertible mapping within an element such that $\boldsymbol{\xi} = \boldsymbol{X}^{e\,-1}(\boldsymbol{X})$ in $\mathcal{B}^e$. Thus the approximations (4.58) for the unknown fields within an element can be rewritten in terms of local shape functions $\hat{N}^i_{(\cdot)}(\boldsymbol{\xi})$ as

$$\begin{aligned}
\boldsymbol{\varphi}^e(\boldsymbol{X}) &= \sum_{i=1}^{m_{\boldsymbol{\varphi}}} \hat{N}^i_{\boldsymbol{\varphi}} \left(\boldsymbol{\xi} = \boldsymbol{X}^{e-1}(\boldsymbol{X})\right) \boldsymbol{\varphi}^i \ , \\
\mathbb{H}^e(\boldsymbol{X}) &= \sum_{i=1}^{m_{\mathbb{H}}} \hat{N}^i_{\mathbb{H}} \left(\boldsymbol{\xi} = \boldsymbol{X}^{e-1}(\boldsymbol{X})\right) \mathbb{H}^i \ , \\
\mu^e(\boldsymbol{X}) &= \sum_{i=1}^{m_{\mu}} \hat{N}^i_{\mu} \left(\boldsymbol{\xi} = \boldsymbol{X}^{e-1}(\boldsymbol{X})\right) \mu^i \ .
\end{aligned} \tag{4.60}$$

The advantage of using the interpolation (4.60) is that the shape functions $\hat{N}^i_{(\cdot)}(\boldsymbol{\xi})$ are defined on $\mathcal{A}$ and thus independent of the geometry of the element $\mathcal{B}^e$ in the physical space. For scalar-valued shape functions the connection between the shape functions $\check{N}^{e,i}_{(\cdot)}$ in (4.58) and $\hat{N}^i_{(\cdot)}$ (4.60) is given by

$$\check{N}^{e,i}_{(\cdot)}(\boldsymbol{X}) = \hat{N}^i_{(\cdot)} \left(\boldsymbol{\xi} = \boldsymbol{X}^{e-1}(\boldsymbol{X})\right) \quad \text{for } \boldsymbol{X} \in \mathcal{B}^e \ . \tag{4.61}$$

The simple relation (4.61) is not true for vector-valued shape functions, see below.

If the parent element $\mathcal{A}$ can guarantee continuity of the geometry approximation (4.59) and of the shape functions (4.61) over element boundaries, then it is possible to introduce continuous global shape functions $N^I_{(\cdot)}(\boldsymbol{X})$ defined on $\mathcal{B}^h$ and associated to global interpolation points such that we can write the *approximation of the fields* in $\mathcal{B}^h$ as

$$\begin{aligned}
\boldsymbol{\varphi}(\boldsymbol{X}) \approx \boldsymbol{\varphi}^h(\boldsymbol{X}) &= \sum_{I=1}^{M_{\boldsymbol{\varphi}}} N^I_{\boldsymbol{\varphi}}(\boldsymbol{X}) \boldsymbol{\varphi}^I \ =: \underline{\mathbf{N}}_{\boldsymbol{\varphi}} \underline{\mathbf{d}}_{\boldsymbol{\varphi}} \ , \\
\mathbb{H}(\boldsymbol{X}) \approx \mathbb{H}^h(\boldsymbol{X}) &= \sum_{I=1}^{M_{\mathbb{H}}} N^I_{\mathbb{H}}(\boldsymbol{X}) \mathbb{H}^I \ =: \underline{\mathbf{N}}_{\mathbb{H}} \underline{\mathbf{d}}_{\mathbb{H}} \ , \\
\mu(\boldsymbol{X}) \approx \mu^h(\boldsymbol{X}) &= \sum_{I=1}^{M_{\mu}} N^I_{\mu}(\boldsymbol{X}) \mu^I \ =: \underline{\mathbf{N}}_{\mu} \underline{\mathbf{d}}_{\mu} \ .
\end{aligned} \tag{4.62}$$

In (4.62) $\boldsymbol{\varphi}^I$, $\mathbb{H}^I$ and μ^I are discrete values of deformation, flow vector and chemical potential at the $M_{\boldsymbol{\varphi}}$, $M_{\mathbb{H}}$ and M_{μ} global interpolation points $\boldsymbol{X}^{h,I}_{\boldsymbol{\varphi}}$, $\boldsymbol{X}^{h,I}_{\mathbb{H}}$ and $\boldsymbol{X}^{h,I}_{\mu}$ in $\mathcal{B}^h$.

Here we assume that the union of all interpolation points $\boldsymbol{X}^{h,i}_{e,\boldsymbol{\varphi}}$, $\boldsymbol{X}^{h,i}_{e,\mathbb{H}}$ and $\boldsymbol{X}^{h,i}_{e,\mu}$ of all elements e equals the set of global interpolation points, that is

$$\begin{aligned}
\left\{\boldsymbol{X}^{h,1}_{\boldsymbol{\varphi}},...,\boldsymbol{X}^{h,M_{\boldsymbol{\varphi}}}_{\boldsymbol{\varphi}}\right\} &= \bigcup_{e=1}^{n_e}\left\{\boldsymbol{X}^{h,1}_{e,\boldsymbol{\varphi}},...,\boldsymbol{X}^{h,m_{\boldsymbol{\varphi}}}_{e,\boldsymbol{\varphi}}\right\}\ , \\
\left\{\boldsymbol{X}^{h,1}_{\mathbb{H}},...,\boldsymbol{X}^{h,M_{\mathbb{H}}}_{\mathbb{H}}\right\} &= \bigcup_{e=1}^{n_e}\left\{\boldsymbol{X}^{h,1}_{e,\mathbb{H}},...,\boldsymbol{X}^{h,m_{\mathbb{H}}}_{e,\mathbb{H}}\right\}\ , \\
\left\{\boldsymbol{X}^{h,1}_{\mu},...,\boldsymbol{X}^{h,M_{\mu}}_{\mu}\right\} &= \bigcup_{e=1}^{n_e}\left\{\boldsymbol{X}^{h,1}_{e,\mu},...,\boldsymbol{X}^{h,m_{\mu}}_{e,\mu}\right\}\ .
\end{aligned} \tag{4.63}$$

Furthermore, in order to have a compact notation, we introduced in (4.62) the vectors of global discrete values of unknowns $\underline{\mathbf{d}}_{\boldsymbol{\varphi}}$, $\underline{\mathbf{d}}_{\mathbb{H}}$ and $\underline{\mathbf{d}}_{\mu}$ as well as symbolic representations of global matrices of shape functions $\underline{\mathbf{N}}_{\boldsymbol{\varphi}}$, $\underline{\mathbf{N}}_{\mathbb{H}}$ and $\underline{\mathbf{N}}_{\mu}$. In particular, for the case of nodal-based degrees of freedom, we can write the vectors of discrete unknown as

$$\underline{\mathbf{d}}_{\boldsymbol{\varphi}} := \left[\,\boldsymbol{\varphi}^1,...,\boldsymbol{\varphi}^{M_{\boldsymbol{\varphi}}}\,\right]^T\ ,\quad \underline{\mathbf{d}}_{\mathbb{H}} := \left[\,\mathbb{H}^1,...,\mathbb{H}^{M_{\mathbb{H}}}\,\right]^T \quad\text{and}\quad \underline{\mathbf{d}}_{\mu} := \left[\,\mu^1,...,\mu^{M_{\mu}}\,\right]^T\ , \tag{4.64}$$

as well as the global matrices containing scalar-valued global interpolation functions $N^I_{\boldsymbol{\varphi}}$, $N^I_{\mathbb{H}}$ and N^I_{μ} as

$$\begin{aligned}
\underline{\mathbf{N}}_{\boldsymbol{\varphi}} &:= \begin{bmatrix} N^1_{\boldsymbol{\varphi}} & 0 & 0 & & N^{M_{\boldsymbol{\varphi}}}_{\boldsymbol{\varphi}} & 0 & 0 \\ 0 & N^1_{\boldsymbol{\varphi}} & 0 & ... & 0 & N^{M_{\boldsymbol{\varphi}}}_{\boldsymbol{\varphi}} & 0 \\ 0 & 0 & N^1_{\boldsymbol{\varphi}} & & 0 & 0 & N^{M_{\boldsymbol{\varphi}}}_{\boldsymbol{\varphi}} \end{bmatrix}\ , \\
\underline{\mathbf{N}}_{\mathbb{H}} &:= \begin{bmatrix} N^1_{\mathbb{H}} & 0 & 0 & & N^{M_{\mathbb{H}}}_{\mathbb{H}} & 0 & 0 \\ 0 & N^1_{\mathbb{H}} & 0 & ... & 0 & N^{M_{\mathbb{H}}}_{\mathbb{H}} & 0 \\ 0 & 0 & N^1_{\mathbb{H}} & & 0 & 0 & N^{M_{\mathbb{H}}}_{\mathbb{H}} \end{bmatrix}\ , \\
\underline{\mathbf{N}}_{\mu} &:= \begin{bmatrix} N^1_{\mu} & & ... & & N^{M_{\mu}}_{\mu} \end{bmatrix}\ .
\end{aligned} \tag{4.65}$$

The global shape function $N^I_{(\cdot)}(\boldsymbol{X})$ associated to the global point $\boldsymbol{X}^{h,I}_{(\cdot)}$ is constructed as a piecewise combination of the local shape functions $\check{N}^{e,i}_{(\cdot)}(\boldsymbol{X})$ of adjoining elements e that are associated to the local point $\boldsymbol{X}^{h,i}_{e,(\cdot)} = \boldsymbol{X}^{h,I}_{(\cdot)}$, that is

$$N^I_{(\cdot)}(\boldsymbol{X}) = \begin{cases} \check{N}^{e,i}_{(\cdot)}(\boldsymbol{X}) & \text{if } \boldsymbol{X}\in\mathcal{B}^e \text{ and } \boldsymbol{X}^{h,I}_{(\cdot)} = \boldsymbol{X}^{h,i}_{e,(\cdot)} \\ 0 & \text{else} \end{cases} \tag{4.66}$$

Besides the interpolations of the fields $\boldsymbol{\varphi}^h$, $\mathbb{H}^h$ and μ^h itself also derivatives of these fields are needed. In particular these are the material gradients $\boldsymbol{F} = \nabla\boldsymbol{\varphi}$ and $\nabla\mu$ of the deformation and chemical potential as well as the material divergence $\mathrm{Div}[\mathbb{H}]$ of the fluid mass flow vector. Using the Voigt notation to rewrite the tensorial deformation gradient $\boldsymbol{F}$ as a vectorial object, that is $\boldsymbol{F} = [\,F_{11},F_{12},F_{13},F_{21},F_{22},F_{23},F_{31},F_{32},F_{33}\,]^T$ we write in

analogy to (4.62)

$$\begin{aligned} \boldsymbol{F}(\boldsymbol{X}) &\approx \boldsymbol{F}^h(\boldsymbol{X}) &&= \underline{\mathbf{B}}_{\boldsymbol{F}} \underline{\mathbf{d}}_{\boldsymbol{\varphi}} \,, \\ \mathrm{Div}[\mathbb{H}](\boldsymbol{X}) &\approx \mathrm{Div}[\mathbb{H}^h](\boldsymbol{X}) &&= \underline{\mathbf{B}}_{m} \underline{\mathbf{d}}_{\mathbb{H}} \,, \\ \nabla\mu(\boldsymbol{X}) &\approx \nabla\mu^h(\boldsymbol{X}) &&= \underline{\mathbf{B}}_{\nabla\mu} \underline{\mathbf{d}}_{\mu} \,, \end{aligned} \tag{4.67}$$

where $\underline{\mathbf{B}}_{\boldsymbol{F}}$, $\underline{\mathbf{B}}_{m}$ and $\underline{\mathbf{B}}_{\nabla\mu}$ are symbolic representations of global matrices of shape function derivatives. In particular, for the case of nodal-based degrees of freedom, we evaluate

$$\underline{\mathbf{B}}_{\boldsymbol{F}} := \begin{bmatrix} N^1_{\boldsymbol{\varphi},1} & 0 & 0 & & N^{M_{\boldsymbol{\varphi}}}_{\boldsymbol{\varphi},1} & 0 & 0 \\ N^1_{\boldsymbol{\varphi},2} & 0 & 0 & & N^{M_{\boldsymbol{\varphi}}}_{\boldsymbol{\varphi},2} & 0 & 0 \\ N^1_{\boldsymbol{\varphi},3} & 0 & 0 & & N^{M_{\boldsymbol{\varphi}}}_{\boldsymbol{\varphi},3} & 0 & 0 \\ 0 & N^1_{\boldsymbol{\varphi},1} & 0 & & 0 & N^{M_{\boldsymbol{\varphi}}}_{\boldsymbol{\varphi},1} & 0 \\ 0 & N^1_{\boldsymbol{\varphi},2} & 0 & \dots & 0 & N^{M_{\boldsymbol{\varphi}}}_{\boldsymbol{\varphi},2} & 0 \\ 0 & N^1_{\boldsymbol{\varphi},3} & 0 & & 0 & N^{M_{\boldsymbol{\varphi}}}_{\boldsymbol{\varphi},3} & 0 \\ 0 & 0 & N^1_{\boldsymbol{\varphi},1} & & 0 & 0 & N^{M_{\boldsymbol{\varphi}}}_{\boldsymbol{\varphi},1} \\ 0 & 0 & N^1_{\boldsymbol{\varphi},2} & & 0 & 0 & N^{M_{\boldsymbol{\varphi}}}_{\boldsymbol{\varphi},2} \\ 0 & 0 & N^1_{\boldsymbol{\varphi},3} & & 0 & 0 & N^{M_{\boldsymbol{\varphi}}}_{\boldsymbol{\varphi},3} \end{bmatrix} ,$$

$$\underline{\mathbf{B}}_{m} := \begin{bmatrix} N^1_{\mathbb{H},1} & N^1_{\mathbb{H},2} & N^1_{\mathbb{H},3} & \dots & N^{M_{\mathbb{H}}}_{\mathbb{H},1} & N^{M_{\mathbb{H}}}_{\mathbb{H},2} & N^{M_{\mathbb{H}}}_{\mathbb{H},3} \end{bmatrix} ,$$

$$\underline{\mathbf{B}}_{\nabla\mu} := \begin{bmatrix} N^1_{\mu,1} & 0 & 0 & & N^{M_{\mu}}_{\mu,1} & 0 & 0 \\ 0 & N^1_{\mu,2} & 0 & \dots & 0 & N^{M_{\mu}}_{\mu,2} & 0 \\ 0 & 0 & N^1_{\mu,3} & & 0 & 0 & N^{M_{\mu}}_{\mu,3} \end{bmatrix} . \tag{4.68}$$

Here the subscript denotes the material derivatives $(\cdot)_{,i} = \partial_{X_i}(\cdot)$.

4.4.2. Space-time-discrete canonical variational minimization principle

For the minimization formulation the unknown fields are the deformation map $\boldsymbol{\varphi}$ and the fluid flow vector $\mathbb{H}$, see (4.50). We introduce the global vector of unknowns $\underline{\mathbf{d}}$ of the space-discrete system as

$$\underline{\mathbf{d}} = [\, \underline{\mathbf{d}}_{\boldsymbol{\varphi}} \,,\, \underline{\mathbf{d}}_{\mathbb{H}}]^T \,. \tag{4.69}$$

With (4.69) at hand, the space-discrete fields (4.62) can be rewritten as

$$\boldsymbol{\varphi}^h(\boldsymbol{X}) = \underline{\mathbf{N}}_{\boldsymbol{\varphi}}\, \underline{\mathbf{d}}_{\boldsymbol{\varphi}} =: \hat{\underline{\mathbf{N}}}_{\boldsymbol{\varphi}}\, \underline{\mathbf{d}} \quad \text{and} \quad \mathbb{H}^h(\boldsymbol{X}) = \underline{\mathbf{N}}_{\mathbb{H}}\, \underline{\mathbf{d}}_{\mathbb{H}} =: \hat{\underline{\mathbf{N}}}_{\mathbb{H}}\, \underline{\mathbf{d}} \,. \tag{4.70}$$

Before stating the space-time-discrete variational principle we introduce the vector of *constitutive state* $\mathbf{f}$ in order to keep the notation compact. The constitutive state vector is an assembly of state variables entering the free energy and the dissipation potential function. For the minimization formulation this is $\mathbf{f} := [\, \boldsymbol{F}, \mathrm{Div}[\mathbb{H}], \mathbb{H}\,]^T$ and can be written by use of (4.67), (4.69) and (4.70) as

$$\mathbf{f}(\boldsymbol{X}) \approx \mathbf{f}^h(\boldsymbol{X}) = \begin{bmatrix} \underline{\mathbf{B}}_{\boldsymbol{F}}\, \underline{\mathbf{d}}_{\boldsymbol{\varphi}} \\ \underline{\mathbf{B}}_{m}\, \underline{\mathbf{d}}_{\mathbb{H}} \\ \underline{\mathbf{N}}_{\mathbb{H}}\, \underline{\mathbf{d}}_{\mathbb{H}} \end{bmatrix} =: \underline{\mathbf{B}}\, \underline{\mathbf{d}} \,, \tag{4.71}$$

in terms of a global matrix $\underline{\mathbf{B}}$ of shape functions and material shape function derivatives. The deformation gradient is written in Voigt-notation within the definition of the vector $\mathbf{f}$. Note that for the case of edge-based degrees of freedom and associated vector-valued shape functions for the interpolation of the fluid flow as proposed below, the dimensions of the global matrices $\underline{\mathbf{N}}_{\mathbb{H}}$ and $\underline{\mathbf{B}}_m$ as well as the dimension of the vector $\underline{\mathbf{d}}_{\mathbb{H}}$ change. However it is still possible to express the approximations for $\mathbb{H}$ and $\mathrm{Div}[\mathbb{H}]$ in the form $\mathbb{H}^h = \underline{\mathbf{N}}_{\mathbb{H}}\underline{\mathbf{d}}_{\mathbb{H}}$ and $\mathrm{Div}[\mathbb{H}^h] = \underline{\mathbf{B}}_m\underline{\mathbf{d}}_{\mathbb{H}}$.

With the approximations (4.70) and (4.71) at hand, the space-discrete counterpart of the incremental potential (4.48) is given by

$$\begin{aligned}\Pi^{\tau h}(\underline{\mathbf{d}}) = & \int_{\mathcal{B}^h} \left\{ \hat{\psi}(\underline{\mathbf{B}}\,\underline{\mathbf{d}}) - \hat{\psi}_n + \tau\hat{\phi}_{\mathrm{con}}(\underline{\mathbf{B}}\,\underline{\mathbf{d}}; \underline{\mathbf{B}}\,\underline{\mathbf{d}}_n) \right\} dV \\ & - \int_{\mathcal{B}^h} (m_0 + m_n)\bar{g} \cdot \hat{\underline{\mathbf{N}}}_{\boldsymbol{\varphi}}[\underline{\mathbf{d}} - \underline{\mathbf{d}}_n]\, dV - \int_{\partial\mathcal{B}^h_{\boldsymbol{T}}} \bar{\boldsymbol{T}} \cdot \hat{\underline{\mathbf{N}}}_{\boldsymbol{\varphi}}[\underline{\mathbf{d}} - \underline{\mathbf{d}}_n]\, dA \\ & - \int_{\mathcal{B}^h} \tau\bar{g} \cdot \boldsymbol{F}_n \hat{\underline{\mathbf{N}}}_{\mathbb{H}}\,\underline{\mathbf{d}}\, dV + \int_{\partial\mathcal{B}^h_{\mu}} \tau\bar{\mu}\hat{\underline{\mathbf{N}}}_{\mathbb{H}}\,\underline{\mathbf{d}} \cdot \boldsymbol{N}\, dA\end{aligned} \tag{4.72}$$

where we introduced $\hat{\psi}_n = \hat{\psi}(\underline{\mathbf{B}}\,\underline{\mathbf{d}}_n)$. Then, the space-time-discrete canonical variational minimization principle can be written as

$$\underline{\mathbf{d}} = \arg\left\{ \inf_{\underline{\mathbf{d}}} \Pi^{\tau h}(\underline{\mathbf{d}}) \right\} . \tag{4.73}$$

The necessary condition of the variational principle (4.73) is that its variation vanishes. Approximation of the variations $\{\delta\boldsymbol{\varphi}^h, \delta\mathbb{H}^h\}$ analogously to the approximation of the fields $\{\boldsymbol{\varphi}^h, \mathbb{H}^h\}$ in (4.70) yields the necessary condition as

$$\inf_{\underline{\mathbf{d}}} \Pi^{\tau h}(\underline{\mathbf{d}}) \quad \rightarrow \quad \Pi^{\tau h}_{,\underline{\mathbf{d}}} = \boldsymbol{0} . \tag{4.74}$$

In order to solve $(4.74)_2$ algorithmically we use an iterative Newton-Raphson scheme. To this end, consider the linearization of $(4.74)_2$ about $\underline{\mathbf{d}}^{(k)}$

$$\mathrm{Lin}\big[\Pi^{\tau h}_{,\underline{\mathbf{d}}}\big]_{\underline{\mathbf{d}}^{(k)}}(\Delta\underline{\mathbf{d}}) = \Pi^{\tau h}_{,\underline{\mathbf{d}}}(\underline{\mathbf{d}}^{(k)}) + \Pi^{\tau h}_{,\underline{\mathbf{d}}\,\underline{\mathbf{d}}}(\underline{\mathbf{d}}^{(k)}) \cdot \Delta\underline{\mathbf{d}} . \tag{4.75}$$

This yields the update of the iterative Newton-Raphson scheme as

$$\underline{\mathbf{d}}^{(k+1)} = \underline{\mathbf{d}}^{(k)} - \big[\Pi^{\tau h}_{,\underline{\mathbf{d}}\,\underline{\mathbf{d}}}(\underline{\mathbf{d}}^{(k)})\big]^{-1}\big[\Pi^{\tau h}_{,\underline{\mathbf{d}}}(\underline{\mathbf{d}}^{(k)})\big] . \tag{4.76}$$

The iteration update is performed until convergence $|\Pi^{\tau h}_{,\underline{\mathbf{d}}}| < tol$ is achieved.

In order to have a compact notation we introduce the vector of *generalized stresses* and the matrix of *generalized moduli*

$$\underline{\mathbf{S}} := \begin{bmatrix} \partial_{\boldsymbol{F}}\hat{\psi} \\ -\tau\partial_m\hat{\psi} \\ \tau\partial_{\mathbb{H}}\hat{\phi}_{\mathrm{con}} \end{bmatrix} \quad \text{and} \quad \underline{\mathbf{C}} := \begin{bmatrix} \partial^2_{\boldsymbol{F}\boldsymbol{F}}\hat{\psi} & -\tau\partial^2_{\boldsymbol{F}m}\hat{\psi} & \boldsymbol{0} \\ -\tau\partial^2_{m\boldsymbol{F}}\hat{\psi} & \tau^2\partial^2_{mm}\hat{\psi} & \boldsymbol{0} \\ \boldsymbol{0} & \boldsymbol{0} & \tau\partial^2_{\mathbb{H}\mathbb{H}}\hat{\phi}_{\mathrm{con}} \end{bmatrix} . \tag{4.77}$$

With (4.77) at hand, the necessary condition $(4.74)_2$ of the space-time-discrete variational principle can be written as

$$\begin{aligned}\boldsymbol{0} = \Pi^{\tau h}(\boldsymbol{d})_{,\underline{\mathbf{d}}} = & \int_{\mathcal{B}^h} \underline{\mathbf{B}}^T \cdot \underline{\mathbf{S}}\, dV - \int_{\mathcal{B}^h} \hat{\underline{\mathbf{N}}}^T_{\boldsymbol{\varphi}} \cdot (m_0 + m_n)\bar{g}\, dV - \int_{\partial\mathcal{B}^h_{\boldsymbol{T}}} \hat{\underline{\mathbf{N}}}^T_{\boldsymbol{\varphi}} \cdot \bar{\boldsymbol{T}}\, dA \\ & - \int_{\mathcal{B}^h} \hat{\underline{\mathbf{N}}}^T_{\mathbb{H}} \cdot \boldsymbol{F}^T_n \tau\bar{g}\, dV + \int_{\partial\mathcal{B}^h_{\mu}} \hat{\underline{\mathbf{N}}}^T_{\mathbb{H}} \cdot \tau\bar{\mu}\boldsymbol{N}\, dA .\end{aligned} \tag{4.78}$$

With the generalized tangent moduli $\underline{\mathbf{C}}$ in $(4.77)_2$ the second derivative of the potential that is needed for the iterative update (4.76) yields the form

$$\Pi^{\tau h}_{,\underline{\boldsymbol{d}}\,\underline{\boldsymbol{d}}} = \int_{\mathcal{B}^h} \underline{\mathbf{B}}^T \underline{\mathbf{C}} \underline{\mathbf{B}} \, dV \ . \tag{4.79}$$

4.4.3. Finite element design for minimiziation formulation

After introducing the space-time-discrete variational principle for the canonical two-field setting, three different finite element approximations are introduced. Note that due to the minimization structure of the formulation, *no particular restrictions* to the ansatz spaces are needed which is advantageous compared to mixed saddle-point formulations. Furthermore the minimization structure leads to a *symmetric and positive definite* global tangent matrix. Care has to be taken of the admissible space $\mathcal{W}_{\mathbb{H}}$ that requires the fluid flow vector $\mathbb{H}$ as an element of the $H(\mathrm{Div}, \mathcal{B})$. This is the prize to pay for the minimization structure of poro-elasticity.

Similar numerical schemes with the solid's displacement $\boldsymbol{u}$ and the fluid's velocity $\boldsymbol{v}^f$ as global degrees of freedom can be found in the literature for dynamical problems of poro-elasticity, see for example Simon et al. [242] or Prevost [215, 217]. However in these works the issue of conformity of the ansatz for the fluid velocity is not addressed or the treatment within the multidimensional setting is not performed.

Conforming finite element for minimizer. In order to account for the admissible space $\mathcal{W}_{\mathbb{H}}$ for the approximation of the fluid flow vector, an $H(\mathrm{Div}, \mathcal{B})$-conforming finite element design is chosen. Examples for such kind of elements are given by Raviart & Thomas [218] (RT_k element family), Brezzi et al. [48] (BDM_k element family) or the Arnold-Boffi-Falk element, see Arnold et al. [12]. These elements introduce normal fluxes across the element faces as degrees of freedom, the continuity of which provides that global divergence operators are well defined. The application of these elements in pure solid mechanics can be found in Klaas et al. [149], Schroeder et al. [234], Schwarz et al. [235] in combination with least-square methods, and in poromechanics in Ferronato et al. [102], however in the context of mixed variational concepts.

To this end we propose a Q_1-RT_0 finite element with *bilinear* (Q_1) approximation of the deformation field $\boldsymbol{\varphi}^h$ and *linear* (RT_0) approximation of the fluid flow $\mathbb{H}^h$ within an element. Here the discrete deformation degrees of freedom $\underline{\mathbf{d}}_{\boldsymbol{\varphi}}$ are located at the nodes of an element, whereas the fluid flux degrees of freedom $\underline{\mathbf{d}}_{\mathbb{H}}$ are located at the element edges, see Figure 4.6a). In particular, the lowest order quadrilateral RT element introduces constant normal fluxes across each element edge k as degrees of freedom

$$H^k := \int_{\partial \mathcal{B}^e_k} \mathbb{H} \cdot \boldsymbol{N}_k \, dA \ . \tag{4.80}$$

For a proof of conformity of this ansatz, the reader is referred to Brezzi & Fortin [47]. For our Q_1-RT_0 finite element design we specify the approximations (4.60) on the quadrilateral reference element $\mathcal{A} = [-1, 1] \times [-1, 1]$ as

$$\boldsymbol{\varphi}^e(\boldsymbol{\xi}) = \sum_{i=1}^{4} \hat{N}^i_{\mathrm{Q}_1}(\boldsymbol{\xi}) \boldsymbol{\varphi}^i \quad \text{and} \quad \mathbb{H}^e(\boldsymbol{\xi}) = \sum_{k=1}^{4} \hat{\boldsymbol{N}}^k_{\mathrm{RT}_0}(\boldsymbol{\xi}) H^k \, , \tag{4.81}$$

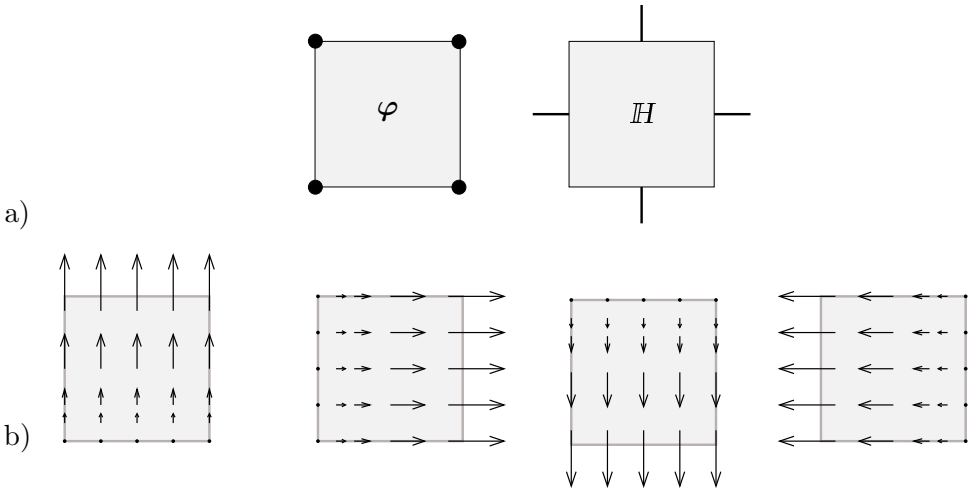

Figure 4.6: *Conforming finite element for minimizer.* a) Q_1-RT_0 element with bilinear shapes for φ and lowest-order Raviart-Thomas shapes for $\mathbb{H}$. b) Vectorial RT_0 shape functions for the fluid mass flow $\mathbb{H}$ provide a conforming ansatz for $H(\mathrm{Div}, \mathcal{B})$.

where $i = \{1, 2, 3, 4\}$ is the number of the corner node of the quadrilateral element and $k = \{1, 2, 3, 4\}$ indicates the k edges of the element. Here, the scalar shape functions $\hat{N}^i_{Q_1}$ and the vectorial shape functions $\hat{\boldsymbol{N}}^k_{RT_0}$ are explicitly given by

$$
\begin{aligned}
\hat{N}^1_{Q_1} &= \tfrac{1}{4}(1-\xi_1)(1-\xi_2)\ , & \hat{N}^2_{Q_1} &= \tfrac{1}{4}(1+\xi_1)(1-\xi_2)\ , \\
\hat{N}^3_{Q_1} &= \tfrac{1}{4}(1+\xi_1)(1+\xi_2)\ , & \hat{N}^4_{Q_1} &= \tfrac{1}{4}(1-\xi_1)(1+\xi_2)\ , \\
\hat{\boldsymbol{N}}^1_{RT_0} &= \begin{bmatrix} 0 \\ \frac{1}{4}(\xi_2-1) \end{bmatrix}\ , & \hat{\boldsymbol{N}}^2_{RT_0} &= \begin{bmatrix} \frac{1}{4}(\xi_1+1) \\ 0 \end{bmatrix}\ , \\
\hat{\boldsymbol{N}}^3_{RT_0} &= \begin{bmatrix} 0 \\ \frac{1}{4}(\xi_2+1) \end{bmatrix}\ , & \hat{\boldsymbol{N}}^4_{RT_0} &= \begin{bmatrix} \frac{1}{4}(\xi_1-1) \\ 0 \end{bmatrix}\ .
\end{aligned}
\tag{4.82}
$$

Because of the vectorial nature of the Raviart-Thomas shape functions one has to take care of the transformation from the elemental coordinate system to the physical space $\boldsymbol{X}$. In particular one has to use a contravariant Piola transformation $\mathcal{P} : \mathcal{A} \to \mathcal{B}^e$ that does not change the component of a vector normal to the element edge up to a constant built by the lengths of the same element-edges in parameter and physical space. The contravariant Piola transformation reads

$$
\check{\boldsymbol{N}}^k_{RT_0}(\boldsymbol{X}) = \mathcal{P}[\hat{\boldsymbol{N}}^k_{RT_0}(\boldsymbol{\xi})] := \frac{1}{J(\boldsymbol{\xi})}\boldsymbol{J}(\boldsymbol{\xi})\hat{\boldsymbol{N}}^k_{RT_0}(\boldsymbol{\xi})\ . \tag{4.83}
$$

The matrix $\boldsymbol{J}(\boldsymbol{\xi})$ denotes the classical Jacobian with determinant $J = \det[\boldsymbol{J}]$. For a visualization of the contravariant Piola transformation, see Figure 4.7. Another thing one has to take care about is the orientation of the global fluid flux degree of freedom H over the edges of the finite elements. In order to ensure consistency of the fluid flux direction for two neighboring finite elements, a global orientation for each global degree of freedom H has to be set. An appropriate decision criterion suitable for implementation is proposed by Anjam & Valdman [8]: Fix a direction to check the numbering of the global nodes per element (clockwise or counter clockwise) and decide the positive direction of the flux H on the edge by checking if a higher or lower numbered node follows the first edge node.

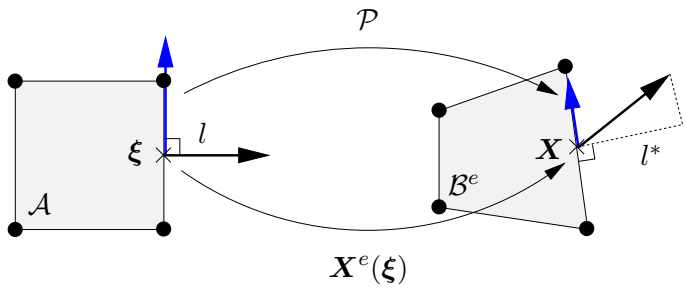

Figure 4.7: *Contravariant Piola transformation for vectorial shape functions.* The length l of the edge-normal component of a vector is preserved up to a constant, i.e. $l^* = |L_e|/|l_e|l$. The constant $|L_e|/|l_e|$ is evaluated as the ratio between the length L_e of the element edge in parameter space and the length l_e of the edge in physical space. Hence the contravariant Piola transformation map tangent vectors onto tangent vectors.

Therefore the edge-corresponding shape function $\check{\boldsymbol{N}}^k_{\mathrm{RT}_0}$ changes to negative sign for one of the two elements sharing the same edge k.

Non-conforming finite element for minimizer. A non-conforming finite element design is provided by the use of *bilinear* Q_1 shape functions for both fields $\boldsymbol{\varphi}$ and $\mathbb{H}$. For the Q_1-Q_1 element, the interpolations are given by

$$\boldsymbol{\varphi}^e(\boldsymbol{\xi}) = \sum_{i=1}^{4} \hat{N}^i_{\mathrm{Q}_1}(\boldsymbol{\xi})\boldsymbol{\varphi}^i \quad \text{and} \quad \mathbb{H}^e(\boldsymbol{\xi}) = \sum_{i=1}^{4} \hat{N}^i_{\mathrm{Q}_1}(\boldsymbol{\xi})\mathbb{H}^i\,, \tag{4.84}$$

with the shape functions $\hat{N}^i_{\mathrm{Q}_1}$ introduced in (4.82). Though non-conforming, this finite element has the advantage of an easy implementation without having combined nodal and edge degrees of freedom for the coupled problem. Note that in contrast to the RT_0-interpolation, the shape functions $\hat{N}^i_{\mathrm{Q}_1}$ are scalar and the discrete degrees of freedom $\mathbb{H}_i$ are vectorial. Thus the amount of fluid flux degrees of freedom is doubled compared to the conforming Q_1-RT_0 element design. However, this approximation is in general non-conforming. Exception is the one-dimensional case where the spaces $H(\mathrm{Div}, \mathcal{B})$ and $H^1(\mathcal{B})$ coincide and hence the element is conforming.

Nodal-based element with reduced integration. A combination of the Q_1-Q_1 element together with a reduced numerical integration for the volumetric coupling part $\hat{\psi}_{\mathrm{fluid}}$ provides an element design that yields promising results. For the reduced integration the space-time-discrete variational potential (4.72) is split into two contributions

$$\Pi^{\tau h}(\underline{\boldsymbol{d}}) = \Pi^{\tau h}_{\mathrm{full}}(\underline{\mathbf{d}}) + \Pi^{\tau h}_{\mathrm{red}}(\underline{\mathbf{d}}) \quad \text{with} \quad \Pi^{\tau h}_{\mathrm{red}}(\underline{\mathbf{d}}) = \int_{\mathcal{B}^h} \hat{\psi}_{\mathrm{fluid}}(\underline{\mathbf{B}}\,\underline{\mathbf{d}})\, dV\,. \tag{4.85}$$

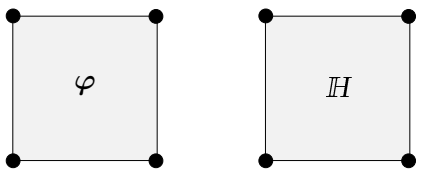

Figure 4.8: *Non-conforming finite element for minimizer.* The Q_1-Q_1 element with bilinear shape functions for both $\boldsymbol{\varphi}$ and $\mathbb{H}$ provides a non-conforming ansatz. Combined with a reduced integration the Q_1-Q_1-red element yields good results.

For the first term $\Pi^{\tau h}_{\text{full}}(\underline{\mathbf{d}})$ a full numerical integration with 2x2 Gauss quadrature points is performed and for the second term $\Pi^{\tau h}_{\text{red}}(\underline{\mathbf{d}})$ a reduced numerical integration with 1 Gauss point is used. In the following this finite element design is denoted as Q_1-Q_1-red.

Raviart-Thomas-type element with reduced integration. A fourth type of finite element is provided by combining the conforming Q_1-RT_0 element introduced above with the reduced integration scheme (4.85). We denote this finite element design in the following as Q_1-RT_0-red.

4.4.4. Space-time-discrete mixed variational saddle-point principle

For the mixed saddle-point formulation the unknown fields are the deformation map $\boldsymbol{\varphi}$, the relative fluid mass content m and the chemical potential μ, see (4.54). However note that the admissible space of the fluid mass content is $m \in L^2$ and no prescription of boundary values is necessary. This can also be seen with the time-discrete Euler equation $(4.56)_2$ which is an *ordinary differential equations* in contrast to the partial differential equations $(4.56)_1$ and $(4.56)_3$. Hence for the space-discretization it is sufficient to approximate m peace-wise linear within a finite element e without continuity over element boundaries. For the finite element method this means that the Euler equation $(4.56)_2$ is solved locally at the Gauss quadrature points and m takes the role of an *internal variable*. Hence the global unknowns reduce to $\boldsymbol{\varphi}$ and μ. As before we introduce the vector of discrete unknown values $\underline{\mathbf{d}}^*$ of the space-discrete variational principle

$$\underline{\mathbf{d}}^* = [\,\underline{\mathbf{d}}_{\boldsymbol{\varphi}}\,,\,\underline{\mathbf{d}}_{\mu}\,]^T\,. \tag{4.86}$$

With (4.86) at hand, the space-discrete fields (4.62) can be rewritten as

$$\boldsymbol{\varphi}^h(\boldsymbol{X}) = \underline{\mathbf{N}}_{\boldsymbol{\varphi}}\,\underline{\mathbf{d}}_{\boldsymbol{\varphi}} =: \hat{\underline{\mathbf{N}}}_{\boldsymbol{\varphi}}\,\underline{\mathbf{d}}^* \quad \text{and} \quad \mu^h(\boldsymbol{X}) = \underline{\mathbf{N}}_{\mu}\,\underline{\mathbf{d}}_{\mu} =: \hat{\underline{\mathbf{N}}}_{\mu}\,\underline{\mathbf{d}}^*\,. \tag{4.87}$$

Analogously to the minimiziation formulation we furthermore introduce the vector of *constitutive state* $\mathbf{f}^* := [\,\boldsymbol{F}, \mu, -\nabla\mu\,]^T$ for the sake of a compact notation. With the approximations (4.67), (4.86) and (4.87) $\mathbf{f}^{*h}$ is given by

$$\mathbf{f}^*(\boldsymbol{X}) \approx \mathbf{f}^{*h}(\boldsymbol{X}) = \begin{bmatrix} \underline{\mathbf{B}}_{\boldsymbol{F}}\,\underline{\mathbf{d}}_{\boldsymbol{\varphi}} \\ \underline{\mathbf{N}}_{\mu}\,\underline{\mathbf{d}}_{\mu} \\ -\underline{\mathbf{B}}_{\nabla\mu}\,\underline{\mathbf{d}}_{\mu} \end{bmatrix} =: \underline{\mathbf{B}}\,\underline{\mathbf{d}}^*\,, \tag{4.88}$$

in terms of a global matrix $\underline{\mathbf{B}}$ of shape functions and their derivatives with respect to the material coordinates $\boldsymbol{X}$. The deformation gradient is written in Voigt-notation within the definition of the vector $\mathbf{f}^*$.

With the approximations (4.87) and (4.88) at hand the space-discrete counterpart of the incremental mixed potential (4.49) is given by

$$\begin{aligned} \tilde{\Pi}^{*\tau h}(\underline{\mathbf{d}}^*) = & \int_{\mathcal{B}^h} \Big\{ \hat{\psi}(\underline{\mathbf{B}}\,\underline{\mathbf{d}}^*) - \hat{\psi}^h_n - \hat{\underline{\mathbf{N}}}_{\mu}\underline{\mathbf{d}}^*(m - m_n) - \tau\hat{\phi}^*_{\text{con}}(\underline{\mathbf{B}}\,\underline{\mathbf{d}}^*; \underline{\mathbf{B}}\,\underline{\mathbf{d}}^*_n) \Big\}\, dV \\ & - \int_{\mathcal{B}^h} (m_0 + m_n)\bar{g} \cdot \hat{\underline{\mathbf{N}}}_{\boldsymbol{\varphi}}[\underline{\mathbf{d}}^* - \underline{\mathbf{d}}^*_n]\, dV - \int_{\partial\mathcal{B}^h_{\boldsymbol{T}}} \bar{\boldsymbol{T}} \cdot \hat{\underline{\mathbf{N}}}_{\boldsymbol{\varphi}}[\underline{\mathbf{d}}^* - \underline{\mathbf{d}}^*_n]\, dA \\ & - \int_{\partial\mathcal{B}^h_H} \tau\hat{\underline{\mathbf{N}}}_{\mu}\underline{\mathbf{d}}^*\bar{H}\, dA \end{aligned} \tag{4.89}$$

where we introduced $\hat{\psi}_n^h = \hat{\psi}(\underline{\mathbf{B}}\,\underline{\mathbf{d}}_n^*)$. Then, the space-time-discrete variational saddle-point principle can be written as

$$\underline{\mathbf{d}}^* = \arg\left\{ \operatorname*{stat}_{\underline{\mathbf{d}}^*} \tilde{\Pi}^{*\tau h}(\underline{\mathbf{d}}^*) \right\} . \tag{4.90}$$

The necessary condition of the variational principle (4.90) is that its variation vanishes. Approximation of the variations $\{\delta\boldsymbol{\varphi}^h, \delta\mu^h\}$ analogously to the approximation of the fields $\{\boldsymbol{\varphi}^h, \mu^h\}$ in (4.87) yields the necessary condition as

$$\operatorname*{stat}_{\underline{\mathbf{d}}^*} \tilde{\Pi}^{*\tau h}(\underline{\mathbf{d}}^*) \quad \rightarrow \quad \tilde{\Pi}^{*\tau h}_{,\underline{\mathbf{d}}^*} = \boldsymbol{0} . \tag{4.91}$$

In order to solve $(4.91)_2$ algorithmically we use an iterative Newton-Raphson scheme. According to the considerations above the discrete update of the scheme is given by

$$\underline{\mathbf{d}}^{*(k+1)} = \underline{\boldsymbol{d}}^{*(k)} - \left[\tilde{\Pi}^{*\tau h}_{,\underline{\mathbf{d}}^*\underline{\mathbf{d}}^*}(\underline{\mathbf{d}}^{*(k)})\right]^{-1} \left[\tilde{\Pi}^{*\tau h}_{,\underline{\mathbf{d}}^*}(\underline{\mathbf{d}}^{*(k)})\right] \tag{4.92}$$

that is performed until convergence $|\tilde{\Pi}^{*\tau h}_{,\underline{\mathbf{d}}^*}| < tol$ is achieved.

In order to have a compact notation we introduce the vector of *generalized stresses*

$$\underline{\mathbf{S}}^* := \begin{bmatrix} \partial_{\boldsymbol{F}}\hat{\psi} \\ -(m - m_n) \\ -\tau\partial_{\mathbb{B}}\hat{\phi}^*_{\text{con}} \end{bmatrix} , \tag{4.93}$$

where the update of the relative fluid mass content m is obtained from the ordinary differential equation $(4.56)_2$

$$\partial_m\hat{\psi}(\boldsymbol{F}, m) - \mu = 0 . \tag{4.94}$$

Equation (4.94) is solved locally at the Gauss quadrature points. Furthermore we introduce the *generalized moduli* which have to take into account the sensitivity of m with respect to the global unknown fields $\boldsymbol{\varphi}$ and μ. It can be evaluated as

$$\underline{\mathbf{C}}^* := \begin{bmatrix} \partial^2_{\boldsymbol{F}\boldsymbol{F}}\hat{\psi} - \partial^2_{\boldsymbol{F}m}\hat{\psi}[\partial^2_{mm}\hat{\psi}]^{-1}\partial^2_{m\boldsymbol{F}}\hat{\psi} & \partial^2_{\boldsymbol{F}m}\hat{\psi}\left[\partial^2_{mm}\hat{\psi}\right]^{-1} & \boldsymbol{0} \\ \left[\partial^2_{mm}\hat{\psi}\right]^{-1}\partial^2_{m\boldsymbol{F}}\hat{\psi} & -\left[\partial^2_{mm}\hat{\psi}\right]^{-1} & \boldsymbol{0} \\ \boldsymbol{0} & \boldsymbol{0} & -\tau\partial^2_{\mathbb{B}\mathbb{B}}\hat{\phi}^*_{\text{con}} \end{bmatrix} . \tag{4.95}$$

With (4.93) at hand, the necessary condition $(4.91)_2$ of the space-time-discrete variational principle can be written as

$$\begin{aligned} \boldsymbol{0} = \Pi^{\tau h}(\underline{\mathbf{d}}^*)_{,\underline{\mathbf{d}}^*} = & \int_{\mathcal{B}^h} \underline{\mathbf{B}}^T \cdot \underline{\mathbf{S}}^* \, dV - \int_{\mathcal{B}^h} \underline{\hat{\mathbf{N}}}^T_{\boldsymbol{\varphi}} \cdot (m_0 + m_n)\bar{\boldsymbol{g}} \, dV \\ & - \int_{\partial\mathcal{B}^h_{\boldsymbol{T}}} \underline{\hat{\mathbf{N}}}^T_{\boldsymbol{\varphi}} \cdot \bar{\boldsymbol{T}} \, dA - \int_{\partial\mathcal{B}^h_H} \underline{\hat{\mathbf{N}}}^T_{\mu} \cdot \tau\bar{H} \, dA . \end{aligned} \tag{4.96}$$

Furthermore the generalized tangent moduli $\underline{\mathbf{C}}^*$ in (4.95) can be used to rewrite the second derivative of the potential in compact notation

$$\Pi^{\tau h}_{,\underline{\mathbf{d}}^*\underline{\mathbf{d}}^*} = \int_{\mathcal{B}^h} \underline{\mathbf{B}}^T \underline{\mathbf{C}}^* \underline{\mathbf{B}} \, dV . \tag{4.97}$$

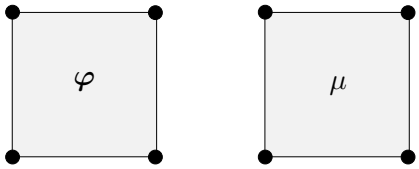

Figure 4.9: *Unstable finite element for mixed principle.* The Q_1-Q_1 element design with bilinear interpolations for deformation φ and chemical potential μ provides an inf-sup unstable pairing.

4.4.5. Finite element design for saddle-point formulation

In contrast to the minimization formulation, the admissible spaces are $\varphi \in H^1(\mathcal{B})$ and $\mu \in H^1(\mathcal{B})$ such that standard nodal-based finite element approximations are conforming for both fields. Furthermore the variational structure leads to a *symmetric* global tangent matrix. The saddle-point structure of the principle however causes this global tangent to be *indefinite*.

Furthermore the mixed saddle-point principle requires the interpolations to be *inf-sup-stable*. This condition disallows the sets of interpolation spaces for the unknown fields φ and μ to be chosen independently from each other. The use of approximations of same polynomial order for both fields φ and μ is unstable. The theoretical bases for stable element design in the context of poro-mechanics is discussed in Murad & Loula [200, 201] or in a recent publication of Rodrigo et al. [227]. Stable pairings are for example provided by the Taylor-Hood element or the Mini-element, see below.

Another approach to get over instability problems of saddle point principles is provided by stabilized finite elements. These types of elements were originally used for the Stokes problem and go back to Douglas & Wang [89], Hughes & Franca [140] and Hughes et al. [141]. For the coupled problem of poro-mechanics such elements are suggested very often, for example Mira et al. [196], Truty & Zimmermann [262], White & Borja [270], Rodrigo et al. [227], Preisig & Prévost [213] or Sun et al. [250]. However the stabilized finite elements have the big disadvantage of the additional stabilization parameter. Using a sufficient high parameter leads to stable numerical solutions, that is oscillation free solutions. However it also leads to nonpyhsical results due to over-diffusion. Furthermore the choice of the stabilization parameter is dependent on the boundary value problem.

For the case of poro-mechanics or more generally for diffusion-type problems, which are parabolic systems, oscillations in the chemical potential field can also occur due to small time steps, as for example shown in Gresho & Lee [119] or Vermeer & Verruijt [263]. It has been demonstrated that this can be overcome by fulfilling some stability restrictions between the time step size and the mesh size of the finite element discretization, see Aguilar et al. [5] or Vermeer & Verruijt [263].

In what follows four different types of finite element approximations are introduced for the saddle-point formulation of coupled poro-mechanics. Here both unstable and stable elements are proposed and compared later in the numerical boundary value problems.

Unstable finite element for mixed principle. The first finite element design is a Q_1-Q_1 element with *bilinear* approximations for both the deformation field φ as well as

the chemical potential μ, that is

$$\boldsymbol{\varphi}^e(\boldsymbol{\xi}) = \sum_{i=1}^{4} \hat{N}^i_{\mathrm{Q}_1}(\boldsymbol{\xi})\boldsymbol{\varphi}^i \quad \text{and} \quad \mu^e(\boldsymbol{\xi}) = \sum_{i=1}^{4} \hat{N}^i_{\mathrm{Q}_1}(\boldsymbol{\xi})\mu^i \ , \tag{4.98}$$

with the particular shape functions $\hat{N}^i_{\mathrm{Q}_1}$ introduced in (4.82). As already mentioned this finite element design is inf-sup unstable and leads to spurious oscillations in the fluid chemical potential field μ in the undrained limit case, that is in cases where the permeability is very low and/or the time step is very small. Although not inf-sup stable this finite element is often used in literature and provides good results away from the undrained limit.

Stable Taylor-Hood finite element for mixed principle. An inf-sup stable finite element design is the *Taylor-Hood element* originally proposed by Taylor & Hood [253] for the incompressible Navier-Stokes equation. For the flow problem of saturated porous elastic medium the element is proposed by Sandhu & Wilson [231]. Furthermore Bouklas et al. [40] recently used the element for the modeling of hydrogels. The Taylor-Hood element provides *biquadratic* (Q_2) interpolations for the deformation field $\boldsymbol{\varphi}$ and *bilinear* interpolations for the chemical potential μ

$$\boldsymbol{\varphi}^e(\boldsymbol{\xi}) = \sum_{i=1}^{9} \hat{N}^i_{\mathrm{Q}_2}(\boldsymbol{\xi})\boldsymbol{\varphi}^i \quad \text{and} \quad \mu^e(\boldsymbol{\xi}) = \sum_{i=1}^{4} \hat{N}^i_{\mathrm{Q}_1}(\boldsymbol{\xi})\mu^i \ , \tag{4.99}$$

where the finite element has additional to the four corner nodes, four nodes in the middle of the edges and one in its center, see Figure 4.10. For the specific forms of the Q_2 interpolations the reader is referred to classical textbooks of the finite element method, for example Hughes [139]. The disadvantage of the Taylor-Hood element lies in the fact that for the two fields two different shape function families are needed and that the number of interpolation nodes is different. In the following the Taylor-Hood element is denoted as Q_2-Q_1.

Stable Mini-type finite element for mixed principle. Another stable finite element is the Mini-type element, originally proposed by Arnold et al. [11] for the Stokes problem. For poro-elastic solids Rodrigo et al. [227] showed that this element provides an inf-sup stable pairing of interpolation for $\boldsymbol{\varphi}$ and μ. The Mini element is a triangular element with three global nodes located at its corners. The interpolation of the deformation $\boldsymbol{\varphi}$ is extended by an additional bubble mode that is condensed out on element level.

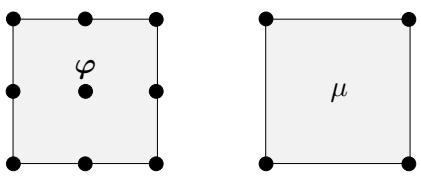

Figure 4.10: *Stable Taylor-Hood finite element for mixed principle.* The Q_2-Q_1 element with biquadratic interpolation $\boldsymbol{\varphi}$ and bilinear interpolation for μ provides an inf-sup stable pairing.

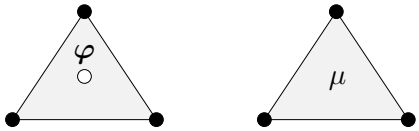

Figure 4.11: *Stable Mini-type element for mixed principle.* The P_{1b}-P_1 triangular element with linear interpolations for $\boldsymbol{\varphi}$ and μ. The interpolation of $\boldsymbol{\varphi}$ is enriched by an internal quadratic bubble mode.

Within an element e we have the approximations of the fields

$$\boldsymbol{\varphi}^e(\boldsymbol{\xi}) = \sum_{i=1}^{3} \hat{N}^i_{\mathrm{P}_1}(\boldsymbol{\xi})\boldsymbol{\varphi}^i + \hat{N}_{\mathrm{P}_b}(\boldsymbol{\xi})\boldsymbol{\varphi}^e_b \quad \text{and} \quad \mu^e(\boldsymbol{\xi}) = \sum_{i=1}^{3} \hat{N}^i_{\mathrm{P}_1}(\boldsymbol{\xi})\mu^i \ , \tag{4.100}$$

in terms of the element's area coordinates $\boldsymbol{\xi}$ and where $\boldsymbol{\varphi}^e_b$ is the additional deformation degree of freedom of element e. In particular, the *linear* shape functions $\hat{N}^i_{\mathrm{P}_1}$ and the *quadratic* bubble shape function $\hat{N}_{\mathrm{P}_b}$ are given by

$$\hat{N}^1_{\mathrm{P}_1} = \xi_1 \ , \quad \hat{N}^2_{\mathrm{P}_1} = \xi_2 \ , \quad \hat{N}^3_{\mathrm{P}_1} = \xi_3 \ , \quad \hat{N}_{\mathrm{P}_b} = \xi_1\xi_2\xi_3 \ , \tag{4.101}$$

with $\xi_3 = 1 - \xi_1 - \xi_2$. The advantage over the Taylor-Hood element is that the same interpolation functions P_1 are used for the nodal degrees of freedom and hence only one shape function family is needed. The Mini element is in the following denoted as P_{1b}-P_1.

EAS-type finite element for mixed principle. Another very popular element is the non-conforming enhanced assumed strain (EAS) element that goes back to Simo & Rifai [239]. In the context of coupled problems this element was used by Papastavrou et al. [205] and Zhou et al. [278] for porous media and recently by Krischok & Linder [156] for hydrogels. In what follows only the specific ansatz functions of the quantities are presented. For a deeper insight into the enhanced assumed strain element and the underlying Hu-Washizu variational principle we refer to the literature, for example Simo & Rifai [239] or Simo & Armero [238]. The underlying element geometry is that of a four-noded quadrilateral element and the interpolation of the deformation and the chemical potential fields are the same than for the Q_1-Q_1 element that is

$$\boldsymbol{\varphi}^e(\boldsymbol{\xi}) = \sum_{i=1}^{4} \hat{N}^i_{\mathrm{Q}_1}(\boldsymbol{\xi})\boldsymbol{\varphi}^i \quad \text{and} \quad \mu^e(\boldsymbol{\xi}) = \sum_{i=1}^{4} \hat{N}^i_{\mathrm{Q}_1}(\boldsymbol{\xi})\mu^i \ . \tag{4.102}$$

In contrast to all the other elements introduced, for the EAS-type element the approximation of the deformation gradient $\boldsymbol{F}$ is *non-conforming*. In particular we introduce two

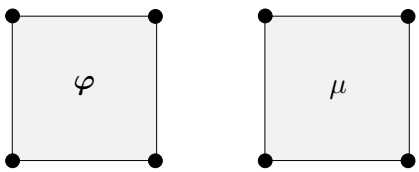

Figure 4.12: *EAS-type finite element for mixed principle.* The Q_1E_4-Q_1 element with bilinear interpolations for $\boldsymbol{\varphi}$ and μ. The deformation gradient $\boldsymbol{F}$ is interpolated non-conforming and in particular it is enriched by an EAS ansatz with four internal degrees of freedom.

Table 4.1: Material parameters used for numerical simulations.

no.	par.	name	unit	value
1.	μ	shear modulus	[MN/m^2]	98.0
2.	ν	Poisson's ratio	[-]	0.3
3.	ρ^f	fluid density	[kg/m^3]	1000.0
4.	M	Biot's modulus	[MN/m^2]	100.0–20000.0
5.	b	Biot's coefficient	[-]	1.0
6.	K	spatial permeability	[m^{3}s/kg]	$2.11 \cdot 10^{-13}$
7.	m_0	initial density of porous medium	[kg/m^3]	700.0

additional modes $\boldsymbol{\alpha}_e^i \in \mathcal{R}^2$ with associated shape functions $\hat{N}^1_{\text{EAS}}(\boldsymbol{\xi}) = (\xi_1^2 - 1)/2$ and $\hat{N}^2_{\text{EAS}}(\boldsymbol{\xi}) = (\xi_2^2 - 1)/2$. For the approximation of the deformation gradient we write

$$\boldsymbol{F}^e(\boldsymbol{\xi}) = \sum_{i=1}^{4} \boldsymbol{\varphi}^i \otimes \partial_{\boldsymbol{X}} \hat{N}^i_{\text{Q}_1}(\boldsymbol{\xi}) + \sum_{i=1}^{2} \boldsymbol{\alpha}_e^i \otimes \boldsymbol{G}^i(\boldsymbol{\xi}) \ , \tag{4.103}$$

where the matrices $\boldsymbol{G}^i$ have to be constructed such that the typical orthogonality condition in the enhanced assumed strain element is fulfilled. Evaluation yields

$$\boldsymbol{G}^i(\boldsymbol{\xi}) = \frac{J_0}{J} \boldsymbol{J}_0^{-T} \partial_{\boldsymbol{\xi}} \hat{N}^i_{\text{EAS}}(\boldsymbol{\xi}) \ , \tag{4.104}$$

where $J = \det[\boldsymbol{J}]$ is the determinant of the Jacobian of the element mapping, $\boldsymbol{J}_0$ is the Jacobian evaluated at the middle of the element at $\boldsymbol{\xi} = \boldsymbol{0}$ and $J_0 = \det[\boldsymbol{J}_0]$ its determinant. In the following this element is denoted as Q_1E_4-Q_1.

4.5. Representative numerical examples

In the following we demonstrate the modeling capabilities of the proposed variational approaches of coupled poro-elasticity. Here the focus lies on a comparison of the minimization formulation and the saddle-point formulation. In contrast to the saddle-point formulation that is also treated extensively in the literature, the minimization formulation is not constrained to the BBL condition and therefor leads to stable results. This is an immense advantage concerning the design of finite elements. Furthermore the minimization principle leads to positive definite tangent matrices and is thus advantageous with respect to iterative solvers. A quantitative fitting to experimental data is not the purpose of the simulations. For all the numerical boundary value problems the chosen material parameters are given in Table 4.1. Graviational effects are neglected in the subsequent boundary value problems, that is $\bar{g} = \boldsymbol{0}$. For the case of $M = 100.0$ MN/m^2 the consolidation coefficient can be evaluated as $c_v = 1.63 \cdot 10^{-5}$.

4.5.1. One-dimensional flow problem

Consider a square specimen $\mathcal{B} = \{\boldsymbol{X} \in \mathcal{R}^2 | \boldsymbol{X} \in [0, L] \times [0, L]\}$ with side lengths $L = 1$ m. The bottom and side surfaces are assumed to be impermeable, that is $\bar{H} = 0$. The bottom side is mechanically fixed in y direction. At the top surface a fluid flux $\bar{H} = -0.01$ kg/m^{2}s

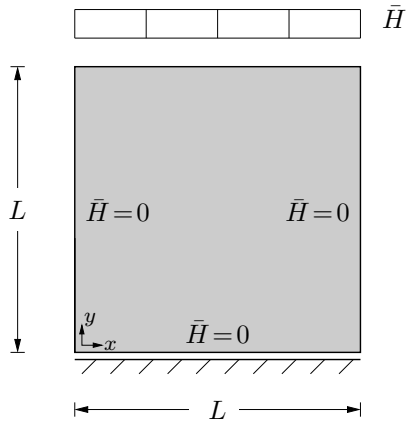

Figure 4.13: *One-dimensional flow problem. Boundary value problem*: Square plate, in which fluid is injected from the top surface. The bottom is fixed in y direction. The bottom and side edges are impervious ($\bar{H} = 0$).

inside the body is prescribed. The geometric setup of the boundary value problem is visualized in Figure 4.13. Note that the setup results in a quasi one-dimensional boundary value problem. The Biot's modulus is chosen to be $M = 100\,\mathrm{MN/m^2}$ and for the numerical simulation the specimen is discretized by 20×20 finite elements. We are interested in the behavior of the different finite element designs in the undrained limit case. Thus we compute the numerical results for only one tiny time step of $\Delta T = 8 \cdot 10^{-7}$. Here, $T = c_v t / L^2$ is a non-dimensional time.

In Figure 4.14 the fluid volume pressure $p = \rho^f \mu$ is plotted over the height of the specimen for different finite element interpolations. In Figure 4.14a) the results of two different implementations of the *minimization formulation* are shown. In particular we use the Q_1-RT_0 element and the Q_1-Q_1 element. Both formulations produce a stable non-oscillatory behavior. Note that the non-conforming finite element design Q_1-Q_1 also yields a stable result. The reason therefor is that in an one-dimensional setting, as given in this boundary value problem, the divergence of a field reduces to a single derivative and thus the bilinear Q_1 interpolation spans a conforming ansatz space for $H(\mathrm{Div}, \mathcal{B})$. Different finite element designs for the *saddle-point formulation* are compared in Figure 4.14b). The inf-sup unstable Q_1-Q_1 element shows high oscillations in the fluid pressure field p. This finite element is not applicable in the undrained limit state which is well known in

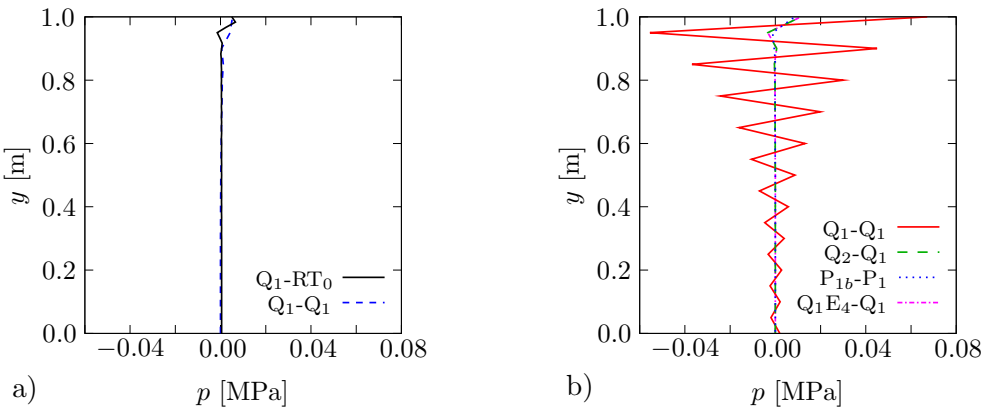

Figure 4.14: *One-dimensional flow problem. Results*: Fluid pressure p over the height of the body for a) minimization formulation and b) saddle-point formulation.

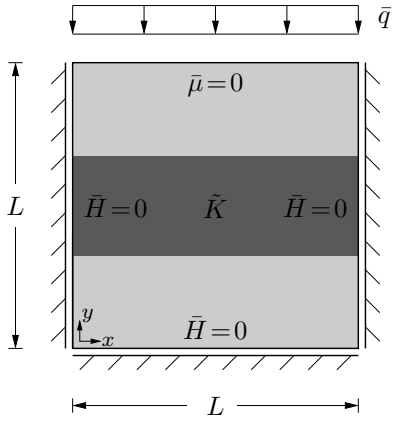

Figure 4.15: *One-dimensional mechanically driven problem. Boundary value problem*: A square plate with uniformly distributed mechanical loading $\bar{q}$ at the drained top surface with $\bar{\mu} = 0$. All other surfaces are impermeable ($\bar{H} = 0$). This is a benchmark problems to show oscillatory behavior in low permeable porous media, see HAGA ET AL. [128].

the literature. In contrast, the BBL stable Q_2-Q_1 and P_{1b}-P_1 elements yield good results without oscillations. Also the Q_1E_4-Q_1 shows a stable behavior.

4.5.2. One-dimensional mechanically driven problem

As a second boundary value problem consider the benchmark problem proposed by HAGA ET AL. [128] and also investigated recently in RODRIGO ET AL. [227]. A square specimen $\mathcal{B} = \{\boldsymbol{X} \in \mathcal{R}^2 | \boldsymbol{X} \in [0, L] \times [0, L]\}$ with side lengths $L = 1$ m is loaded with a constant uniformly distributed mechanical load $\bar{q} = 30$ MN/m^2. The specimen consists of three different layers in vertical direction with equal height. The middle layer of soil material is assumed to be low-permeable, which is realized by assuming a very low spatial permeability of $\tilde{K} = 10^{-8}K$. The bottom and side surfaces are assumed to be impermeable, $\bar{H} = 0$, whereas the top surface is drained such that $\bar{\mu} = 0$. The bottom surface is mechanically fixed in y direction and the side surfaces are fixed in x direction. The geometry of the boundary value problem is visualized in Figure 4.15. Note that the setup of the boundary value problem again is quasi one-dimensional. As before, Biot's modulus is chosen to $M = 100$ MN/m^2. The specimen is discretized by 60×60 finite elements for the simulation and a time step of $\Delta T = 1.63 \cdot 10^{-1}$ is used. $T = c_v t / L^2$ is the non-dimensional time. We compare the numerical results of the different element formulations at time $T = 1.63$, that is after ten time steps.

Figure 4.16a) shows the results for the *minimization formulation* with Q_1-RT_0 and Q_1-Q_1 finite elements. Both yield stable results and reproduce the jump in the fluid pressure p correct. As in the previous boundary value problem the Q_1-ansatz spans a conforming space for $H(\mathrm{Div}, \mathcal{B})$ due to the one-dimensional setup of the problem. The results for the *saddle-point formulation* are shown in Figure 4.16b). The inf-sup unstable Q_1-Q_1 element produces high oscillations and useless results in the low-permeable layer whereas the Q_2-Q_1 element yields good results. Note that the Taylor-Hood element gives one overshoot at the interface of the layers. This is due to the jump in μ, and hence p, that cannot be approximated by the chosen continuous bilinear Q_1 shape functions for the discretization of the chemical potential μ.

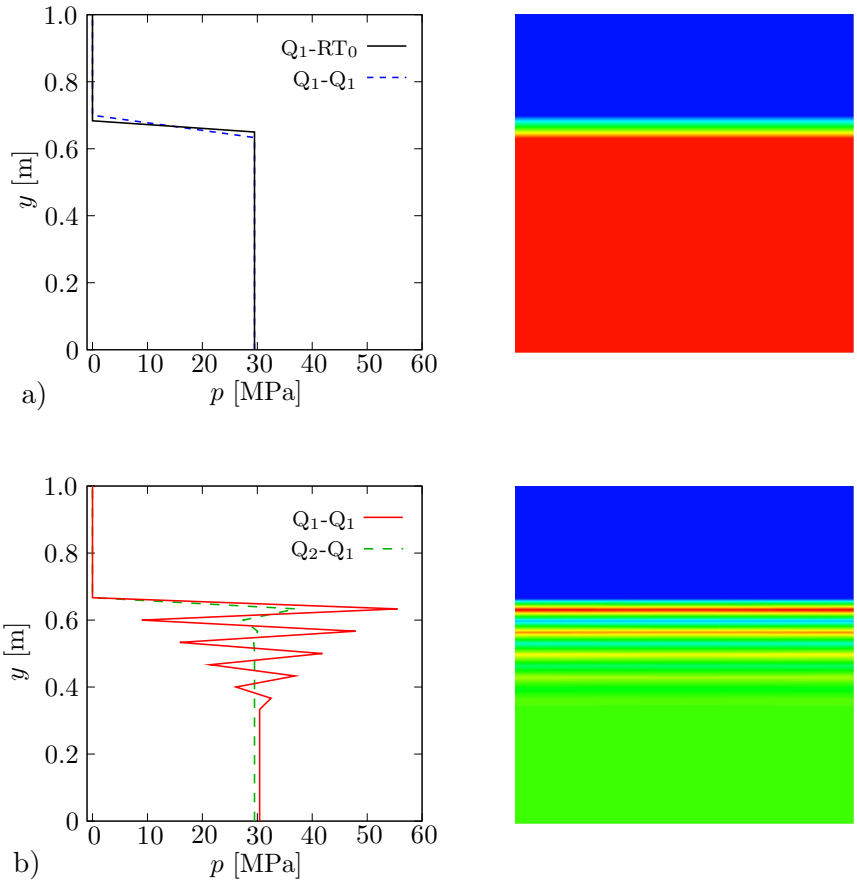

Figure 4.16: *One-dimensional mechanically driven problem. Results*: Fluid pressure p over the height of the body and contour plot of the fluid pressure p at time $T = 1.63$ for a) minimization formulation and b) saddle point formulation.

4.5.3. Mandel's Problem

The objective of this boundary value problem is to compare both the minimization and saddle-point formulation with an analytical solution. Consider a rectangular plate with dimensions $\mathcal{B} = \{\boldsymbol{X} \in \mathcal{R}^2 | \boldsymbol{X} \in [0, 2L] \times [0, 2H]\}$ with $L = 100$ m and $H = 30$ m that is subject to a constant vertical force $2\bar{F} = 40$ MN through a rigid and frictionless plate at its top. The bottom of the specimen is fixed in vertical direction and assumed to be impermeable, that is $\bar{H} = 0$. The two side surfaces of the specimen are permeable and considered as fluid potential free, that is $\bar{\mu} = 0$. The mechanical load is applied instantaneously at time $t = 0$ and hold constant during the whole simulation time. The Biot's modulus is chosen to be $M = 100\ \mathrm{MN/m^2}$. The geometry and boundary conditions are visualized in Figure 4.17. This problem is known as Mandel's problem and has been observed analytically by Mandel [167] and Abousleiman et al. [1] among others. The derivation of the analytical solution for the permeable case can also be found in Verruijt [264] but is beyond the scope of this work. Due to symmetry, only one fourth of the specimen is discretized by 30×100 finite elements. For the numerical simulation with the minimization formulation we use the Q_1-RT_0 element and for the saddle-point formulation the Q_1-Q_1 element is used.

Figure 4.18 compares the fluid pressure p for the two formulations with the analytical solution at different time steps. For both formulations the results fit very good with

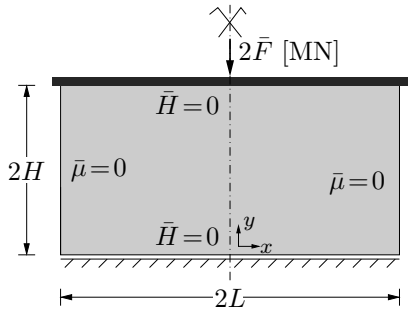

Figure 4.17: *Mandel's problem. Boundary value problem*: A square plate is fixed at the impermeable surface in y direction. At the top surface an impermeable rigid plate is attached that is loaded by a mechanical force of $2\bar{F}$. The side surfaces are assumed to be permeable and potential free ($\bar{\mu} = 0$).

the analytical data. In the saddle-point formulation the fluid pressure shows one small oscillation at the potential free boundary at the smallest time $T = 3.26 \cdot 10^{-5}$. At this time step we observe a nearly constant fluid pressure p_0 in the whole domain except the drained boundary where boundary conditions for the potential μ, and hence for p, are prescribed. With proceeding time fluid squeezes out of the domain at the side boundaries which leads to a decrease in fluid pressure. The mechanical load is carried more and more by the solid skeleton. However note that the fluid pressure p in the center of the specimen at $X = 0$ m is higher at time $T = 3.26 \cdot 10^{-2}$ than at time $T = 3.26 \cdot 10^{-5}$, which is the so-called *Mandel-Cryer effect*, see Mandel [167] or Cryer [69].

Although the results for both the minimization and saddle-point formulation are very good, the two models differ dramatically with regard to their computational efficiency. Figure 4.19 compares the computation times t_c for the minimization formulation, the (symmetric) saddle-point formulation and a non-symmetric formulation. The non-symmetric formulation is gained from the saddle-point formulation by multiplication of $-1/\tau$ of the residuum related to the fluid chemical potential degrees of freedom. This formulation is very often found in the literature, see for example Preisig & Prévost [213]. In Figure 4.19a) the computation time t_c is compared for different mesh sizes h_m

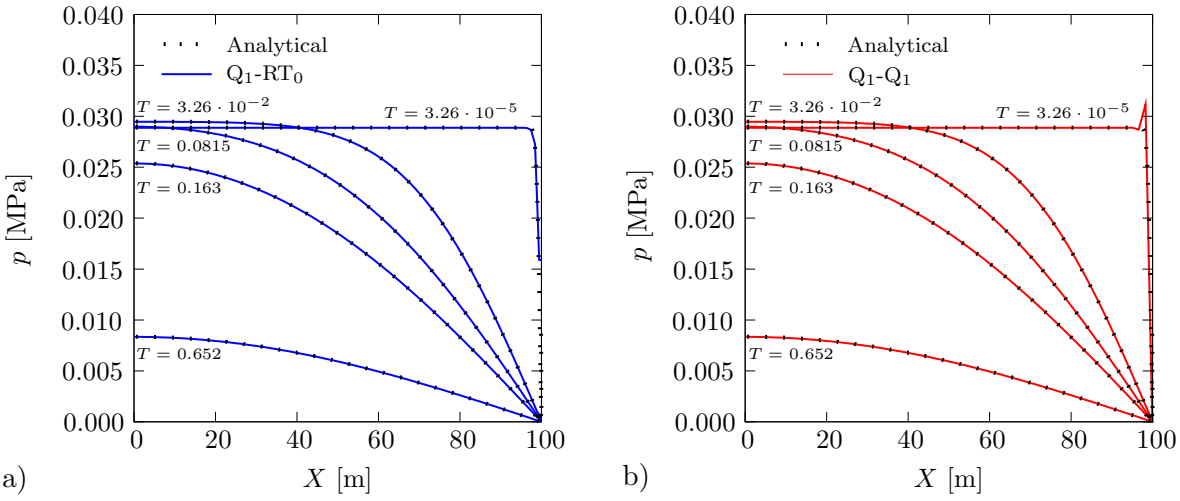

Figure 4.18: *Mandel's problem. Results*: Comparison of the numerical solution for fluid pressure p with analytical solution at different time steps for a) minimization formulation with Q_1-RT_0 element and b) saddle-point formulation with Q_1-Q_1 element.

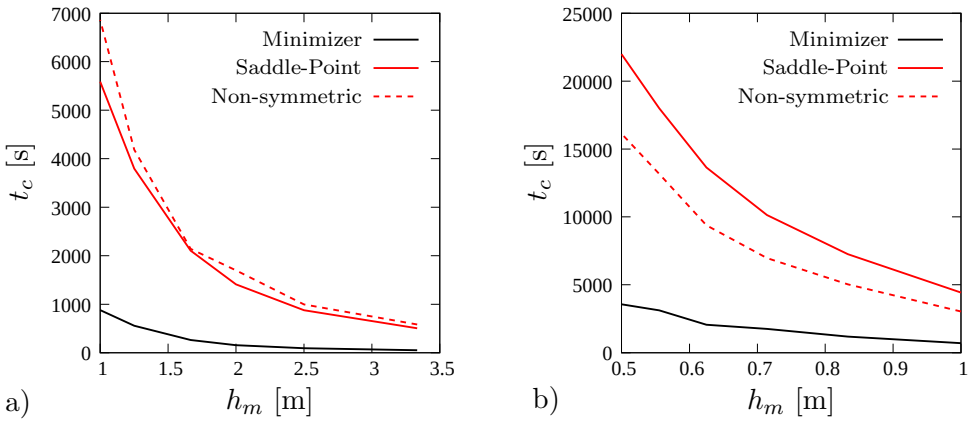

Figure 4.19: *Mandel's Problem. Comparison of computation time*: Computation time t_c over mesh size h_m for a) direct sparse solver in a serial computation and b) iterative CG/BiCGStab solver with ILU preconditioning in a parallel computation on 2 CPUs.

of a simulation that was computed on one single CPU and using a direct sparse solver. As can be seen the symmetric saddle-point formulation is faster than the non-symmetric formulation, which is due to the fact that the direct solver exploits the symmetry of the saddle-point formulation and furthermore just the upper part of the tangent matrix has to be assembled. The minimization formulation however is way more efficient than the two formulations with saddle-point structure even when using a direct solver. The speed-up in computation time is up to a factor 6 compared to the saddle-point formulation and up to a factor 7.8 to the non-symmetric formulation. Figure 4.19 b) compares the computation time t_c again for different meshes h_m of a parallel computation run on 2 CPUs and using iterative solvers. In particular, for the minimization formulation a symmetric CG-method in combination with an incomplete LU-factorization preconditioner is used. For the saddle-point, as well as for the non-symmetric formulation, the BiCGSTAB iterative solver and again the incomplete LU-factorization preconditioner is used. Here, the implementations of the preconditioners and the parallel iterative solvers are taken from the PETSc library. The solvers and preconditioners are chosen such that the best performance is attained. First, we obtain that the non-symmetric formulation is now faster than the symmetric saddle-point-formulation. However, we used the non-symmetric BiCGSTAB iterative solver for both formulations. A comparison between these two formulations that exploits the symmetry of the saddle-point formulation has been done by Toh & Phoon [258]. They observed a faster and more stable convergence for the symmetric formulation. However, the more interesting fact is that again the minimization formulation is up to a factor 4 faster than the two other formulations. Hence, for both direct and iterative solvers, the minimization formulation provides a substantial speed-up in numerical computation. Furthermore note, that for the numerical investigations, Q_1-Q_1 finite elements are used. For the saddle-point formulation this finite element design is unstable, as discussed before. Despite this instability, this finite element design results in a faster computation time compared to the other stable finite element designs due to the smaller amount of global degrees of freedom.

In Table 4.2 the computation time and the number of iterations of the iterative solver is shown for different time steps ΔT. Observe that the symmetric saddle-point formulation as well as the non-symmetric formulation does not converge at all for very small time steps. Furthermore, the smaller the time step, the more iterations are needed for these

Table 4.2: *Mandel's problem. Iterative solver details*: Number of iterations and computation time of parallel solver for different time steps ΔT obtained with mesh size $h_m = 1$ m.

	$\Delta T = 3.6 \cdot 10^{-8}$ Time (Iterations)	$\Delta T = 3.6 \cdot 10^{-7}$ Time (Iterations)	$\Delta T = 3.6 \cdot 10^{-6}$ Time (Iterations)
Minimizer	0.36 (11)	0.51 (11)	0.58 (11)
Saddle-Point	fail	fail	7.49 (929)
Non-symmetric	fail	fail	6.88 (1170)

	$\Delta T = 3.6 \cdot 10^{-5}$ Time (Iterations)	$\Delta T = 3.6 \cdot 10^{-4}$ Time (Iterations)	$\Delta T = 3.6 \cdot 10^{-3}$ Time (Iterations)
Minimizer	0.61 (12)	0.42 (11)	0.56 (13)
Saddle-Point	4.52 (118)	4.18 (133)	4.93 (205)
Non-symmetric	3.52 (119)	4.22 (140)	6.14 (152)

two formulations. This is also in line with observations in the literature, see Phoon et al. [212] or Toh & Phoon [258]. In contrast the minimization formulation needs nearly the same number of iterations and the same computation time for all ΔT.

4.5.4. Two-dimensional flow problem

The next boundary value problem demonstrates the problem of the non-conforming Q_1-Q_1 finite element space in the minimization formulation for the general two-dimensional case. Consider a square domain $\mathcal{B} = \{\boldsymbol{X} \in \mathcal{R}^2 | \boldsymbol{X} \in [0, L] \times [0, L]\}$ with side lengths $L = 1$ m that is mechanically fixed at the whole boundary $\partial\mathcal{B}$. Furthermore the boundary $\partial\mathcal{B}$ is assumed to be impermeable. In the middle of the domain a fluid mass is injected. This is realized by introducing an additional mass source term $\dot{\bar{m}}$ in the fluid mass balance $(4.3)_1$, such that $\dot{m} = -\operatorname{Div}[\mathbb{H}] + \dot{\bar{m}}$. The source term is chosen to the value $\dot{\bar{m}} = 0.1$ kg/m^{3}s. For the numerical simulation the domain is discretized by 30×30 finite elements. We are testing three elements of the minimization formulation: (i) The conforming Q_1-RT_0 element, (ii) the non-conforming Q_1-Q_1 element and (iii) the Q_1-Q_1-red element.

The obtained results are shown in Figure 4.21. As supposed, the fluid spreads out

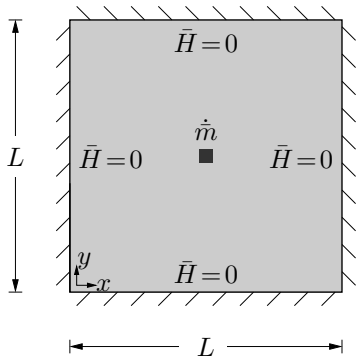

Figure 4.20: *Two-dimensional flow problem. Boundary value problem*: A square plate with impermeable boundaries and in the center of which fluid mass $\dot{\bar{m}}$ is injected.

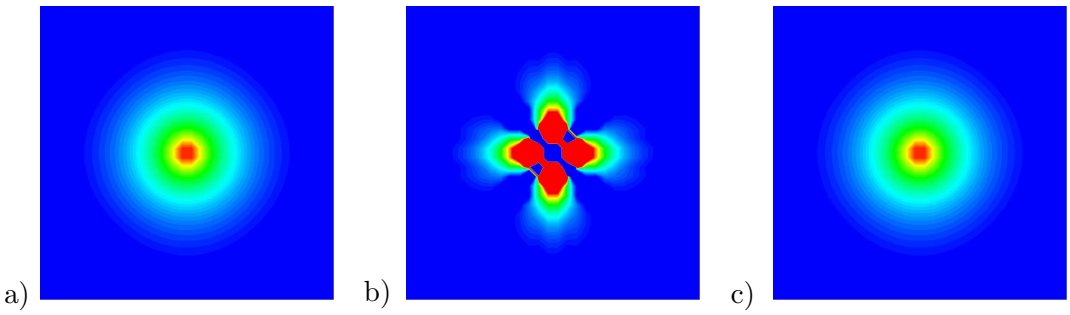

Figure 4.21: *Two-dimensional flow problem. Results*: Contour plot of relative fluid mass m for the minimization formulation interpolated with a) conforming Q_1-RT_0 element, b) non-conforming Q_1-Q_1 element and c) non-conforming Q_1-Q_1-red element with reduced integration.

isotropically in all directions for the conforming Q_1-RT_0 finite element in Figure 4.21a). However the non-conforming Q_1-Q_1 finite element is not able to capture this behavior. For this element design we get nonphysical distributions and unrealistic high values for the fluid mass m, see Figure 4.21b). Combining the non-conforming Q_1-Q_1 element with a reduced numerical integration for the volumetric coupling part ψ_{fluid} between mechanical and fluid contribution, yields reasonable results, see Figure 4.21c).

4.5.5. Two-dimensional consolidation problem

As a last boundary value problem consider a square specimen $\mathcal{B} = \{\boldsymbol{X} \in \mathcal{R}^2 | \boldsymbol{X} \in [0, L] \times [0, L/2]\}$ with $L = 1$ m which is mechanically loaded. The specimen is fixed at the bottom surface and in addition fixed in horizontal direction at the side surfaces. The bottom and side surfaces are furthermore assumed to be impermeable. Two different loading scenarios are considered: (i) An impermeable, rigid plate of length $b = 0.28$ m in the middle of the drained top surface is mechanically loaded by a force $\bar{F} = 25$ MN. This is a standard consolidation test and considered as a benchmark in poro-elasticity. In the second loading scenario, (ii) a fully drained top surface is loaded by a uniformly distributed mechanical load $\bar{q} = 89.29$ MN/m^2 in an area of length $b = 0.28$ m. This boundary value problem is considered as a benchmark in Preisig & Prévost [213]. The setup for the two cases is shown in Figure 4.22. For the simulation, a time step of $\Delta T = 6.52 \cdot 10^{-9}$ is chosen, where $T = c_v t/(L/2)^2$ is the non-dimensional time. For this boundary value

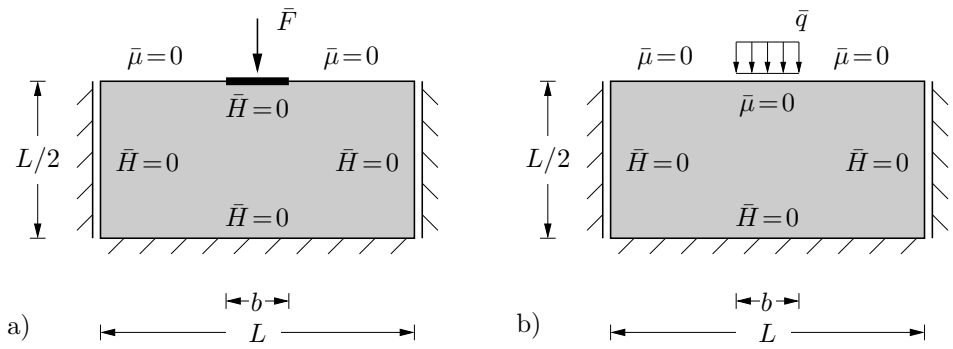

Figure 4.22: *Two dimensional consolidation problem. Boundary value problem*: Square plate with impermeable bottom and side surfaces. a) Impermeable, rigid plate, loaded by a mechanical force $\bar{F}$ and b) fully drained top surface with uniformly distributed mechanical load $\bar{q}$.

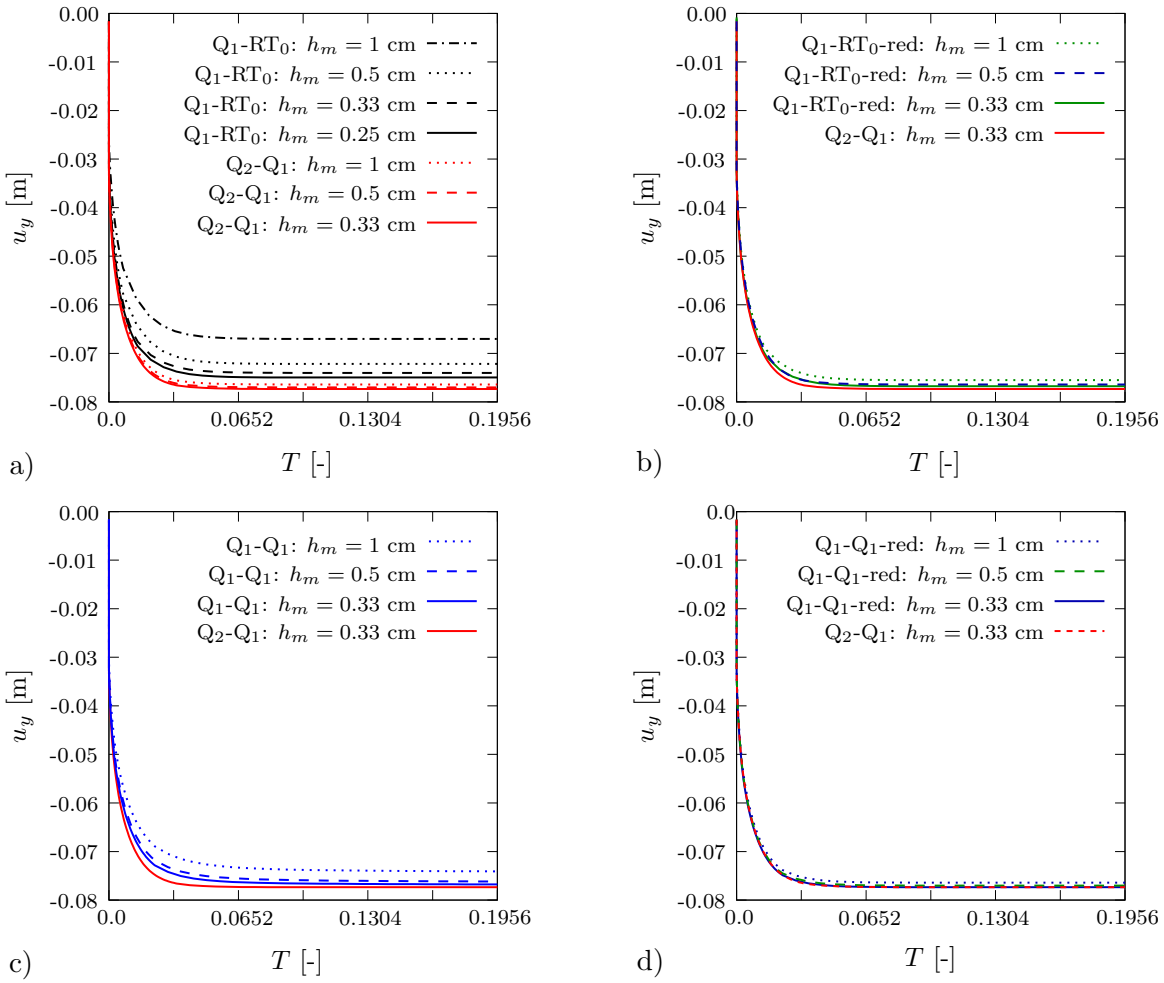

Figure 4.23: *Two-dimensional consolidation problem. Settlement of the plate*: Comparison of different mesh sizes for the different element designs of the minimization problem compared to the Taylor-Hood element (red curves). a) Q_1-RT_0 element and Taylor-Hood element, b) Q_1-RT_0-red element, c) Q_1-Q_1 element and d) Q_1-Q_1-red element.

problem we assume the fluid to be incompressible and thus $1/M \to 0$, which is realized numerically by choosing a high Biot's modulus of $M = 20.000$ MPa. Numerical results are compared for all four element designs proposed for the minimization formulation and the Taylor-Hood element for the saddle-point formulation. First, consider the loading case in Figure 4.22a). The load is linearly increased in the first 20 time steps up to the final value $\bar{F}$ and then held constant.

We are interested in the evolution of the vertical displacement u_y of the plate in time. Numerical results are shown in Figure 4.23a) for the minimization formulation with the Q_1-RT_0 finite element and the saddle-point formulation with the Q_2-Q_1 element. The Taylor-Hood element provides good agreement of the settlement of the plate for the different mesh sizes h_m such that this curve is considered as reference solution for the minimization formulation. For the Q_1-RT_0 element a weak convergence behavior of the final deformation is observed. We understand this to be a locking phenomena because of the incompressibility of the fluid. Due to this suspicion, the results are compared for the Q_1-RT_0-red finite element with reduced integration of the volumetric coupling term, see Figure 4.23b). We observe a good result even for the coarse mesh. Furthermore the non-conforming minimization elements are compared to the reference solution

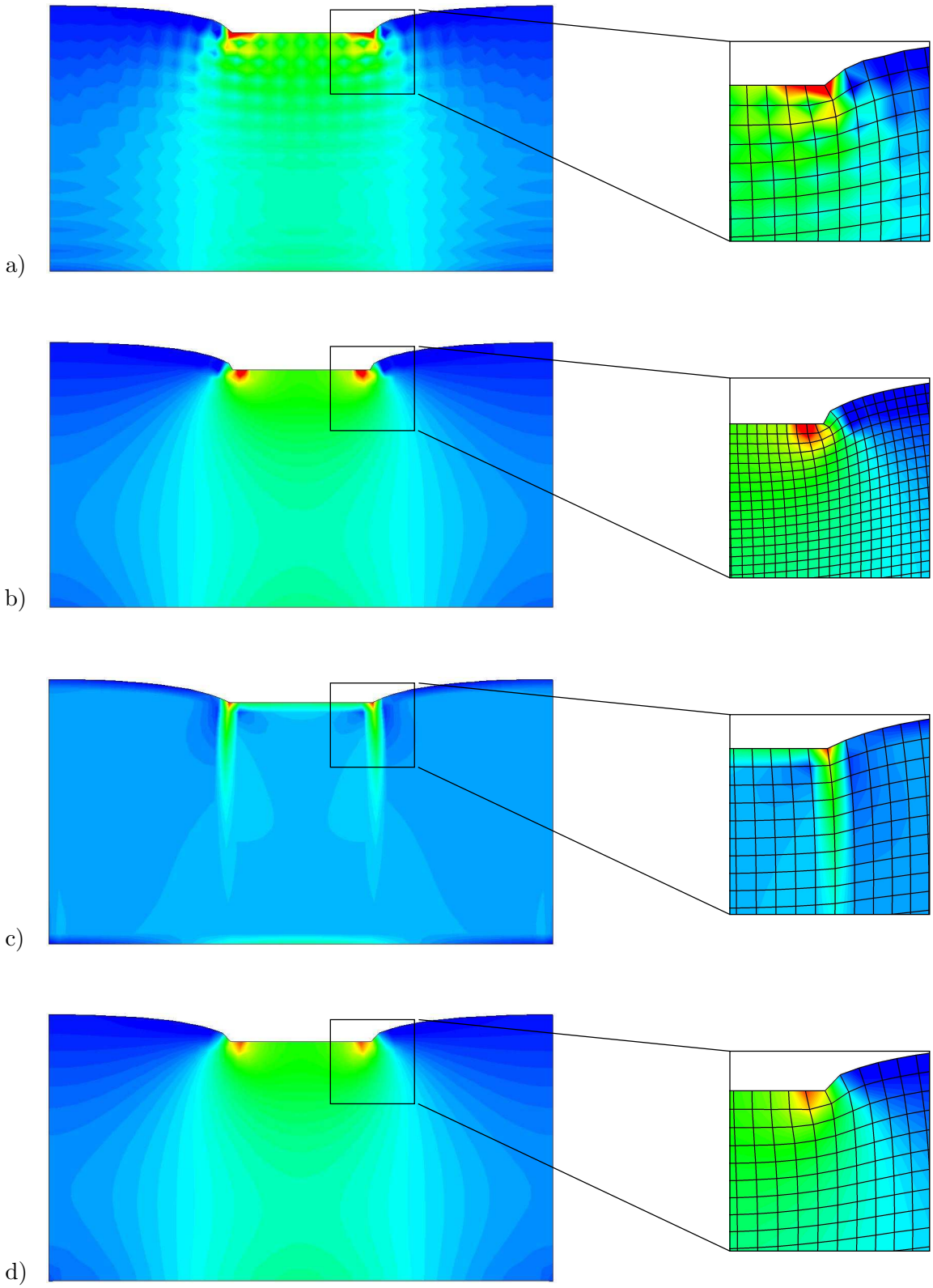

Figure 4.24: *Two-dimensional consolidation problem. Results*: Contour plots of fluid pressure p for minimization formulation and saddle-point formulation: Saddle-point formulation with a) Q_1-Q_1 element, b) Q_2-Q_1 element and minimization formulation with c) Q_1-RT_0 element and d) Q_1-RT_0-red element.

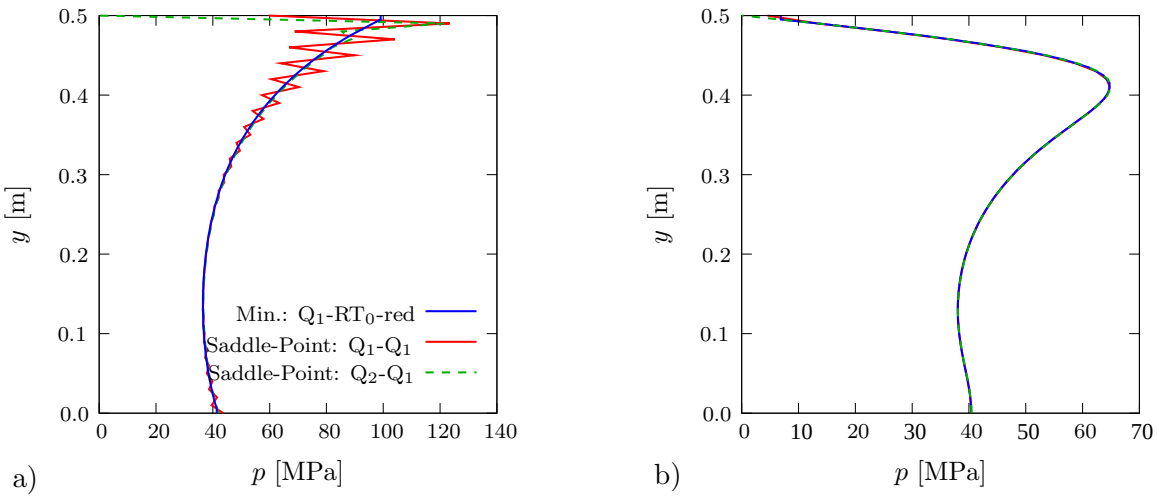

Figure 4.25: *Two-dimensional consolidation problem. Results.* Fluid pressure p at cross section $x = L/2$ for minimization and saddle-point formulation at a) $T = 1.3{\cdot}10^{-7}$ and b) $T = 1.47{\cdot}10^{-5}$.

in Figure 4.23c) for the Q_1-Q_1 element and in Figure 4.23d) for the Q_1-Q_1-red element. Qualitatively the same result can be observed as for the conforming element family: The element with full integration seems to lock, whereas the element with reduced integration yields good results. Figure 4.24 shows contour plots of the fluid pressure p for both formulations with different finite element designs: for the saddle point formulation with a) the inf-sup unstable Q_1-Q_1 element and b) the inf-sup stable Q_2-Q_1 (Taylor-Hood) element and for the minimization formulation with c) the Q_1-RT_0 element and d) Q_1-RT_0-red finite element. For the unstable Q_1-Q_1 element, we observe characteristic oscillations, whereas the Taylor-Hood saddle-point formulation yields smooth results. Qualitatively same observations have been made for the saddle point problem of coupled diffusion in hydrogels in Krischok & Linder [156]. For the minimization formulation with the Q_1-RT_0 element, we observe a behavior that is in line with our understanding of a locking phenomena, see Figure 4.24c). A classical characteristic property of locking is the appearance of nonphysical values and oscillations in local fields, that in this case the fluid pressure field p. For the element with reduced integration, Q_1-RT_0-red good results are obtained, see Figure 4.24d). The plots for the non-conforming Q_1-Q_1 and Q_1-Q_1-red minimization elements are not shown. The results are similar to their conforming counterparts: Non-physical fluid pressure distribution in the element with full integration and good results for the reduced integration scheme. The method of under-integration of the volumetric coupling term is in this boundary value problem motivated from the suspicion of locking. This issue for pure minimization formulations is well known in elasticity of incompressible solids and has also been addressed in the "minimization formulation" of poro-elasticity in Prevost [217].

Next, consider the loading case depicted in Figure 4.22b). The load is linearly increased in the first 20 time steps up to the final value $\bar{q}$ and then held constant. This boundary value problem was considered as benchmark in Preisig & Prévost [213]. In Figure 4.25 the fluid pressure p is shown at a vertical cross section in the center at $x = L/2$. The fluid pressure shows oscillations for the unstable Q_1-Q_1 saddle point finite element at an early time $T = 1.3 \cdot 10^{-7}$, see Figure 4.25a). The minimization formulation leads to stable results. At a later time step during the process, $T = 1.47 \cdot 10^{-5}$, all finite elements yield the same fluid pressure p in Figure 4.25b).

Chapter 5

Variational Modeling of Diffusion in Elastic Solids

In this Chapter another model problem associated with diffusion processes in elastic solids as well as related phase segregation phenomena are considered. For the modeling of such behavior advanced Cahn-Hilliard type phase-field models are required. The fundamentals of these models go back to Cahn [51] or Cahn & Hilliard [52] and are applied to diffusion processes for example in Anand [6], Burch et al. [50], Singh et al. [244], Deshpande et al. [81], Bohn et al. [35], Di Leo et al. [85] and Miehe et al. [185, 187]. An alternative motivation of such an approach is proposed by Gurtin [125] or Gurtin et al. [124] in terms of microforce balances. The consequence of this gradient-enhanced theory is that the gradient of the species concentration enters the constitutive functions. Hence the constitutive equation for the chemical potential turns from an ordinary differential equation into a partial differential equation. Further basic ingredients of the Cahn-Hilliard theory are a *non-convex energy* function in terms of the species concentration and an additional *surface energy* accounting for the domain walls between two interfaces.

The goal of this section is the development of rate-type and time-discrete variational principles for the coupled chemo-mechanical problem at finite strains that account for gradient-extended Cahn-Hilliard type diffusion. Starting point is the variational framework for modeling of non-standard continuum models outlined by Miehe [176] that has been applied to a wide range of gradient-enhanced problems before, see Miehe [178], Hildebrand [132], Miehe et al. [183, 184, 186] or Hildebrand & Miehe [133]. In particular the following considerations are in line with the works Miehe et al. [185], Dal & Miehe [70] and especially Miehe et al. [187]. As in Chapter 4 two alternative formulations are proposed that are connected to a *canonical minimization principle* and a dual saddle-point principle. The former one defines the basic kinematic fields, which are the rate of solid deformation $\dot{\boldsymbol{\varphi}}$ and the species flow vector $\tilde{I\!H}$, by the principle

$$\{\dot{\boldsymbol{\varphi}}, \tilde{I\!H}\} = \arg \left\{ \inf_{\dot{\boldsymbol{\varphi}} \in \mathcal{W}_{\dot{\boldsymbol{\varphi}}}} \inf_{\tilde{I\!H} \in \mathcal{W}_{\tilde{I\!H}}} \Pi(\dot{\boldsymbol{\varphi}}, \tilde{I\!H}) \right\} , \tag{5.1}$$

where the rate potential Π depends on only two constitutive functions connected to the energy storage and dissipative behavior. For the numerical treatment with the finite element method the formulation (5.1) however proves inappropriate as the gradient-enhanced

structure requires the use of finite elements with higher inter-element continuity for the species flow vector $\tilde{\mathbb{H}}$.

Thus a dual *saddle-point variational formulation* is proposed that circumvents this drawback. However the price to pay for C^0-continuous finite elements in the mixed formulation is an additional global degree of freedom. The global fields that are namely the rate of deformation $\dot{\boldsymbol{\varphi}}$, the rate of species content $\dot{c}$ and the chemical potential $\tilde{\mu}$, are then obtained from the rate-type variational principle

$$\{\dot{\boldsymbol{\varphi}}, \dot{c}, \tilde{\mu}\} = \arg \left\{ \inf_{\dot{\boldsymbol{\varphi}} \in \mathcal{W}_{\dot{\boldsymbol{\varphi}}}} \inf_{\dot{c} \in \mathcal{W}_{\dot{c}}} \sup_{\tilde{\mu} \in \mathcal{W}_{\tilde{\mu}}} \tilde{\Pi}^*(\dot{\boldsymbol{\varphi}}, \dot{c}, \tilde{\mu}) \right\} \tag{5.2}$$

in terms of the dual rate potential Π^* that is connected via a partial Legendre transformation to Π in (5.1).

Besides treating the advanced Cahn-Hilliard phase-field model, the saddle-point formulation (5.2) is boiled down to the case of diffusion without phase segregation. The model structure is then analogous to the one of Chapter 4 and the species concentration c can numerically be treated as a local internal variable at the Gauss points. This is due to the constitutive equation for the chemical potential $\tilde{\mu}$ which reduces from a partial differential equation to an ordinary differential equation.

Section 5.1 starts with a summary of the initial boundary value problem for gradient-enhanced diffusion in elastic solids undergoing finite strains. Furthermore the functionals and constitutive relations are introduced. Then the rate-type minimization variational formulation (5.1) and the dual rate-type saddle-point variational formulation (5.2) are stated. A reduction to diffusion without phase segregation is obtained for the saddle-point formulation (5.2). For the numerical investigation the saddle-point principle (5.2) is discretized in time in Section 5.3 resulting in an incremental variational formulation for finite elasticity coupled to diffusion both with and without considering phase segregation phenomena. The incremental problem is discretized in space by use of the finite element method in Section 5.4. The modeling capabilities are finally demonstrated in Section 5.5 by means of numerical boundary value problems in two as well as three dimensions.

5.1. Initial boundary value problem of diffusion in elastic solids

This section provides an introduction to the modeling framework of coupled diffusion in elastic solids undergoing finite strains. It is based on the general considerations of the macroscopic multicomponent theory presented in Chapter 3. Modifications of the general theory are due to the specific modeling assumptions and simplifications presumed.

5.1.1. Modeling assumptions

For the model problem under consideration we make the following four simplifications:

- Isothermal conditions, such that $\dot{\theta} = 0$ and $\nabla\theta = \boldsymbol{0}$,
- elastic solid behavior, such that $\mathfrak{q} = \emptyset$,

- quasi-static conditions, such that $|\ddot{\boldsymbol{\varphi}}| \approx 0$ and $|\boldsymbol{A}^{\beta}| \approx 0$,
- no body forces are considered, such that $\boldsymbol{b} = \boldsymbol{0}$.

In the context of diffusion processes the mass balance is usually rewritten as a balance of species. To this end the relative mass m of species is rewritten in terms of the *dimensionless species concentration* $c \in [0, 1]$ as

$$m_0^{\beta} + m = cr\tilde{M} \ , \tag{5.3}$$

where r is a given reference value such that cr is the number of species per unit reference volume and $\tilde{M}$ is the molar mass of the species. As both r and $\tilde{M}$ are constant the mass balance can be reformulated as a *species balance*

$$\dot{m} = -\operatorname{Div}[\mathit{H}] \quad \Rightarrow \quad \dot{c} = -\operatorname{Div}[\tilde{\mathit{H}}] \quad \text{with} \quad \tilde{\mathit{H}} = \frac{1}{r\tilde{M}}\mathit{H} \ , \tag{5.4}$$

where $\tilde{\mathit{H}}$ is denoted as the *species flow vector*. The dimensionless species concentration c is taken as state variable instead of m, that is the free energy function is dependent on c. To account for this change of state variable we also introduce a *dimensionless chemical potential* $\tilde{\mu}$. The relation to the chemical potential can be obtained by the equality $\mu\dot{m} = \tilde{\mu}\dot{c}$ and leads to $\tilde{\mu} = r\tilde{M}\mu$.

For the model problem of Cahn-Hilliard-type diffusion the free energy function contains not only bulk terms but also a surface term accounting for the interface energy between regions with different species mass densities. This surface term is a function of the gradient of the species concentration ∇c such that

$$\psi = \hat{\psi}(\boldsymbol{F}, c, \nabla c) \ . \tag{5.5}$$

For this form of free energy the local dissipation inequality is not fulfilled strongly at any point but weakly in the domain, that is constraints (3.64) are to hold. With these modeling assumptions, the balance equations and constitutive functions under consideration can be summarized as follows:

Balance of species content	$\dot{c} = -\operatorname{Div}[\tilde{\mathit{H}}]$
Balance of linear momentum	$\boldsymbol{0} = \operatorname{Div}[\boldsymbol{P}]$
Definition of driving force	$\tilde{\mathit{B}} = -\nabla\tilde{\mu}$
Constitutive stress	$\boldsymbol{P} = \partial_{\boldsymbol{F}}\hat{\psi}$
Constitutive chemical potential	$\tilde{\mu} = \partial_c\hat{\psi} - \operatorname{Div}[\partial_{\nabla c}\hat{\psi}]$
Constitutive driving force	$\hat{\tilde{\mathit{B}}} = \partial_{\tilde{\mathit{H}}}\hat{\phi}_{\text{con}}$

(5.6)

5.1.2. Initial boundary value problem

We now recall the coupled initial boundary value problem introduced in Subsection 3.4.1. The unknown kinematic fields of the coupled problem are the deformation map and the species flow vector

$$\boldsymbol{\varphi} : \begin{cases} \mathcal{B} \times T \to \mathcal{S} \subset \mathcal{R}^3, \\ (\boldsymbol{X}, t) \mapsto \boldsymbol{\varphi}(\boldsymbol{X}, t) \end{cases} \quad \text{and} \quad \tilde{\mathit{H}} : \begin{cases} \mathcal{B} \times T \to \mathcal{R}^3, \\ (\boldsymbol{X}, t) \mapsto \tilde{\mathit{H}}(\boldsymbol{X}, t) \ . \end{cases} \tag{5.7}$$

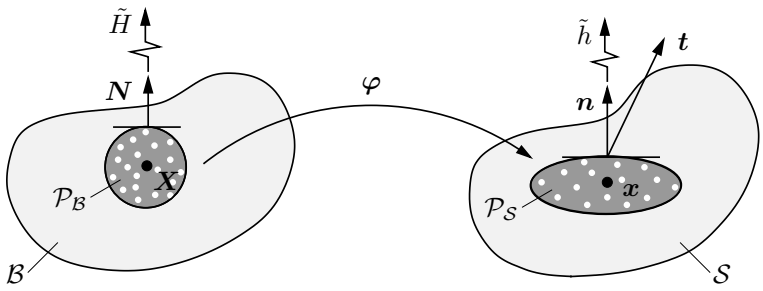

Figure 5.1: *Phenomenological quantities in diffusion in elastic solids at finite strains.* The total traction vector $\boldsymbol{t}$ represents the action of contact forces on surfaces of the cut-out part $\partial\mathcal{P}_\mathcal{S}$. The material and spatial species transports $\tilde{H}$ and $\tilde{h}$ characterize the species out-flux with respect to the areas $\partial\mathcal{P}_\mathcal{B}$ and $\partial\mathcal{P}_\mathcal{S}$.

The flow vector $\tilde{\mathbb{H}}$ and the species concentration c that appear as state variables in the constitutive functions are connected via the mass balance equation $(5.6)_1$. For the two global fields boundary values have to be prescribed. Therefor the boundary of $\mathcal{B}$ is split into *Dirichlet boundaries*, where the deformation map and the species flux is prescribed and *Neumann boundaries*, where the mechanical traction and the chemical potential is prescribed. Thus

$$\begin{aligned} \boldsymbol{\varphi}(\boldsymbol{X},t) &= \bar{\boldsymbol{\varphi}}(\boldsymbol{X},t) \text{ on } \partial\mathcal{B}_{\boldsymbol{\varphi}} \ , \quad \boldsymbol{T}(\boldsymbol{X},t) = \bar{\boldsymbol{T}}(\boldsymbol{X},t) \text{ on } \partial\mathcal{B}_{\boldsymbol{T}} = \partial\mathcal{B} \setminus \partial\mathcal{B}_{\boldsymbol{\varphi}} \ , \\ \tilde{H}(\boldsymbol{X},t) &= \bar{H}(\boldsymbol{X},t) \text{ on } \partial\mathcal{B}_{\tilde{H}} \ , \quad \tilde{\mu}(\boldsymbol{X},t) = \bar{\mu}(\boldsymbol{X},t) \text{ on } \partial\mathcal{B}_{\tilde{\mu}} = \partial\mathcal{B} \setminus \partial\mathcal{B}_{\tilde{H}} \ . \end{aligned} \tag{5.8}$$

Furthermore initial conditions have to be prescribed for the two kinematic fields $\boldsymbol{\varphi}$ and $\tilde{\mathbb{H}}$ as well as for the concentration field c

$$\boldsymbol{\varphi}(\boldsymbol{X},t_0) = \bar{\boldsymbol{\varphi}}_0(\boldsymbol{X}) \ , \ \tilde{\mathbb{H}}(\boldsymbol{X},t_0) = \bar{\mathbb{H}}_0(\boldsymbol{X}) \ , \ c(\boldsymbol{X},t_0) = \bar{c}_0(\boldsymbol{X}) \ . \tag{5.9}$$

As we are restricting ourselves to the quasi-static case initial conditions for the solid's velocity $\boldsymbol{V}$ are not needed. The initial boundary value problem is now to find the deformation $\boldsymbol{\varphi}$ and the species flow vector $\tilde{\mathbb{H}}$ that satisfy the boundary conditions (5.8), the initial conditions (5.9) and the balance equations (5.6). In this initial boundary value problem the two unknown fields $\boldsymbol{\varphi}$ and $\tilde{\mathbb{H}}$ are the kinematic variables of the two components of the material. Therefor we denote this as the *canonical form* of initial boundary value problem.

Alternative *mixed formulations* can be stated based on Legendre transformations of the two canonical constitutive functions ψ and ϕ. For example the classical $\{\boldsymbol{\varphi}, c, \mu\}$-formulation of coupled Cahn-Hilliard-type diffusion-mechanics results from an exchange of the convective dissipation potential ϕ with its dual ϕ^*. This formulation is widely used in the literature, see for example Anand [6], Zhao et al. [277] and Miehe et al. [185, 187]. In the numerical treatment of Cahn-Hilliard-type coupled problems with the finite element method, the mixed formulation is advantageous over the canonical setting, as only C^0-continuity is required for the discrete fields between elements. The canonical setting requires C^1-continuity for the species flow vector $\tilde{\mathbb{H}}$. For a reduction to diffusion without phase segregation the mixed formulation can furthermore be simplified to a $\{\boldsymbol{\varphi}, \mu\}$-formulation, see for example Miehe et al. [187] or Dal & Miehe [70]. Such a setting is then in line with the formulation of the previous Chapter of poro-elasticity with Darcy-type fluid flow.

5.1.3. Stored energy, dissipation potential and load functionals

In the following we introduce three functionals needed to state the variational principle. They are related to the energy storage, the convective dissipative mechanism and the external loading. The first two are based on two constitutive functions, the free energy function and the convective dissipation potential.

Rate of energy functional. The *stored energy functional* depends on the deformation field $\boldsymbol{\varphi}$, the concentration field c and its gradient ∇c

$$E(\boldsymbol{\varphi}, c) := \int_{\mathcal{B}} \hat{\psi}(\boldsymbol{F}, c, \nabla c)\, dV \tag{5.10}$$

and characterizes the energy stored in the multicomponent solid. It is governed by the constitutive energy density function $\hat{\psi}$. The rate of energy is evaluated as

$$\frac{d}{dt} E(\dot{\boldsymbol{\varphi}}, \dot{c}, \nabla \dot{c}) = \int_{\mathcal{B}} \{\, \partial_{\boldsymbol{F}} \hat{\psi} : \nabla \dot{\boldsymbol{\varphi}} + \partial_c \hat{\psi} \dot{c} + \partial_{\nabla c} \hat{\psi} \cdot \nabla \dot{c} \}\, dV \tag{5.11}$$

and can be considered as a functional of the rates $\dot{\boldsymbol{\varphi}}$, $\dot{c}$ and $\nabla \dot{c}$ at given state $\{\boldsymbol{\varphi}, c, \nabla c\}$.

Dissipation potential functional. The *canonical dissipation potential functional* depends on the species flow vector $\tilde{\mathbb{H}}$ and is assumed to have the form

$$D(\tilde{\mathbb{H}}) := \int_{\mathcal{B}} \hat{\phi}_{\text{con}}(\tilde{\mathbb{H}}; \boldsymbol{F}, c)\, dV \tag{5.12}$$

in terms of the convective dissipation potential function $\hat{\phi}_{\text{con}}$ and evaluated at a given state $\{\boldsymbol{F}, c\}$ of deformation and species concentration. Alternatively to the representation (5.12) the dissipation potential functional can be expressed in terms of the dual convective dissipation potential function $\hat{\phi}^*_{\text{con}}$. Recalling the definition of the Legendre transformation, we have

$$\hat{\phi}_{\text{con}}(\tilde{\mathbb{H}}) = \sup_{\tilde{\mathbb{B}}} \left[\tilde{\mathbb{B}} \cdot \tilde{\mathbb{H}} - \hat{\phi}^{\text{con}*}(\tilde{\mathbb{B}}; \boldsymbol{F}, c) \right] \tag{5.13}$$

in terms of the force $\tilde{\mathbb{B}}$ dual to $\tilde{\mathbb{H}}$. Insertion of (5.13) into (5.12) suggests the introduction of an *extended dissipation potential functional* $D^*(\tilde{\mathbb{H}}, \tilde{\mathbb{B}})$ defined as

$$D^*(\tilde{\mathbb{H}}, \tilde{\mathbb{B}}) = \int_{\mathcal{B}} \left[\tilde{\mathbb{B}} \cdot \tilde{\mathbb{H}} - \hat{\phi}^{\text{con}*}(\tilde{\mathbb{B}}; \boldsymbol{F}, c) \right] dV \ . \tag{5.14}$$

The extended dissipation functional (5.14) is connected to the dissipation potential functional (5.12) by the relationship

$$D(\tilde{\mathbb{H}}) = \sup_{\tilde{\mathbb{B}}} \left[D^*(\tilde{\mathbb{H}}, \tilde{\mathbb{B}}) \right] \ . \tag{5.15}$$

External load functional. The external load functional decomposes into mechanical and species contributions

$$P_{\text{ext}}(\dot{\boldsymbol{\varphi}}, \tilde{\mathbb{H}}) = P^{\boldsymbol{T}}_{\text{ext}}(\dot{\boldsymbol{\varphi}}) + P^{\tilde{\mu}}_{\text{ext}}(\tilde{\mathbb{H}}) \,. \tag{5.16}$$

Introducing the species flux $\tilde{H} = \tilde{\mathbb{H}} \cdot \boldsymbol{N}$ the two parts are given by

$$P^{\boldsymbol{T}}_{\text{ext}}(\dot{\boldsymbol{\varphi}}) := \int_{\partial\mathcal{B}_{\boldsymbol{T}}} \bar{\boldsymbol{T}} \cdot \dot{\boldsymbol{\varphi}} \, dA \quad \text{and} \quad P^{\tilde{\mu}}_{\text{ext}}(\tilde{\mathbb{H}}) = -\int_{\partial\mathcal{B}_{\tilde{\mu}}} \bar{\mu}\tilde{H} \, dA \tag{5.17}$$

representing the mechanical power due to surface tractions $\bar{\boldsymbol{T}}$ and a power contribution due to species flux over the boundary.

5.1.4. Constitutive functions for the model problem

Before stating the variational principle of coupled diffusion in elastic solids the two constitutive functions are specified. These are the free energy function ψ and the convective dissipation potential ϕ_{con}.

Free energy function. Consider a decomposition of the free energy function introduced in (5.10) into three parts, namely an elastic and a chemical contributions, as well as an interface term

$$\hat{\psi}(\boldsymbol{F}, c, \nabla c) = \hat{\psi}_{\text{el}}(\boldsymbol{F}^e(\boldsymbol{F}, c)) + \hat{\psi}_{\text{che}}(c) + \hat{\psi}_{\text{int}}(\nabla c) \,. \tag{5.18}$$

The elastic contribution is given in terms of the elastic (stress-producing) deformation $\boldsymbol{F}^e$. The elastic deformation map is obtained by a multiplicative split of the deformation gradient $\boldsymbol{F} = \boldsymbol{F}^e\boldsymbol{F}^c$ into an elastic contribution and a volumetric swelling part $\boldsymbol{F}^c := (J_c)^{1/3}\boldsymbol{1}$. In particular we have

$$\boldsymbol{F}^e = (J_c)^{-1/3}\boldsymbol{F} \quad \text{with} \quad J_c = 1 + \Omega(c - c_0) \,, \tag{5.19}$$

where the volumetric swelling deformation J_c is due to the species concentration c. Such a multiplicative split is in line with treatments in thermoelasticity as outlined in Lu & Pister [166]. For the elastic contribution a compressible neo-Hookean form is chosen

$$\hat{\psi}_{\text{el}}(\boldsymbol{F}^e) = \frac{\gamma}{2}\big[\boldsymbol{F}^e : \boldsymbol{F}^e - 3\big] + \frac{\gamma}{\beta}\big[\big(\det[\boldsymbol{F}^e]\big)^{-\beta} - 1\big] \,. \tag{5.20}$$

Here, $\gamma > 0$ is the shear modulus and the parameter $\beta > 0$ describes a weak volumetric compressibility and can be linked to the classical Poisson ratio of linear elasticity via $\beta = 2\nu/1 - 2\nu$. For the *chemical contribution* to the free energy a classical form proposed by Cahn & Hilliard [53] is assumed

$$\hat{\psi}_{\text{che}}(c) = A[\, c\ln c + (1-c)\ln(1-c)\,] + Bc(1-c) \,. \tag{5.21}$$

The first term, governed by the parameter A, ensures that the concentration remains in the range $c \in [0, 1]$. This is achieved by growth conditions for $c \to 0$ and $c \to 1$ as depicted in Figure 5.2b). The second term, governed by the parameter B, induces for $B > 2A$ a non-convexity as shown in Figure 5.2a) that models a phase decomposition. Finally, consistent with the classical Cahn-Hilliard theory, the interface contribution to the free energy is assumed to be a quadratic function of the concentration gradient ∇c

$$\hat{\psi}_{\text{int}}(\nabla c) = \frac{C}{2}|\nabla c|^2 \,. \tag{5.22}$$

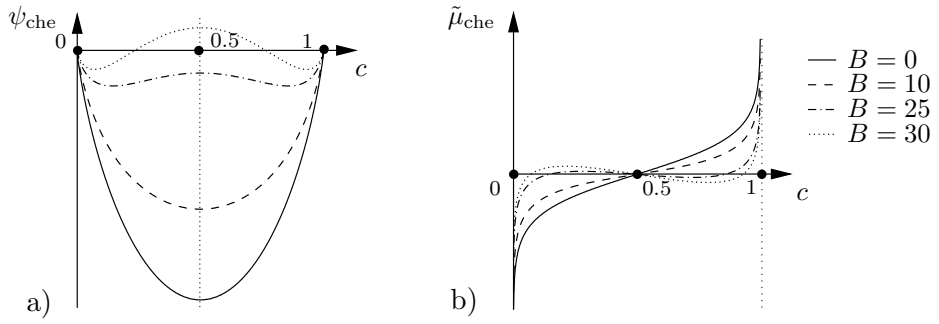

Figure 5.2: *Chemical contribution to the energy function.* Plots of a) chemical energy $\hat{\psi}_{\text{che}}(c) = A[\, c\ln c + (1-c)\ln(1-c)\,] + Bc(1-c)$ and b) its derivative $\tilde{\mu}_{che} := \hat{\psi}'_{\text{che}}(c) = A\ln(c/(1-c)) + B(1-2c)$ for $A = 10$ and different parameters $B = \{0, 10, 25, 30\}$.

Dissipation potential function. The *convective dissipation potential* introduced in (5.12) is assumed to be of quadratic form in terms of the species flow vector

$$\hat{\phi}_{\text{con}}(\tilde{\mathbb{H}}; \boldsymbol{C}, c) = \frac{1}{2}\widehat{\boldsymbol{K}}^{-1} : (\tilde{\mathbb{H}} \otimes \tilde{\mathbb{H}}) \quad \text{with} \quad \widehat{\boldsymbol{K}} = Mc(1-c)\boldsymbol{C}^{-1} \tag{5.23}$$

at a given state $\{\boldsymbol{F}, c\}$. The parameter $M > 0$ is denoted as the species mobility. The Legendre transformation yields the dual convective dissipation potential as

$$\hat{\phi}^*_{\text{con}}(\tilde{\mathbb{B}}; \boldsymbol{C}, c) = \frac{1}{2}\widehat{\boldsymbol{K}} : (\tilde{\mathbb{B}} \otimes \tilde{\mathbb{B}}) \ . \tag{5.24}$$

Constitutive total stress tensor. The local dissipation inequality leads us to the constitutive equation for the total stresses in terms of the free energy function as $\boldsymbol{P} = \partial_{\boldsymbol{F}}\hat{\psi}$, see (3.66). Evaluation of (5.18) yields

$$\boldsymbol{P} = \partial_{\boldsymbol{F}}\hat{\psi} = J_c^{-1/3}\gamma\big[\boldsymbol{F}^e - \big(\det[\boldsymbol{F}^e]\big)^{-\beta}\boldsymbol{F}^{e\,-T}\big] \ . \tag{5.25}$$

Note that the coupling effect to the stress is due to the volumetric chemical swelling J_c.

Constitutive chemical potential. For the gradient-extended modeling framework evaluation of the dissipation inequality leads to the chemical potential in terms of the free energy function $\tilde{\mu} = \partial_c\hat{\psi} - \text{Div}[\partial_{\nabla \mathbf{q}}\hat{\psi}]$, see $(5.6)_4$. With the energy (5.18) we get

$$\tilde{\mu} = \partial_c\hat{\psi} - \text{Div}[\partial_{\nabla \mathbf{q}}\hat{\psi}] = A\ln\left[\frac{c}{1-c}\right] + B(1-2c) + \Omega J_c^{-1}p - \text{Div}[C\nabla c] \ , \tag{5.26}$$

where $p = -1/3\partial_{\boldsymbol{F}}\hat{\psi}_{\text{el}} : \boldsymbol{F}$ is the hydrostatic pressure. For the reduced setting the interface contribution $\hat{\psi}_{\text{int}}$ vanishes, that is $C = 0$. Thus (5.26) reduces to

$$\tilde{\mu} = \partial_c\hat{\psi} = A\ln\left[\frac{c}{1-c}\right] + B(1-2c) + \Omega J_c^{-1}p \ . \tag{5.27}$$

Constitutive species flow. Using the constitutive relation $(5.6)_6$ the driving force dual to the species flow vector is obtained as $\tilde{\mathbb{B}} = \partial_{\tilde{\mathbb{H}}}\hat{\phi}_{\text{con}}$. With the dissipation potential function (5.23) at hand we get $\tilde{\mathbb{B}} = \widehat{\boldsymbol{K}}^{-1}\tilde{\mathbb{H}}$. Together with the definition of the driving force $(5.6)_3$ we can evaluate the species flow law as

$$\tilde{\mathbb{H}} = -\widehat{\boldsymbol{K}}\nabla\mu \ . \tag{5.28}$$

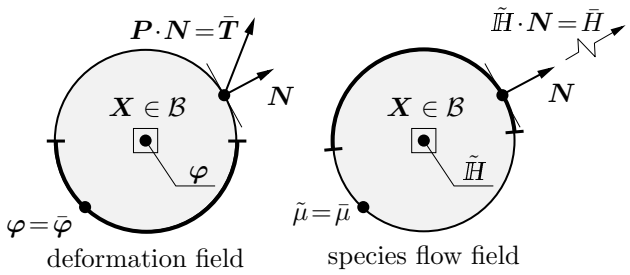

Figure 5.3: *Two-field problem of diffusion in elastic solids at finite strains.* The boundary $\partial\mathcal{B}$ of the solid's reference configuration $\mathcal{B}$ is decomposed into Dirichlet and Neumann parts $\partial\mathcal{B}_{\boldsymbol{\varphi}} \cup \partial\mathcal{B}_T$ for the deformation field and $\partial\mathcal{B}_{\tilde{H}} \cup \partial\mathcal{B}_{\tilde{\mu}}$ for the species flow field.

5.2. Variational principles for the evolution problem

With the functionals introduced above the variational principles for the coupled problem of diffusion both with and without phase segregation phenomena in elastic solids can be stated. In analogy to the considerations of Chapter 4 three variational principles are proposed, namely a minimization principle, a mixed saddle-point principle and a reduced mixed saddle-point principle. The latter is proposed in Miehe et al. [187].

5.2.1. Rate-type variational potential

Based on the energy E introduced in (5.10), the dissipation potential functional D in (5.12) and the external load functional P_{ext} in (5.16) the *canonical two-field potential* is defined as

$$\underbrace{\Pi(\dot{\boldsymbol{\varphi}}, \dot{\tilde{H}})}_{\text{rate potential}} := \underbrace{\frac{d}{dt}E(\boldsymbol{\varphi}, \tilde{H})}_{\text{rate of energy}} + \underbrace{D(\dot{\tilde{H}})}_{\text{dissipation}} - \underbrace{P_{\text{ext}}(\dot{\boldsymbol{\varphi}}, \dot{\tilde{H}})}_{\text{external power}} \tag{5.29}$$

at a given state $\{\boldsymbol{\varphi}, c\}$. Evaluation of the mixed rate potential by use of (5.11), (5.12) and (5.17) yields

$$\begin{aligned}\Pi(\dot{\boldsymbol{\varphi}}, \dot{\tilde{H}}) = & \int_{\mathcal{B}} \Big\{ \frac{\partial\hat{\psi}(\boldsymbol{F}, c, \nabla c)}{\partial \boldsymbol{F}} : \dot{\boldsymbol{F}} - \frac{\partial\hat{\psi}(\boldsymbol{F}, c, \nabla c)}{\partial c}\,\mathrm{Div}[\tilde{H}] \\ & - \frac{\partial\hat{\psi}(\boldsymbol{F}, c, \nabla c)}{\partial \nabla c} \cdot \nabla\big(\mathrm{Div}[\tilde{H}]\big) + \hat{\phi}_{\text{con}}(\tilde{H}; \boldsymbol{F}, c) \Big\}\, dV \\ & - \int_{\partial\mathcal{B}_{\boldsymbol{T}}} \bar{\boldsymbol{T}} \cdot \dot{\boldsymbol{\varphi}}\, dA + \int_{\partial\mathcal{B}_{\tilde{\mu}}} \bar{\mu}\dot{\tilde{H}}\, dA\ ,\end{aligned} \tag{5.30}$$

where the balance of species content $\dot{c} = -\mathrm{Div}[\dot{\tilde{H}}]$ is used in the second and third term. Note that this is a potential containing higher-order derivatives of the species flow $\nabla\big(\mathrm{Div}[\tilde{H}]\big)$.

5.2.2. Rate-type variational minimization principle

With the rate-type potential (5.29) at hand we can state a *two-field variational principle*

$$\{\dot{\boldsymbol{\varphi}}, \dot{\tilde{H}}\} = \arg\left\{ \inf_{\dot{\boldsymbol{\varphi}}\in\mathcal{W}_{\dot{\boldsymbol{\varphi}}}} \inf_{\dot{\tilde{H}}\in\mathcal{W}_{\dot{\tilde{H}}}} \Pi(\dot{\boldsymbol{\varphi}}, \dot{\tilde{H}}) \right\}\ , \tag{5.31}$$

which defines at the given state $\{\boldsymbol{\varphi}, c\}$ at time t the rate $\dot{\boldsymbol{\varphi}}$ of the deformation fields and the species flow vector field $\tilde{H}$. The admissible spaces for $\dot{\boldsymbol{\varphi}}$ and $\tilde{H}$ are given by

$$\begin{aligned} \mathcal{W}_{\dot{\boldsymbol{\varphi}}} &:= \{\dot{\boldsymbol{\varphi}} \in H^1(\mathcal{B}) |\ \dot{\boldsymbol{\varphi}} = \bar{\dot{\boldsymbol{\varphi}}} \text{ on } \partial\mathcal{B}_{\boldsymbol{\varphi}}\} \ , \\ \mathcal{W}_{\tilde{H}} &:= \{\tilde{H} \in H^1(\mathrm{Div}, \mathcal{B}) |\ \tilde{H} \cdot \boldsymbol{N} = \bar{H} \text{ on } \partial\mathcal{B}_{\tilde{H}}\} \ . \end{aligned} \tag{5.32}$$

The necessary condition of the variational principle (5.31) is that its variation vanishes. Taking the variation of the potential (5.30) and requiring arbitrary $\delta\dot{\boldsymbol{\varphi}}$ and $\delta\tilde{H}$ as well as an arbitrary divergence $\mathrm{Div}[\delta\tilde{H}]$ yields the Euler equations of the variational principle

$$\begin{aligned} &\textit{Balance of linear momentum} && -\mathrm{Div}[\partial_{\boldsymbol{F}}\hat{\psi}] = \boldsymbol{0} && \text{in } \mathcal{B} \\ &\textit{Species flow equation} && \nabla\big(\partial_c\hat{\psi} - \mathrm{Div}[\partial_{\nabla c}\hat{\psi}]\big) + \partial_{\tilde{H}}\hat{\phi}_{\mathrm{con}} = \boldsymbol{0} && \text{in } \mathcal{B} \\ &\textit{Traction boundary conditions} && \partial_{\boldsymbol{F}}\hat{\psi} \cdot \boldsymbol{N} = \bar{\boldsymbol{T}} && \text{on } \partial\mathcal{B}_{\boldsymbol{T}} \\ &\textit{Potential boundary conditions} && \partial_c\hat{\psi} - \mathrm{Div}[\partial_{\nabla c}\hat{\psi}] = \bar{\mu} && \text{on } \partial\mathcal{B}_{\mu} \\ &\textit{Micro-force boundary conditions} && \partial_{\nabla c}\hat{\psi} \cdot \boldsymbol{N} = 0 && \text{on } \partial\mathcal{B} \end{aligned} \tag{5.33}$$

and turn out to be the linear momentum balance $(5.6)_2$ and the species flow equation in inverse form as a combination of $(5.6)_3$ and $(5.6)_5$, along with the Neumann boundary conditions (5.8). Note that the micro-force boundary conditions $(5.33)_6$ fulfill the thermodynamical constraint $(3.68)_2$ and hence the variational principle (5.31) constitutes a thermodynamically consistent model. Furthermore note that the balance of species content $(5.6)_1$ was used in (5.30) in order to express the rate of species content $\dot{c}$ by the species flow vector $\tilde{H}$. Hence the species' content balance is fulfilled strongly.

5.2.3. Rate-type mixed variational potential

A mixed variational principle is obtained by exchanging the dissipation potential functional $D(\tilde{H})$ in (5.29) by the *extended* dissipation potential function $D^*(\tilde{H}, \tilde{B})$ introduced in (5.14). The *mixed three-field potential* is hence defined as

$$\underbrace{\Pi^*(\dot{\boldsymbol{\varphi}}, \tilde{H}, \tilde{B})}_{\text{rate potential}} := \underbrace{\frac{d}{dt}E(\boldsymbol{\varphi}, c)}_{\text{rate of energy}} + \underbrace{D^*(\tilde{H}, \tilde{B})}_{\text{dissipation}} - \underbrace{P_{\mathrm{ext}}(\dot{\boldsymbol{\varphi}}, \tilde{H})}_{\text{external power}} \tag{5.34}$$

at a given state $\{\boldsymbol{\varphi}, c\}$. Evaluation of the mixed rate potential by use of (5.11), (5.14) and (5.17) yields

$$\begin{aligned} \Pi^*(\dot{\boldsymbol{\varphi}}, \tilde{H}, \tilde{B}) = \int_{\mathcal{B}} \Big\{ &\frac{\partial\hat{\psi}(\boldsymbol{F}, c, \nabla c)}{\partial \boldsymbol{F}} : \dot{\boldsymbol{F}} - \frac{\partial\hat{\psi}(\boldsymbol{F}, c, \nabla c)}{\partial c}\,\mathrm{Div}[\tilde{H}] \\ &- \frac{\partial\hat{\psi}(\boldsymbol{F}, c, \nabla c)}{\partial \nabla c} \cdot \nabla\big(\mathrm{Div}[\tilde{H}]\big) + \tilde{H}\cdot\tilde{B} - \hat{\phi}^*_{\mathrm{con}}(\tilde{B}; \boldsymbol{F}, c)\Big\}\, dV \\ - \int_{\partial\mathcal{B}_{\boldsymbol{T}}} \bar{\boldsymbol{T}} \cdot \dot{\boldsymbol{\varphi}}\, dA + \int_{\partial\mathcal{B}_{\bar{\mu}}} \bar{\mu}\tilde{H}\, dA \ , \end{aligned} \tag{5.35}$$

where the balance of species content $\dot{c} = -\mathrm{Div}[\tilde{H}]$ is used in the second and third term. Note that the potential Π^* is *concave* with respect to the driving force vector $\tilde{B}$. This is due to the dual dissipation potential function $\hat{\phi}^*_{\mathrm{con}}$, the convexity of which is implied by the convexity of $\hat{\phi}_{\mathrm{con}}$. Furthermore note that this is a potential containing higher-order derivatives of the species flow $\nabla\big(\mathrm{Div}[\tilde{H}]\big)$.

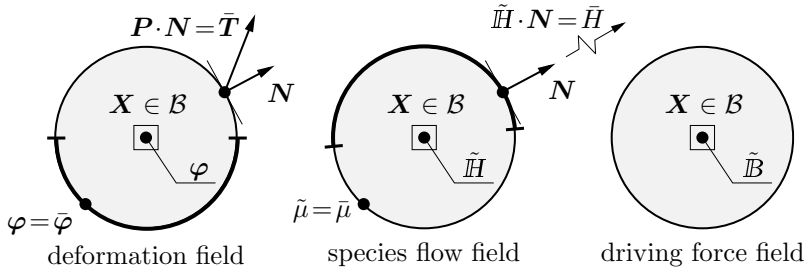

Figure 5.4: *Three-field problem of diffusion in elastic solids at finite strains.* The boundary $\partial\mathcal{B}$ of the solid's reference configuration $\mathcal{B}$ is decomposed into Dirichlet and Neumann parts $\partial\mathcal{B}_{\boldsymbol{\varphi}} \cup \partial\mathcal{B}_T$ for the deformation field and $\partial\mathcal{B}_{\tilde{H}} \cup \partial\mathcal{B}_{\tilde{\mu}}$ for the species flow field.

5.2.4. Rate-type variational saddle-point principle

With the rate-potential (5.34) at hand we can state the *mixed three-field variational principle*

$$\{\dot{\boldsymbol{\varphi}}, \tilde{H}, \tilde{\mathbb{B}}\} = \arg \left\{ \inf_{\dot{\boldsymbol{\varphi}}\in\mathcal{W}_{\dot{\boldsymbol{\varphi}}}} \inf_{\tilde{\mathbb{H}}\in\mathcal{W}_{\tilde{\mathbb{H}}}} \sup_{\tilde{\mathbb{B}}\in\mathcal{W}_{\tilde{\mathbb{B}}}} \Pi^*(\dot{\boldsymbol{\varphi}}, \tilde{\mathbb{H}}, \tilde{\mathbb{B}}) \right\} , \tag{5.36}$$

which defines at the given state $\{\boldsymbol{\varphi}, c\}$ at time t the rate $\dot{\boldsymbol{\varphi}}$ of the deformation fields, the species flow vector field $\tilde{\mathbb{H}}$ and the dual driving force field $\tilde{\mathbb{B}}$. Due to the concavity of (5.35) with respect to $\tilde{\mathbb{B}}$ this variational principle has a *saddle-point structure*. The admissible spaces for $\dot{\boldsymbol{\varphi}}$, $\tilde{\mathbb{H}}$ and $\tilde{\mathbb{B}}$ are given by

$$\begin{aligned} \mathcal{W}_{\dot{\boldsymbol{\varphi}}} &:= \{\dot{\boldsymbol{\varphi}} \in H^1(\mathcal{B}) |\ \dot{\boldsymbol{\varphi}} = \dot{\bar{\boldsymbol{\varphi}}} \text{ on } \partial\mathcal{B}_{\boldsymbol{\varphi}}\} , \\ \mathcal{W}_{\tilde{\mathbb{H}}} &:= \{\tilde{\mathbb{H}} \in H^1(\mathrm{Div}, \mathcal{B}) |\ \tilde{\mathbb{H}} \cdot \boldsymbol{N} = \bar{H} \text{ on } \partial\mathcal{B}_{\tilde{H}}\} , \\ \mathcal{W}_{\tilde{\mathbb{B}}} &:= \{\tilde{\mathbb{B}} \in L^2\} . \end{aligned} \tag{5.37}$$

The necessary condition of the variational principle (5.36) is that its variation vanishes. Taking the variation of the potential (5.35) and requiring arbitrary $\delta\dot{\boldsymbol{\varphi}}$, $\delta\tilde{\mathbb{H}}$, $\delta\tilde{\mathbb{B}}$ as well as an arbitrary divergence $\mathrm{Div}[\delta\tilde{\mathbb{H}}]$ yields the Euler equations of the variational principle

$$\begin{aligned} &\textit{Balance of linear momentum} && -\mathrm{Div}[\partial_{\boldsymbol{F}}\hat{\psi}] = \boldsymbol{0} && \text{in } \mathcal{B} \\ &\textit{Constitutive driving force} && \nabla\big(\partial_c\hat{\psi} - \mathrm{Div}[\partial_{\nabla c}\hat{\psi}]\big) + \tilde{\mathbb{B}} = \boldsymbol{0} && \text{in } \mathcal{B} \\ &\textit{Species flow equation} && \tilde{\mathbb{H}} - \partial_{\tilde{\mathbb{B}}}\hat{\phi}^*_{\mathrm{con}} = \boldsymbol{0} && \text{in } \mathcal{B} \\ &\textit{Traction boundary conditions} && \partial_{\boldsymbol{F}}\hat{\psi}\cdot\boldsymbol{N} = \bar{\boldsymbol{T}} && \text{on } \partial\mathcal{B}_{\boldsymbol{T}} \\ &\textit{Potential boundary conditions} && \partial_c\hat{\psi} - \mathrm{Div}[\partial_{\nabla c}\hat{\psi}] = \bar{\mu} && \text{on } \partial\mathcal{B}_{\tilde{\mu}} \\ &\textit{Micro-force boundary conditions} && \partial_{\nabla c}\hat{\psi}\cdot\boldsymbol{N} = 0 && \text{on } \partial\mathcal{B} \end{aligned} \tag{5.38}$$

and turn out to be the governing equations $(5.6)_2$, $(5.6)_3$ and the species flow equation, along with the Neumann boundary conditions (5.8). Note that the micro-force boundary conditions $(5.38)_6$ fulfill the thermodynamical constraint $(3.68)_2$ and hence the variational principle (5.36) constitutes a thermodynamically consistent model. Furthermore note that the balance of species content $(5.6)_1$ was used in (5.35) in order to express the rate of species content $\dot{c}$ by the species flow vector $\tilde{\mathbb{H}}$. Hence the species' content balance is fulfilled strongly.

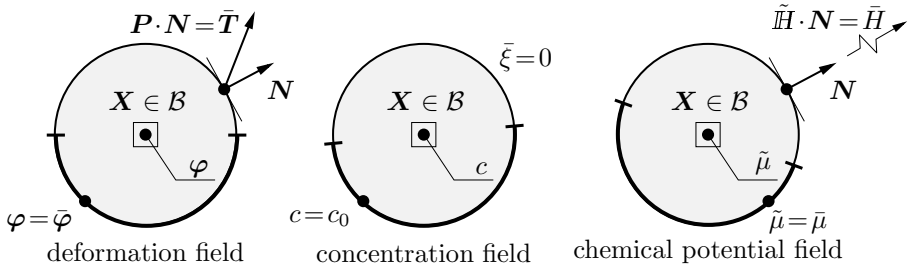

Figure 5.5: *Reduced three-field problem of diffusion in elastic solids at finite strains.* The boundary $\partial\mathcal{B}$ of the solid's reference configuration $\mathcal{B}$ is decomposed into Dirichlet and Neumann parts $\partial\mathcal{B}_{\boldsymbol{\varphi}}\cup\partial\mathcal{B}_T$ for the deformation field, $\partial\mathcal{B}_c\cup\partial\mathcal{B}_\xi$ for the concentration field and $\partial\mathcal{B}_{\tilde{\mu}}\cup\partial\mathcal{B}_{\tilde{H}}$ for the chemical potential field.

5.2.5. Reduced rate-type mixed variational potential

The mixed variational principle (5.36) is an initial boundary value problem containing nine scalar unknown fields $\{\dot{\boldsymbol{\varphi}},\tilde{H},\tilde{\mathbb{B}}\}$. Based on the knowledge of the Euler equation $(5.38)_3$ the unknown fields can be reduced to five. To this end we introduce the chemical potential field $\tilde{\mu}=\partial_c\hat{\psi}-\mathrm{Div}[\partial_{\nabla c}\hat{\psi}]$, see $(5.6)_5$. With this relation at hand the Euler equation $(5.38)_2$ can be rewritten as

$$\tilde{\mathbb{B}}=-\nabla\tilde{\mu}\ \text{in}\ \mathcal{B}\ . \tag{5.39}$$

Thus by reinsertion of the species' content balance and by use of (5.39), a *reduced mixed three-field potential* can be obtained from (5.35) as

$$\begin{aligned}\tilde{\Pi}^*(\dot{\boldsymbol{\varphi}},\dot{c},\tilde{\mu})=\ &\int_{\mathcal{B}}\Big\{\frac{\partial\hat{\psi}(\boldsymbol{F},c,\nabla c)}{\partial\boldsymbol{F}}:\dot{\boldsymbol{F}}+\frac{\partial\hat{\psi}(\boldsymbol{F},c,\nabla c)}{\partial c}\dot{c}\\&+\frac{\partial\hat{\psi}(\boldsymbol{F},c,\nabla c)}{\partial\nabla c}\cdot\nabla\dot{c}-\tilde{\mu}\dot{c}-\hat{\phi}^*_{\mathrm{con}}(\tilde{\mathbb{B}};\boldsymbol{F},c)\Big\}\,dV\\&-\int_{\partial\mathcal{B}_{\boldsymbol{T}}}\bar{\boldsymbol{T}}\cdot\dot{\boldsymbol{\varphi}}\,dA-\int_{\partial\mathcal{B}_{\tilde{H}}}\tilde{\mu}\bar{H}\,dA\ .\end{aligned}\tag{5.40}$$

Note that in order to obtain (5.40) the boundary conditions $(5.8)_2$ have to be evaluated. The potential $\tilde{\Pi}^*$ is *concave* with respect to the chemical potential field $\tilde{\mu}$. This is due to the dual dissipation potential function $\hat{\phi}^*_{\mathrm{con}}$, the convexity of which is implied by the convexity of the canonical dissipation potential $\hat{\phi}_{\mathrm{con}}$.

5.2.6. Reduced rate-type mixed variational principle

With the reduced rate-type potential (5.40) at hand we can state a *reduced mixed three-field variational principle*

$$\{\dot{\boldsymbol{\varphi}},\dot{c},\tilde{\mu}\}=\arg\left\{\inf_{\dot{\boldsymbol{\varphi}}\in\mathcal{W}_{\dot{\boldsymbol{\varphi}}}}\inf_{\dot{c}\in\mathcal{W}_{\dot{c}}}\sup_{\tilde{\mu}\in\mathcal{W}_{\tilde{\mu}}}\tilde{\Pi}^*(\dot{\boldsymbol{\varphi}},\dot{c},\tilde{\mu})\right\}\ , \tag{5.41}$$

which defines at the given state $\{\boldsymbol{\varphi},c\}$ at time t the rates $\dot{\boldsymbol{\varphi}}$ and $\dot{c}$ of the deformation and concentration fields along with the chemical potential $\tilde{\mu}$. The admissible spaces for

the rates of deformation $\dot{\boldsymbol{\varphi}}$ and concentration $\dot{c}$ as well as for the chemical potential $\tilde{\mu}$ are given by

$$\begin{aligned} \mathcal{W}_{\dot{\boldsymbol{\varphi}}} &:= \{\dot{\boldsymbol{\varphi}} \in H^1(\mathcal{B}) |\ \dot{\boldsymbol{\varphi}} = \dot{\bar{\boldsymbol{\varphi}}} \text{ on } \partial\mathcal{B}_{\boldsymbol{\varphi}}\} \ , \\ \mathcal{W}_{\dot{c}} &:= \{\dot{c} \in H^1(\mathcal{B}) |\ \dot{c} = 0 \text{ on } \partial\mathcal{B}_c\} \ , \\ \mathcal{W}_{\tilde{\mu}} &:= \{\tilde{\mu} \in H^1(\mathcal{B}) |\ \tilde{\mu} = \bar{\mu} \text{ on } \partial\mathcal{B}_{\tilde{\mu}}\} \ . \end{aligned} \tag{5.42}$$

Note that the admissible space $\mathcal{W}_{\dot{c}}$ fulfills the thermodynamical constraint $(3.68)_2$ on the boundary $\partial\mathcal{B}_c$. The necessary condition of the variational principle (5.41) is that its variation vanishes. Taking the variation of the potential (5.40) the Euler equations of the variational principle are obtained as

$$\begin{aligned} &\textit{Balance of linear momentum} && -\operatorname{Div}[\partial_{\boldsymbol{F}}\hat{\psi}] = \boldsymbol{0} && \text{in } \mathcal{B} \\ &\textit{Constitutive chemical potential} && -\tilde{\mu} + \partial_c\hat{\psi} - \operatorname{Div}[\partial_{\nabla c}\hat{\psi}] = 0 && \text{in } \mathcal{B} \\ &\textit{Balance of species content} && -\dot{c} - \operatorname{Div}[\partial_{\tilde{\mathbb{B}}}\hat{\phi}^*_{\text{con}}] = 0 && \text{in } \mathcal{B} \\ &\textit{Traction boundary conditions} && \partial_{\boldsymbol{F}}\hat{\psi}\cdot\boldsymbol{N} = \bar{\boldsymbol{T}} && \text{on } \partial\mathcal{B}_{\boldsymbol{T}} \\ &\textit{Species flux boundary conditions} && \partial_{\tilde{\mathbb{B}}}\hat{\phi}^*_{\text{con}}\cdot\boldsymbol{N} = \bar{H} && \text{on } \partial\mathcal{B}_{\tilde{H}} \\ &\textit{Micro-force boundary conditions} && \partial_{\nabla c}\hat{\psi}\cdot\boldsymbol{N} = 0 && \text{on } \partial\mathcal{B}_{\xi} \end{aligned} \tag{5.43}$$

and turn out to be the governing equations $(5.6)_2$, $(5.6)_5$ and $(5.6)_1$ along with the Neumann boundary conditions (5.8). The micro-force boundary conditions $(5.39)_6$ fulfill the thermodynamical constraint $(3.68)_2$ on the boundary $\partial\mathcal{B}_\xi$. On the part $\partial\mathcal{B}_c = \partial\mathcal{B} \setminus \partial\mathcal{B}_\xi$ the inequality condition is fulfilled by the admissible space $\mathcal{W}_{\dot{c}}$ in $(5.42)_2$. Thus also this variational formulation constitutes a thermodynamical model.

5.2.7. Reduction to diffusion without phase segregation

If we restrict our considerations to diffusion without phase segregation the interface contribution $\hat{\psi}_{\text{int}}$ of the free energy vanishes. Then the free energy is only a function of the deformation gradient and the concentration field $\psi = \hat{\psi}(\boldsymbol{F}, c)$. For this setting a prescription of boundary values for the species concentration c is not necessary and the admissible space for the rate of concentration $(5.42)_2$ reduces to

$$\mathcal{W}_{\dot{c}} := \{\dot{c} \in L^2\} \ . \tag{5.44}$$

The Euler equations of the variational principle (5.41) of the coupled chemo-mechanical system reduce for this case to

$$\begin{aligned} &\textit{Balance of linear momentum} && -\operatorname{Div}[\partial_{\boldsymbol{F}}\hat{\psi}] = \boldsymbol{0} && \text{in } \mathcal{B} \\ &\textit{Constitutive chemical potential} && -\tilde{\mu} + \partial_c\hat{\psi} = 0 && \text{in } \mathcal{B} \\ &\textit{Balance of species content} && -\dot{c} - \operatorname{Div}[\partial_{\tilde{\mathbb{B}}}\hat{\phi}^*_{\text{con}}] = 0 && \text{in } \mathcal{B} \\ &\textit{Traction boundary conditions} && \partial_{\boldsymbol{F}}\hat{\psi}\cdot\boldsymbol{N} = \bar{\boldsymbol{T}} && \text{on } \partial\mathcal{B}_{\boldsymbol{T}} \\ &\textit{Species flux boundary conditions} && \partial_{\tilde{\mathbb{B}}}\hat{\phi}^*_{\text{con}}\cdot\boldsymbol{N} = \bar{H} && \text{on } \partial\mathcal{B}_{\tilde{H}} \end{aligned} \tag{5.45}$$

In particular the constitutive equation for the chemical potential $(5.45)_2$ degenerates to an ordinary differential equation and no boundary conditions for the mico-forces are present any more.

5.3. Time-discrete variational principle

We now perform a time-discretization of the rate-type variational principle for the initial boundary value problem of the coupled chemo-mechanical problem derived in Section 5.2. The procedure closely follows the considerations of MIEHE [176]. As most convenient for the numerical implementation we restrict our attention to the *reduced saddle-point variational principle* introduced in Subsection 5.2.6.

5.3.1. Time-discretization and incremental variational potential

Consider discrete points in time $[t_0, ..., t_n, t_{n+1}, ..., t_\infty]$ of the process time $[t_0, t_\infty]$. Here $\tau := t_{n+1} - t_n$ is the time step size. The objective is now to determine the unknown fields $\boldsymbol{\varphi}_{n+1}$, c_{n+1} and $\tilde{\mu}_{n+1}$ at time t_{n+1}, whereas all fields $\{\boldsymbol{\varphi}_n, c_n, \tilde{\mu}_n\}$ at time t_n are assumed to be known. The rate of a quantity $\dot{q}(t)$ is considered to be constant within a time step τ and thus can be written as $\dot{q}_{n+1}(t_{n+1}) = (q_{n+1} - q_n)/\tau$. For sake of a compact notation in the further considerations all subscripts $n+1$ are dropped, such that all variables without index are associated with time t_{n+1}.

The incremental counterpart $\tilde{\Pi}^{*\tau}$ of the variational functional given in (5.40) within the time step $[t_n, t]$ under consideration is obtained from an algorithmic integration scheme. With the above stated assumption of *constant* rates of field quantities within a time step the incremental potential is considered of the form

$$\begin{aligned}\tilde{\Pi}^{*\tau}(\boldsymbol{\varphi}, c, \tilde{\mu}) = & \int_{\mathcal{B}} \left\{ \hat{\psi}(\boldsymbol{F}, c, \nabla c) - \hat{\psi}_n - \tilde{\mu}(c - c_n) - \tau \hat{\phi}^*_{\text{con}}(\tilde{\mathcal{B}}; \boldsymbol{F}_n, c_n) \right\} dV \\ & - \int_{\partial \mathcal{B}_{\boldsymbol{T}}} \bar{\boldsymbol{T}} \cdot [\boldsymbol{\varphi} - \boldsymbol{\varphi}_n] \, dA - \int_{\partial \mathcal{B}_{\tilde{H}}} \tau \tilde{\mu} \bar{H} \, dA \end{aligned} \tag{5.46}$$

where we introduced $\hat{\psi}_n = \hat{\psi}(\boldsymbol{F}_n, c_n, \nabla c_n)$. Note that the dual convective dissipation potential $\hat{\phi}^*_{\text{con}}(\mathcal{B}; \boldsymbol{F}_n, c_n)$ is evaluated at frozen state $\{\boldsymbol{F}_n, c_n\}$ of deformation gradient and concentration at time t_n.

5.3.2. Incremental mixed variational principle

With the incremental potential (5.46) at hand, the time-discrete counterpart of the variational principle (5.40) can be stated as

$$\{\boldsymbol{\varphi}, c, \tilde{\mu}\} = \arg \left\{ \inf_{\boldsymbol{\varphi} \in \mathcal{W}_{\boldsymbol{\varphi}}} \inf_{c \in \mathcal{W}_c} \sup_{\tilde{\mu} \in \mathcal{W}_{\tilde{\mu}}} \tilde{\Pi}^{*\tau}(\boldsymbol{\varphi}, c, \tilde{\mu}) \right\} . \tag{5.47}$$

The variational principle determines the fields $\{\boldsymbol{\varphi}, c, \tilde{\mu}\}$ at current time t as a *saddle point* of the time-discrete potential $\tilde{\Pi}^{*\tau}$. The admissible spaces for the time-discrete fields are

$$\begin{aligned} \mathcal{W}_{\boldsymbol{\varphi}} &:= \{\boldsymbol{\varphi} \in H^1(\mathcal{B}) |\ \boldsymbol{\varphi} = \bar{\boldsymbol{\varphi}} \text{ on } \partial \mathcal{B}_{\boldsymbol{\varphi}}\} , \\ \mathcal{W}_c &:= \{c \in H^1(\mathcal{B}) |\ c = c_0 \text{ on } \partial \mathcal{B}_c\} , \\ \mathcal{W}_{\tilde{\mu}} &:= \{\tilde{\mu} \in H^1(\mathcal{B}) |\ \tilde{\mu} = \bar{\mu} \text{ on } \partial \mathcal{B}_{\tilde{\mu}}\} . \end{aligned} \tag{5.48}$$

The necessary condition of the variational principle (5.47) is that its variation vanishes. Taking the variation of the potential (5.46) the Euler equations of the variational principle are obtained as

$$\begin{aligned}
&\textit{Balance of linear momentum} && -\operatorname{Div}[\partial_{\boldsymbol{F}}\hat{\psi}] = \boldsymbol{0} && \text{in } \mathcal{B}\\
&\textit{Constitutive chemical potential} && -\tilde{\mu} + \partial_c\hat{\psi} - \operatorname{Div}[\partial_{\nabla c}\hat{\psi}] = 0 && \text{in } \mathcal{B}\\
&\textit{Balance of species content} && -(c - c_n) - \tau \operatorname{Div}[\partial_{\tilde{\mathbb{B}}}\hat{\phi}^*_{\text{con}}] = 0 && \text{in } \mathcal{B}\\
&\textit{Traction boundary conditions} && \partial_{\boldsymbol{F}}\hat{\psi}\cdot\boldsymbol{N} = \bar{\boldsymbol{T}} && \text{on } \partial\mathcal{B}_{\boldsymbol{T}}\\
&\textit{Species flux boundary conditions} && \tau\partial_{\tilde{\mathbb{B}}}\hat{\phi}^*_{\text{con}}\cdot\boldsymbol{N} = \tau\bar{H} && \text{on } \partial\mathcal{B}_{\tilde{H}}\\
&\textit{Micro-force boundary conditions} && \partial_{\nabla c}\hat{\psi}\cdot\boldsymbol{N} = 0 && \text{on } \partial\mathcal{B}_{\xi}
\end{aligned} \tag{5.49}$$

These are consistent algorithmic counterparts of the continuous governing equations $(5.6)_2$, $(5.6)_5$ and $(5.6)_1$ together with the discrete Neumann boundary conditions (5.8). The micro-force boundary conditions $(5.49)_6$ fulfill the thermodynamical constraint $(3.68)_2$ on $\partial\mathcal{B}_\xi$. On the other part $\partial\mathcal{B}_c = \partial\mathcal{B} \setminus \partial\mathcal{B}_\xi$ the inequality condition is fulfilled by the admissible space $\mathcal{W}_c$ in $(5.48)_2$.

5.3.3. Reduction to diffusion without phase segregation

Consider the time-discretization of the reduced setting of diffusion without phase segregation. Here, the interface contribution $\hat{\psi}_{\text{int}}$ vanishes and thus $\psi = \hat{\psi}(\boldsymbol{F}, c)$. Hence a prescription of boundary values for the species concentration c is not needed and the admissible space in $(5.48)_2$ reduces to

$$\mathcal{W}_c := \{c \in L^2\} \,. \tag{5.50}$$

The Euler equations of the incremental variational principle (5.47) reduce compared to the ones for the Cahn-Hilliard-type formulation in (5.49) to

$$\begin{aligned}
&\textit{Balance of linear momentum} && -\operatorname{Div}[\partial_{\boldsymbol{F}}\hat{\psi}] = \boldsymbol{0} && \text{in } \mathcal{B}\\
&\textit{Constitutive chemical potential} && -\tilde{\mu} + \partial_c\hat{\psi} = 0 && \text{in } \mathcal{B}\\
&\textit{Balance of species content} && -(c - c_n) - \tau \operatorname{Div}[\partial_{\tilde{\mathbb{B}}}\hat{\phi}^*_{\text{con}}] = 0 && \text{in } \mathcal{B}\\
&\textit{Traction boundary conditions} && \partial_{\boldsymbol{F}}\hat{\psi}\cdot\boldsymbol{N} = \bar{\boldsymbol{T}} && \text{on } \partial\mathcal{B}_{\boldsymbol{T}}\\
&\textit{Species flux boundary conditions} && \tau\partial_{\tilde{\mathbb{B}}}\hat{\phi}^*_{\text{con}}\cdot\boldsymbol{N} = \tau\bar{H} && \text{on } \partial\mathcal{B}_{\tilde{H}}
\end{aligned} \tag{5.51}$$

In particular the constitutive equation for the chemical potential $(5.51)_2$ degenerates to an ordinary differential equation and no boundary conditions for the mico-forces are present any more.

5.4. Space-discrete incremental variational principle

In what follows the time-discrete variational principle (5.47) is discretized in space by use of the finite element method. To this end, first the finite element approximations of the geometry and the fields of unknowns are introduced. Then the space-time-discrete variational principle is stated.

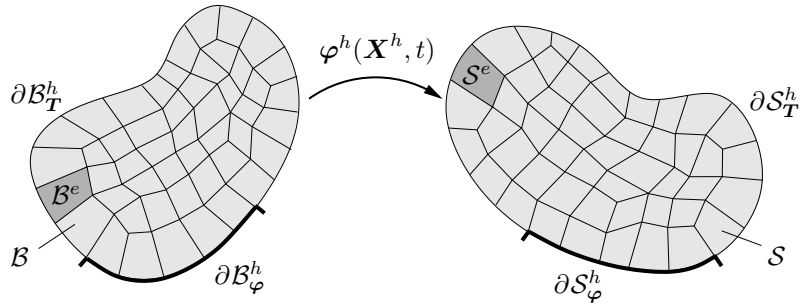

Figure 5.6: *Finite element discretization.* The material body $\mathcal{B}$ is approximated by the discrete body $\mathcal{B}^h \approx \mathcal{B}$. The discretization $\mathcal{B}^h$ is the union of n_e finite elements $\mathcal{B}^e$. The deformation field $\boldsymbol{\varphi}$ and all other unknown fields are approximated based on discrete values at interpolation points and so-called shape functions.

5.4.1. Finite element approximation

Before stating the space-discrete incremental variational principle for the model problem of diffusion in elastic solids, we first introduce the finite element approximations of the unknown fields $\boldsymbol{\varphi}$, c and $\tilde{\mu}$. The considerations here are in analogy to the finite element approximation in Subsection 4.4.1 for porous media. Thus we directly introduce the approximations on the parent element $\mathcal{A}$ and the global interpolation for the unknown fields. For further details we refer to the previous Chapter. Within the isoparametric setting the interpolations of the unknown fields within an element $\mathcal{B}^e$ are based on shape functions in terms of the parent element's coordinates $\boldsymbol{\xi}$ and in particular given by

$$\begin{aligned}
\boldsymbol{\varphi}^e(\boldsymbol{X}) &= \sum_{i=1}^{m_{\boldsymbol{\varphi}}} \hat{N}^i_{\boldsymbol{\varphi}}\left(\boldsymbol{\xi} = \boldsymbol{X}^{e-1}(\boldsymbol{X})\right) \boldsymbol{\varphi}^i \,, \\
c^e(\boldsymbol{X}) &= \sum_{i=1}^{m_c} \hat{N}^i_c\left(\boldsymbol{\xi} = \boldsymbol{X}^{e-1}(\boldsymbol{X})\right) c^i \,, \\
\tilde{\mu}^e(\boldsymbol{X}) &= \sum_{i=1}^{m_{\tilde{\mu}}} \hat{N}^i_{\tilde{\mu}}\left(\boldsymbol{\xi} = \boldsymbol{X}^{e-1}(\boldsymbol{X})\right) \tilde{\mu}^i \,.
\end{aligned} \tag{5.52}$$

Here we introduced the local shape functions $\hat{N}^i_{\boldsymbol{\varphi}}(\boldsymbol{\xi})$, $\hat{N}^i_c(\boldsymbol{\xi})$ and $\hat{N}^i_{\tilde{\mu}}(\boldsymbol{\xi})$ associated to $m_{\boldsymbol{\varphi}}$, m_c and $m_{\tilde{\mu}}$ interpolation points with discrete values $\boldsymbol{\varphi}^i$, c^i and $\tilde{\mu}^i$ in $\mathcal{B}^e$. The transformation from parameter space to physical space for isoparametric finite elements is conducted by the invertible geometry mapping $\boldsymbol{X}^e(\boldsymbol{\xi})$ introduced in (4.59). Furthermore it is possible to interpolate the global fields in the whole domain $\mathcal{B}^h$ by the approximations

$$\begin{aligned}
\boldsymbol{\varphi}(\boldsymbol{X}) \approx \boldsymbol{\varphi}^h(\boldsymbol{X}) &= \sum_{I=1}^{M_{\boldsymbol{\varphi}}} N^I_{\boldsymbol{\varphi}}(\boldsymbol{X})\boldsymbol{\varphi}^I =: \underline{\mathbf{N}}_{\boldsymbol{\varphi}}\underline{\mathbf{d}}_{\boldsymbol{\varphi}} \,, \\
c(\boldsymbol{X}) \approx c^h(\boldsymbol{X}) &= \sum_{I=1}^{M_c} N^I_c(\boldsymbol{X})c^I =: \underline{\mathbf{N}}_c\underline{\mathbf{d}}_c \,, \\
\tilde{\mu}(\boldsymbol{X}) \approx \tilde{\mu}^h(\boldsymbol{X}) &= \sum_{I=1}^{M_{\tilde{\mu}}} N^I_{\tilde{\mu}}(\boldsymbol{X})\tilde{\mu}^I =: \underline{\mathbf{N}}_{\tilde{\mu}}\underline{\mathbf{d}}_{\tilde{\mu}} \,,
\end{aligned} \tag{5.53}$$

in terms of global vectors $\underline{\mathbf{d}}_{\boldsymbol{\varphi}}$, $\underline{\mathbf{d}}_c$ and $\underline{\mathbf{d}}_{\tilde{\mu}}$ containing $M_{\boldsymbol{\varphi}}$, M_c and $M_{\tilde{\mu}}$ global discrete values of unknowns $\boldsymbol{\varphi}^I$, c^I and $\tilde{\mu}^I$. Furthermore we introduced the global matrices $\underline{\mathbf{N}}_{\boldsymbol{\varphi}}$, $\underline{\mathbf{N}}_c$

and $\underline{\mathbf{N}}_{\tilde{\mu}}$ containing the shape functions $N^I_{\boldsymbol{\varphi}}$, N^I_c and $N^I_{\tilde{\mu}}$. When considering nodal-based degrees of freedom, the vectors of discrete unknowns are given by

$$\underline{\mathbf{d}}_{\boldsymbol{\varphi}} := \left[\boldsymbol{\varphi}^1, ..., \boldsymbol{\varphi}^{M_{\boldsymbol{\varphi}}}\right]^T, \quad \underline{\mathbf{d}}_c := \left[c^1, ..., c^{M_c}\right]^T \quad \text{and} \quad \underline{\mathbf{d}}_{\tilde{\mu}} := \left[\tilde{\mu}^1, ..., \tilde{\mu}^{M_{\tilde{\mu}}}\right]^T, \tag{5.54}$$

as well as the global matrices containing the scalar-valued global interpolation functions

$$\begin{aligned}
\underline{\mathbf{N}}_{\boldsymbol{\varphi}} &:= \begin{bmatrix} N^1_{\boldsymbol{\varphi}} & 0 & 0 & & N^{M_{\boldsymbol{\varphi}}}_{\boldsymbol{\varphi}} & 0 & 0 \\ 0 & N^1_{\boldsymbol{\varphi}} & 0 & ... & 0 & N^{M_{\boldsymbol{\varphi}}}_{\boldsymbol{\varphi}} & 0 \\ 0 & 0 & N^1_{\boldsymbol{\varphi}} & & 0 & 0 & N^{M_{\boldsymbol{\varphi}}}_{\boldsymbol{\varphi}} \end{bmatrix}, \\
\underline{\mathbf{N}}_c &:= \begin{bmatrix} N^1_c & & ... & & N^{M_c}_c \end{bmatrix}, \\
\underline{\mathbf{N}}_{\mu} &:= \begin{bmatrix} N^1_{\tilde{\mu}} & & ... & & N^{M_{\tilde{\mu}}}_{\tilde{\mu}} \end{bmatrix}.
\end{aligned} \tag{5.55}$$

For a connection between the shape functions $N^I_{(\cdot)}(\boldsymbol{X}) \in \mathcal{B}^h$ and $\hat{N}^i_{(\cdot)}(\boldsymbol{\xi}) \in \mathcal{A}$, see Subsection 4.4.1. Besides the interpolations of the fields $\boldsymbol{\varphi}^h$, c^h and $\tilde{\mu}^h$ itself also their gradients are needed. Using the Voigt notation to rewrite the tensorial deformation gradient $\boldsymbol{F}$ as a vectorial object, we write in analogy to (4.67)

$$\begin{aligned}
\boldsymbol{F}(\boldsymbol{X}) &\approx \boldsymbol{F}^h(\boldsymbol{X}) &&= \underline{\mathbf{B}}_{\boldsymbol{F}} \underline{\mathbf{d}}_{\boldsymbol{\varphi}}, \\
\nabla c(\boldsymbol{X}) &\approx \nabla c^h(\boldsymbol{X}) &&= \underline{\mathbf{B}}_{\nabla c} \underline{\mathbf{d}}_c, \\
\nabla \tilde{\mu}(\boldsymbol{X}) &\approx \nabla \tilde{\mu}^h(\boldsymbol{X}) &&= \underline{\mathbf{B}}_{\nabla \tilde{\mu}} \underline{\mathbf{d}}_{\tilde{\mu}},
\end{aligned} \tag{5.56}$$

where $\underline{\mathbf{B}}_{\boldsymbol{F}}$, $\underline{\mathbf{B}}_{\nabla c}$ and $\underline{\mathbf{B}}_{\nabla \tilde{\mu}}$ are symbolic representations of global matrices of shape function derivatives. Using the abbreviation $(\cdot)_{,i} = \partial_{X_i}(\cdot)$, we can evaluate for the case of nodal-based degrees of freedom

$$\begin{aligned}
\underline{\mathbf{B}}_{\boldsymbol{F}} &:= \begin{bmatrix}
N^1_{\boldsymbol{\varphi},1} & 0 & 0 & & N^{M_{\boldsymbol{\varphi}}}_{\boldsymbol{\varphi},1} & 0 & 0 \\
N^1_{\boldsymbol{\varphi},2} & 0 & 0 & & N^{M_{\boldsymbol{\varphi}}}_{\boldsymbol{\varphi},2} & 0 & 0 \\
N^1_{\boldsymbol{\varphi},3} & 0 & 0 & & N^{M_{\boldsymbol{\varphi}}}_{\boldsymbol{\varphi},3} & 0 & 0 \\
0 & N^1_{\boldsymbol{\varphi},1} & 0 & & 0 & N^{M_{\boldsymbol{\varphi}}}_{\boldsymbol{\varphi},1} & 0 \\
0 & N^1_{\boldsymbol{\varphi},2} & 0 & ... & 0 & N^{M_{\boldsymbol{\varphi}}}_{\boldsymbol{\varphi},2} & 0 \\
0 & N^1_{\boldsymbol{\varphi},3} & 0 & & 0 & N^{M_{\boldsymbol{\varphi}}}_{\boldsymbol{\varphi},3} & 0 \\
0 & 0 & N^1_{\boldsymbol{\varphi},1} & & 0 & 0 & N^{M_{\boldsymbol{\varphi}}}_{\boldsymbol{\varphi},1} \\
0 & 0 & N^1_{\boldsymbol{\varphi},2} & & 0 & 0 & N^{M_{\boldsymbol{\varphi}}}_{\boldsymbol{\varphi},2} \\
0 & 0 & N^1_{\boldsymbol{\varphi},3} & & 0 & 0 & N^{M_{\boldsymbol{\varphi}}}_{\boldsymbol{\varphi},3}
\end{bmatrix}, \\
\underline{\mathbf{B}}_{\nabla c} &:= \begin{bmatrix}
N^1_{c,1} & 0 & 0 & & N^{M_c}_{c,1} & 0 & 0 \\
0 & N^1_{c,2} & 0 & ... & 0 & N^{M_c}_{c,2} & 0 \\
0 & 0 & N^1_{c,3} & & 0 & 0 & N^{M_c}_{c,3}
\end{bmatrix}, \\
\underline{\mathbf{B}}_{\nabla \tilde{\mu}} &:= \begin{bmatrix}
N^1_{\tilde{\mu},1} & 0 & 0 & & N^{M_{\tilde{\mu}}}_{\tilde{\mu},1} & 0 & 0 \\
0 & N^1_{\tilde{\mu},2} & 0 & ... & 0 & N^{M_{\tilde{\mu}}}_{\tilde{\mu},2} & 0 \\
0 & 0 & N^1_{\tilde{\mu},3} & & 0 & 0 & N^{M_{\tilde{\mu}}}_{\tilde{\mu},3}
\end{bmatrix}.
\end{aligned} \tag{5.57}$$

5.4.2. Space-time-discrete mixed variational saddle-point principle

For the reduced mixed saddle-point formulation the unknown fields are the deformation map $\boldsymbol{\varphi}$, the species concentration c and the chemical potential $\tilde{\mu}$, see (5.47). For sake of a compact notation consider the vector of discrete unknowns of the space-discrete variational principle given by

$$\underline{\mathbf{d}}^* = \left[\, \underline{\mathbf{d}}_{\boldsymbol{\varphi}} \,,\, \underline{\mathbf{d}}_c \,,\, \underline{\mathbf{d}}_{\tilde{\mu}} \right]^T \,. \tag{5.58}$$

With (5.58) at hand, the space-discrete fields (5.53) can be rewritten as

$$\boldsymbol{\varphi}^h(\boldsymbol{X}) = \underline{\mathbf{N}}_{\boldsymbol{\varphi}} \underline{\mathbf{d}}_{\boldsymbol{\varphi}} = \hat{\underline{\mathbf{N}}}_{\boldsymbol{\varphi}} \underline{\mathbf{d}}^* \;,\; c^h(\boldsymbol{X}) = \underline{\mathbf{N}}_c \underline{\mathbf{d}}_c = \hat{\underline{\mathbf{N}}}_c \underline{\mathbf{d}}^* \;,\; \tilde{\mu}^h(\boldsymbol{X}) = \underline{\mathbf{N}}_{\tilde{\mu}} \underline{\mathbf{d}}_{\tilde{\mu}} = \hat{\underline{\mathbf{N}}}_{\tilde{\mu}} \underline{\mathbf{d}}^* \,. \tag{5.59}$$

Furthermore we introduce the vector of *constitutive state* $\mathbf{f}^* := [\, \boldsymbol{F}, c, \nabla c, \tilde{\mu}, -\nabla \tilde{\mu} \,]^T$. With the approximation (5.54), (5.58) and (5.59) $\mathbf{f}^{*h}$ can be evaluated as

$$\mathbf{f}^*(\boldsymbol{X}) \approx \mathbf{f}^{*h}(\boldsymbol{X}) = \begin{bmatrix} \underline{\mathbf{B}}_{\boldsymbol{F}}\, \underline{\mathbf{d}}_{\boldsymbol{\varphi}} \\ \underline{\mathbf{N}}_c\, \underline{\mathbf{d}}_c \\ \underline{\mathbf{B}}_{\nabla c}\, \underline{\mathbf{d}}_c \\ \underline{\mathbf{N}}_{\tilde{\mu}}\, \underline{\mathbf{d}}_{\tilde{\mu}} \\ -\underline{\mathbf{B}}_{\nabla \tilde{\mu}}\, \underline{\mathbf{d}}_{\tilde{\mu}} \end{bmatrix} =: \underline{\mathbf{B}}\, \underline{\mathbf{d}}^* \,, \tag{5.60}$$

in terms of a global matrix $\underline{\mathbf{B}}$ of shape functions and their derivatives with respect to the material coordinates $\boldsymbol{X}$. The deformation gradient is written in Voigt-notation within the definition of the vector $\mathbf{f}$.

With the approximations (5.59) and (5.60) at hand, the space-discrete counterpart of the incremental mixed potential (5.46) is given by

$$\begin{aligned} \tilde{\Pi}^{*\tau h}(\underline{\mathbf{d}}^*) = & \int_{\mathcal{B}^h} \left\{ \hat{\psi}(\underline{\mathbf{B}}\, \underline{\mathbf{d}}^*) - \hat{\psi}_n^h - \underline{\mathbf{N}}_{\tilde{\mu}} \underline{\mathbf{d}}^* \cdot \underline{\mathbf{N}}_c (\underline{\mathbf{d}}^* - \underline{\mathbf{d}}_n^*) - \tau \hat{\phi}^*_{\mathrm{con}}(\underline{\mathbf{B}}\, \underline{\mathbf{d}}^*; \underline{\mathbf{B}}\, \underline{\mathbf{d}}_n^*) \right\} dV \\ & - \int_{\partial \mathcal{B}_{\boldsymbol{T}}^h} \bar{\boldsymbol{T}} \cdot \underline{\mathbf{N}}_{\boldsymbol{\varphi}} [\underline{\mathbf{d}}^* - \underline{\mathbf{d}}_n^*] \, dA - \int_{\partial \mathcal{B}_H^h} \tau \underline{\mathbf{N}}_{\tilde{\mu}} \underline{\mathbf{d}}^* \bar{H} \, dA \end{aligned} \tag{5.61}$$

where we introduced $\hat{\psi}_n^h = \hat{\psi}(\underline{\mathbf{B}}\, \underline{\mathbf{d}}_n^*)$. Then, the space-time-discrete variational saddle-point principle can be written as

$$\underline{\mathbf{d}}^* = \arg \left\{ \operatorname*{stat}_{\underline{\mathbf{d}}^*} \tilde{\Pi}^{*\tau h}(\underline{\mathbf{d}}^*) \right\} \,. \tag{5.62}$$

The necessary condition of the variational principle (5.62) is that its variation vanishes. Approximation of the variations $\{\delta \boldsymbol{\varphi}^h, \delta c^h, \delta \tilde{\mu}^h\}$ analogously to the approximation of the fields $\{\boldsymbol{\varphi}^h, c^h, \tilde{\mu}^h\}$ in (5.59) yields the necessary condition as

$$\operatorname*{stat}_{\underline{\mathbf{d}}^*} \tilde{\Pi}^{*\tau h}(\underline{\mathbf{d}}^*) \quad \rightarrow \quad \tilde{\Pi}^{*\tau h}_{,\underline{\mathbf{d}}^*} = \boldsymbol{0} \,. \tag{5.63}$$

In order to solve $(5.63)_2$ algorithmically we use an iterative Newton-Raphson scheme yielding the iterative update

$$\underline{\mathbf{d}}^{*(k+1)} = \underline{\mathbf{d}}^{*(k)} - \left[\tilde{\Pi}^{*\tau h}_{,\underline{\mathbf{d}}^* \underline{\mathbf{d}}^*}(\underline{\mathbf{d}}^{*(k)}) \right]^{-1} \left[\tilde{\Pi}^{*\tau h}_{,\underline{\mathbf{d}}^*}(\underline{\mathbf{d}}^{*(k)}) \right] \tag{5.64}$$

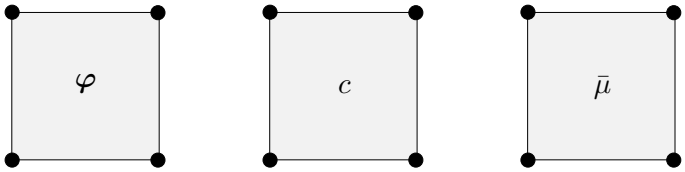

Figure 5.7: *Finite element for mixed principle in 2D.* The Q_1-Q_1-Q_1 element design for deformation $\boldsymbol{\varphi}$, species concentration c and chemical potential $\tilde{\mu}$ provides an inf-sup unstable pairing, however is widely used and yields accurate results.

that is performed until convergence $|\tilde{\Pi}^{*\tau h}_{,\underline{\mathbf{d}}^*}| < tol$ is achieved.

In order to have a compact notation we introduce the vector of *generalized stresses* and the matrix of *generalized moduli*. Based on the incremental potential (5.46) we have

$$\underline{\mathbf{S}}^* := \begin{bmatrix} \partial_{\boldsymbol{F}}\hat{\psi} \\ \partial_c\hat{\psi} - \tilde{\mu} \\ \partial_{\nabla c}\hat{\psi} \\ -(c - c_n) \\ -\tau\partial_{\tilde{\mathbb{B}}}\hat{\phi}^*_{\text{con}} \end{bmatrix} , \quad \underline{\mathbf{C}}^* := \begin{bmatrix} \partial^2_{\boldsymbol{F}\boldsymbol{F}}\hat{\psi} & \partial^2_{\boldsymbol{F}c}\hat{\psi} & \boldsymbol{0} & \boldsymbol{0} & \boldsymbol{0} \\ \partial^2_{c\boldsymbol{F}}\hat{\psi} & \partial^2_{cc}\hat{\psi} & \boldsymbol{0} & -1 & \boldsymbol{0} \\ \boldsymbol{0} & \boldsymbol{0} & \partial^2_{\nabla c\nabla c}\hat{\psi} & \boldsymbol{0} & \boldsymbol{0} \\ \boldsymbol{0} & -1 & \boldsymbol{0} & 0 & \boldsymbol{0} \\ \boldsymbol{0} & \boldsymbol{0} & \boldsymbol{0} & \boldsymbol{0} & -\tau\partial^2_{\tilde{\mathbb{B}}\tilde{\mathbb{B}}}\hat{\phi}^*_{\text{con}} \end{bmatrix} . \tag{5.65}$$

With (5.65) at hand, the necessary condition (5.63) of the space-time-discrete variational principle can be written as

$$\boldsymbol{0} = \tilde{\Pi}^{*\tau h}(\underline{\mathbf{d}}^*)_{,\underline{\mathbf{d}}^*} = \int_{\mathcal{B}^h} \underline{\mathbf{B}}^T \cdot \underline{\mathbf{S}}^* \, dV - \int_{\partial\mathcal{B}^h_{\boldsymbol{T}}} \underline{\mathbf{N}}^T_{\boldsymbol{\varphi}} \cdot \bar{\boldsymbol{T}} \, dA - \int_{\partial\mathcal{B}^h_H} \underline{\mathbf{N}}^T_{\tilde{\mu}} \cdot \tau\bar{H} \, dA \, . \tag{5.66}$$

With the generalized tangent moduli $\underline{\mathbf{C}}^*$ in (5.65) the second derivative of the potential that is needed for the iterative update (5.64) can be written compact as

$$\tilde{\Pi}^{*\tau h}_{,\underline{\mathbf{d}}^*\,\underline{\mathbf{d}}^*} = \int_{\mathcal{B}^h} \underline{\mathbf{B}}^T \underline{\mathbf{C}}^* \underline{\mathbf{B}} \, dV \, . \tag{5.67}$$

5.4.3. Finite element design for saddle-point formulation

Analogously to the mixed principle in Chapter 4, the saddle-point structure requires the interpolations to build an inf-sup stable pairing. Considering two space dimensions this can be achieved for example by using Taylor-Hood-type elements, where the deformation and concentration fields are discretized with second order Q_2 shape functions whereas the dual variable, that is the chemical potential $\tilde{\mu}$ is discretized with first order Q_1 approximation functions. However our focus here is not on stable finite element design but rather on a computationally fast and simple implementation that leads to appropriate results and shows the accuracy of the formulation. To this end, we propose an interpolation with *bilinear* and *trilinear* ansatz functions for all three fields and denote this element design as Q_1-Q_1-Q_1. Although not inf-sup stable this element type is widely used in the literature and is shown to be an adequate choice. The interpolations (5.52) of the fields

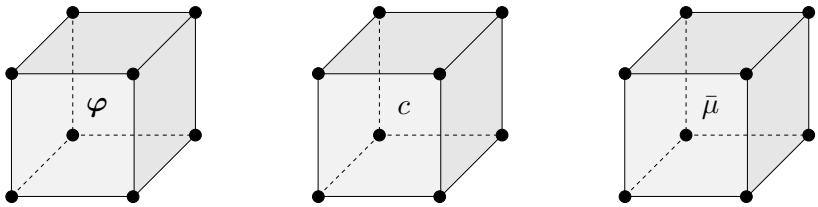

Figure 5.8: *Finite element for mixed principle in 3D.* The Q_1-Q_1-Q_1 element design for deformation $\boldsymbol{\varphi}$, species concentration c and chemical potential $\tilde{\mu}$ provides an inf-sup unstable pairing, however is widely used and yields accurate results.

within an element e are hence given by

$$\boldsymbol{\varphi}^e(\boldsymbol{\xi}) = \sum_{i=1}^{n^e} \hat{N}^i_{Q_1}(\boldsymbol{\xi})\boldsymbol{\varphi}^i \ , \quad c^e(\boldsymbol{\xi}) = \sum_{i=1}^{n^e} \hat{N}^i_{Q_1}(\boldsymbol{\xi})c^i \quad \text{and} \quad \tilde{\mu}^e(\boldsymbol{\xi}) = \sum_{i=1}^{n^e} \hat{N}^i_{Q_1}(\boldsymbol{\xi})\tilde{\mu}^i \ . \tag{5.68}$$

In the two-dimensional case this is a four-noded quadrilateral $\mathcal{A} = [-1,1] \times [-1,1]$ with $n^e = 4$ and with the bilinear shape functions introduced in (4.82) and given by

$$\begin{aligned} \hat{N}^1_{Q_1} &= \tfrac{1}{4}(1-\xi_1)(1-\xi_2) \ , & \hat{N}^2_{Q_1} &= \tfrac{1}{4}(1+\xi_1)(1-\xi_2) \ , \\ \hat{N}^3_{Q_1} &= \tfrac{1}{4}(1+\xi_1)(1+\xi_2) \ , & \hat{N}^4_{Q_1} &= \tfrac{1}{4}(1-\xi_1)(1+\xi_2) \ , \end{aligned} \tag{5.69}$$

see Figure 5.7. For the case of three space dimensions this a eight-noded brick element $\mathcal{A} = [-1,1] \times [-1,1] \times [-1,1]$ with $n^e = 8$, see Figure 5.8, and with the trilinear shape functions given by

$$\begin{aligned} \hat{N}^1_{Q_1} &= \tfrac{1}{8}(1-\xi_1)(1-\xi_2)(1-\xi_3) \ , & \hat{N}^2_{Q_1} &= \tfrac{1}{8}(1+\xi_1)(1-\xi_2)(1-\xi_3) \ , \\ \hat{N}^3_{Q_1} &= \tfrac{1}{8}(1+\xi_1)(1+\xi_2)(1-\xi_3) \ , & \hat{N}^4_{Q_1} &= \tfrac{1}{8}(1-\xi_1)(1+\xi_2)(1-\xi_3) \ , \\ \hat{N}^5_{Q_1} &= \tfrac{1}{8}(1-\xi_1)(1-\xi_2)(1+\xi_3) \ , & \hat{N}^6_{Q_1} &= \tfrac{1}{8}(1+\xi_1)(1-\xi_2)(1+\xi_3) \ , \\ \hat{N}^7_{Q_1} &= \tfrac{1}{8}(1+\xi_1)(1+\xi_2)(1+\xi_3) \ , & \hat{N}^8_{Q_1} &= \tfrac{1}{8}(1-\xi_1)(1+\xi_2)(1+\xi_3) \ . \end{aligned} \tag{5.70}$$

5.4.4. Reduction to diffusion without phase segregation

For the case when phase segregation is excluded the interface contribution $\hat{\psi}_{\text{int}}$ of the free energy vanishes and the constitutive definition of the potential $(5.51)_2$ reduces to

$$-\tilde{\mu} + \partial_c \hat{\psi} = 0 - \text{Div}[\partial_{\nabla c}\hat{\psi}] = 0 \quad \Rightarrow \quad -\tilde{\mu} + \partial_c \hat{\psi} = 0 \ . \tag{5.71}$$

The partial differential equation $(5.71)_1$ for the definition of the chemical potential reduces to an *ordinary differential equation* that does not require the prescription of boundary values for the concentration c. The admissible space for the species concentration in the incremental setting reduces to

$$\mathcal{W}_c := \{c \in L^2\} \ , \tag{5.72}$$

see (5.50). Thus, according to the considerations in Subsection 4.4.4 for the model problem of poro-elasticity, it is sufficient to interpolate c peacewise linear within a finite element $\mathcal{B}^e$ and without continuity over element boundaries. For the finite element method this

means that the Euler equation $(5.51)_2$ is solved locally at the Gauss quadrature points and the concentration field c takes the role of an *internal variable*. The global unknowns then reduce to $\boldsymbol{\varphi}$ and $\tilde{\mu}$. The vector of discrete unknown values of the space-discrete variational principle (5.58) reduces to

$$\underline{\mathbf{d}}^*_{\text{red}} = \left[\underline{\mathbf{d}}_{\boldsymbol{\varphi}} \, , \, \underline{\mathbf{d}}_{\tilde{\mu}} \right]^T \, . \tag{5.73}$$

The vector of constitutive state also reduces by the concentration c and its gradient to

$$\mathbf{f}^*_{\text{red}}(\boldsymbol{X}) \approx \mathbf{f}^{*h}_{\text{red}}(\boldsymbol{X}) = \begin{bmatrix} \underline{\mathbf{B}}_{\boldsymbol{F}} \, \underline{\mathbf{d}}_{\boldsymbol{\varphi}} \\ \underline{\mathbf{N}}_{\tilde{\mu}} \, \underline{\mathbf{d}}_{\tilde{\mu}} \\ -\underline{\mathbf{B}}_{\nabla \tilde{\mu}} \, \underline{\mathbf{d}}_{\tilde{\mu}} \end{bmatrix} =: \underline{\mathbf{B}}_{\text{red}} \, \underline{\mathbf{d}}^*_{\text{red}} \, . \tag{5.74}$$

Accordingly, we introduce the reduced generalized stress vector

$$\underline{\mathbf{S}}^*_{\text{red}} := \begin{bmatrix} \partial_{\boldsymbol{F}} \hat{\psi} \\ -(c - c_n) \\ -\tau \partial_{\tilde{\mathbb{B}}} \hat{\phi}^*_{\text{con}} \end{bmatrix} \, , \tag{5.75}$$

where the concentration field c is obtained by evaluating the ordinary differential equation $(5.71)_2$ locally at each Gauss quadrature point. Note that the reduced constitutive state vector in (5.74) and the reduced generalized stresses in (5.75) only reduces its dimension as the concentration field c is not globally discretized any more. In contrast the generalized moduli $\underline{\mathbf{C}}^*$ does not only reduce its dimension however the sensitivity of the concentration field c with respect to a change of the global fields $\boldsymbol{\varphi}$ and $\tilde{\mu}$ has to be taken into account. Analogously to the considerations in Subsection 4.4.4 we get

$$\underline{\mathbf{C}}^*_{\text{red}} := \begin{bmatrix} \partial^2_{\boldsymbol{F}\boldsymbol{F}} \hat{\psi} - \partial^2_{\boldsymbol{F}c} \hat{\psi} \left[\partial^2_{cc} \hat{\psi} \right]^{-1} \partial^2_{c\boldsymbol{F}} \hat{\psi} & \partial^2_{\boldsymbol{F}c} \hat{\psi} \left[\partial^2_{cc} \hat{\psi} \right]^{-1} & \boldsymbol{0} \\ \left[\partial^2_{cc} \hat{\psi} \right]^{-1} \partial^2_{c\boldsymbol{F}} \hat{\psi} & - \left[\partial^2_{cc} \hat{\psi} \right]^{-1} & \boldsymbol{0} \\ \boldsymbol{0} & \boldsymbol{0} & -\tau \partial^2_{\tilde{\mathbb{B}}\tilde{\mathbb{B}}} \hat{\phi}^*_{\text{con}} \end{bmatrix} \, . \tag{5.76}$$

With (5.75) at hand, the necessary condition (5.66) of the space-time-discrete variational principle as a function of the reduced set of unknown $\underline{\boldsymbol{d}}_{\text{red}}$ can be obtained as

$$\boldsymbol{0} = \tilde{\Pi}^{*\tau h}(\underline{\mathbf{d}}^*_{\text{red}}), _{\underline{\mathbf{d}}^*_{\text{red}}} = \int_{\mathcal{B}^h} \underline{\mathbf{B}}^T_{\text{red}} \cdot \underline{\mathbf{S}}^*_{\text{red}} \, dV - \int_{\partial \mathcal{B}^h_{\boldsymbol{T}}} \underline{\mathbf{N}}^T_{\boldsymbol{\varphi}} \cdot \bar{\boldsymbol{T}} \, dA - \int_{\partial \mathcal{B}^h_H} \underline{\mathbf{N}}^T_{\tilde{\mu}} \cdot \tau \bar{H} \, dA \tag{5.77}$$

and the second derivative of the mixed potential is given in terms of the reduced generalized tangent in (5.76) as

$$\tilde{\Pi}^{*\tau h}_{, \underline{\mathbf{d}}^*_{\text{red}} \underline{\mathbf{d}}^*_{\text{red}}} = \int_{\mathcal{B}^h} \underline{\mathbf{B}}^T_{\text{red}} \underline{\mathbf{C}}^*_{\text{red}} \underline{\mathbf{B}}_{\text{red}} \, dV \, . \tag{5.78}$$

5.5. Representative boundary value problems

In the following we demonstrate the modeling capabilities of the proposed variational approach for coupled chemo-mechanical material behavior. Here the purpose is to capture

Table 5.1: Material parameters used for numerical simulations.

no.	par.	name	unit	value
1.	γ	shear modulus	[N/m^2]	3.0
2.	ν	Poisson's ratio	[-]	0.3
3.	Ω	swelling parameter	[-]	1.0–10.0
4.	A	chemical energy parameter	[N/m^2]	10.0
5.	B	mixing energy parameter	[N/m^2]	0.0/25.0
6.	C	gradient parameter	[N]	0.0/0.001
7.	M	diffusion parameter	[m^4/Ns]	0.001–100.0
8.	c_0	initial concentration	[-]	0.5

the basic coupling effects rather than a quantitative fitting to experimental data. The first two boundary value problems concentrate on diffusion processes in elastic solids without phase segregation whereas the last simulation is concerned with phase segregation in the Cahn-Hilliard-type gradient-extended diffusion setting. The material parameters used in the subsequent boundary value problems are given in Table 5.1.

5.5.1. Diffusion induced free swelling

The first boundary value problem demonstrates the coupling effect of swelling of a solid caused by species diffusion. To this end, consider a cuboid $\mathcal{B} = \left\{ \boldsymbol{X} \in \mathcal{R}^3 \,\middle|\, \boldsymbol{X} \in [0, L] \times [0, L] \times [0, L] \right\}$ with $L = 100$ m at the surfaces of which a chemical potential $\bar{\mu}$ is applied. This induces a species diffusion process from the surfaces into the body. The applied chemical potential is first linearly increased until $t_1 = 1000.0$ s to $\bar{\mu}_1 = 100.0$ kgN/m^5 and then held constant. The geometry and boundary conditions are visualized in Figure 5.9. In this boundary value problem phase segregation is excluded and thus we choose the gradient parameter $C = 0$ N as well as the mixing energy parameter $B = 0$ N/m^2. In order to obtain large deformations the swelling parameter is chosen to $\Omega = 10.0$. Due to symmetry only one fourth of the domain $\mathcal{B}$ is discretized by $10 \times 10 \times 10$ Q_1-Q_1 finite elements. A time step of $\tau = 1.0$ s is used up to $t_1 = 1000.0$ s and for $t > t_1$ the time step size is sequentially increased up to $t_\infty = 10^6$ s.

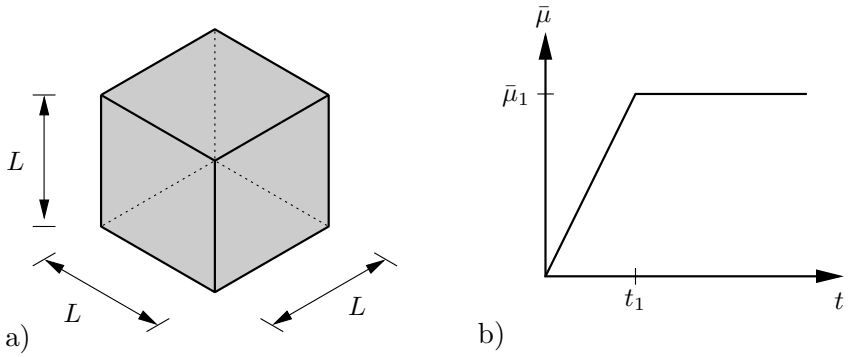

Figure 5.9: *Diffusion induced free swelling. Boundary value problem*: Cuboid with side lengths $L = 100$ m is loaded by a chemical potential $\bar{\mu}$ at all surfaces. b) Applied chemical potential $\bar{\mu}$ is increased linearly up to $\bar{\mu}_1 = 100.0$ kgN/m^5 at time $t_1 = 1000.0$ s. Then the chemical potential is held constant.

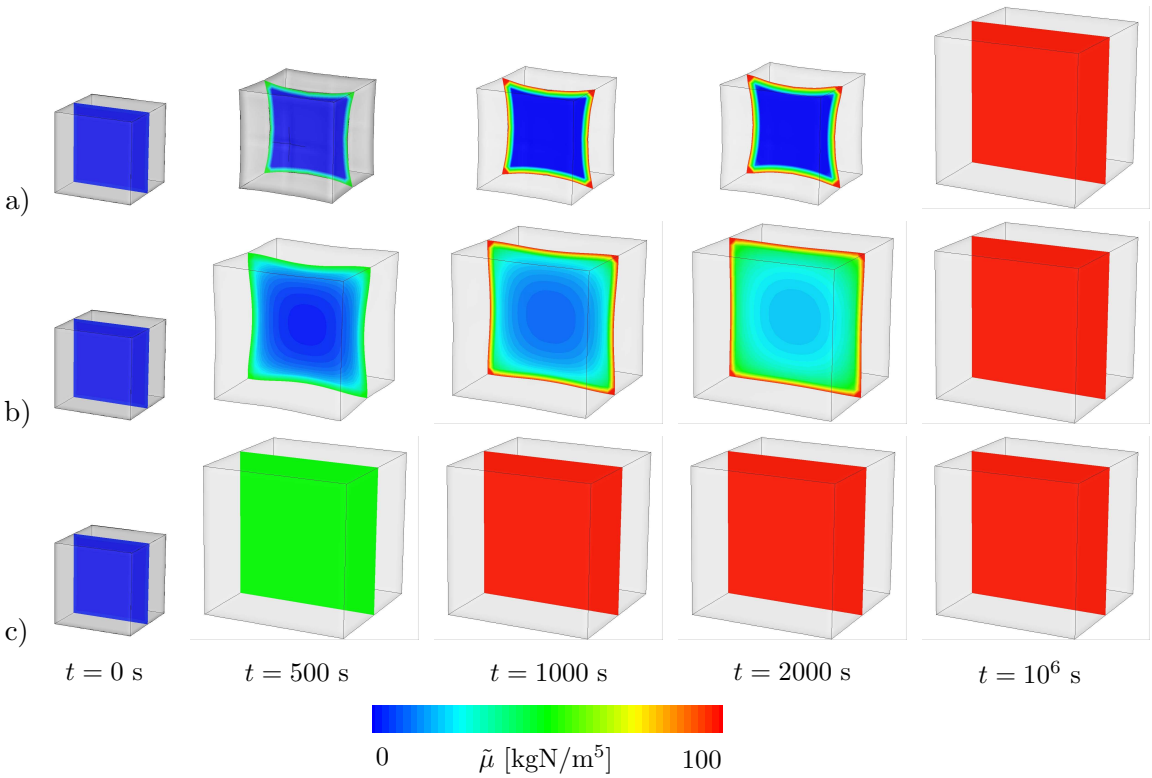

Figure 5.10: *Diffusion induced free swelling. Results*: Chemical potential $\tilde{\mu}$ on deformed configuration at different times $t = [0, 500, 1000, 2000, 10^6]$ s and for different diffusion parameters a) $M = 0.001$ m^4/Ns, b) $M = 0.1$ m^4/Ns and c) $M = 100.0$ m^4/Ns.

We study the influence of the mobility of species flow on the mechanical swelling by varying the diffusion parameter M. Figure 5.10 depicts the evolving chemical potential $\tilde{\mu}$ in a vertical slice through the deformed cuboid for three different diffusion parameters M and at different times t. For the smallest parameter $M = 0.001$ m^4/Ns in Figure 5.10a) the induced species diffusion is a slow process yielding an inhomogeneous distribution of potential $\tilde{\mu}$ and hence an inhomogeneous deformation. In contrast if the diffusion process is fast compared to the time of loading the distribution of the chemical potential as well as the deformation state is homogeneous in the whole cuboid, see Figure 5.10c) for a high

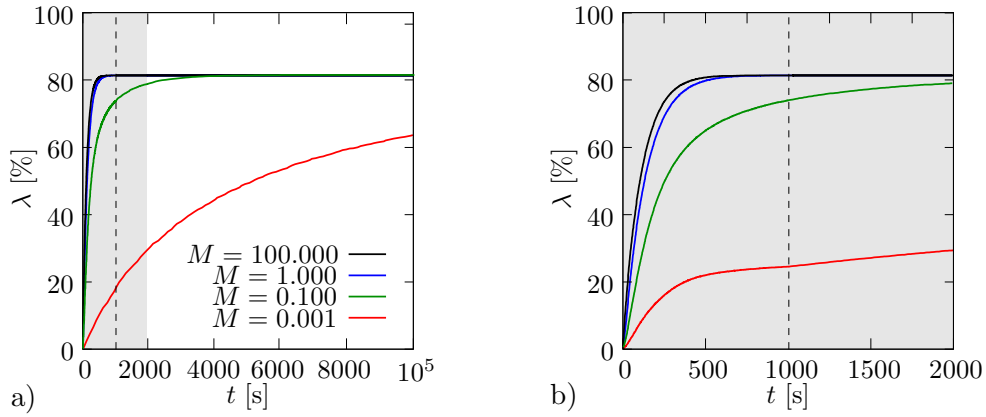

Figure 5.11: *Diffusion induced free swelling. Results*: Stretch $\lambda = u_x/0.5L$ of the right top corner of the cuboid over time t for different diffusion parameters M. The dashed line depicts the time t_1 from where on the applied chemical potential is held constant at $\partial\mathcal{B}$.

mobility of $M = 100$ m^4/Ns. The inhomogeneity can also be observed in Figure 5.11 where the stretch $\lambda = u_x/0.5L$ of the right top corner of the cuboid is plotted against the time t. For small parameters M the deformation increases even after the applied potential $\tilde{\mu}$ is held constant at $t_1 = 1000$ s which is depicted with the dashed line in the diagrams. This is due to the diffusion process where species flows into the body until a homogeneous state $\tilde{\mu} = \bar{\mu}$ in $\mathcal{B}$ is reached. For small parameters M this state is not reached at time t_1 and hence produces a further swelling for $t > t_1$. For the high parameter $M = 100$ m^4/Ns a homogeneous response can be observed within the whole process time $t = [t_1, t_\infty]$, see Figure 5.10c) and thus no further deformation is observed for $t > t_1$. Given enough time the final equilibrium state is the same no matter what diffusion parameter is chosen.

5.5.2. Mechanically induced diffusion process

Now the vice versa coupling effect of diffusion induced by a prescribed mechanical deformation is observed. Consider a rigid plate lying on a body $\mathcal{B} = \left\{ \boldsymbol{X} \in \mathcal{R}^3 \,\middle|\, \boldsymbol{X} \in [0, 5L] \times [0, 5L] \times [0, 2L] \right\}$ with $L = 0.1$ m. The body is mechanically clamped at its bottom surface. All surfaces are assumed to be impermeable such that no species flux outside the body can occur and hence the species volume in the body remains constant. The rigid plate is uniformly pushed into the body with a prescribed velocity of $\dot{\bar{u}} = 0.01$ m/s. The geometry and boundary conditions are visualized in Figure 5.12. In this boundary value problem no phase segregation is assumed and the material parameters are chosen to be $C = 0$ N and $B = 0$ N/m^2. In order to obtain a strong interaction between chemical and mechanical effects we assume $\Omega = 10.0$. For the numerical simulation the body $\mathcal{B}$ is discretized by use of $25 \times 25 \times 10$ Q_1-Q_1 finite elements and the time step is chosen to $\tau = 0.01$ s.

Figure 5.13 shows the chemo-mechanical coupling response at three different times. The spatial distribution of the species concentration c is plotted on the deformed configuration. The concentration decreases under the rigid plate due to the mechanical indentation and flows to the corners of the specimen. Due to the impermeable boundaries the species volume is constant in the domain and the concentration increases steadily in the corners, which in term induces a mechanical swelling. The chemical potential $\tilde{\mu}$ at the same instances of time is plotted in Figure 5.14. The potential $\tilde{\mu}$ increases in the whole body, that is both under the rigid plate as well as in the corners of the specimen. Here the higher values of $\tilde{\mu}$ are observed under the plate. Thus note that the chemical potential

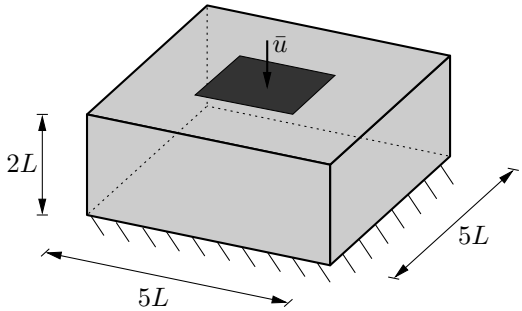

Figure 5.12: *Mechanically induced diffusion process. Boundary value problem*: A cuboid with side lengths $5L = 5$ m and height $2L = 2$ m is clamped at the bottom and a rigid plate located in the middle of the top surface is pushed into the body with constant velocity $\dot{\bar{u}} = 0.01$ m/s.

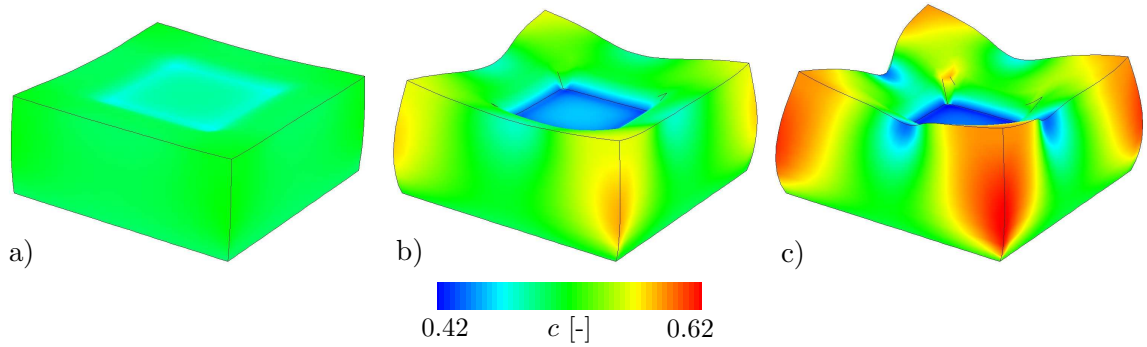

Figure 5.13: *Mechanically induced diffusion process. Results*: Species concentration c plotted on deformed configuration at a) $t = 1.5$ s, b) $t = 5.5$ s and c) $t = 8.0$ s.

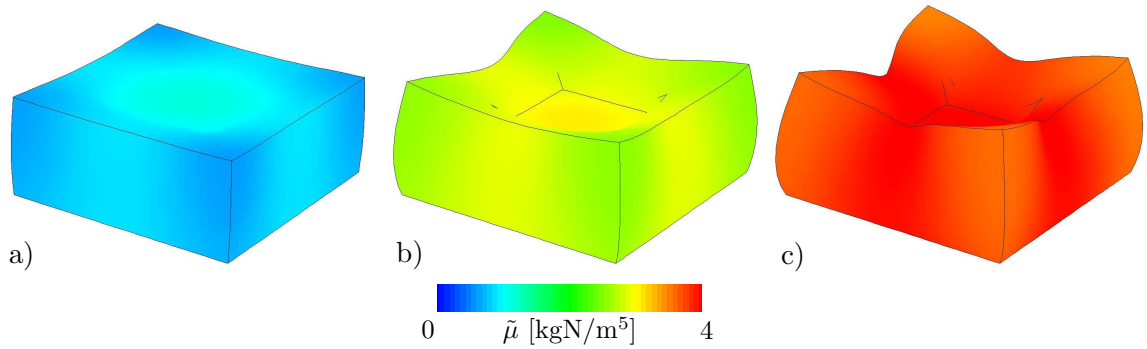

Figure 5.14: *Mechanically induced diffusion process. Results*: Chemical potential $\tilde{\mu}$ plotted on deformed configuration at a) $t = 1.5$ s, b) $t = 5.5$ s and c) $t = 8.0$ s.

not only increases in areas where the species concentration increases, $c > c_0$, but also in areas with $c < c_0$. This is due to the chemo-mechanical coupling of the potential $\tilde{\mu}$ to the mechanical pressure p, see (5.27). A positive pressure p leads to an increasing potential $\tilde{\mu}$ and the high swelling parameter $\Omega = 10.0$ results in high interaction.

5.5.3. Cahn-Hilliard diffusion in two and three dimensions

In the last boundary value problem the modeling capability of the gradient-extended Cahn-Hilliard theory is explored in two and three space dimensions. To this end, consider a domain $\mathcal{B}$ with side lengths $L = 1.0$ m. Mechanically the domain is fixed statically determined. Furthermore, for the two dimensional boundary value problem, periodic boundary conditions are assumed on opposite boundary edges, that is $\bar{\boldsymbol{\varphi}}(\partial\mathcal{B}_i^+) = \bar{\boldsymbol{\varphi}}(\partial\mathcal{B}_i^-)$ for $i = 1, 2$. The concentration and chemical potential, c and $\tilde{\mu}$, are also supposed to be periodic in the two-dimensional setting. The geometric setup for both two and three space dimensions is visualized in Figure 5.15. The material parameters that are not specified in Table 5.1 are chosen to be $B = 25.0$ N/m^2, $C = 0.001$ N and $\Omega = 1.0$. For the chosen set of parameters $A = 10.0$ and $B = 25.0$ we detect a bulk phase network of phases $c = 0.145$ and $c = 0.855$, see Figure 5.2a). That is for $\bar{c} \in (0.145, 0.855)$ we expect the formation and the consequent coarsening of precipitates. We choose random initial conditions for the species concentration, that is for each global node I we have

$$c_0^I = r^I \quad \text{with} \quad r^I \in (0, 1) \,, \tag{5.79}$$

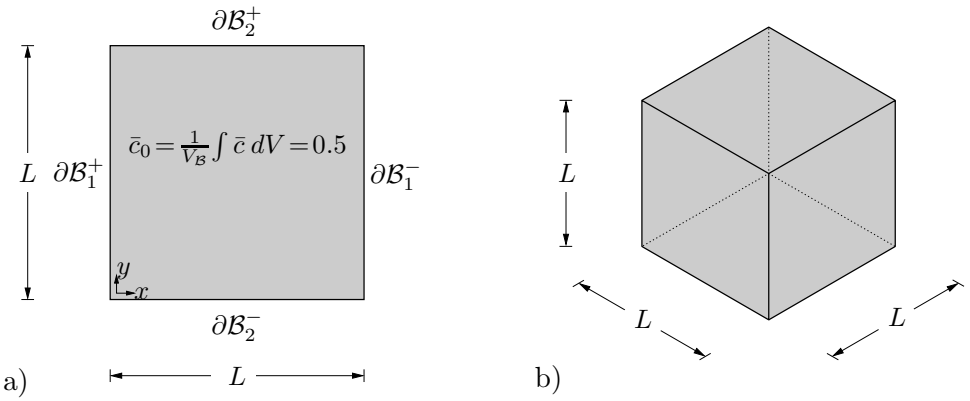

Figure 5.15: *Cahn-Hilliard diffusion in two and three dimensions. Boundary value problem*: Body $\mathcal{B}$ with impermeable boundaries and random initial values $c_0 \in (0, 1)$ of species concentration at each nodal point with average $\bar{c}_0 = 0.5$. Periodic boundary conditions are assumed for opposite surfaces $\partial\mathcal{B}_i^\pm$ for $i = 1, ..., d$ with space dimension d. a) Two-dimensional setup and b) three-dimensional setup.

where r^I are random numbers between 0 and 1. The random numbers are chosen such that the resulting average concentration in the domain $\mathcal{B}$ is $\bar{c}_0 = 0.5$.

As first consider the two-dimensional case. The square domain $\mathcal{B}$ is for the numerical simulation discretized by 50×50 Q_1-Q_1-Q_1 quadrilateral elements and a time step of $\tau = 0.1$ s is applied. The results for this simulation are shown in Figure 5.16, where the species concentration c is plotted for different time steps. The initial setup of the random species concentration c_0 can be seen in Figure 5.16a). Then the initial random distribution evolves to an equal mixture of two strongly interwoven bulk phase networks of phases $c = 0.145$ and $c = 0.855$. Subsequently, this microstructure evolves to a coarser and coarser structure. Due to the chemo-mechanical coupling the volume decreases in the regions with $c = 0.145$ and increases in regions with $c = 0.855$.

For the three-dimensional setup given in Figure 5.15b) the cuboid $\mathcal{B}$ is discretized by $50 \times 50 \times 50$ Q_1-Q_1-Q_1 brick elements and the numerical time step is again chosen to $\tau = 0.1$ s. The species concentration c in the domain $\mathcal{B}$ is shown in Figure 5.17 at different time steps of the numerical simulation. As in the two-dimensional setting above the initial random distribution, see Figure 5.17a), evolves to an equal mixture of two strongly interwoven bulk phase networks of phases $c = 0.145$ and $c = 0.855$. Again this microstructure evolves to a coarser and coarser structure and the chemo-mechanical coupling leads to decreasing volume in regions with $c = 0.145$ and increasing volume in regions with $c = 0.855$.

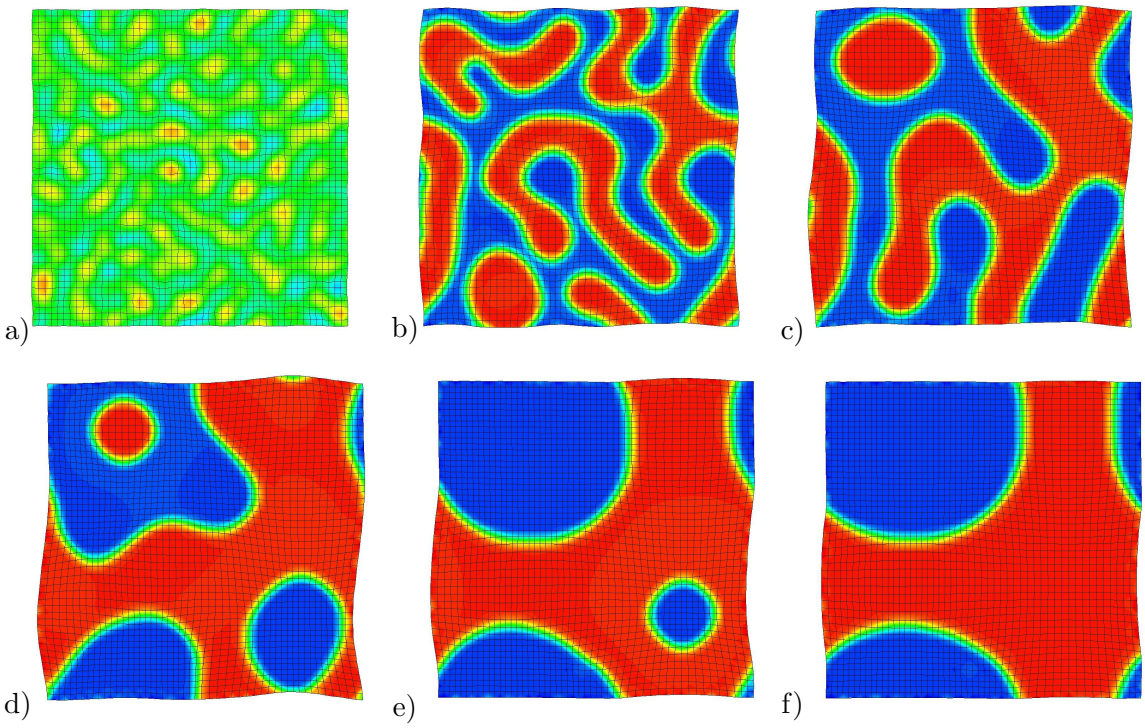

Figure 5.16: *Cahn-Hilliard diffusion in two and three dimensions. 2D Results*: Species concentration c (blue $\rightarrow$ 0.145, red $\rightarrow$ 0.855) in $\mathcal{B}$ starting from random initial conditions with $\bar{c}_0 = 0.5$ at different time steps a) $t = 0$ s, b) $t = 1$ s, c) $t = 11$ s, d) $t = 250$ s, e) $t = 720$ s and f) $t = 1580$ s.

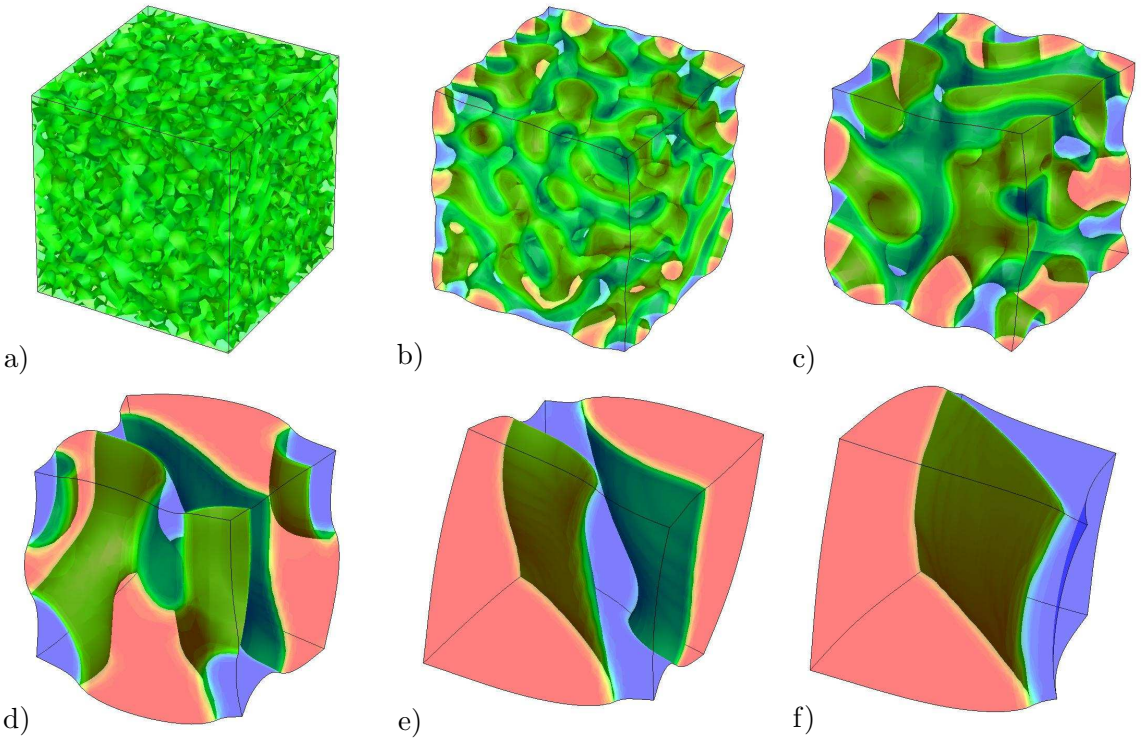

Figure 5.17: *Cahn-Hilliard diffusion in two and three dimensions. 3D Results*: Species concentration c (blue $\rightarrow$ 0.145, red $\rightarrow$ 0.855) in $\mathcal{B}$ starting from random initial conditions with $\bar{c}_0 = 0.5$ at different time steps a) $t = 0$ s, b) $t = 1$ s, c) $t = 10$ s, d) $t = 70$ s, e) $t = 300$ s and f) $t = 1680$ s.

— Part II —

Phase-Field Modeling of Poro-Hydro-Elasticity at Fracture

Chapter 6

Fundamentals of Phase-Field Modeling of Fracture

The aim of this Chapter is to give a short introduction into fracture mechanics of solids as well as to the idea of phase-field modeling of fracture. It has an introductory character to fracture mechanics and has by no means the intention to be complete. In particular only these quantities are introduced that are required for the model in Chapter 8. The more interested reader is referred to the classical textbooks of Freund [108], Knott [150], Kanninen & Popelar [147], Meguid [170], Lawn [160], Anderson [7], Gross & Seelig [122] and Lemaitre & Chaboche [163]. Among different possibilities, we follow the work Miehe et al. [183] where the phase-field fracture is motivated as regularization of a sharp crack profile. This provides an intuitive approach with a clear geometrical character.

6.1. Fundamentals of fracture mechanics

Fracture mechanics describes the macroscopic propagation of cracks up to total failure of the structure. Here a crack is defined as a cut through a body $\mathcal{B}$ where two *crack surfaces* occurs. The crack surfaces meet in the *crack front*. In a two-dimensional context the crack surfaces and crack front are referred to as *crack lips* and *crack tip*. In classical fracture mechanics three different *crack opening modes* are distinguished according to the load direction in relation to the direction of the crack lip, see Figure 6.1. The symmetric,

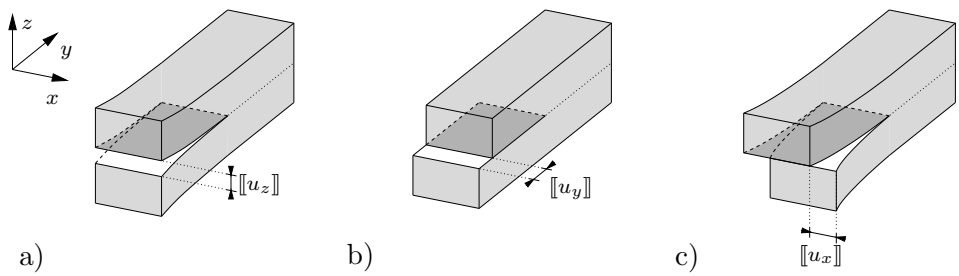

Figure 6.1: *Crack opening modes.* The modes are defined by load direction in relation to crack lip direction. a) Mode I crack with displacement discontinuity $[\![u_z]\!]$, b) mode II crack with discontinuity $[\![u_y]\!]$ and c) mode III crack with discontinuity $[\![u_x]\!]$.

pure opening crack mode is denoted as *mode I*. It is characterized by a displacement discontinuity in z direction and symmetry with respect to the x-y plane. The *mode II* crack is referred to as plane shear mode or sliding mode. The displacement discontinuity occurs perpendicular to the crack lip in y direction. The anti-plane shear mode or also tearing mode is designated *mode III*. In this mode the discontinuity of the displacement appears tangential to the crack lip in x direction. Note that not every physical crack can be assigned to one of these modes but can be described as a superposition of all three.

6.1.1. Stress intensity factors

One approach for stating a crack propagation criterion is the *concept of stress intensity factors* that was proposed by Irwin [142, 143] for isotropic linear elastic materials under static loading condition. The concept is based on a representation of the stress in the crack tip in terms of a polar coordinate system (r, θ, s) with its origin at the crack tip, that is

$$\boldsymbol{\sigma}(r,\theta,s) = \frac{1}{\sqrt{2\pi r}}\left[K_I \boldsymbol{f}_I + K_{II}\boldsymbol{f}_{II} + K_{III}\boldsymbol{f}_{III}\right] . \tag{6.1}$$

Here $\boldsymbol{f}_i$ are dimensionless functions depending on θ and K_i are the stress intensity factors. The intensity factors K_i are related to the three crack modes and determine the intensity of the stress. Thus K_i can be considered as a measure of the loading in the vicinity of the crack lip. They are dependent on the geometry of the body and the crack, the loading as well as the boundary conditions. The concept of stress intensity factor states

$$K_i = K_{ic} \tag{6.2}$$

for $i = 1, 2, 3$ and where K_{ic} is denoted as fracture toughness and characterizes the resistance of a material against a mode i crack propagation. In the most general case where all three crack modes are considered, a condition can be stated as

$$B(K_I, K_{II}, K_{III}) = B_c . \tag{6.3}$$

6.1.2. Griffith approach to energetic fracture

Another approach for a crack propagation criterion goes back to Griffith [120] and is based on an energetic viewpoint. Griffith [120] found out that failure occurs whenever a critical value of energy release rate is reached. This *critical energy release rate* g_c is a material parameter dependent only on the material under consideration. In particular it is independent of the geometry, the loading and the boundary conditions. g_c can be considered as the "energy needed for formation of the two crack surfaces". The criterion for crack propagation can then be stated as

$$g = g_c . \tag{6.4}$$

In order to provide a physical insight into this approach and to emphasize the energetic viewpoint we investigate a brittle crack mechanism of an elastic body. This consideration is in line with the works Gross & Seelig [122] or Kuna [158]. Recall the energy conservation law introduced in (2.36)

$$\frac{d}{dt}\left[\mathcal{K} + \mathcal{E} + \mathcal{D}\right] = \mathcal{P} + \mathcal{Q} . \tag{6.5}$$

Note that the energy balance is enhanced by $\dot{\mathcal{D}}$ describing the energy that dissipates during crack propagation. It represents the energy needed for formation of the two crack surfaces. Thus we write

$$\mathcal{D} = 2\gamma A \ , \tag{6.6}$$

where γ is a material constant and A is the surface of the crack. For quasi-static, isothermal processes and by introduction of the total potential defined via its rate as $\dot{\Pi} := \dot{\mathcal{E}} - \mathcal{P}$, equation (6.5) can be rewritten as

$$-\dot{\Pi} = \dot{\mathcal{D}} \quad \Rightarrow \quad -\Pi = \mathcal{D} \ . \tag{6.7}$$

Now consider the difference in total energy at two instances in time, t_1 and t_2 with crack surfaces A_1 and A_2. Evaluation of (6.7) with (6.6) yields

$$2\gamma = -\frac{\Pi_2 - \Pi_1}{A_2 - A_1} = -\frac{\Delta\Pi}{\Delta A} \ . \tag{6.8}$$

The right-hand side of equation (6.8) is denoted as the *energy release rate*. It is the energy that is available for crack propagation. Considering an infinitesimal crack evolution process we may conclude

$$g := -\frac{d\Pi}{dA} \ . \tag{6.9}$$

The left-hand side of equation (6.8) describes the energy that is needed for the creation of two new crack surfaces $2\,dA$ and is denoted as the *critical energy release rate* g_c. It is a material parameter and according to (6.8) given by

$$g_c := 2\gamma \ . \tag{6.10}$$

6.2. Phase-field modeling of fracture

In the following Section the phase-field modeling approach to fracture is introduced based on a regularization of a sharp crack profile in the one-dimensional setting. This provides an intuitive motivation for the approach and is in analogy to Miehe et al. [183].

6.2.1. One-dimensional motivation for phase-field regularization

Consider a one-dimensional bar of infinite length $\mathcal{B} \in [-\infty, \infty]$ with a sharp crack at $x = 0$. In order to describe this scenario we introduce a time-dependent crack phase-field

$$d : \begin{cases} \mathcal{B} \times \mathcal{T} \to [0,1] \\ (\boldsymbol{X}, t) \mapsto d(\boldsymbol{X}, t) \end{cases} \tag{6.11}$$

that indicates for $d = 0$ an unbroken material state and for $d = 1$ a broken material state. For the considered sharp crack we have $d = 1$ at $x = 0$ and $d = 0$ everywhere else but $x = 0$, see Figure 6.2a) for a visualization. This discontinuous scenario is regularized by the exponential function $d(x) = \exp[-|x|/l]$. Here l is a regularization parameter controlling the approximation and yielding for $l \to 0$ the sharp crack profile. Geometrically the exponential ansatz smears out the crack phase-field $d(x)$ over a certain length of the bar. This can be seen as a regularization or a diffusive crack topology and is visualized in

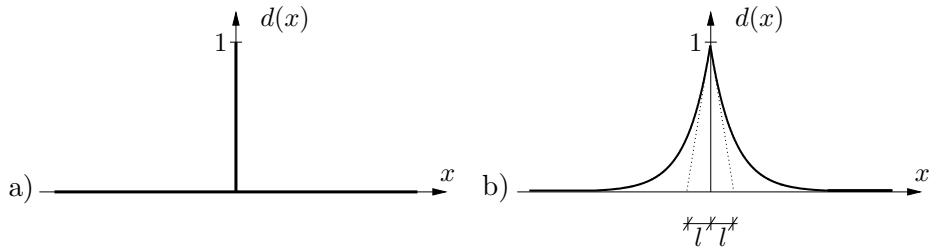

Figure 6.2: *One-dimensional regularization of sharp crack.* a) Sharp crack at $x = 0$ yields a discontinuous phase-field. b) Diffusive crack at $x = 0$ regularized by the exponential function $d(x) = \exp[-|x|/l]$ satisfying $d(0) = 1$ as proposed by Miehe et al. [183].

Figure 6.2b). This exponential function can be obtained as solution of the homogeneous differential equation

$$d(x) - l^2 d''(x) = 0 \quad \text{in } \mathcal{B} \tag{6.12}$$

subject to the boundary conditions $d(0) = 1$ and $d(\pm\infty) = 0$. Miehe et al. [183] showed that the differential equation (6.12) is obtained as Euler equation of the variational principle

$$d = \arg\left\{ \inf_{d \in \mathcal{W}_d} \Gamma_l(d) \right\} \quad \text{with} \quad \Gamma_l(d) := \int_{\mathcal{B}} \frac{1}{2l} \left[d^2 + l^2 (d')^2 \right] dV \tag{6.13}$$

and where the boundary conditions are fulfilled by the admissible space $\mathcal{W}_d = \{d(x) \,|\, d(0) = 1 \vee d(\pm\infty) = 0\}$. In (6.13) the functional Γ_l can be geometrically motivated as the regularized crack surface.

6.2.2. Regularized crack topology for isotropic solids

Motivated by this one-dimensional consideration of diffusive crack topology we extend the functional (6.13) to the multidimensional setting. Assuming isotropic material response we have

$$\Gamma_l(d) := \int_{\mathcal{B}} \frac{1}{2l} \left[d^2 + l^2 |\nabla d|^2 \right] dV = \int_{\mathcal{B}} \gamma_l(d, \nabla d)\, dV \ , \tag{6.14}$$

where we introduced the crack surface density function γ_l in terms of the phase-field d and its spatial gradient ∇d.

Now consider a sharp crack $\Gamma(t) \subset \mathcal{R}^{\delta-1}$ inside the material body $\mathcal{B} \subset \mathcal{R}^{\delta}$ of dimension δ. Its regularization, the diffusive crack phase-field $d(\boldsymbol{X}, t)$, can in analogy to (6.13) be obtained from the variational minimization principle

$$d(\boldsymbol{X}, t) = \arg\left\{ \inf_{d \in \mathcal{W}_d(t)} \Gamma_l(d) \right\} \tag{6.15}$$

with the admissible space $\mathcal{W}_d(t) = \{d \,|\, d = 1 \text{ on } \Gamma(t)\}$ fulfilling the Dirichlet boundary conditions $d = 1$ at $\boldsymbol{X} \in \Gamma(t)$. The Euler equations of the principle (6.15) are the multidimensional counterpart of (6.12) and evaluated as

$$d - l^2 \Delta d = 0 \quad \text{in } \mathcal{B} \quad \text{and} \quad \nabla d \cdot \boldsymbol{N} = 0 \quad \text{on } \partial\mathcal{B} \ , \tag{6.16}$$

where $\boldsymbol{N}$ is the outward normal on the boundary $\partial\mathcal{B}$. The equation $(6.16)_2$ provide Neumann-type boundary conditions for the crack phase-field. For vanishing length scale

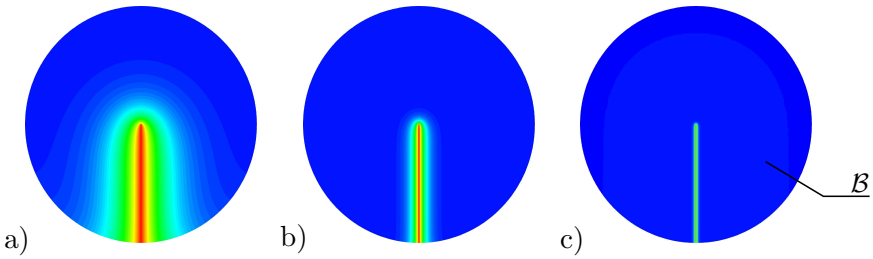

Figure 6.3: *Regularized crack phase-field for different length scales.* Solutions of (6.15) for a circular specimen with a prescribed sharp crack Γ. For $l \to 0$ the diffusive phase-field approaches to the sharp crack topology as visualized by the sequence.

parameter $l \to 0$ the sharp crack topology is recaptured, that is

$$\lim_{l \to 0} \left\{ \inf_{d \in \mathcal{W}_d(t)} \Gamma_l(d) \right\} = \Gamma(t) \ . \tag{6.17}$$

Numerical solutions of the minimization problem of regularized crack topology (6.15) for two dimensions and for different length scale parameters l are shown in Figure 6.3.

Chapter 7

Fundamentals of Fluid Mechanics in Cracks

A crack in an hydraulic fracturing scenario is not an "empty space" but filled with fluid. In such a scenario the fluid motion inside the crack does clearly not follow the flow law of Darcy but the Stokes or Navier-Stokes equation has to be used to describe the fluid motion in a crack. Among others, Witherspoon et al. [272] showed that using the Poiseuille law, which results from an evaluation of an order reduction of the Navier-Stokes equation, is appropriate for the very thin cracks in the given scenario.

To this end, a small introduction into the basics of fluid mechanics is given in Section 7.1. Here we restrict the considerations to the necessary equations. By no means this is an complete introduction to the field of fluid mechanics. The interested reader is referred to the classical textbooks of Spurk & Aksel [246], Helmig & Class [131] or Batchelor [17] among others. The basic fundamentals are then applied to a crack with small height-length ratio in Section 7.2. This results in two equations describing the velocity of the fluid in the crack and a constitutive relation for the fluid pressure p inside the crack. Here the considerations are similar to Vinci et al. [265] and Mikelic et al. [195].

7.1. Basic equations of fluid mechanics

To start with, we review the basic equations of fluid mechanics needed for a description of fluid-filled cracks. These are the physical balance equations as well as the constitutive equations for the fluid stress state. Combining the mass and momentum balance equations leads to the well-known Navier-Stokes equation.

7.1.1. Physical balance equations in Eulerian setting

In contrast to solid mechanics, in fluid mechanics one usually uses an Eulerian description of the physics. That is rather than observing individual material points and their motion, a control volume $\mathcal{S}$ is chosen and all quantities of interest are observed at positions $\boldsymbol{x} \in \mathcal{S}$. That implies that at each instant of time different material points may be present at a fixed position $\boldsymbol{x}$.

The local physical balance equations have been introduced in their Eulerian representation in Chapter 2 and are given by

$$\begin{aligned}
&\textit{Balance of mass} && 0 = \dot{\rho}^f + \rho^f \operatorname{div}[\boldsymbol{v}] \\
&\textit{Balance of linear momentum} && \rho^f \dot{\boldsymbol{v}} = \operatorname{div}[\boldsymbol{\sigma}] + \rho^f \bar{\boldsymbol{g}} \\
&\textit{Balance of angular momentum} && \boldsymbol{\sigma} = \boldsymbol{\sigma}^T \\
&\textit{Balance of energy} && \dot{e} = \boldsymbol{\sigma} : \boldsymbol{g}\boldsymbol{l} + \rho^f r - \operatorname{div}[\boldsymbol{q}] \\
&\textit{Balance of entropy} && \dot{\eta} = \frac{\delta}{\theta} + \frac{1}{\theta}\left(\rho^f r - \operatorname{div}[\boldsymbol{q}]\right) + \frac{1}{\theta^2}\boldsymbol{q} \cdot \nabla_{\boldsymbol{x}}\theta
\end{aligned} \tag{7.1}$$

Here, ρ^f is the spatial density of the fluid and $\boldsymbol{l} = \nabla_{\boldsymbol{x}}\boldsymbol{v}$ is denoted as the spatial velocity gradient. Furthermore the abbreviation $\dot{f}(\boldsymbol{x}, t) := df(\boldsymbol{x}, t)/dt = \partial_t f + \nabla_{\boldsymbol{x}} f \cdot \boldsymbol{v}$ is introduced for the total time derivative of a spatial field $f(\boldsymbol{x}, t)$.

For the special case of incompressible fluids, that is $\rho^f = const.$, the balance of mass $(7.1)_1$ reduces to

$$\operatorname{div}[\boldsymbol{v}] = 0 \ . \tag{7.2}$$

7.1.2. Constitutive equation

After reviewing the physical balance laws a constitutive equation for the stress tensor $\boldsymbol{\sigma}$ is specified. As standard in fluid mechanics $\boldsymbol{\sigma}$ is split into the hydrostatic fluid pressure p and a viscous contribution $\boldsymbol{\tau}$. We choose a simple linear constitutive relation for compressible, viscous fluids

$$\boldsymbol{\sigma} = -p\boldsymbol{1} + \boldsymbol{\tau} \quad \text{with} \quad \boldsymbol{\tau} = 2\mu\boldsymbol{d} + \lambda \operatorname{tr}[\boldsymbol{d}]\boldsymbol{1} \ , \tag{7.3}$$

with the symmetric velocity gradient $\boldsymbol{d} = \operatorname{sym}[\nabla_{\boldsymbol{x}}\boldsymbol{v}]$, see also Spurk & Aksel [246]. Here, λ and μ are the two Lamé material constants. Within the isothermal setting the fluid pressure at rest is a function of the density, that is $p = \hat{p}(\rho^f)$. Introducing a constant fluid's bulk modulus κ^f we write

$$\rho^f = \rho_0^f \exp[(p - p_0)/\kappa^f] \quad \text{with} \quad \frac{1}{\kappa^f} = \frac{1}{\rho^f}\frac{d\rho^f}{dp} \ . \tag{7.4}$$

Here ρ_0^f and p_0^f are the initial density and pressure of the fluid. For the special case of an incompressible, viscous fluid, the stress $\boldsymbol{\sigma}$ introduced in equation (7.3) can be reduced to

$$\boldsymbol{\sigma} = -p\boldsymbol{1} + 2\mu\boldsymbol{d} \ . \tag{7.5}$$

7.1.3. Navier-Stokes equation

Now the constitutive equations (7.3) and (7.4) for the case of a compressible, viscous fluid are inserted into the balance equations $(7.1)_1$ and $(7.1)_2$ yielding

$$\dot{p} = -\kappa^f \operatorname{div}[\boldsymbol{v}] \quad \text{and} \quad \rho^f \dot{\boldsymbol{v}} = -\nabla_{\boldsymbol{x}} p + \mu\Delta_{\boldsymbol{x}}\boldsymbol{v} + (\mu + \lambda)\nabla_{\boldsymbol{x}}\big(\operatorname{div}[\boldsymbol{v}]\big) + \rho^f \boldsymbol{b} \ . \tag{7.6}$$

A well-known equation in fluid dynamics is the Navier-Stokes equation for incompressible fluids. It can be obtained from $(7.6)_2$ by inserting the incompressibility condition (7.2) as

$$\rho^f \dot{\boldsymbol{v}} = -\nabla_{\boldsymbol{x}} p + \mu\Delta_{\boldsymbol{x}}\boldsymbol{v} + \rho^f \boldsymbol{b} \ . \tag{7.7}$$

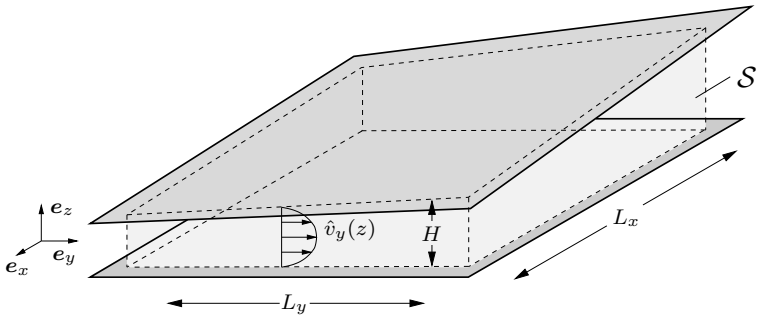

Figure 7.1: *Geometric setup for the lubrication theory.* The control volume $\mathcal{S}$ (bright shaded) is confined by two rigid plates (dark shaded). The height H of the domain is much smaller than the two other dimensions, such that $\epsilon_i = H/L_i = \mathcal{O}(10^{-3})$. In this setup the fluid film lubrication theory is a good approximation.

7.1.4. Fluid film lubrication theory

Consider a domain with one space dimension being much smaller than the other two dimensions, see Figure 7.1. For an aspect ratio $\epsilon = H/L_{i=\{x,y\}} = \mathcal{O}(10^{-3})$ application of the fluid film lubrication theory is reasonable. Here a space dimension reduction is considered by assuming the approximation $\epsilon^2 \approx 0$. Furthermore, within the classical lubrication theory the inertia terms as well as the body forces are neglected. Transforming equation $(7.6)_2$ for compressible, viscous fluids into a dimensionless form and applying the approximation $\epsilon^2 = 0$ yields

$$\frac{\partial p}{\partial x} = \mu \frac{\partial^2 v_x}{\partial z^2} \ , \quad \frac{\partial p}{\partial y} = \mu \frac{\partial^2 v_y}{\partial z^2} \quad \text{and} \quad \frac{\partial p}{\partial z} = 0 \ . \tag{7.8}$$

From $(7.8)_3$ one sees that the fluid pressure p is constant over the height of the domain. Integration of equations $(7.8)_1$ and $(7.8)_2$ leads to

$$\mu v_x = \frac{1}{2}\frac{\partial p}{\partial x} z^2 + C_1 z + C_2 \quad \text{and} \quad \mu v_y = \frac{1}{2}\frac{\partial p}{\partial y} z^2 + C_3 z + C_4 \tag{7.9}$$

in terms of four integration constants C_1–C_4 that has to be specified by appropriate boundary conditions. For the considered case of viscous fluid and the model problem of Figure 7.1, the boundary conditions are the velocities of the two plates defining the domain.

7.2. Fluid flow in cracks

After introducing the basic equations of fluid mechanics we now want to apply them to fluid-filled cracks. For the scenario of deformable rock fracture, Witherspoon et al. [272] showed that it is valid to use the lubrication theory which is also done in many existing models, see for example Mikelic et al. [195], Secchi & Schrefler [236, 237] or Miehe & Mauthe [181]. The goal of this section is to obtain relations for the fluid flow as well as an equation for the fluid pressure inside the crack based on the approximations of the lubrication theory. Similar considerations can be found in Mikelic et al. [195], Kovalyshen [152] and Vinci et al. [265].

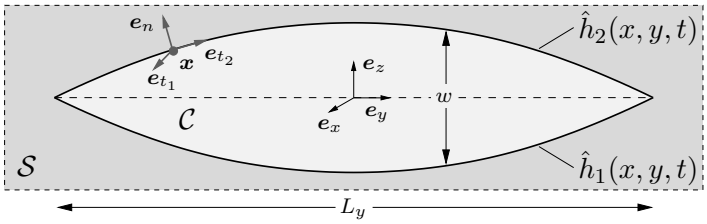

Figure 7.2: *Geometric setup of fluid filled crack.* The width w of the crack is assumed to be much smaller than its lengths L_x and L_y. The crack surfaces are described by two functions $\hat{h}_1(x,y,t)$ and $\hat{h}_2(x,y,t)$.

7.2.1. Crack geometry and fluid flow inside the crack

Consider a crack $\mathcal{C}$ embedded into a porous bulk material $\mathcal{S}$ and the boundary surfaces of which are described by two functions $z = \hat{h}_1(x,y,t)$ and $z = \hat{h}_2(x,y,t)$, see Figure 7.2. At a point $\boldsymbol{X} \in \partial\mathcal{C}$ with $z = \hat{h}_i(x,y,t)$ at the crack surface the tangential and normal vectors to the surface can be evaluated as

$$\boldsymbol{e}_n = \boldsymbol{e}_z - \partial_z \hat{h}_i \boldsymbol{e}_x - \partial_z \hat{h}_i \boldsymbol{e}_y \;, \boldsymbol{e}_{t_1} = \boldsymbol{e}_x + \partial_x \hat{h}_i \boldsymbol{e}_z \quad \text{and} \quad \boldsymbol{e}_{t_2} = \boldsymbol{e}_y + \partial_y \hat{h}_i \boldsymbol{e}_z \;. \tag{7.10}$$

Now we assume validity of the lubrication theory, that is the fluid velocity inside the crack is described by (7.9). In order to obtain the integration constants C_1–C_4 we have the boundary conditions for a viscous fluid given by

$$\boldsymbol{v} \cdot \boldsymbol{e}_{t_1} = 0 \quad \text{and} \quad \boldsymbol{v} \cdot \boldsymbol{e}_{t_2} = 0 \;. \tag{7.11}$$

Here a pure mode I crack opening is assumed. Evaluation of (7.11) by use of (7.10) together with the classical assumption of the lubrication theory, i.e. $(w/L_i)^2 \approx 0$, yields

$$\begin{aligned} v_{t_1}(x,y,t) &:= \boldsymbol{v} \cdot \boldsymbol{e}_{t_1} = v_x + \partial_z \hat{h}_i v_z \approx v_x = 0 \;, \\ v_{t_2}(x,y,t) &:= \boldsymbol{v} \cdot \boldsymbol{e}_{t_2} = v_y + \partial_z \hat{h}_i v_z \approx v_y = 0 \;. \end{aligned} \tag{7.12}$$

Then the integration constants can be evaluated yielding the fluid velocity inside the crack

$$v_x = \frac{1}{2\mu}(h_2 - z)(h_1 - z)\frac{\partial p}{\partial x} \quad \text{and} \quad v_y = \frac{1}{2\mu}(h_2 - z)(h_1 - z)\frac{\partial p}{\partial y} \;. \tag{7.13}$$

This quadratic velocity profile over the height (7.13) is known as *Poiseuille flow*. From (7.13) the fluid fluxes q_x and q_y can be obtained by integration over the height from which then the average velocities $\bar{v}_x$ and $\bar{v}_y$ follow with the crack opening $w := h_2 - h_1$ as

$$\begin{aligned} q_x &= \int_{\tilde{z}=h_1}^{h_2} v_x(\tilde{z})\, d\tilde{z} := \bar{v}_x(h_2 - h_1) \Rightarrow \quad \bar{v}_x = -\frac{1}{12\mu} w^2 \frac{\partial p}{\partial x} \;, \\ q_y &= \int_{\tilde{z}=h_1}^{h_2} v_y(\tilde{z})\, d\tilde{z} := \bar{v}_y(h_2 - h_1) \Rightarrow \quad \bar{v}_y = -\frac{1}{12\mu} w^2 \frac{\partial p}{\partial y} \;. \end{aligned} \tag{7.14}$$

7.2.2. Fluid flow perpendicular to the crack surface

In order to obtain the fluid flow perpendicular to the crack surface we follow Mikelic et al. [195] and integrate the fluid mass balance equation $(7.6)_1$ over the height

$$\int_{\tilde{z}=h_1}^{z} \frac{\dot{p}}{\kappa^f} = \int_{\tilde{z}=h_1}^{z} \frac{\partial v_x}{\partial x} + \frac{\partial v_y}{\partial y} + \frac{\partial v_z}{\partial z} \;. \tag{7.15}$$

Evaluation of (7.15) with the fluid velocities (7.13) inside the crack yields

$$v_z(z) = v_z(h_1) - \frac{\dot{p}}{\kappa^f}(z - h_1) - K(z)\left[\frac{\partial^2 p}{\partial x^2} + \frac{\partial^2 p}{\partial y^2}\right] - \left[\frac{\partial K(z)}{\partial x}\frac{\partial p}{\partial x} + \frac{\partial K(z)}{\partial y}\frac{\partial p}{\partial y}\right] \tag{7.16}$$

with $K(z) = -(-2z^3 - h_1^3 + 3h_2 z^2 + 3h_2 h_1^2 + 3h_1 z^2 - 6h_1 h_2 z)/12\mu$. Another integration with $\tilde{z} \in [h_1, h_2]$ and insertion into (7.16) yields the fluid velocity in z direction as

$$v_z(z) = -K(z)\left\{\frac{\partial}{\partial x}\left[\ln\left(\frac{K(z)}{K(h_2)}\right)\right]\frac{\partial p}{\partial x} + \frac{\partial}{\partial y}\left[\ln\left(\frac{K(z)}{K(h_2)}\right)\right]\frac{\partial p}{\partial y}\right\} + \hat{v}_z \tag{7.17}$$

with

$$\hat{v}_z = \left(1 - \frac{K(z)}{K(h_2)}\right)\hat{v}_z(h_1) + \frac{K(z)}{K(h_2)}\hat{v}_z(h_2) - \frac{\dot{p}}{\kappa^f}\left(z - h_1 + \frac{K(z)}{K(h_2)}(h_2 - h_1)\right) . \tag{7.18}$$

Here the boundary conditions $v_z(h_1) = \hat{v}_z(h_1)$ and $v_z(h_2) = \hat{v}_z(h_2)$ for the velocity component $v_n = \boldsymbol{v} \cdot \boldsymbol{e}_n \approx v_z$ at material points $\boldsymbol{X} \in \partial\mathcal{C}$ at the crack surfaces are assumed to be known.

7.2.3. Averaged fluid pressure equation

Evaluating (7.16) for $z = h_2$ yields for given $\hat{v}_z(h_1)$ and $\hat{v}_z(h_2)$ the classical *Reynolds lubrication equation*, a second-order differential equation for the fluid pressure p. In the following we want to obtain an *averaged fluid pressure equation* based on the average velocities (7.14). Recalling the fluid mass balance $(7.6)_1$ and inserting the average velocities

$$\frac{\dot{p}}{\kappa^f} = -\operatorname{div}[\boldsymbol{v}] = -(\partial_x \bar{v}_x + \partial_y \bar{v}_y) - \partial_z v_z \ . \tag{7.19}$$

The term $\partial_z v_z$ is averaged by a differential quotient as $\partial_z v_z \approx (v_z(h_2) - v_z(h_1)/(h_2 - h_1)$. Analogously to Mikelic et al. [195] we apply the kinematic boundary conditions

$$v_z(h_i) = \frac{dh_i}{dt} = \frac{\partial h_i}{\partial t} + \frac{\partial h_i}{\partial x}v_x + \frac{\partial h_i}{\partial t}v_y \tag{7.20}$$

for $i = 1, 2$. With the velocities $\bar{v}_x$ and $\bar{v}_y$ from (7.14) we finally get an averaged fluid pressure equation for compressible, viscous fluids inside the crack as

$$\dot{p} = -\kappa^f(\partial_x \bar{v}_x + \partial_y \bar{v}_y) - \frac{\kappa^f}{w}\frac{\partial w}{\partial t} + \frac{w}{12\mu}\left[\frac{\partial w}{\partial x}\frac{\partial p}{\partial x} + \frac{\partial w}{\partial y}\frac{\partial p}{\partial y}\right] \ , \tag{7.21}$$

where $w = h_2 - h_1$ is the crack opening width. Equation (7.21) is equivalent to the result observed in Vinci et al. [265] for the radial-symmetric case.

Chapter 8

Phase-Field Modeling of Poro-Hydro-Elasticity coupled with Fracture

The goal of this Chapter is to extend the framework and the porous media model of Chapter 4 by including crack propagation. In particular we are interested in hydraulically driven fracture scenarios, which furthermore increases the difficulty in modeling due to the additional fluid flow along the fluid filled cracks. In this work we make use of the phase-field modeling of fracture that provides a continuum approach with straightforward numerical treatment as well as the possibility to simulate complex crack patterns such as branching. For an introduction into hydraulically driven fracture the interested reader is referred to the works of Rubin [228], Zhang et al. [275], Adachi et al. [2], Bažant et al. [18] and Simoni & Schrefler [243]. In analogy to the previous model problems we propose a canonical variational formulation of finite strain poro-hydro-elasticity at fracture that governs the evolution of the two basic kinematic fields, that is the rate of solid deformation $\dot{\boldsymbol{\varphi}}$ and the fluid mass flow vector $\mathbb{H}$, as well as the evolution of the crack phase field $\dot{d}$

$$\{\dot{\boldsymbol{\varphi}}, \mathbb{H}, \dot{d}\} = \arg \left\{ \inf_{\dot{\boldsymbol{\varphi}} \in \mathcal{W}_{\dot{\boldsymbol{\varphi}}}} \inf_{\mathbb{H} \in \mathcal{W}_{\mathbb{H}}} \inf_{\dot{d} \in \mathcal{W}_{\dot{d}}} \Pi(\dot{\boldsymbol{\varphi}}, \mathbb{H}, \dot{d}) \right\} . \tag{8.1}$$

The formulation is based on the rate potential Π that depends on only two constitutive functions connected to the energy storage and the dissipative behavior. The framework (8.1) provides a *canonical minimization principle* for the evolution problem, the Euler equations of which are the total linear momentum balance, the fluid flow equation and in addition the evolution equation of the crack phase-field. Using a Legendre transformation of the dissipation potential function, (8.1) can be transformed into a *saddle-point variational formulation* for the evolution problem based on a dual rate potential $\tilde{\Pi}^*$

$$\{\dot{\boldsymbol{\varphi}}, \dot{m}, \mu, \dot{d}\} = \arg \left\{ \inf_{\dot{\boldsymbol{\varphi}} \in \mathcal{W}_{\dot{\boldsymbol{\varphi}}}} \inf_{\dot{m} \in \mathcal{W}_{\dot{m}}} \sup_{\mu \in \mathcal{W}_{\mu}} \inf_{\dot{d} \in \mathcal{W}_{\dot{d}}} \tilde{\Pi}^*(\dot{\boldsymbol{\varphi}}, \dot{m}, \mu, \dot{d}) \right\} . \tag{8.2}$$

In what follows the initial boundary value problem and the constitutive functions are introduced in Section 8.1. Then a consistent extension of the minimization principle and the dual saddle-point principle of Chapter 4 by including phase-field fracture is conducted

in Section 8.2. A rate-potential Π is introduced that accounts for the degrading bulk response, the crack propagation as well as the upgrading Poiseuille-type fluid flow within the crack. For the numerical treatment of the different formulations first a time-discretization is performed in Section 8.3. The results are incremental counterparts of the minimization and saddle-point variational principles. A space discretization using finite element approximations is obtained in Section 8.4. Furthermore the fracture evolution equation appearing as an Euler equation of the presented variational principles is rewritten and modified in Section 8.5. Different driving forces for the crack evolution are introduced that are appropriate for hydraulically driven fracture scenarios within the finite strain theory. Finally the modeling capabilities of the proposed approach is shown by means of different numerical boundary value problems in two and three dimensions in Section 8.6.

8.1. Initial boundary value problem of coupled poro-hydro-elasticity at fracture

This section provides an introduction to the modeling framework of coupled poro-hydro-elasticity at fracture. It is based on the coupled poro-mechanical model in Chapter 4 and enhanced by the fracture phase-field introduced in Chapter 6.

8.1.1. Modeling assumptions

The basis for the modeling of poro-hydro-elasticity at fracture is again the framework of multicomponent solids introduced in Chapter 3. The second component is a fluid, wherefor we specify $\beta := f$. For the subsequent considerations we make the following simplifications:

- Isothermal conditions, such that $\dot{\theta} = 0$ and $\nabla\theta = \boldsymbol{0}$,
- elastic solid behavior,
- quasi-static conditions, such that $|\ddot{\boldsymbol{\varphi}}| \approx 0$ and $|\boldsymbol{A}^f| \approx 0$,
- no body forces are considered, such that $\boldsymbol{b} = \boldsymbol{0}$,
- the free energy density $\hat{\psi}$ is not a function of ∇m,
- fracture is described by a diffusive phase-field variable d, such that $\mathfrak{q} = \{d\}$.

Assumptions 5 and 6 imply the free energy density to be a constitutive function in terms of the deformation gradient, the relative fluid mass, the phase-field variable and its gradient

$$\psi = \hat{\psi}(\boldsymbol{F}, m, d, \nabla d) \ . \tag{8.3}$$

For the gradient of the phase-field variable ∇d being an argument of $\hat{\psi}$ the local dissipation inequality constraint is fulfilled weakly in the domain, that is the constraints (3.64) are to

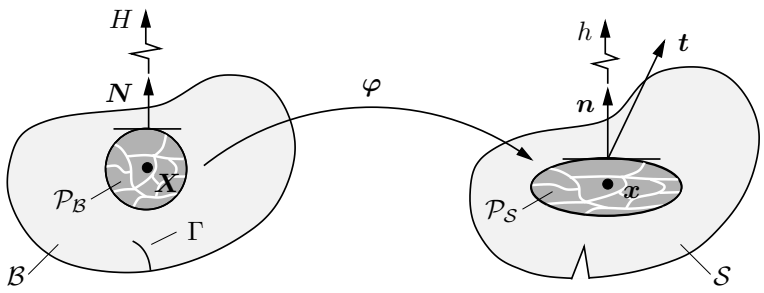

Figure 8.1: *Phenomenological quantities in finite poro-hydro-elasticity at fracture.* The total traction vector $\boldsymbol{t}$ represents the action of contact forces on the surface of the cut-out part $\partial\mathcal{P}_\mathcal{S}$. The material and spatial fluid transports H and h characterize the fluid out-flux with respect to the areas $\partial\mathcal{P}_\mathcal{B}$ and $\partial\mathcal{P}_\mathcal{S}$. Indicated is the development of a sharp crack Γ.

hold. With these modeling assumptions, the balance equations and constitutive functions under consideration are summarized as follows:

$$
\boxed{
\begin{aligned}
&\textit{Balance of fluid mass} && \dot{m} = -\operatorname{Div}[\mathbb{H}] \\
&\textit{Balance of linear momentum} && \boldsymbol{0} = \operatorname{Div}[\boldsymbol{P}] \\
&\textit{Definition of driving force} && \mathbb{B} = -\nabla\mu \\
&\textit{Constitutive crack evolution} && 0 \in \partial_d\hat{\psi} - \operatorname{Div}[\partial_{\nabla d}\hat{\psi}] + \partial_{\dot{d}}\hat{\phi}(\dot{d}) \\
&\textit{Constitutive stresses} && \boldsymbol{P} = \partial_{\boldsymbol{F}}\hat{\psi} \\
&\textit{Constitutive chemical potential} && \mu = \partial_m\hat{\psi} \\
&\textit{Constitutive driving force} && \hat{\mathbb{B}} = \partial_{\mathbb{H}}\hat{\phi}_{\text{con}}
\end{aligned}
} \tag{8.4}
$$

Here we introduced the general form $(8.4)_4$ of evolution equation for the fracture phase-field d in line with the concept of dissipation potentials introduced in Subsection 3.4.3.

8.1.2. Initial boundary value problem

We now recall the coupled initial boundary value problem introduced in Subsection 3.4.1 for the considered model problem of poro-hydro-elasticity at fracture. The unknown kinematic fields of the coupled problem are the deformation map and the fluid mass flow vector

$$
\boldsymbol{\varphi} : \begin{cases} \mathcal{B} \times T \to \mathcal{S} \subset \mathcal{R}^3, \\ (\boldsymbol{X}, t) \mapsto \boldsymbol{\varphi}(\boldsymbol{X}, t) \end{cases} \quad \text{and} \quad \mathbb{H} : \begin{cases} \mathcal{B} \times T \to \mathcal{R}^3, \\ (\boldsymbol{X}, t) \mapsto \mathbb{H}(\boldsymbol{X}, t) \ . \end{cases} \tag{8.5}
$$

The fluid mass flow vector $\mathbb{H}$ and the relative fluid mass m that appears as a state variable in the constitutive functions are connected via the mass balance equation $(8.4)_1$. Additionally to the kinematic variables (8.5) the fracture phase-field is an unknown field

$$
d : \begin{cases} \mathcal{B} \times T \to [0, 1], \\ (\boldsymbol{X}, t) \mapsto d(\boldsymbol{X}, t) \ . \end{cases} \tag{8.6}
$$

For the two global fields (8.5) boundary values have to be prescribed. To this end, the boundary of $\mathcal{B}$ is split into *Dirichlet boundaries*, where the deformation map and the

fluid flux is prescribed and *Neumann boundaries*, where the mechanical traction and the chemical potential is prescribed

$$\begin{aligned} \boldsymbol{\varphi}(\boldsymbol{X},t) &= \bar{\boldsymbol{\varphi}}(\boldsymbol{X},t) \text{ on } \partial\mathcal{B}_{\boldsymbol{\varphi}} \ , \quad \boldsymbol{T}(\boldsymbol{X},t) = \bar{\boldsymbol{T}}(\boldsymbol{X},t) \text{ on } \partial\mathcal{B}_{\boldsymbol{T}} = \partial\mathcal{B} \setminus \partial\mathcal{B}_{\boldsymbol{\varphi}} \ , \\ H(\boldsymbol{X},t) &= \bar{H}(\boldsymbol{X},t) \text{ on } \partial\mathcal{B}_{H} \ , \quad \mu(\boldsymbol{X},t) = \bar{\mu}(\boldsymbol{X},t) \text{ on } \partial\mathcal{B}_{\mu} = \partial\mathcal{B} \setminus \partial\mathcal{B}_{H} \ . \end{aligned} \tag{8.7}$$

For the fracture phase-field (8.6) the boundary conditions are not a priori thermodynamically consistent but have to fulfill $(3.68)_3$. Assuming pure Neumann boundary conditions for d at the whole boundary $\partial\mathcal{B}$, thermodynamical consistency is guaranteed by

$$\left(\partial_{\nabla \mathbf{q}} \hat{\psi}\right) \cdot \boldsymbol{N} = 0 \text{ on } \partial\mathcal{B} \ . \tag{8.8}$$

Furthermore initial conditions have to be prescribed for the two kinematic fields $\boldsymbol{\varphi}$ and $\mathbb{H}$, the fracture phase-field d as well as for the relative fluid mass field m

$$\begin{aligned} \boldsymbol{\varphi}(\boldsymbol{X},t_0) &= \bar{\boldsymbol{\varphi}}_0(\boldsymbol{X}) \ , \quad d(\boldsymbol{X},t_0) = \bar{d}_0(\boldsymbol{X}) \ , \\ \mathbb{H}(\boldsymbol{X},t_0) &= \bar{\mathbb{H}}_0(\boldsymbol{X}) \ , \quad m(\boldsymbol{X},t_0) = 0 \ . \end{aligned} \tag{8.9}$$

As we are restricting ourselves to the quasi-static case initial conditions for the solid skeleton velocity $\boldsymbol{V}$ are not needed. The initial boundary value problem is now to find the deformation $\boldsymbol{\varphi}$, the fluid mass flow vector $\mathbb{H}$ and the fracture phase field d that satisfy the boundary conditions (8.7) and (8.8), the initial conditions (8.9) and the balance equations (8.4). In this initial boundary value problem the two fields $\boldsymbol{\varphi}$ and $\mathbb{H}$ are kinematic variables of the multicomponent material. Therefor we denote this as the *canonical form* of initial boundary value problem.

Analogously to Chapter 4 *mixed formulations* can be deduced from the canonical formulation by means of Legendre transformations. Hence additional to the canonical $\{\boldsymbol{\varphi}, \mathbb{H}, d\}$-formulation we propose the $\{\boldsymbol{\varphi}, \mu, d\}$-formulation that is also used in the literature by Miehe et al. [190], Miehe & Mauthe [181], Ehlers & Luo [96], Timothy & Meschke [257], Wheeler et al. [269] or Mikelic et al. [192, 193, 194, 195]. A formulation where both $\mathbb{H}$ and μ are degrees of freedom was recently proposed by Wilson & Landis [271].

8.1.3. Stored energy, dissipation potential and load functionals

In the following we introduce three functionals needed to state the variational principle. They are related to the energy storage, the dissipative mechanism and the external loading. The first two are based on two constitutive potentials, the free energy function and the dissipation potential.

Rate of energy functional. The *stored energy functional* depends on the deformation field $\boldsymbol{\varphi}$, the relative fluid mass field m and the fracture phase field d

$$E(\boldsymbol{\varphi}, m, d) := \int_{\mathcal{B}} \hat{\psi}(\boldsymbol{F}, m, d, \nabla d) \, dV \tag{8.10}$$

and characterizes the poro-mechanical energy stored in the solid-fluid mixture. It is governed by the constitutive energy storage function $\hat{\psi}$. The rate of energy is evaluated

from (8.10) as

$$\frac{d}{dt}E(\dot{\boldsymbol{\varphi}},\dot{m},\dot{d}) = \int_{\mathcal{B}} \{\, \partial_{\boldsymbol{F}}\hat{\psi} : \nabla\dot{\boldsymbol{\varphi}} + \partial_m\hat{\psi}\dot{m} + \partial_d\hat{\psi}\dot{d} + \partial_{\nabla d}\hat{\psi}\cdot\nabla\dot{d}\} \, dV \tag{8.11}$$

and can be considered as a functional of the rates $\{\dot{\boldsymbol{\varphi}},\dot{m},\dot{d}\}$ at given state $\{\boldsymbol{\varphi},m,d\}$.

Dissipation potential functional. The *canonical dissipation potential functional* depends on the fluid mass flow vector $\mathbb{H}$ and the rate of phase-field $\dot{d}$. It is assumed to have the form

$$D(\mathbb{H},\dot{d}) := \int_{\mathcal{B}} \hat{\phi}(\mathbb{H},\dot{d};\boldsymbol{F},m,d)\, dV \ . \tag{8.12}$$

in terms of the dissipation potential function $\hat{\phi}$ and evaluated at a given state $\{\boldsymbol{F},m,d\}$ of deformation gradient, fluid mass and fracture phase-field. Alternatively to the representation (8.12) the dissipation potential functional can be expressed in terms of a partial dual dissipation potential function $\hat{\phi}^*$. Recalling the definition of the partial Legendre-transformation, we have

$$\phi(\mathbb{H},\dot{d}) = \sup_{\mathbb{B}} \big[\mathbb{B}\cdot\mathbb{H} - \hat{\phi}^*(\mathbb{B},\dot{d};\boldsymbol{F},m,d)\big] \tag{8.13}$$

Insertion of (8.13) into (8.12) suggests the introduction of an *extended dissipation potential functional* $D^*(\mathbb{H},\mathbb{B})$ defined as

$$D^*(\mathbb{H},\mathbb{B},\dot{d}) = \int_{\mathcal{B}} \big[\mathbb{B}\cdot\mathbb{H} - \hat{\phi}^*(\mathbb{B},\dot{d};\boldsymbol{F},m,d)\big]\, dV \ . \tag{8.14}$$

The extended dissipation functional (8.14) is connected to the dissipation potential functional (8.12) by the relationship

$$D(\mathbb{H},\dot{d}) = \sup_{\mathbb{B}} \big[D^*(\mathbb{H},\mathbb{B},\dot{d})\big] \ . \tag{8.15}$$

External load functional. The external load functional decomposes into mechanical and fluid contributions

$$P_{\text{ext}}(\dot{\boldsymbol{\varphi}},\mathbb{H}) = P^{\boldsymbol{T}}_{\text{ext}}(\dot{\boldsymbol{\varphi}}) + P^{\mu}_{\text{ext}}(\mathbb{H})\,. \tag{8.16}$$

In the absence of body forces $\boldsymbol{b} = \boldsymbol{0}$ the two contributions are given by

$$P^{\boldsymbol{T}}_{\text{ext}}(\dot{\boldsymbol{\varphi}}) := \int_{\partial\mathcal{B}_{\boldsymbol{T}}} \bar{\boldsymbol{T}}\cdot\dot{\boldsymbol{\varphi}}\, dA \quad \text{and} \quad P^{\mu}_{\text{ext}}(\mathbb{H}) = -\int_{\partial\mathcal{B}_{\mu}} \bar{\mu}H\, dA \ , \tag{8.17}$$

where $H = \mathbb{H}\cdot\boldsymbol{N}$ is the fluid mass flux.

8.1.4. Constitutive functions for the model problem

Before stating the variational principle of coupled poro-hydro-elasticity at fracture the two constitutive functions ψ and ϕ are specified. We consider the formulation here to be an extension of the poro-elasticity model of Chapter 4. This means the constitutive functions introduced there are the basis and are extended by terms that model the fracture effects. The constitutive functions are in line with the considerations in Miehe et al. [190] or Miehe & Mauthe [181].

Free energy function. We assume the free energy function $\hat{\psi}$ to be split into three contributions that are associated with the solid skeleton, the pore fluid behavior and the fracture surface energy density. We write

$$\hat{\psi}(\boldsymbol{F}, m, d, \nabla d) = (1-d)^2 \hat{\psi}_{\text{eff}}(\boldsymbol{F}) + \hat{\psi}_{\text{fluid}}(\boldsymbol{F}, m; d) + \hat{\psi}_{\text{frac}}(d, \nabla d) \tag{8.18}$$

The first two contributions are chosen to be a compressible neo-Hookean material model for the solid skeleton contribution and a quadratic fluid contribution

$$\begin{aligned} \hat{\psi}_{\text{eff}}(\boldsymbol{F}) &= \frac{\gamma}{2}\big[\, (\boldsymbol{F} : \boldsymbol{F} - 3) + \frac{2}{\beta}(J^{-\beta} - 1) \,\big] \,, \\ \hat{\psi}_{\text{fluid}}(\boldsymbol{F}, m; d) &= \frac{M}{2}\big[\, b(J-1) - (m/\rho^f) \big]^2 \end{aligned} \tag{8.19}$$

Here, $\gamma > 0$ is the shear modulus of the skeleton and $\beta > 0$ a parameter describing its volumetric compressibility. It is possible to link β to the classical Poisson number of linear elasticity via the relation $\beta = 2\nu/(1-2\nu)$. The material parameter M and b are denoted as Biot's modulus and Biot's coefficient. Note that the term $(1-d)^2$ in front of $\hat{\psi}_{\text{eff}}$ implies a full degradation of the energy related to the solid skeleton whereas the fluid contribution $\hat{\psi}_{\text{fluid}}$ is not degraded. The fracture contribution $\hat{\psi}_{\text{frac}}$ represents the regularized fracture surface energy density and is given by

$$\hat{\psi}_{\text{frac}}(d, \nabla d) = g_c \gamma_l(d, \nabla d) = \frac{g_c}{2l}\big[d^2 + l^2 |\nabla d|^2\big] \,, \tag{8.20}$$

where g_c is Griffith's critical energy release rate of the solid skeleton.

Dissipation potential function. The *canonical dissipation potential* (4.26) of the fluid-solid mixture without fracture is extended by a term governing the evolution of the fracture phase-field, that is

$$\hat{\phi}(\mathbb{H}, \dot{d}; \boldsymbol{F}, m, d) = \hat{\phi}_{\text{con}}(\mathbb{H}; \boldsymbol{F}, d) + \hat{\phi}_{\text{frac}}(\dot{d}) \,. \tag{8.21}$$

The convective dissipation potential $\hat{\phi}_{\text{con}}(\mathbb{H}; \boldsymbol{F}, d)$ is chosen to have the same structure as in (4.26) for the considerations without fracture and is a function of the flow vector $\mathbb{H}$

$$\hat{\phi}_{\text{con}}(\mathbb{H}; \boldsymbol{F}, d) = \frac{1}{2}\widehat{\boldsymbol{K}}^{-1}(\boldsymbol{F}, d) : (\mathbb{H} \otimes \mathbb{H}) \,, \tag{8.22}$$

at given state $\{\boldsymbol{F}, d\}$ and where $\widehat{\boldsymbol{K}}$ is denoted as the spatial permeability tensor that is specified below. From (8.22) the dual convective dissipation potential ϕ^*_{con} can be evaluated as

$$\hat{\phi}^*_{\text{con}}(\mathbb{B}; \boldsymbol{F}, d) = \frac{1}{2}\widehat{\boldsymbol{K}}(\boldsymbol{F}, d) : (\mathbb{B} \otimes \mathbb{B}) \,. \tag{8.23}$$

The contribution of the dissipation potential due to fracture is chosen to

$$\hat{\phi}_{\text{frac}}(\dot{d}) = I(\dot{d}) + \frac{\eta}{2}\dot{d}^2 \,. \tag{8.24}$$

where the latter part provides a viscous regularization of the fracture evolution with a mobility coefficient η. The first term accounts for the irreversibility of the fracture phase-field evolution and is given in terms of the non-smooth indicator function

$$I(\dot{d}) = \begin{cases} 0 & \text{for } \dot{d} \geq 0 \\ \infty & \text{otherwise} \end{cases} \quad \text{with} \quad \partial_{\dot{d}} I(\dot{d}) = \begin{cases} 0 & \text{for } \dot{d} \geq 0 \\ \mathcal{R}_- & \text{otherwise} \end{cases} \,. \tag{8.25}$$

This non-smooth contribution is also used in damage theories to model the irreversibility constraint, see for example Dimitrijevic & Hackl [86, 87]. Note that $\eta \to 0$ yields a rate-independent phase-field evolution.

Constitutive total stress tensor. An evaluation of the local dissipation inequality yields the constitutive equation for the total stresses in terms of the free energy function as $\boldsymbol{P} = \partial_{\boldsymbol{F}} \hat{\psi}$, see (3.70). Evaluation of (8.18) leads to

$$\boldsymbol{P} = \partial_{\boldsymbol{F}} \hat{\psi} = (1-d)^2 \tilde{\boldsymbol{P}}_{\text{eff}} - b\rho^f \mu J \boldsymbol{F}^{-T} \quad \text{with} \quad \tilde{\boldsymbol{P}}_{\text{eff}} = \partial_{\boldsymbol{F}} \hat{\psi}_{\text{eff}} = \gamma \big[\boldsymbol{F} - J^{-\beta} \boldsymbol{F}^{-T} \big] \ . \tag{8.26}$$

The fluid contribution $\hat{\psi}_{\text{fluid}}(\boldsymbol{F}, m)$ is constructed such that the chemical potential (and hence the fluid pressure) is independent of the energy contribution $\hat{\psi}_{\text{eff}}$. Using the relations (2.23) and (4.22), the Cauchy stresses are obtained as

$$\boldsymbol{\sigma} = (1-d)^2 \tilde{\boldsymbol{\sigma}}_{\text{eff}} - bp\boldsymbol{1} \quad \text{with} \quad \tilde{\boldsymbol{\sigma}}_{\text{eff}} = \frac{\gamma}{J} \big[\boldsymbol{F}\boldsymbol{F}^T - J^{-\beta} \boldsymbol{1} \big] \ . \tag{8.27}$$

Note that the term $(1-d)^2$ in front of $\tilde{\boldsymbol{P}}_{\text{eff}}$ implies a full degradation of the effective stress related to the solid skeleton contribution. The fluid contribution to the stress is not degraded within the crack. For the choice $b = 1$ we have the isotropic stress $\boldsymbol{\sigma} = -p\boldsymbol{1}$ inside the crack in terms of the fluid pressure p.

Constitutive chemical potential. An evaluation of the local dissipation inequality yields the constitutive equation for the chemical potential in terms of the free energy function as $\mu = \partial_m \hat{\psi}$, see (3.70). Evaluation of (8.18) leads to

$$\mu = \partial_m \hat{\psi} = \frac{M}{\rho^f} \left[\frac{m}{\rho^f} - b(J-1) \right] \ . \tag{8.28}$$

Note that the chemical potential μ is not affected by the state of fracture phase-field and hence valid in the unbroken bulk material as well as inside the crack.

Fluid pressure equation. For (8.28) to be an adequate constitutive equation within the crack we compare the rate of (8.28) to the rate of pressure relation (7.21) that was obtained by considering the lubrication theory inside the crack. To this end, taking the time derivative of (8.28) yields for the semilinear setting with $\rho^f \approx \rho_0^f$ and thus $\dot{\rho}^f \approx 0$ an evolution equation for the chemical potential

$$\dot{\mu} = \frac{1}{\rho^f} \dot{p} = \frac{M}{\rho^f} \left[\frac{\dot{m}}{\rho^f} - b\dot{J} \right] \ . \tag{8.29}$$

Inserting the fluid mass balance $(8.4)_1$ and using the identities $\text{Div}[\mathbb{H}] = J \, \text{div}[\mathbb{h}]$ as well as $\dot{J} = J \, \text{div}[\boldsymbol{v}]$ yields

$$\dot{p} = -MJ \left[\frac{1}{\rho^f} \, \text{div}[\mathbb{h}] + b \, \text{div}[\boldsymbol{v}] \right] \ . \tag{8.30}$$

Now consider the crack geometry visualized in Figure 7.2 with a crack in x and y direction and crack opening in z direction. In such a scenario the fluid mass flow in z direction is much smaller than in x and y direction, which is prescribed by the Poiseuille law, see

(8.37) below. Thus we assume the fluid velocity perpendicular to the crack surface to be negligible compared to the other two directions. Furthermore the crack opening is assumed to represent the main part of the solids deformation. Hence we draw the two assumptions

$$\mathbb{h} \approx \bar{v}_x \boldsymbol{e}_x + \bar{v}_y \boldsymbol{e}_y \quad \text{and} \quad \boldsymbol{v} \approx \frac{\partial w}{\partial t} \boldsymbol{e}_z \quad \text{in } \mathcal{C} \ . \tag{8.31}$$

Equation (8.30) with (8.31) and for the choice $b = 1$ is now compared to the fluid pressure rate equation (7.21) from the lubrication theory

$$\begin{aligned} &\text{lubrication :} \quad \dot{p} = -\kappa^f (\partial_x \bar{v}_x + \partial_y \bar{v}_y) \quad -\frac{\kappa^f}{w} \frac{\partial w}{\partial t} \qquad\qquad + \frac{w}{12\mu} \left[\frac{\partial w}{\partial x} \frac{\partial p}{\partial x} + \frac{\partial w}{\partial y} \frac{\partial p}{\partial y} \right] \\ &\text{constitutive :} \quad \dot{p} = -MJ(\partial_x \bar{v}_x + \partial_y \bar{v}_y) \quad -MJ \frac{\partial}{\partial z} \left(\frac{\partial w}{\partial t} \right) \ . \end{aligned} \tag{8.32}$$

Thus for $M = \kappa^f / J$ inside the crack, the difference is only due to the third term on the right hand side of $(8.32)_1$. However for a long crack with moderate opening width as assumed by the lubrication theory, the derivatives $\partial_x w$ and $\partial_y w$ are small and this term is negligible. Thus (8.28) seems to be a good approximation for the fluid's chemical potential μ also inside the crack. This consideration is in analogy to the observations in Vinci et al. [265] for the small strain regime. They also showed the very good agreement of the two approaches in numerical simulations.

Constitutive fluid flow in the bulk material and in cracks. Using the constitutive relation $(8.4)_7$ the driving force dual to the fluid flow vector is obtained as $\mathbb{B} = \partial_{\mathbb{H}} \hat{\phi}_{\text{con}}$. By ealuation of the dissipation potential function (8.22) we have

$$\hat{\mathbb{B}} = \widehat{\boldsymbol{K}}^{-1} \mathbb{H} \ . \tag{8.33}$$

In order to obtain a constitutive equation for the permeability tensor $\widehat{\boldsymbol{K}}$ which can model a Darcy-type fluid flow in the unbroken bulk material as well as a Poiseuille-type fluid flow within a crack we rewrite (8.33) as

$$\mathbb{H}(d) = \widehat{\boldsymbol{K}}(d) \mathbb{B} = -1/\rho^f \widehat{\boldsymbol{K}}(d) \cdot \nabla p \quad \text{with} \quad \nabla \mu = 1/\rho^f \nabla p \ . \tag{8.34}$$

Here we used the definition $\mathbb{B} = -\nabla \mu$ of the driving force given in $(8.4)_3$ and Gibb's relation for the gradient of the chemical potential.

Using the relationship $\mathbb{H} = J \boldsymbol{F}^{-1} \mathbb{h}$ and $\nabla(\cdot) = \boldsymbol{F}^T \nabla_{\boldsymbol{x}}(\cdot)$ yields the constitutive fluid flow per unit deformed area as

$$\mathbb{h}(d) = -1/\rho^f \widehat{\boldsymbol{k}}(d) \cdot \nabla_{\boldsymbol{x}} p \quad \text{with} \quad \widehat{\boldsymbol{k}} := \frac{1}{J} \boldsymbol{F} \widehat{\boldsymbol{K}} \boldsymbol{F}^T \ . \tag{8.35}$$

Note that (8.34) and (8.35) specify constitutively the fluid mass flow $\mathbb{H}$ and $\mathbb{h}$ both in the unbroken bulk material as well as within the crack. The transition between unbroken and broken material state is provided by the permeability tensor $\widehat{\boldsymbol{K}}(d)$. In the unbroken bulk material an isotropic Darcy-type fluid flow is assumed. According to (4.26) we have

$$\widehat{\boldsymbol{K}}(d=0) = \widehat{\boldsymbol{K}}_{\text{Darcy}} = (\rho^f)^2 K J \boldsymbol{C}^{-1} \quad \text{and} \quad \widehat{\boldsymbol{k}}(d=0) = \widehat{\boldsymbol{k}}_{\text{Darcy}} = (\rho^f)^2 K \boldsymbol{g}^{-1} \tag{8.36}$$

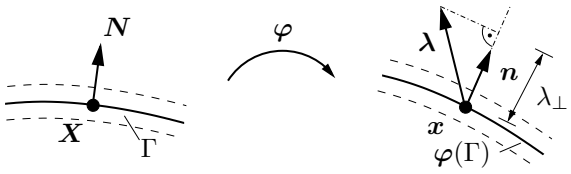

Figure 8.2: *Evaluation of crack opening width suiting the phase-field approach.* A line element $\boldsymbol{N}$ perpendicular to the material crack surface Γ deforms to $\boldsymbol{\lambda} = \boldsymbol{F}\boldsymbol{N}$ in the current configuration. A measure for the stretch perpendicular to the crack is the projection $\lambda_\perp = \boldsymbol{\lambda}\cdot\boldsymbol{n}$ onto the normal $\boldsymbol{n}$ on the deformed crack surface $\boldsymbol{\varphi}(\Gamma)$. $\lambda_\perp$ is used to estimate the crack opening width w.

at given state $\boldsymbol{F}$ in terms of the spatial permeability K, the Jacobian $J = \det[\boldsymbol{F}]$ and the right Cauchy-Green tensor $\boldsymbol{C}$.

When a crack opens the fluid transport changes. According to our considerations in Chapter 7 we do not explicitly model a Navier-Stokes- or Stokes-flow within the crack but account for the increased fluid flow by a *Poiseuille law*. Within our constitutive model this is done by adding a part to the mass flow vector

$$\mathbb{H} = \mathbb{H}_{\text{Darcy}} + \mathbb{H}_{\text{Crack}} \quad \text{with} \quad |\mathbb{H}_{\text{Crack}}| \propto \frac{1}{12\eta} w^2 \,, \tag{8.37}$$

where $\mathbb{H}_{\text{Crack}}$ is proportional to the square of the crack opening width w, see (7.14), and where η is the dynamic viscosity of the fluid. The additional mass flow can be written in the form

$$\mathbb{H}_{\text{Crack}} = -\widehat{\boldsymbol{K}}_{\text{Crack}} \cdot \nabla\mu \quad \text{with} \quad \|\widehat{\boldsymbol{K}}_{\text{Crack}}\| \propto \frac{w^2}{12\eta} \,. \tag{8.38}$$

Within the phase-field approach to fracture the location of a crack is described by the phase-field variable $d(\boldsymbol{X}, t)$. The crack opening width w however is not explicitly provided by the model. The idea is now to evaluate the crack opening width from the localized stretches in the crack perpendicular to its surface. Consider the crack scenario in Figure 8.2 that is regularized by the phase-field approach. $\boldsymbol{N}$ and $\boldsymbol{n}$ are the unit normals to the crack surface Γ in the reference and spatial configuration at the point $\boldsymbol{X} \in \mathcal{B}$ and $\boldsymbol{x} = \boldsymbol{\varphi}(\boldsymbol{X}) \in \mathcal{S}$. In a diffusive setting, if $\boldsymbol{N}$ is considered as material line element perpendicular to the crack,

$$\boldsymbol{\lambda} = \boldsymbol{F}\boldsymbol{N} \tag{8.39}$$

is the deformed line element in the current configuration, see Figure 8.2. However note that $\boldsymbol{\lambda}$ is not generally perpendicular to the deformed crack surface with normal $\boldsymbol{n}$. Splitting the stretch vector $\boldsymbol{\lambda}$ in normal and tangential components with respect to $\boldsymbol{n}$ may be interpreted in the diffusive phase-field setting as local mode I and II openings of the crack. Thus the mode I opening stretch is evaluated as

$$\lambda_\perp := \boldsymbol{\lambda} \cdot \boldsymbol{n} \,. \tag{8.40}$$

Furthermore the crack surface normals $\boldsymbol{N}$ and $\boldsymbol{n}$ in the material and spatial configuration are approximated by use of the phase-field variable d as

$$\boldsymbol{N} = \frac{\nabla d}{|\nabla d|} \quad \text{and} \quad \boldsymbol{n} = \frac{\nabla_{\boldsymbol{x}} d}{|\nabla_{\boldsymbol{x}} d|} = \frac{\boldsymbol{F}^{-T}\nabla d}{|\boldsymbol{F}^{-T}\nabla d|} \,. \tag{8.41}$$

Insertion of (8.41) into (8.40) and taking the square yields

$$\lambda_\perp^2 = \frac{\nabla d \cdot \nabla d}{\nabla d \cdot \boldsymbol{C}^{-1} \cdot \nabla d} \tag{8.42}$$

in terms of the right Cauchy-Green tensor $\boldsymbol{C}$ and the material gradient ∇d of the phase-field variable. Equation (8.42) constitutes an objective deformation measure from which the square of the crack opening width w^2 can be evaluated as

$$w^2 = \begin{cases} (\lambda_\perp - 1)^2 L_\perp^2 & \text{for } d > c \\ 0 & \text{otherwise .} \end{cases} \tag{8.43}$$

Here $c < 1$ defines a level set of crack phase-field that provides a numerical onset of the incorporation of Poiseuille-type fluid flow and $L_\perp = H^e$ is a given *characteristic length* of a line element perpendicular to the crack that in the numerical treatment is equal to a typical finite element size. As can be seen in the numerical boundary value problem Subsection 8.6.1, this assumption provides a good estimate of the crack opening w in extreme mesh distortions where the diffusive crack band covers just a few elements. With the crack opening width w at hand, the permeability tensor accounting for the Poiseuille-type fluid flow is defined in spatial configuration as

$$\widehat{\boldsymbol{k}}_{\text{Crack}} = (\rho^f)^2 K_c [\boldsymbol{g}^{-1} - (\boldsymbol{g}^{-1}\boldsymbol{n}) \otimes (\boldsymbol{g}^{-1}\boldsymbol{n})] \quad \text{with} \quad K_c = \frac{w^2}{12\eta} - K \ . \tag{8.44}$$

The material permeability tensor is then obtained by a pull-back of (8.44) as

$$\widehat{\boldsymbol{K}}_{\text{Crack}}(\boldsymbol{F}, \nabla d) = (\rho^f)^2 K_c J \left[\boldsymbol{C}^{-1} - \frac{1}{|\boldsymbol{F}^{-T}\nabla d|^2} (\boldsymbol{C}^{-1}\nabla d) \otimes (\boldsymbol{C}^{-1}\nabla d) \right] \ . \tag{8.45}$$

The overall permeability is now constructed by using a transition rule that interpolates between unbroken and fully broken response

$$\widehat{\boldsymbol{K}}(\boldsymbol{F}, d, \nabla d) = \widehat{\boldsymbol{K}}_{\text{Darcy}}(\boldsymbol{F}) + d^\epsilon \, \widehat{\boldsymbol{K}}_{\text{Crack}}(\boldsymbol{F}, \nabla d) \tag{8.46}$$

governed by the growing function d^ϵ with the additional material parameter $\epsilon \geq 1$.

8.2. Variational principle for the evolution problem

After introducing the functionals and constitutive functions we state the variational principles for the model problem of poro-hydro-elasticity at fracture. As before, a canonical *minimization principle* and two *saddle-point principles* are proposed.

8.2.1. Rate-type variational potential

Based on the energy E introduced in (8.10), the dissipation potential functional D in (8.12) and the external load functional P_{ext} in (8.16) the *three-field potential* is defined as

$$\underbrace{\Pi(\dot{\boldsymbol{\varphi}}, \mathbb{H}, \dot{d})}_{\text{rate potential}} := \underbrace{\frac{d}{dt} E(\boldsymbol{\varphi}, \mathbb{H}, d)}_{\text{rate of energy}} + \underbrace{D(\mathbb{H}, \dot{d})}_{\text{dissipation}} - \underbrace{P_{\text{ext}}(\dot{\boldsymbol{\varphi}}, \mathbb{H})}_{\text{external power}} \tag{8.47}$$

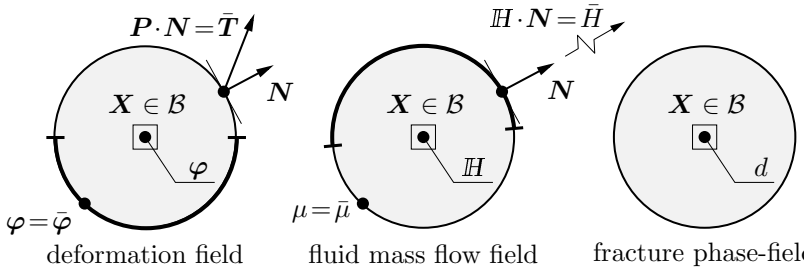

Figure 8.3: *Three-field minimization problem of poro-hydro-elasticity at fracture.* The boundary $\partial\mathcal{B}$ of the solid's reference configuration $\mathcal{B}$ is decomposed into Dirichlet and Neumann parts $\partial\mathcal{B}_{\boldsymbol{\varphi}} \cup \partial\mathcal{B}_T$ for the deformation field and $\partial\mathcal{B}_H \cup \partial\mathcal{B}_\mu$ for the fluid mass flow field. For the crack phase-field zero Neumann conditions are applied at the whole boundary $\partial\mathcal{B}$, see (8.8).

at a given state $\{\boldsymbol{\varphi}, m, d\}$. Evaluation of the rate potential by use of (8.11), (8.12) and (8.17) yields

$$\begin{aligned}\Pi(\dot{\boldsymbol{\varphi}}, \mathbb{H}, \dot{d}) = & \int_{\mathcal{B}} \left\{ \frac{\partial \hat{\psi}}{\partial \boldsymbol{F}} : \dot{\boldsymbol{F}} - \frac{\partial \hat{\psi}}{\partial m} \operatorname{Div}[\mathbb{H}] + \frac{\partial \hat{\psi}}{\partial d}\dot{d} + \frac{\partial \hat{\psi}}{\partial \nabla d} \cdot \nabla \dot{d} \right\} dV \\ & + \int_{\mathcal{B}} \left\{ \hat{\phi}_{\text{con}}(\mathbb{H}; \boldsymbol{F}, m, d) + \hat{\phi}_{\text{frac}}(\dot{d}) \right\} dV \\ & - \int_{\partial\mathcal{B}_{\boldsymbol{T}}} \bar{\boldsymbol{T}} \cdot \dot{\boldsymbol{\varphi}} \, dA + \int_{\partial\mathcal{B}_\mu} \bar{\mu} H \, dA \, ,\end{aligned} \tag{8.48}$$

where in the first integral the balance of fluid mass $\dot{m} = -\operatorname{Div}[\mathbb{H}]$ is used. Note that the potential Π is *linear* with respect to the rate $\dot{\boldsymbol{F}}$ and *convex* with respect to the fluid mass flow vector $\mathbb{H}$. The latter is due to the dissipation potential function $\hat{\phi}_{\text{con}}$, the convexity of which ensures a thermodynamically consistent formulation, see Subsection 3.4.3.

8.2.2. Rate-type variational minimization principle

With the rate-type potential (8.47) at hand, the *three-field variational minimization principle* is given by

$$\{\dot{\boldsymbol{\varphi}}, \mathbb{H}, \dot{d}\} = \arg \left\{ \inf_{\dot{\boldsymbol{\varphi}} \in \mathcal{W}_{\dot{\boldsymbol{\varphi}}}} \inf_{\mathbb{H} \in \mathcal{W}_{\mathbb{H}}} \inf_{\dot{d} \in \mathcal{W}_{\dot{d}}} \Pi(\dot{\boldsymbol{\varphi}}, \mathbb{H}, \dot{d}) \right\} \, , \tag{8.49}$$

which defines at the given state $\{\boldsymbol{\varphi}, m, d\}$ at time t the rates $\dot{\boldsymbol{\varphi}}$ and $\dot{d}$ of the deformation field and the fracture phase-field, as well as the fluid mass flow field $\mathbb{H}$. The admissible spaces for $\dot{\boldsymbol{\varphi}}$, $\dot{d}$ and $\mathbb{H}$ are

$$\begin{aligned}\mathcal{W}_{\dot{\boldsymbol{\varphi}}} &:= \{\dot{\boldsymbol{\varphi}} \in H^1(\mathcal{B}) |\ \dot{\boldsymbol{\varphi}} = \dot{\bar{\boldsymbol{\varphi}}} \text{ on } \partial\mathcal{B}_{\boldsymbol{\varphi}}\} \, , \\ \mathcal{W}_{\mathbb{H}} &:= \{\mathbb{H} \in H(\operatorname{Div}, \mathcal{B}) |\ \mathbb{H} \cdot \boldsymbol{N} = \bar{H} \text{ on } \partial\mathcal{B}_H\} \, , \\ \mathcal{W}_{\dot{d}} &:= \{\dot{d} \in H^1(\mathcal{B})\} \, .\end{aligned} \tag{8.50}$$

The necessary condition of the variational principle (8.49) is that its variation vanishes. Taking the variation of the potential (8.48) the Euler equations of the variational principle

are obtained as

$$\begin{aligned}
&\textit{Balance of linear momentum} && -\operatorname{Div}[\partial_{\boldsymbol{F}}\hat{\psi}] = \boldsymbol{0} && \text{in } \mathcal{B}\\
&\textit{Fluid flow equation} && \nabla[\partial_m\hat{\psi}] + \partial_{\mathbb{H}}\hat{\phi}_{\text{con}} = \boldsymbol{0} && \text{in } \mathcal{B}\\
&\textit{Fracture evolution} && \partial_d\hat{\psi} - \operatorname{Div}[\partial_{\nabla d}\hat{\psi}] + \partial_{\dot{d}}\hat{\phi}_{\text{frac}} \ni 0 && \text{in } \mathcal{B}\\
&\textit{Traction boundary conditions} && \partial_{\boldsymbol{F}}\hat{\psi}\cdot\boldsymbol{N} = \bar{\boldsymbol{T}} && \text{on } \partial\mathcal{B}_{\boldsymbol{T}}\\
&\textit{Potential boundary conditions} && \partial_m\hat{\psi} = \bar{\mu} && \text{on } \partial\mathcal{B}_{\mu}\\
&\textit{Phase-field boundary conditions} && \partial_{\nabla d}\hat{\psi}\cdot\boldsymbol{N} = 0 && \text{on } \partial\mathcal{B}
\end{aligned} \tag{8.51}$$

and turn out to be the linear momentum balance $(8.4)_2$, the fluid flow equation (8.34) in its inverse form and the phase-field evolution equation $(8.4)_4$, along with the Neumann boundary conditions (8.7). Note that the balance of fluid mass $(8.4)_1$ was used in (8.48) in order to express the rate of relative fluid content $\dot{m}$ by the fluid flow vector $\mathbb{H}$. Hence the fluid mass balance is fulfilled strongly. Furthermore note that the boundary conditions $(8.51)_6$ for the fracture phase-field d fulfill the thermodynamical constraint $(3.68)_3$ and hence the variational principle (8.49) constitutes a thermodynamically consistent model.

8.2.3. Rate-type mixed variational potential

A mixed variational principle is obtained by exchanging the dissipation potential functional $D(\mathbb{H})$ in (8.47) by the *extended* dissipation potential function $D^*(\mathbb{H}, \mathbb{B}, \dot{d})$ introduced in (8.14). The *mixed four-field potential* is hence defined as

$$\underbrace{\Pi^*(\dot{\boldsymbol{\varphi}}, \mathbb{H}, \mathbb{B}, \dot{d})}_{\text{rate potential}} := \underbrace{\frac{d}{dt}E(\boldsymbol{\varphi}, \mathbb{H}, d)}_{\text{rate of energy}} + \underbrace{D^*(\mathbb{H}, \mathbb{B}, \dot{d})}_{\text{dissipation}} - \underbrace{P_{\text{ext}}(\dot{\boldsymbol{\varphi}}, \mathbb{H})}_{\text{external power}} \tag{8.52}$$

at a given state $\{\boldsymbol{\varphi}, m, d\}$. Evaluation of this mixed rate potential by use of (8.11), (8.14) and (8.17) yields

$$\begin{aligned}
\Pi^*(\dot{\boldsymbol{\varphi}}, \mathbb{H}, \mathbb{B}, \dot{d}) = &\int_{\mathcal{B}} \left\{ \frac{\partial\hat{\psi}}{\partial\boldsymbol{F}} : \dot{\boldsymbol{F}} - \frac{\partial\hat{\psi}}{\partial m}\operatorname{Div}[\mathbb{H}] + \frac{\partial\hat{\psi}}{\partial d}\dot{d} + \frac{\partial\hat{\psi}}{\partial\nabla d}\cdot\nabla\dot{d} \right\} dV\\
&+ \int_{\mathcal{B}} \left\{ \mathbb{H}\cdot\mathbb{B} - \hat{\phi}^*_{\text{con}}(\mathbb{B}; \boldsymbol{F}, m, d) + \hat{\phi}_{\text{frac}}(\dot{d}) \right\} dV\\
&- \int_{\partial\mathcal{B}_{\boldsymbol{T}}} \bar{\boldsymbol{T}}\cdot\dot{\boldsymbol{\varphi}}\, dA + \int_{\partial\mathcal{B}_{\mu}} \bar{\mu}H\, dA\ ,
\end{aligned} \tag{8.53}$$

where in the first integral the balance of fluid mass $\dot{m} = -\operatorname{Div}[\mathbb{H}]$ is used. The potential Π^* is *linear* with respect to the rate of deformation gradient $\dot{\boldsymbol{F}}$ and the fluid mass flow vector $\mathbb{H}$ and *concave* with respect to the driving force vector $\mathbb{B}$. The latter is due to the dual dissipation potential function $\hat{\phi}^*_{\text{con}}$, the convexity of which is implied by the convexity of $\hat{\phi}_{\text{con}}$.

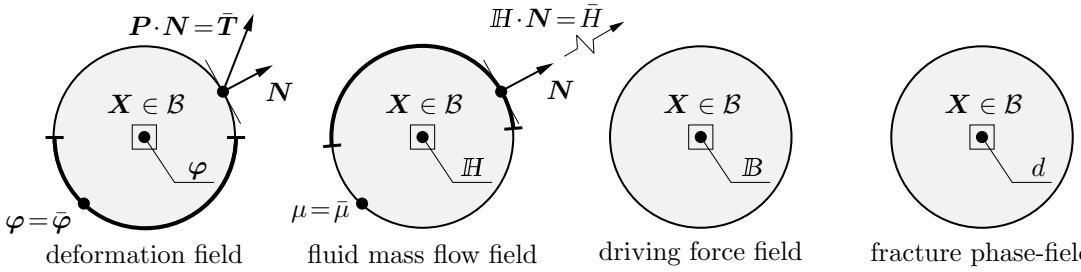

Figure 8.4: *Four-field saddle-point problem of poro-hydro-elasticity at fracture.* The boundary $\partial\mathcal{B}$ of the solid's reference configuration $\mathcal{B}$ is decomposed into Dirichlet and Neumann parts $\partial\mathcal{B}_{\boldsymbol{\varphi}} \cup \partial\mathcal{B}_T$ for the deformation field and $\partial\mathcal{B}_H \cup \partial\mathcal{B}_\mu$ for the fluid mass flow field. For the crack phase-field zero Neumann conditions are applied at the whole boundary $\partial\mathcal{B}$.

8.2.4. Rate-type variational saddle-point principle

With the rate-type potential (8.53) at hand, the *four-field mixed variational principle* is given by

$$\{\dot{\boldsymbol{\varphi}}, \mathbb{H}, \mathbb{B}, \dot{d}\} = \arg \left\{ \inf_{\dot{\boldsymbol{\varphi}} \in \mathcal{W}_{\dot{\boldsymbol{\varphi}}}} \inf_{\mathbb{H} \in \mathcal{W}_{\mathbb{H}}} \sup_{\mathbb{B} \in \mathcal{W}_{\mathbb{B}}} \inf_{\dot{d} \in \mathcal{W}_{\dot{d}}} \Pi^*(\dot{\boldsymbol{\varphi}}, \mathbb{H}, \mathbb{B}, \dot{d}) \right\} , \tag{8.54}$$

which defines at the given state $\{\boldsymbol{\varphi}, m, d\}$ at time t the rates $\dot{\boldsymbol{\varphi}}$ and $\dot{d}$ of the deformation field and fracture phase-field, the fluid mass flow field $\mathbb{H}$ and the dual driving force field $\mathbb{B}$. Note that due to the concavity of (8.53) with respect to $\mathbb{B}$ this variational principle has a *saddle-point structure*. The admissible spaces for $\dot{\boldsymbol{\varphi}}$, $\mathbb{H}$, $\mathbb{B}$ and $\dot{d}$ are

$$\begin{aligned} \mathcal{W}_{\dot{\boldsymbol{\varphi}}} &:= \{\dot{\boldsymbol{\varphi}} \in H^1(\mathcal{B}) |\ \dot{\boldsymbol{\varphi}} = \dot{\bar{\boldsymbol{\varphi}}} \text{ on } \partial\mathcal{B}_{\boldsymbol{\varphi}}\} , \\ \mathcal{W}_{\mathbb{H}} &:= \{\mathbb{H} \in H(\mathrm{Div}, \mathcal{B}) |\ \mathbb{H} \cdot \boldsymbol{N} = \bar{H} \text{ on } \partial\mathcal{B}_H\} , \\ \mathcal{W}_{\mathbb{B}} &:= \{\mathbb{B} \in L^2\} , \\ \mathcal{W}_{\dot{d}} &:= \{\dot{d} \in H^1(\mathcal{B})\} . \end{aligned} \tag{8.55}$$

The necessary condition of the variational principle (8.54) is that its variation vanishes. Taking the variation of the potential (8.53) the Euler equations of the variational principle are obtained as

$$\begin{aligned} &\textit{Balance of linear momentum} && -\mathrm{Div}[\partial_{\boldsymbol{F}}\hat{\psi}] = \boldsymbol{0} && \text{in } \mathcal{B} \\ &\textit{Constitutive driving force} && \nabla\partial_m\hat{\psi} + \mathbb{B} = \boldsymbol{0} && \text{in } \mathcal{B} \\ &\textit{Fluid flow equation} && \mathbb{H} - \partial_{\mathbb{B}}\hat{\phi}^*_{\mathrm{con}} = \boldsymbol{0} && \text{in } \mathcal{B} \\ &\textit{Fracture evolution} && \partial_d\hat{\psi} - \mathrm{Div}[\partial_{\nabla d}\hat{\psi}] + \partial_{\dot{d}}\hat{\phi}_{\mathrm{frac}} \ni 0 && \text{in } \mathcal{B} \\ &\textit{Traction boundary conditions} && \partial_{\boldsymbol{F}}\hat{\psi} \cdot \boldsymbol{N} = \bar{\boldsymbol{T}} && \text{on } \partial\mathcal{B}_{\boldsymbol{T}} \\ &\textit{Potential boundary conditions} && \partial_m\hat{\psi} = \bar{\mu} && \text{on } \partial\mathcal{B}_\mu \\ &\textit{Phase-field boundary conditions} && \partial_{\nabla d}\hat{\psi} \cdot \boldsymbol{N} = 0 && \text{on } \partial\mathcal{B} \end{aligned} \tag{8.56}$$

and turn out to be the governing equations $(8.4)_2$, $(8.4)_3$, the fluid flow equation (8.34) in its inverse form and the phase-field evolution equation $(8.4)_4$, along with the Neumann boundary conditions (8.7). Note that the balance of fluid mass $(8.4)_1$ was used in (8.53) in order to express the rate of relative fluid content $\dot{m}$ by the fluid flow vector $\mathbb{H}$. Hence the fluid mass balance is fulfilled strongly. Again the boundary conditions $(8.56)_7$ for the fracture phase-field d fulfill the thermodynamical constraint $(3.68)_3$ and hence the variational principle (8.54) constitutes a thermodynamically consistent model.

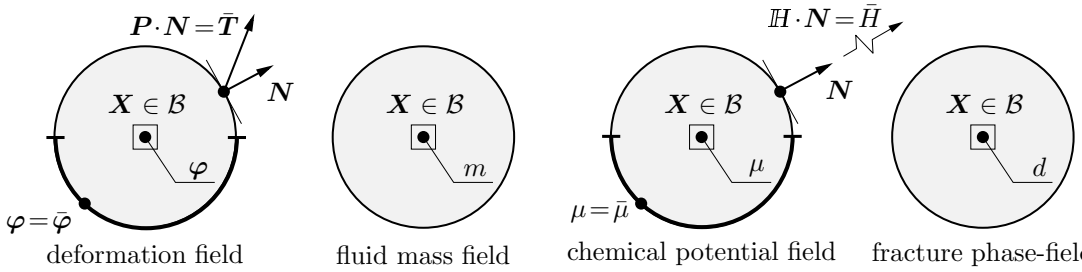

Figure 8.5: *Four-field reduced saddle-point problem of poro-hydro-elasticity at fracture.* The boundary $\partial\mathcal{B}$ of the solid's reference configuration $\mathcal{B}$ is decomposed into Dirichlet and Neumann parts $\partial\mathcal{B}_{\boldsymbol{\varphi}} \cup \partial\mathcal{B}_T$ for the deformation field and $\partial\mathcal{B}_\mu \cup \partial\mathcal{B}_H$ for the chemical potential field. For the crack phase-field zero Neumann conditions are applied at the whole boundary $\partial\mathcal{B}$.

8.2.5. Reduced rate-type mixed variational potential

The mixed variational principle (8.54) is an initial boundary value problem containing ten scalar unknown fields $\{\dot{\boldsymbol{\varphi}}, H, \mathbb{B}, \dot{d}\}$. Based on the knowledge of the Euler equation $(8.56)_3$ the unknown fields can be reduced to six. To this end, we introduce the chemical potential field $\mu = \partial_m \hat{\psi}$, see (3.70). Hence $(8.56)_3$ can be rewritten as

$$\mathbb{B} = -\nabla\mu \text{ in } \mathcal{B} \,. \tag{8.57}$$

Thus by reinsertion of the fluid mass balance and by use of (8.57), a *reduced mixed four-field potential* can be obtained from (8.53) as

$$\begin{aligned}\tilde{\Pi}^*(\dot{\boldsymbol{\varphi}}, \dot{m}, \mu, \dot{d}) = & \int_{\mathcal{B}} \Big\{ \frac{\partial\hat{\psi}}{\partial\boldsymbol{F}} : \dot{\boldsymbol{F}} + \frac{\partial\hat{\psi}}{\partial m}\dot{m} + \frac{\partial\hat{\psi}}{\partial d}\dot{d} + \frac{\partial\hat{\psi}}{\partial\nabla d}\cdot\nabla\dot{d} \Big\}\, dV \\ & + \int_{\mathcal{B}} \big\{ -\mu\dot{m} - \hat{\phi}^*_{\text{con}}(\mathbb{B}; \boldsymbol{F}, m, d) + \hat{\phi}_{\text{frac}}(\dot{d}) \big\}\, dV \\ & - \int_{\partial\mathcal{B}_{\boldsymbol{T}}} \bar{\boldsymbol{T}}\cdot\dot{\boldsymbol{\varphi}}\, dA - \int_{\partial\mathcal{B}_H} \mu\bar{H}\, dA \,.\end{aligned} \tag{8.58}$$

Note that in order to obtain (8.58) the boundary conditions $(8.7)_2$ have to be evaluated. The potential $\tilde{\Pi}^*$ is *linear* with respect to the rates $\dot{\boldsymbol{F}}$ and $\dot{m}$ and *concave* with respect to the chemical potential field μ. The latter is due to the dual dissipation potential function $\hat{\phi}^*_{\text{con}}$, the convexity of which is implied by the convexity of $\hat{\phi}_{\text{con}}$.

8.2.6. Reduced rate-type variational saddle-point principle

With the reduced rate-type potential (8.58) at hand, we can state a *reduced mixed four-field variational principle*

$$\{\dot{\boldsymbol{\varphi}}, \dot{m}, \mu, \dot{d}\} = \arg \left\{ \inf_{\dot{\boldsymbol{\varphi}}\in\mathcal{W}_{\dot{\boldsymbol{\varphi}}}} \inf_{\dot{m}\in\mathcal{W}_{\dot{m}}} \sup_{\mu\in\mathcal{W}_\mu} \inf_{\dot{d}\in\mathcal{W}_{\dot{d}}} \tilde{\Pi}^*(\dot{\boldsymbol{\varphi}}, \dot{m}, \mu, \dot{d}) \right\} \tag{8.59}$$

which defines the rates of deformation $\dot{\boldsymbol{\varphi}}$, the relative fluid mass content $\dot{m}$ and the fracture phase-field $\dot{d}$ as well as the chemical potential μ at given state $\{\boldsymbol{\varphi}, m, d\}$ at time t. Due to the concavity of the potential $\tilde{\Pi}^*$ with respect to μ the principle has a *saddle-point*

structure. The admissible spaces for $\dot{\boldsymbol{\varphi}}$,$\dot{m}$, μ and $\dot{d}$ are

$$\begin{aligned} \mathcal{W}_{\dot{\boldsymbol{\varphi}}} &:= \{\dot{\boldsymbol{\varphi}} \in H^1(\mathcal{B}) |\ \dot{\boldsymbol{\varphi}} = \dot{\bar{\boldsymbol{\varphi}}} \text{ on } \partial\mathcal{B}_{\boldsymbol{\varphi}}\} \ , \\ \mathcal{W}_{\dot{m}} &:= \{\dot{m} \in L^2\} \ , \\ \mathcal{W}_{\mu} &:= \{\mu \in H^1(\mathcal{B}) |\ \mu = \bar{\mu} \text{ on } \partial\mathcal{B}_{\mu}\} \ , \\ \mathcal{W}_{\dot{d}} &:= \{\dot{d} \in H^1(\mathcal{B})\} \ . \end{aligned} \tag{8.60}$$

The necessary condition of the variational principle (8.59) is that its variation vanishes. Taking the variation of the potential (8.58) the Euler equations of the variational principle are obtained as

$$\begin{aligned} &\textit{Balance of linear momentum} && -\operatorname{Div}[\partial_{\boldsymbol{F}}\hat{\psi}] = \boldsymbol{0} && \text{in } \mathcal{B} \\ &\textit{Constitutive chemical potential} && \partial_m\hat{\psi} - \mu = 0 && \text{in } \mathcal{B} \\ &\textit{Balance of fluid mass} && -\dot{m} - \operatorname{Div}[\partial_{\mathbb{B}}\hat{\phi}^{\text{con}*}] = 0 && \text{in } \mathcal{B} \\ &\textit{Fracture evolution} && \partial_d\hat{\psi} - \operatorname{Div}[\partial_{\nabla d}\hat{\psi}] + \partial_{\dot{d}}\hat{\phi}_{\text{frac}} \ni 0 && \text{in } \mathcal{B} \\ &\textit{Traction boundary conditions} && \partial_{\boldsymbol{F}}\hat{\psi} \cdot \boldsymbol{N} = \bar{\boldsymbol{T}} && \text{on } \partial\mathcal{B}_{\boldsymbol{T}} \\ &\textit{Flux boundary conditions} && \partial_{\mathbb{B}}\hat{\phi}^{\text{con}*} \cdot \boldsymbol{N} = \bar{H} && \text{on } \partial\mathcal{B}_{H} \\ &\textit{Phase-field boundary conditions} && \partial_{\nabla d}\hat{\psi} \cdot \boldsymbol{N} = 0 && \text{on } \partial\mathcal{B} \end{aligned} \tag{8.61}$$

and turn out to be the governing equations $(8.4)_2$, $(8.4)_1$, $(8.4)_6$ and $(8.4)_4$, along with the Neumann boundary conditions (8.7). Note that in contrast to the other two variational principles $\partial\mathcal{B}_H$ is the Neumann boundary and $\partial\mathcal{B}_\mu$ is the Dirichlet boundary. Again the boundary conditions $(8.61)_7$ for the fracture phase-field d fulfill the thermodynamical constraint $(3.68)_3$ and hence the variational principle (8.59) constitutes a thermodynamically consistent model.

8.3. Incremental variational principle for the update problem

We now perform a time-discretization of the rate-type variational principles introduced above. The procedure closely follows the considerations of Miehe [176]. Here, as most convenient for the numerical treatment, we restrict our attention to the minimization principle and the reduced mixed saddle-point principle introduced in Subsection 8.2.2 and Subsection 8.2.6.

8.3.1. Time-discretization and incremental variational potentials

Consider discrete points in time $[t_0, ..., t_n, t_{n+1}, ..., t_\infty]$ of the process time $[t_0, t_\infty]$. Here $\tau := t_{n+1} - t_n$ is the time step size. The objective is now to determine the unknown fields at time t_{n+1}, whereas all fields at time t_n are assumed to be known. The rate of a quantity $\dot{q}(t)$ is considered to be constant within a time step τ and thus can be written as $\dot{q}_{n+1}(t_{n+1}) = (q_{n+1} - q_n)/\tau$. For sake of a compact notation in the further considerations all subscripts $n+1$ are dropped, such that all variables without index are associated with time t_{n+1}.

Canonical three-field potential. The incremental counterpart of the variational functional Π given in (8.48) within the time step $[t_n, t]$ under consideration is obtained from an algorithmic integration scheme. With the above stated assumption of *constant* rates of field quantities within a time step the incremental potential is considered of the form

$$\begin{aligned}\Pi^\tau(\boldsymbol{\varphi}, \mathbb{H}, d) = & \int_{\mathcal{B}} \left\{ \hat{\psi}(\boldsymbol{F}, m, d; d_n) - \hat{\psi}_n + \tau \hat{\phi}_{\text{con}}(\mathbb{H}; \boldsymbol{F}_n, m_n, d_n) + \tau \hat{\phi}_{\text{frac}}(d) \right\} dV \\ & - \int_{\partial \mathcal{B}_{\boldsymbol{T}}} \bar{\boldsymbol{T}} \cdot [\boldsymbol{\varphi} - \boldsymbol{\varphi}_n] \, dA + \int_{\partial \mathcal{B}_\mu} \tau \bar{\mu} H \, dA \, ,\end{aligned} \tag{8.62}$$

where we introduced $\hat{\psi}_n = \hat{\psi}(\boldsymbol{F}_n, m_n, d_n)$. Note that the convective dissipation potential $\hat{\phi}_{\text{con}}(\mathbb{H}; \boldsymbol{F}_n, m_n, d_n)$ is evaluated at frozen state $\{\boldsymbol{F}_n, m_n, d_n\}$ of deformation gradient, relative fluid mass and fracture phase-field at time t_n.

Reduced mixed four-field potential. The incremental counterpart of the canonical variational functional $\tilde{\Pi}^{*\tau}$ given in (8.58) within the time step $[t_n, t]$ under consideration is also obtained from an algorithmic integration scheme. Again assuming *constant* rates of field quantities within a time step the incremental potential is considered of the form

$$\begin{aligned}\tilde{\Pi}^{*\tau}(\boldsymbol{\varphi}, m, \mu, d) = & \int_{\mathcal{B}} \left\{ \hat{\psi}(\boldsymbol{F}, m, d; d_n) - \hat{\psi}_n \right\} dV \\ & + \int_{\mathcal{B}} \left\{ -\mu(m - m_n) - \tau \hat{\phi}^*_{\text{con}}(\mathbb{B}; \boldsymbol{F}_n, m_n, d_n) + \tau \hat{\phi}_{\text{frac}}(d) \right\} dV \\ & - \int_{\partial \mathcal{B}_{\boldsymbol{T}}} \bar{\boldsymbol{T}} \cdot [\boldsymbol{\varphi} - \boldsymbol{\varphi}_n] \, dA - \int_{\partial \mathcal{B}_H} \tau \mu \bar{H} \, dA \, .\end{aligned} \tag{8.63}$$

Note that the dual convective dissipation potential $\hat{\phi}^*_{\text{con}}(\mathbb{B}; \boldsymbol{F}_n, m_n, d_n)$ is evaluated at frozen state $\{\boldsymbol{F}_n, m_n, d_n\}$ at time t_n.

8.3.2. Incremental canonical variational minimization principle

With the incremental potential (8.62) at hand, the time-discrete counterpart of the *canonical three-field variational principle* (8.49) can be stated as

$$\{\boldsymbol{\varphi}, \mathbb{H}, d\} = \arg \left\{ \inf_{\boldsymbol{\varphi} \in \mathcal{W}_{\boldsymbol{\varphi}}} \inf_{\mathbb{H} \in \mathcal{W}_{\mathbb{H}}} \inf_{d \in \mathcal{W}_d} \Pi^\tau(\boldsymbol{\varphi}, \mathbb{H}, d) \right\} \, . \tag{8.64}$$

The variational principle determines the fields $\boldsymbol{\varphi}$, $\mathbb{H}$ and d at current time t as a *minimum* of the time-discrete potential Π^τ. The admissible spaces for the time-discrete fields are

$$\begin{aligned}\mathcal{W}_{\boldsymbol{\varphi}} &:= \{\boldsymbol{\varphi} \in H^1(\mathcal{B}) | \ \boldsymbol{\varphi} = \bar{\boldsymbol{\varphi}} \text{ on } \partial \mathcal{B}_{\boldsymbol{\varphi}}\} \, , \\ \mathcal{W}_{\mathbb{H}} &:= \{\mathbb{H} \in H(\text{Div}, \mathcal{B}) | \ \mathbb{H} \cdot \boldsymbol{N} = \bar{H} \text{ on } \partial \mathcal{B}_H\} \, , \\ \mathcal{W}_d &:= \{d \in H^1(\mathcal{B})\} \, .\end{aligned} \tag{8.65}$$

The necessary condition of the variational principle (8.64) is that its variation vanishes. Taking the variation of the potential (8.62) the Euler equations of the variational principle

are obtained as

$$\begin{aligned}
&\textit{Balance of linear momentum} && -\operatorname{Div}[\partial_{\boldsymbol{F}}\hat{\psi}] = \boldsymbol{0} && \text{in } \mathcal{B}\\
&\textit{Fluid flow equation} && \tau\nabla\partial_m\hat{\psi} + \tau\partial_{\mathbb{H}}\hat{\phi}_{\text{con}} = \boldsymbol{0} && \text{in } \mathcal{B}\\
&\textit{Fracture evolution} && \partial_d\hat{\psi} - \operatorname{Div}[\partial_{\nabla d}\hat{\psi}] + \tau\partial_d\hat{\phi}_{\text{frac}} \ni 0 && \text{in } \mathcal{B}\\
&\textit{Traction boundary conditions} && \partial_{\boldsymbol{F}}\hat{\psi}\cdot\boldsymbol{N} = \bar{\boldsymbol{T}} && \text{on } \partial\mathcal{B}_{\boldsymbol{T}}\\
&\textit{Potential boundary conditions} && \tau\partial_m\hat{\psi} = \tau\bar{\mu} && \text{on } \partial\mathcal{B}_{\mu}\\
&\textit{Phase-field boundary conditions} && \partial_{\nabla d}\hat{\psi}\cdot\boldsymbol{N} = 0 && \text{on } \partial\mathcal{B}
\end{aligned} \tag{8.66}$$

These are the algorithmic counterparts of the Euler equations (8.51) representing the linear momentum balance $(8.4)_2$, the time-discrete fluid flow equation (8.34) in its inverse form and the time-discrete phase-field evolution equation $(8.4)_4$, along with the Neumann boundary conditions (8.7). Here the algorithmic balance of fluid mass

$$m = m_n + \tau\operatorname{Div}[\mathbb{H}] \tag{8.67}$$

is used in (8.66) in order to express the relative fluid content m in terms of the fluid flow vector $\mathbb{H}$. The fluid mass balance is hence fulfilled strongly. The boundary conditions $(8.66)_6$ for the fracture phase-field d fulfill the thermodynamical constraint $(3.68)_3$.

8.3.3. Incremental reduced mixed variational saddle-point principle

The incremental potential (8.63) leads to the time-discrete counterpart of the *mixed four-field variational principle* (8.59) for the coupled problem and is given by

$$\{\boldsymbol{\varphi}, m, \mu, d\} = \arg\left\{\inf_{\boldsymbol{\varphi}\in\mathcal{W}_{\boldsymbol{\varphi}}}\ \inf_{m\in\mathcal{W}_m}\ \sup_{\mu\in\mathcal{W}_\mu}\ \inf_{d\in\mathcal{W}_d}\ \tilde{\Pi}^{*\tau}(\boldsymbol{\varphi}, m, \mu, d)\right\} . \tag{8.68}$$

It determines the fields $\boldsymbol{\varphi}$, m, μ and d at current time t as a *saddle-point* of the time-discrete potential $\tilde{\Pi}^{*\tau}$. The admissible spaces for the time-discrete fields are

$$\begin{aligned}
\mathcal{W}_{\boldsymbol{\varphi}} &:= \{\boldsymbol{\varphi}\in H^1(\mathcal{B})|\ \boldsymbol{\varphi} = \bar{\boldsymbol{\varphi}} \text{ on } \partial\mathcal{B}_{\boldsymbol{\varphi}}\} ,\\
\mathcal{W}_m &:= \{m\in L^2\} ,\\
\mathcal{W}_\mu &:= \{\mu\in H^1(\mathcal{B})|\ \mu = \bar{\mu} \text{ on } \partial\mathcal{B}_\mu\} ,\\
\mathcal{W}_d &:= \{d\in H^1(\mathcal{B})\} .
\end{aligned} \tag{8.69}$$

The necessary condition of the variational principle (8.68) is that its variation vanishes. Taking the variation of the potential (8.63) the Euler equations of the variational principle are obtained as

$$\begin{aligned}
&\textit{Balance of linear momentum} && -\operatorname{Div}[\partial_{\boldsymbol{F}}\hat{\psi}] = \boldsymbol{0} && \text{in } \mathcal{B}\\
&\textit{Constitutive chemical potential} && \partial_m\hat{\psi} - \mu = 0 && \text{in } \mathcal{B}\\
&\textit{Balance of fluid mass} && -[m - m_n] - \tau\operatorname{Div}[\partial_{\mathbb{B}}\hat{\phi}_{\text{con}*}] = 0 && \text{in } \mathcal{B}\\
&\textit{Fracture evolution} && \partial_d\hat{\psi} - \operatorname{Div}[\partial_{\nabla d}\hat{\psi}] + \tau\partial_d\hat{\phi}_{\text{frac}} \ni 0 && \text{in } \mathcal{B}\\
&\textit{Traction boundary conditions} && \partial_{\boldsymbol{F}}\hat{\psi}\cdot\boldsymbol{N} = \bar{\boldsymbol{T}} && \text{on } \partial\mathcal{B}_{\boldsymbol{T}}\\
&\textit{Flux boundary conditions} && \tau\partial_{\mathbb{B}}\hat{\phi}_{\text{con}*}\cdot\boldsymbol{N} = \tau\bar{H} && \text{on } \partial\mathcal{B}_H\\
&\textit{Phase-field boundary conditions} && \partial_{\nabla d}\hat{\psi}\cdot\boldsymbol{N} = 0 && \text{on } \partial\mathcal{B}
\end{aligned} \tag{8.70}$$

These are the algorithmic counterparts of the continuous governing equations $(8.4)_2$, $(8.4)_1$, $(8.4)_6$ and $(8.4)_4$, together with the Neumann boundary conditions (8.7). Note that in contrast to the variational minimization principle $\partial\mathcal{B}_H$ is the Neumann boundary and $\partial\mathcal{B}_\mu$ is the Dirichlet boundary. The boundary conditions $(8.70)_7$ for the fracture phase-field d fulfill the thermodynamical constraint $(3.68)_3$.

8.4. Space-discrete incremental variational principle

In what follows the time-discrete variational principles (8.64) and (8.68) are discretized in space by use of the finite element method. To this end, first the finite element approximations of the geometry and the fields of unknowns are introduced. Then the space-time-discrete variational principle is stated. In the following the finite element approximation of the poro-elastic solid without fracture in Section 4.4 is extended by the interpolation of the phase-field variable d.

8.4.1. Finite element approximation

Before stating the space-discrete incremental variational principles, we first introduce the finite element approximations of the unknown fields $\boldsymbol{\varphi}$, $\mathbb{H}$, μ and d. The considerations here are in analogy to the finite element approximation in Subsection 4.4.1 for porous media. The only difference is the additional interpolation of the crack phase-field d. Thus we directly introduce the approximations on the parent element $\mathcal{A}$ and the global interpolation for the unknown fields. Within the isoparametric setting the interpolations of the unknown fields within an element $\mathcal{B}^e$ are based on shape functions in terms of the parent element's coordinates $\boldsymbol{\xi}$ and in particular given as an extension of (4.60) by

$$\begin{aligned} \boldsymbol{\varphi}^e(\boldsymbol{X}) &= \sum_{i=1}^{m_{\boldsymbol{\varphi}}} \hat{N}^i_{\boldsymbol{\varphi}}\left(\boldsymbol{\xi} = \boldsymbol{X}^{e-1}(\boldsymbol{X})\right) \boldsymbol{\varphi}^i \,, \quad \mathbb{H}^e(\boldsymbol{X}) = \sum_{i=1}^{m_{\mathbb{H}}} \hat{N}^i_{\mathbb{H}}\left(\boldsymbol{\xi} = \boldsymbol{X}^{e-1}(\boldsymbol{X})\right) \mathbb{H}^i \,, \\ \mu^e(\boldsymbol{X}) &= \sum_{i=1}^{m_{\mu}} \hat{N}^i_{\mu}\left(\boldsymbol{\xi} = \boldsymbol{X}^{e-1}(\boldsymbol{X})\right) \mu^i \,, \quad d^e(\boldsymbol{X}) = \sum_{i=1}^{m_{d}} \hat{N}^i_{d}\left(\boldsymbol{\xi} = \boldsymbol{X}^{e-1}(\boldsymbol{X})\right) d^i \,. \end{aligned} \tag{8.71}$$

Here we introduced the local shape functions $\hat{N}^i_{\boldsymbol{\varphi}}(\boldsymbol{\xi})$, $\hat{N}^i_{\mathbb{H}}(\boldsymbol{\xi})$, $\hat{N}^i_{\mu}(\boldsymbol{\xi})$ and $\hat{N}^i_{d}$ associated to $m_{\boldsymbol{\varphi}}$, $m_{\mathbb{H}}$, m_{μ} and m_d interpolation points with discrete values $\boldsymbol{\varphi}^i$, $\mathbb{H}^i$, μ^i and d^i in $\mathcal{B}^e$. The transformation from parameter space to physical space for isoparametric finite elements is conducted by the invertible geometry mapping $\boldsymbol{X}^e(\boldsymbol{\xi})$ introduced in (4.59). Furthermore it is possible to interpolate the global fields in the whole domain $\mathcal{B}^h$ by the

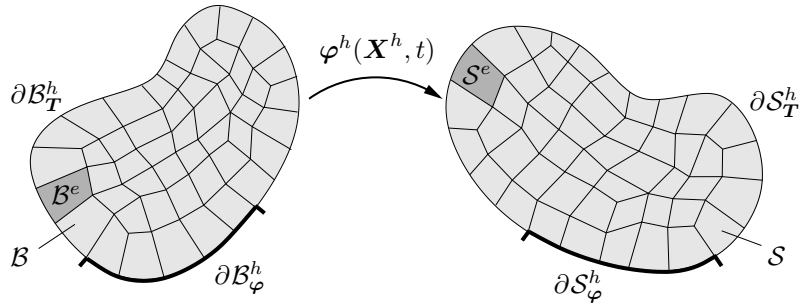

Figure 8.6: *Finite element discretization.* The material body $\mathcal{B}$ is approximated by the discrete body $\mathcal{B}^h \approx \mathcal{B}$. The discretization $\mathcal{B}^h$ is the union of n_e finite elements $\mathcal{B}^e$. The deformation field $\boldsymbol{\varphi}$ and all other unknown fields are approximated based on discrete values at interpolation points and so-called shape functions.

approximations

$$\begin{aligned}
\boldsymbol{\varphi}(\boldsymbol{X}) \approx \boldsymbol{\varphi}^h(\boldsymbol{X}) &= \sum_{I=1}^{M_{\boldsymbol{\varphi}}} N^I_{\boldsymbol{\varphi}}(\boldsymbol{X})\boldsymbol{\varphi}^I &&=: \underline{\mathbf{N}}_{\boldsymbol{\varphi}}\underline{\mathbf{d}}_{\boldsymbol{\varphi}} \,, \\
\mathbb{H}(\boldsymbol{X}) \approx \mathbb{H}^h(\boldsymbol{X}) &= \sum_{I=1}^{M_{\mathbb{H}}} N^I_{\mathbb{H}}(\boldsymbol{X})\mathbb{H}^I &&=: \underline{\mathbf{N}}_{\mathbb{H}}\underline{\mathbf{d}}_{\mathbb{H}} \,, \\
\mu(\boldsymbol{X}) \approx \mu^h(\boldsymbol{X}) &= \sum_{I=1}^{M_{\mu}} N^I_{\mu}(\boldsymbol{X})\mu^I &&=: \underline{\mathbf{N}}_{\mu}\underline{\mathbf{d}}_{\mu} \,, \\
d(\boldsymbol{X}) \approx d^h(\boldsymbol{X}) &= \sum_{I=1}^{M_{d}} N^I_{d}(\boldsymbol{X})d^I &&=: \underline{\mathbf{N}}_{d}\underline{\mathbf{d}}_{d} \,.
\end{aligned} \tag{8.72}$$

in terms of global vectors $\underline{\mathbf{d}}_{\boldsymbol{\varphi}}$, $\underline{\mathbf{d}}_{\mathbb{H}}$, $\underline{\mathbf{d}}_{\mu}$ and $\underline{\mathbf{d}}_{d}$ containing $M_{\boldsymbol{\varphi}}$, $M_{\mathbb{H}}$, M_{μ} and M_d global discrete values of unknowns $\boldsymbol{\varphi}^I$, $\mathbb{H}^I$, μ^I and d^I. Furthermore we introduced the global matrices $\underline{\mathbf{N}}_{\boldsymbol{\varphi}}$, $\underline{\mathbf{N}}_{\mathbb{H}}$, $\underline{\mathbf{N}}_{\mu}$ and $\underline{\mathbf{N}}_{d}$ containing the shape functions $N^I_{\boldsymbol{\varphi}}$, $N^I_{\mathbb{H}}$, N^I_{μ} and N^I_{d}. For a connection between the shape functions $N^I_{(\cdot)}(\boldsymbol{X}) \in \mathcal{B}^h$ and $\hat{N}^i_{(\cdot)}(\boldsymbol{\xi}) \in \mathcal{A}$, see Subsection 4.4.1. Besides the interpolations of the fields $\boldsymbol{\varphi}^h$, $\mathbb{H}^h$, μ^h and d^h itself also derivatives of these fields are needed. In particular these are the material gradients $\boldsymbol{F} = \nabla\boldsymbol{\varphi}$, $\nabla\mu$ and ∇d of the deformation, chemical potential and crack phase-field as well as the material divergence $\mathrm{Div}[\mathbb{H}]$ of the fluid mass flow vector. Using the Voigt notation to rewrite the tensorial deformation gradient $\boldsymbol{F}$ as a vectorial object we write as an extension of (4.67)

$$\begin{aligned}
\boldsymbol{F}(\boldsymbol{X}) \approx \boldsymbol{F}^h(\boldsymbol{X}) &= \underline{\mathbf{B}}_{\boldsymbol{F}}\underline{\mathbf{d}}_{\boldsymbol{\varphi}} \,, \quad & \mathrm{Div}[\mathbb{H}](\boldsymbol{X}) \approx \mathrm{Div}[\mathbb{H}^h](\boldsymbol{X}) &= \underline{\mathbf{B}}_{m}\underline{\mathbf{d}}_{\mathbb{H}} \,, \\
\nabla\mu(\boldsymbol{X}) \approx \nabla\mu^h(\boldsymbol{X}) &= \underline{\mathbf{B}}_{\nabla\mu}\underline{\mathbf{d}}_{\mu} \,, & \nabla d(\boldsymbol{X}) \approx \nabla d^h(\boldsymbol{X}) &= \underline{\mathbf{B}}_{\nabla d}\underline{\mathbf{d}}_{d} \,,
\end{aligned} \tag{8.73}$$

where $\underline{\mathbf{B}}_{\boldsymbol{F}}$, $\underline{\mathbf{B}}_{m}$, $\underline{\mathbf{B}}_{\nabla\mu}$ and $\underline{\mathbf{B}}_{\nabla d}$ are symbolic representations of global matrices of shape function derivatives. For an explicit definition for nodal-based degrees of freedom and scalar-valued shape functions see Subsection 4.4.1.

8.4.2. Space-time-discrete canonical variational minimization principle

For the minimization formulation the unknown fields are the deformation map $\boldsymbol{\varphi}$, the fluid flow vector $\mathbb{H}$ and the fracture phase-field d, see (8.62). Hence we introduce the

global vector of unknowns $\underline{\mathbf{d}}$ of the space-discrete system

$$\underline{\mathbf{d}} = \left[\underline{\mathbf{d}}_{\boldsymbol{\varphi}} , \underline{\mathbf{d}}_{\mathbb{H}} , \underline{\mathbf{d}}_{d} \right]^T \ . \tag{8.74}$$

With (8.74) at hand, the space-discrete fields (8.72) can be rewritten as

$$\boldsymbol{\varphi}^h(\boldsymbol{X}) = \underline{\mathbf{N}}_{\boldsymbol{\varphi}} \underline{\mathbf{d}}_{\boldsymbol{\varphi}} = \hat{\underline{\mathbf{N}}}_{\boldsymbol{\varphi}} \underline{\mathbf{d}} \ , \quad \mathbb{H}^h(\boldsymbol{X}) = \underline{\mathbf{N}}_{\mathbb{H}} \underline{\mathbf{d}}_{\mathbb{H}} = \hat{\underline{\mathbf{N}}}_{\mathbb{H}} \underline{\mathbf{d}} \ , \quad d^h(\boldsymbol{X}) = \underline{\mathbf{N}}_{d} \underline{\mathbf{d}}_{d} = \hat{\underline{\mathbf{N}}}_{d} \underline{\mathbf{d}} \ . \tag{8.75}$$

Furthermore we introduce the vector of *constitutive state* $\mathbf{f} := [\boldsymbol{F}, \mathrm{Div}[\mathbb{H}], \mathbb{H}, d, \nabla d]^T$. With the approximations (8.73), (8.74) and (8.75) $\mathbf{f}^h$ can be evaluated as

$$\mathbf{f}(\boldsymbol{X}) \approx \mathbf{f}^h(\boldsymbol{X}) = \begin{bmatrix} \underline{\mathbf{B}}_{\boldsymbol{F}} \, \underline{\mathbf{d}}_{\boldsymbol{\varphi}} \\ \underline{\mathbf{B}}_{m} \, \underline{\mathbf{d}}_{\mathbb{H}} \\ \underline{\mathbf{N}}_{\mathbb{H}} \, \underline{\mathbf{d}}_{\mathbb{H}} \\ \underline{\mathbf{N}}_{d} \, \underline{\mathbf{d}}_{d} \\ \underline{\mathbf{B}}_{\nabla d} \, \underline{\mathbf{d}}_{d} \end{bmatrix} =: \underline{\mathbf{B}} \, \underline{\mathbf{d}} \ , \tag{8.76}$$

in terms of a global matrix $\underline{\mathbf{B}}$ of shape functions and their derivatives with respect to the material coordinates $\boldsymbol{X}$. The deformation gradient is written in Voigt-notation within the definition of the vector $\mathbf{f}$.

With the approximations (8.75) and (8.76) at hand, the space-discrete counterpart of the incremental potential (8.62) is given by

$$\begin{aligned} \Pi^{\tau h}(\underline{\mathbf{d}}) = & \int_{\mathcal{B}^h} \left\{ \hat{\psi}(\underline{\mathbf{B}} \, \underline{\mathbf{d}}) - \hat{\psi}_n + \tau \hat{\phi}_{\mathrm{con}}(\underline{\mathbf{B}} \, \underline{\mathbf{d}}; \underline{\mathbf{B}} \, \underline{\mathbf{d}}_n) + \tau \hat{\phi}_{\mathrm{frac}}(\underline{\mathbf{B}} \, \underline{\mathbf{d}}) \right\} dV \\ & - \int_{\partial \mathcal{B}^h_{\boldsymbol{T}}} \bar{\boldsymbol{T}} \cdot \hat{\underline{\mathbf{N}}}_{\boldsymbol{\varphi}} [\underline{\mathbf{d}} - \underline{\mathbf{d}}_n] \, dA + \int_{\partial \mathcal{B}^h_{\mu}} \tau \bar{\mu} \hat{\underline{\mathbf{N}}}_{\mathbb{H}} \, \underline{\mathbf{d}} \cdot \boldsymbol{N} \, dA \end{aligned} \tag{8.77}$$

where we introduced $\hat{\psi}_n = \hat{\psi}(\underline{\mathbf{B}} \, \underline{\mathbf{d}}_n)$. Then, the space-time-discrete canonical variational minimization principle can be written as

$$\underline{\mathbf{d}} = \arg \left\{ \inf_{\underline{\mathbf{d}}} \Pi^{\tau h}(\underline{\mathbf{d}}) \right\} \ . \tag{8.78}$$

The necessary condition of the variational principle (8.78) is that its variation vanishes. Approximation of the variations $\{\delta\boldsymbol{\varphi}^h, \delta\mathbb{H}^h, \delta d^h\}$ analogously to the approximation of the fields $\{\boldsymbol{\varphi}^h, \mathbb{H}^h, d^h\}$ in (8.75) yields the necessary condition as

$$\inf_{\underline{\mathbf{d}}} \Pi^{\tau h}(\underline{\mathbf{d}}) \quad \rightarrow \quad \Pi^{\tau h}_{,\underline{\mathbf{d}}} = \boldsymbol{0} \ . \tag{8.79}$$

In order to solve $(8.79)_2$ algorithmically we use an iterative Newton-Raphson scheme. To this end, consider the linearization of $(8.79)_2$ about $\underline{\mathbf{d}}^{(k)}$

$$\mathrm{Lin}\left[\Pi^{\tau h}_{,\underline{\mathbf{d}}}\right]_{\underline{\mathbf{d}}^{(k)}}(\Delta\underline{\mathbf{d}}) = \Pi^{\tau h}_{,\underline{\mathbf{d}}}(\underline{\mathbf{d}}^{(k)}) + \Pi^{\tau h}_{,\underline{\mathbf{d}}\,\underline{\mathbf{d}}}(\underline{\mathbf{d}}^{(k)}) \cdot \Delta\underline{\mathbf{d}} \ . \tag{8.80}$$

This yields the update of the iterative Newton-Raphson scheme as

$$\underline{\mathbf{d}}^{(k+1)} = \underline{\mathbf{d}}^{(k)} - \left[\Pi^{\tau h}_{,\underline{\mathbf{d}}\,\underline{\mathbf{d}}}(\underline{\mathbf{d}}^{(k)})\right]^{-1} \left[\Pi^{\tau h}_{,\underline{\mathbf{d}}}(\underline{\mathbf{d}}^{(k)})\right] \tag{8.81}$$

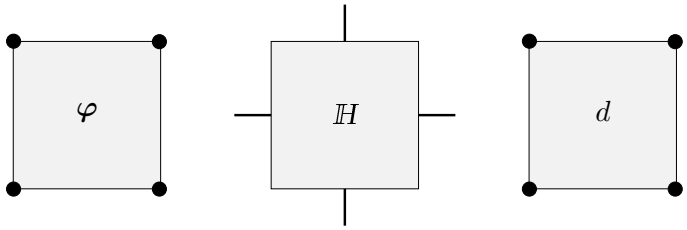

Figure 8.7: *Conforming finite element for minimizer.* Q_1-RT_0-Q_1 element with bilinear shapes for $\boldsymbol{\varphi}$ and d and lowest-order Raviart-Thomas shapes for $\mathbb{H}$.

that is performed until convergence $|\Pi^{\tau h}_{,\underline{\mathbf{d}}}| < tol$ is achieved.

In order to have a compact notation we introduce the vector of *generalized stresses* and the matrix of *generalized moduli*. Based on the incremental potential (8.62) we have

$$\underline{\mathbf{S}} := \begin{bmatrix} \partial_{\boldsymbol{F}}\hat{\psi} \\ -\tau\partial_m\hat{\psi} \\ \tau\partial_{\mathbb{H}}\hat{\phi}_{\text{con}} \\ \partial_d\hat{\psi} + \tau\partial_d\hat{\phi}_{\text{frac}} \\ \partial_{\nabla d}\hat{\psi} \end{bmatrix} \tag{8.82}$$

and

$$\underline{\mathbf{C}} := \begin{bmatrix} \partial^2_{\boldsymbol{F}\boldsymbol{F}}\hat{\psi} & -\tau\partial^2_{\boldsymbol{F}m}\hat{\psi} & \cdot & \partial^2_{\boldsymbol{F}d}\hat{\psi} & \cdot \\ -\tau\partial^2_{m\boldsymbol{F}}\hat{\psi} & \tau^2\partial^2_{mm}\hat{\psi} & \cdot & \cdot & \cdot \\ \cdot & \cdot & \tau\partial^2_{\mathbb{H}\mathbb{H}}\hat{\phi}_{\text{con}} & \cdot & \cdot \\ \partial^2_{d\boldsymbol{F}}\hat{\psi} & \cdot & \cdot & \partial^2_{dd}\hat{\psi} + \tau\partial^2_{dd}\hat{\phi}_{\text{frac}} & \cdot \\ \cdot & \cdot & \cdot & \cdot & \partial^2_{\nabla d\nabla d}\hat{\psi} \end{bmatrix} . \tag{8.83}$$

With (8.82) and (8.83) at hand, the necessary condition $(8.79)_2$ of the space-time-discrete variational principle can be written as

$$\Pi^{\tau h}(\underline{\mathbf{d}})_{,\underline{\mathbf{d}}} = \int_{\mathcal{B}^h} \underline{\mathbf{B}}^T \cdot \underline{\mathbf{S}}\, dV - \int_{\partial\mathcal{B}^h_{\boldsymbol{T}}} \underline{\hat{\mathbf{N}}}^T_{\boldsymbol{\varphi}} \cdot \bar{\boldsymbol{T}}\, dA + \int_{\partial\mathcal{B}^h_{\mu}} \tau\bar{\mu}\underline{\hat{\mathbf{N}}}^T_{\mathbb{H}} \cdot \boldsymbol{N}\, dA = \boldsymbol{0} \ . \tag{8.84}$$

With the generalized tangent moduli $\underline{\mathbf{C}}$ in (8.83) the second derivative of the potential that is needed for the iterative update (8.81) can be written compact as

$$\Pi^{\tau h}_{,\underline{\mathbf{d}}\,\underline{\mathbf{d}}} = \int_{\mathcal{B}^h} \underline{\mathbf{B}}^T\, \underline{\mathbf{C}}\underline{\mathbf{B}}\, dV \ . \tag{8.85}$$

8.4.3. Finite element design for minimiziation formulation

What is still missing is the distinct form of the shape functions for the individual fields $\boldsymbol{\varphi}^h$, $\mathbb{H}^h$ and d^h. The only difference compared to the considerations in Subsection 4.4.3 is due to the additional interpolation for the crack phase-field d. Thus the same finite element designs may be taken and enhanced by an approximation of the phase-field d. Here, as not constraint by any condition, we choose a bilinear approximation with Q_1 shape functions

for d. In the numerical boundary value problems considered only the conforming Q_1-RT_0-Q_1 finite element design is used. For this element we have the approximations (8.71) on the quadrilateral reference element $\mathcal{A} = [-1,1] \times [-1,1]$ given by

$$\boldsymbol{\varphi}^e(\boldsymbol{\xi}) = \sum_{i=1}^{4} \hat{N}^i_{Q_1}(\boldsymbol{\xi}) \boldsymbol{\varphi}^i \ , \quad \mathbb{H}^e(\boldsymbol{\xi}) = \sum_{k=1}^{4} \hat{\boldsymbol{N}}^k_{RT_0}(\boldsymbol{\xi}) H^k \ , \quad d^e(\boldsymbol{\xi}) = \sum_{i=1}^{4} \hat{N}^i_{Q_1}(\boldsymbol{\xi}) d^i \ , \tag{8.86}$$

where $i = \{1,2,3,4\}$ is the number of the corner node of the quadrilateral element and $k = \{1,2,3,4\}$ indicates the k edges of the element. The shape functions $\hat{N}^i_{Q_1}$ and $\hat{\boldsymbol{N}}^k_{RT_0}$ are explicitly given in (4.82). Note that due to the vectorial nature of the Raviart-Thomas shape functions $\hat{\boldsymbol{N}}^k_{RT_0}$ a contravariant Piola transformation is necessary while transforming the flow vector from the elemental coordinate system $\boldsymbol{\xi}$ to the physical space $\boldsymbol{X}$. According to (4.83) this is obtained by

$$\check{\boldsymbol{N}}^k_{RT_0}(\boldsymbol{X}) = \mathcal{P}[\hat{\boldsymbol{N}}^k_{RT_0}(\boldsymbol{\xi})] := \frac{1}{J(\boldsymbol{\xi})} \boldsymbol{J}(\boldsymbol{\xi}) \boldsymbol{N}^k_{RT_0}(\boldsymbol{\xi}) \ , \tag{8.87}$$

where the matrix $\boldsymbol{J}$ denotes the classical Jacobian with its determinant $J = \det[\boldsymbol{J}]$. A three-dimensional Raviart-Thomas element is not implemented.

8.4.4. Space-time-discrete mixed variational saddle-point principle

For the mixed saddle-point formulation the unknown fields are the deformation map $\boldsymbol{\varphi}$, the relative fluid mass content m, the chemical potential μ and the fracture phase-field d, see (8.63). Analogously to the considerations of poro-elasticity without fracture in Chapter 4 the admissible space of the fluid mass content is $m \in L^2$ and no prescription of boundary values is needed neither. This can also be seen in the time-discrete Euler equation $(8.70)_2$ that is an *ordinary differential equations* in contrast to the partial differential equations $(8.70)_1$, $(8.70)_3$ and $(8.70)_4$. Hence for the space-discretization it is sufficient to approximate m peace-wise linear within a finite element $\mathcal{B}^e$ and without continuity over element boundaries. For the finite element method this means that the Euler equation $(8.70)_2$ is solved locally at the Gauss quadrature points and m takes the role of an *internal variable*. Hence the global unknowns reduce to $\{\boldsymbol{\varphi}, \mu, d\}$. The vector of discrete unknown values $\underline{\mathbf{d}}^*$ of the space-discrete variational principle is then given by

$$\underline{\mathbf{d}}^* = [\, \underline{\mathbf{d}}_{\boldsymbol{\varphi}} \, , \, \underline{\mathbf{d}}_{\mu} \, , \, \underline{\mathbf{d}}_{d} \,]^T \ . \tag{8.88}$$

With (8.88) at hand, the space-discrete fields (8.72) can be rewritten as

$$\boldsymbol{\varphi}^h(\boldsymbol{X}) = \underline{\mathbf{N}}_{\boldsymbol{\varphi}} \underline{\mathbf{d}}_{\boldsymbol{\varphi}} = \hat{\underline{\mathbf{N}}}_{\boldsymbol{\varphi}} \underline{\mathbf{d}}^* \ , \quad \mu^h(\boldsymbol{X}) = \underline{\mathbf{N}}_{\mu} \underline{\mathbf{d}}_{\mu} = \hat{\underline{\mathbf{N}}}_{\mu} \underline{\mathbf{d}}^* \ , \quad d^h(\boldsymbol{X}) = \underline{\mathbf{N}}_{d} \underline{\mathbf{d}}_{d} = \hat{\underline{\mathbf{N}}}_{d} \underline{\mathbf{d}}^* \ . \tag{8.89}$$

Analogously to the minimiziation formulation we introduce the vector of *constitutive state* $\mathbf{f}^* := [\, \boldsymbol{F}, \mu, -\nabla\mu, d, \nabla d \,]^T$ for the sake of a compact notation. With the approximations (8.73), (8.88) and (8.89) $\mathbf{f}^{*h}$ is given by

$$\mathbf{f}^*(\boldsymbol{X}) \approx \mathbf{f}^{*h}(\boldsymbol{X}) = \begin{bmatrix} \underline{\mathbf{B}}_{\boldsymbol{F}} \, \underline{\mathbf{d}}_{\boldsymbol{\varphi}} \\ \underline{\mathbf{N}}_{\mu} \, \underline{\mathbf{d}}_{\mu} \\ -\underline{\mathbf{B}}_{\nabla\mu} \, \underline{\mathbf{d}}_{\mu} \\ \underline{\mathbf{N}}_{d} \, \underline{\mathbf{d}}_{d} \\ \underline{\mathbf{B}}_{\nabla d} \, \underline{\mathbf{d}}_{d} \end{bmatrix} =: \underline{\mathbf{B}} \, \underline{\mathbf{d}}^* \ , \tag{8.90}$$

in terms of a global matrix $\underline{\mathbf{B}}$ of shape functions and their derivatives with respect to the material coordinates $\boldsymbol{X}$. The deformation gradient is written in Voigt-notation within the definition of the vector $\mathbf{f}$.

With the approximations (8.89) and (8.90) at hand, the space-discrete counterpart of the incremental mixed potential (8.63) is given by

$$\begin{aligned}\tilde{\Pi}^{*\tau h}(\underline{\mathbf{d}}^*) = & \int_{\mathcal{B}^h} \Big\{ \hat{\psi}(\underline{\mathbf{B}}\,\underline{\mathbf{d}}^*) - \hat{\psi}_n^h - \underline{\hat{\mathbf{N}}}_\mu \underline{\mathbf{d}}^* (m - m_n) - \tau \hat{\phi}^*_{\text{con}}(\underline{\mathbf{B}}\,\underline{\mathbf{d}}^*) + \tau \hat{\phi}_{\text{frac}}(\underline{\mathbf{B}}\,\underline{\mathbf{d}}^*) \Big\} dV \\ & - \int_{\partial \mathcal{B}^h_{\boldsymbol{T}}} \bar{\boldsymbol{T}} \cdot \underline{\hat{\mathbf{N}}}_{\boldsymbol{\varphi}} [\underline{\mathbf{d}}^* - \underline{\mathbf{d}}^*_n] \, dA - \int_{\partial \mathcal{B}^h_H} \tau \underline{\hat{\mathbf{N}}}_\mu \underline{\mathbf{d}}^* \bar{H} \, dA \; .\end{aligned} \tag{8.91}$$

Then the space-time-discrete variational saddle-point principle can be written as

$$\underline{\mathbf{d}}^* = \arg \left\{ \operatorname*{stat}_{\underline{\mathbf{d}}^*} \tilde{\Pi}^{*\tau h}(\underline{\mathbf{d}}^*) \right\} \; . \tag{8.92}$$

The necessary condition of the variational principle (8.92) is that its variation vanishes. Approximation of the variations $\{\delta\boldsymbol{\varphi}^h, \delta\mu^h, \delta d^h\}$ analogously to the approximation of the fields $\{\boldsymbol{\varphi}^h, \mu^h, d^h\}$ in (8.89) yields the necessary condition as

$$\operatorname*{stat}_{\underline{\mathbf{d}}^*} \tilde{\Pi}^{*\tau h}(\underline{\mathbf{d}}^*) \quad \rightarrow \quad \tilde{\Pi}^{*\tau h}_{,\underline{\mathbf{d}}^*} = \boldsymbol{0} \; . \tag{8.93}$$

In order to solve $(8.93)_2$ algorithmically we use an iterative Newton-Raphson scheme. According to the considerations above the discrete update of the scheme is given by

$$\underline{\mathbf{d}}^{*(k+1)} = \underline{\mathbf{d}}^{*(k)} - \big[\tilde{\Pi}^{*\tau h}_{,\underline{\mathbf{d}}^* \underline{\mathbf{d}}^*}(\underline{\mathbf{d}}^{*(k)})\big]^{-1} \big[\tilde{\Pi}^{*\tau h}_{,\underline{\mathbf{d}}^*}(\underline{\mathbf{d}}^{*(k)})\big] \tag{8.94}$$

that is performed until convergence $|\tilde{\Pi}^{*\tau h}_{,\underline{\mathbf{d}}^*}| < tol$ is achieved.

In order to have a compact notation we introduce the vector of *generalized stresses* and the matrix of *generalized moduli*. Based on the incremental potential (8.63) we have

$$\underline{\mathbf{S}}^* := \begin{bmatrix} \partial_{\boldsymbol{F}} \hat{\psi} \\ -(m - m_n) \\ -\tau \partial_{\mathbb{B}} \hat{\phi}^*_{\text{con}} \\ \partial_d \hat{\psi} + \tau \partial_d \hat{\phi}_{\text{frac}} \\ \partial_{\nabla d} \hat{\psi} \end{bmatrix} \tag{8.95}$$

where the update of the relative fluid mass content m is obtained by the ordinary differential equation $(8.70)_2$

$$\partial_m \hat{\psi}(\boldsymbol{F}, m) - \mu = 0 \; , \tag{8.96}$$

which is solved locally at the Gauss quadrature points. The generalized moduli take account for the sensitivity of m with respect to the global unknown fields $\{\boldsymbol{\varphi}, \mu, d\}$ and is given by

$$\underline{\mathbf{C}}^* := \left[\begin{array}{ccc|cc} & & & \partial^2_{\boldsymbol{F}d} \hat{\psi} & \cdot \\ & \underline{\tilde{\mathbf{C}}}^* & & \cdot & \cdot \\ & & & \cdot & \cdot \\ \hline \partial^2_{d\boldsymbol{F}} \hat{\psi} & \cdot & \cdot & \partial^2_{dd} \hat{\psi} + \tau \partial^2_{dd} \hat{\phi}_{\text{frac}} & \cdot \\ \cdot & \cdot & \cdot & \cdot & \partial^2_{\nabla d \nabla d} \hat{\psi} \end{array}\right] \; , \tag{8.97}$$

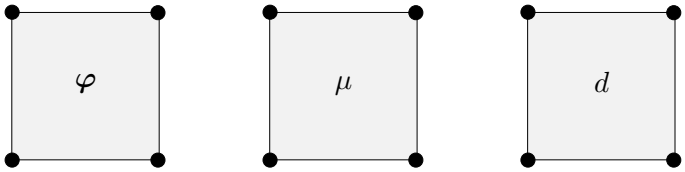

Figure 8.8: *Finite element for mixed principle in 2D.* The two-dimensional Q_1-Q_1-Q_1 quadrilateral element design for $\boldsymbol{\varphi}$, μ and d provides an inf-sup unstable pairing, however yields accurate results.

where $\underline{\tilde{\mathbf{C}}}^*$ is the generalized moduli of the poro-elastic theory without fracture in Chapter 4 as given in (4.95) by

$$\underline{\tilde{\mathbf{C}}}^* := \begin{bmatrix} \partial^2_{\boldsymbol{F}\boldsymbol{F}}\hat{\psi} - \partial^2_{\boldsymbol{F}m}\hat{\psi}[\partial^2_{mm}\hat{\psi}]^{-1}\partial^2_{m\boldsymbol{F}}\hat{\psi} & \partial^2_{\boldsymbol{F}m}\hat{\psi}\left[\partial^2_{mm}\hat{\psi}\right]^{-1} & \cdot \\ \left[\partial^2_{mm}\hat{\psi}\right]^{-1}\partial^2_{m\boldsymbol{F}}\hat{\psi} & -\left[\partial^2_{mm}\hat{\psi}\right]^{-1} & \cdot \\ \cdot & \cdot & -\tau\partial^2_{\mathbb{B}\mathbb{B}}\hat{\phi}^*_{\text{con}} \end{bmatrix} . \tag{8.98}$$

With (8.95) at hand, the necessary condition $(8.93)_2$ of the space-time-discrete variational principle can be written as

$$\Pi^{\tau h}(\underline{\mathbf{d}}^*)_{,\underline{\mathbf{d}}^*} = \int_{\mathcal{B}^h} \underline{\mathbf{B}}^T \cdot \underline{\mathbf{S}}^* \, dV - \int_{\partial\mathcal{B}^h_{\boldsymbol{T}}} \underline{\hat{\mathbf{N}}}^T_{\boldsymbol{\varphi}} \cdot \bar{\boldsymbol{T}} \, dA - \int_{\partial\mathcal{B}^h_H} \tau \underline{\hat{\mathbf{N}}}^T_{\mu} \bar{H} \, dA = \boldsymbol{0} \, . \tag{8.99}$$

With the generalized tangent moduli $\underline{\mathbf{C}}^*$ in (8.97) the second derivative of the potential that is needed for the iterative update (8.94) can be written compact as

$$\Pi^{\tau h}_{,\underline{\mathbf{d}}^*\,\underline{\mathbf{d}}^*} = \int_{\mathcal{B}^h} \underline{\mathbf{B}}^T \underline{\mathbf{C}}^* \underline{\mathbf{B}} \, dV \, . \tag{8.100}$$

8.4.5. Finite element design for saddle-point formulation

Finally the chosen finite element designs for the saddle-point formulation have to be introduced. As for the minimization formulation we use the elements of Subsection 4.4.5 and enhance them with an additional interpolation for the fracture phase-field d. In particular for the numerical boundary value problems we use the unstable Q_1-Q_1-Q_1 finite element design with bilinear and trilinear interpolations for all three fields $\boldsymbol{\varphi}$, μ and d. For this element we have the approximations (8.71) given by

$$\boldsymbol{\varphi}^e(\boldsymbol{\xi}) = \sum_{i=1}^{n^e} \hat{N}^i_{Q_1}(\boldsymbol{\xi})\boldsymbol{\varphi}^i \, , \quad \mu^e(\boldsymbol{\xi}) = \sum_{i=1}^{n^e} \hat{N}^i_{Q_1}(\boldsymbol{\xi})\mu^i \, , \quad d^e(\boldsymbol{\xi}) = \sum_{i=1}^{n^e} \hat{N}^i_{Q_1}(\boldsymbol{\xi})d^i \, . \tag{8.101}$$

In the two-dimensional case this is a four-noded quadrilateral $\mathcal{A} = [-1,1] \times [-1,1]$ with $n^e = 4$ and with the bilinear shape functions given in (4.82), see Figure 8.8. For the case of three space dimensions this a eight-noded brick element $\mathcal{A} = [-1,1]\times[-1,1]\times[-1,1]$ with $n^e = 8$ and with the trilinear shape functions given in (5.70), see Figure 8.9. Furthermore, for the three-dimensional case, four-noded tetrahedral elements with linear interpolation

functions for all three fields $\boldsymbol{\varphi}$, μ and d are used. Thus for the approximations (8.71) we have

$$\boldsymbol{\varphi}^e(\boldsymbol{\xi}) = \sum_{i=1}^{4} \hat{N}^i_{\mathrm{P}_1}(\boldsymbol{\xi})\boldsymbol{\varphi}^i \ , \quad \mu^e(\boldsymbol{\xi}) = \sum_{i=1}^{4} \hat{N}^i_{\mathrm{P}_1}(\boldsymbol{\xi})\mu^i \ , \quad d^e(\boldsymbol{\xi}) = \sum_{i=1}^{4} \hat{N}^i_{\mathrm{P}_1}(\boldsymbol{\xi})d^i \ . \tag{8.102}$$

The linear interpolation functions are expressed in tetrahedral natural coordinates $\boldsymbol{\xi}$ and simply given by

$$\hat{N}^i_{\mathrm{P}_1}(\boldsymbol{\xi}) = \xi_i \ , \tag{8.103}$$

where for the tetrahedral natural coordinates the relation $\xi_4 = 1 - \xi_1 - \xi_2 - \xi_3$ holds. As for the Q_1-Q_1-Q_1 element also this element design is not inf-sup stable but gives reasonable results if not considering the undrained limit case. Following the classical FEM literature this element is called P_1-P_1-P_1 and visualized in Figure 8.10.

8.5. Alternative crack driving forces and staggered solution

In the previous Sections the variational modeling approach for poro-hydro-elasticity coupled with phase-field fracture is introduced. Here a Griffith-type energy fracture criterion is used. In what follows, different alternative crack driving forces are introduced that suit the phase-field modeling of multiphysics problems of solids at large strains. In particular the changes are with regard to a threshold and a fracture evolution only for tensile strains or stresses. The considerations here are in line with Miehe et al. [190, 191] and Miehe & Mauthe [181].

Furthermore a staggered solution scheme for the coupled minimization and saddle-point formulations is introduced. This is in line with the considerations in Miehe et al. [182] and yields a robust numerical implementation.

8.5.1. Generalized Ginzburg-Landau-type fracture evolution equation

Recalling the fracture evolution equation $(8.51)_3$ and $(8.56)_4$ that is the same for both minimization and saddle-point formulation and inserting the specific choice of dissipation potential function introduced in (8.24), we have

$$\delta_d \hat{\psi} + \eta \dot{d} + \partial_{\dot{d}} I(\dot{d}) \ni \boldsymbol{0} \quad \text{with} \quad \partial_{\dot{d}} I(\dot{d}) = \begin{cases} 0 & \text{for } \dot{d} \geq 0 \\ \mathcal{R}_- & \text{otherwise} \end{cases} , \tag{8.104}$$

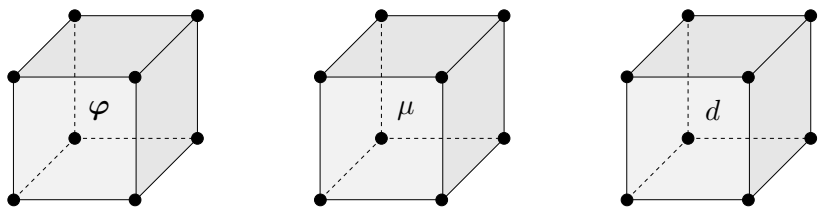

Figure 8.9: *Finite element for mixed principle in 3D.* The three-dimensional Q_1-Q_1-Q_1 hexahedral element design for $\boldsymbol{\varphi}$, μ and d provides an inf-sup unstable pairing, however yields accurate results.

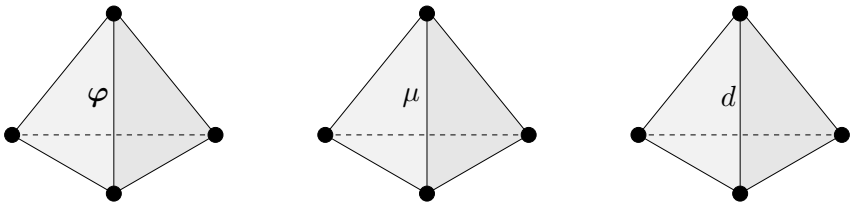

Figure 8.10: *Finite element for mixed principle in 3D.* The three-dimensional P_1-P_1-P_1 tetrahedral element design for φ, μ and d provides an inf-sup unstable pairing, however yields accurate results.

where we denote $\delta_d\hat{\psi} = \partial_d\hat{\psi} - \mathrm{Div}[\partial_{\nabla d}\hat{\psi}]$ as the variational derivative of the free energy function $\hat{\psi}$ with respect to the fracture phase-field d. (8.104) can be rewritten as

$$\dot{d} = \left\langle -\frac{1}{\eta}\delta_d\hat{\psi} \right\rangle \tag{8.105}$$

where $\langle x \rangle := (x + |x|)/2$ is the ramp function of $\mathcal{R}_+$ expressed by the Macauley bracket. (8.105) permits the interpretation of this equation as a generalized Ginzburg-Landau-type evolution equation for d, see Miehe et al. [183] and in line with Gurtin [125]. The Macauley bracket coming from the discontinuous part $I(\dot{d})$ of the dissipation potential function accounts locally for the irreversibility of the crack evolution. For the rate-independent limit with $\eta \to 0$ (8.105) degenerates to the Karush-Kuhn-Tucker conditions

$$\dot{d} \geq 0; \quad -\delta_d\hat{\psi} \leq 0, \quad \dot{d}\,[-\delta_d\hat{\psi}] = 0\ . \tag{8.106}$$

Following Miehe et al. [182] the non-smooth equation (8.105) can be rewritten by inserting the specific choice (8.20) of free energy function and introducing a non-smooth *crack driving history field* $\mathcal{H}$ as

$$\tilde{\eta}\dot{d} = (1-d)\mathcal{H} - \left[d - l^2\Delta d\right]\ , \tag{8.107}$$

with the dimensionless viscosity $\tilde{\eta} = l\eta/g_c$. Here the evolution of the fracture phase-field is governed by a driving force $(1-d)\mathcal{H}$ and a geometric resistance term $d - l^2\Delta d$. The non-smooth crack driving history field $\mathcal{H}$ that accounts for the irreversibility is given by

$$\mathcal{H}(\boldsymbol{X}, t) := \max_{s\in[0,t]} D(\boldsymbol{X}, s) \quad \text{with} \quad D = \frac{2\hat{\psi}_{\text{eff}}(\boldsymbol{F})}{g_c/l}\ . \tag{8.108}$$

D is denoted as the *crack driving state function*. In line with Miehe et al. [189, 190, 191] this crack driving state function D is considered as the constitutive input for the modeling of the diffusive crack propagation. In the following we observe different constitutive forms for D that suit for poro-hydro-elastic solids at large strains and for hydraulically driven fracture scenarios.

8.5.2. Crack driving with threshold

The first modification for the fracture evolution equation is the incorporation of a threshold, that is an elastic range in which no crack evolution takes place. Following Frémond & Nedjar [107], Frémond [106] and the recent contributions Pham et al. [209] and

Miehe [176] such a formulation is achieved by replacing the energy contribution $\hat{\psi}_{\text{frac}}$ in (8.20) by

$$\hat{\psi}_{\text{frac}}(d, \nabla d) = 2\psi_c \big[d + l^2 \nabla d \cdot \nabla d \big] \ , \tag{8.109}$$

where ψ_c is a critical threshold value of fracture energy per unit volume. Note that in contrast to (8.20) d enters the energy $\hat{\psi}_{\text{frac}}$ by a linear term. With (8.109) at hand, the crack driving state function can be evaluated as

$$D = \left\langle \frac{\hat{\psi}_{\text{eff}}(\boldsymbol{F})}{\psi_c} - 1 \right\rangle \ . \tag{8.110}$$

Note that the criterion (8.110) is independent of the length scale l as the threshold value ψ_c refers to a unit volume.

8.5.3. Crack driving by effective stress

In order to have a crack evolution in the tensile regime only we furthermore modify the driving state function D. For the small strain setting Miehe et al. [183] proposed a decomposition of the free energy into tensile and compression parts. However for large strains this is not possible as the deformation gradient $\boldsymbol{F}$ cannot be additively decomposed into these two parts. Following the recent work Miehe et al. [191], we consider a decomposition of the effective Kirchhoff stress tensor $\tilde{\boldsymbol{\sigma}}_{\text{eff}}$ of the undamaged skeleton defined in $(8.27)_2$ into tensile and compression parts

$$\tilde{\boldsymbol{\sigma}}_{\text{eff}} = \tilde{\boldsymbol{\sigma}}^{+}_{\text{eff}} + \tilde{\boldsymbol{\sigma}}^{-}_{\text{eff}} \quad \text{with} \quad \tilde{\boldsymbol{\sigma}}^{+}_{\text{eff}} := \sum_{a=1}^{3} \langle \tilde{\sigma}^{a}_{\text{eff}} \rangle \, \boldsymbol{n}_a \otimes \boldsymbol{n}_a \ . \tag{8.111}$$

In order to obtain a crack driving criterion in line with the ones introduced above consider furthermore a one-dimensional problem of linear elasticity. The tensile part of the free energy function can be written as

$$\hat{\psi}(\varepsilon) = \frac{E}{2} \langle \varepsilon \rangle^2 = \frac{1}{2E} \langle \sigma \rangle^2 = \hat{\psi}^*(\sigma) \tag{8.112}$$

and analogously for the threshold parameter $\psi_c = \sigma_c^2 / 2E$. Thus we can state the relation $\hat{\psi}(\varepsilon)/\psi_c = (\langle \sigma \rangle / \sigma_c)^2$. Motivated by this one-dimensional setting we modify the crack driving state function D in (8.110) to

$$D = \left\langle \sum_{a=1}^{3} \left(\frac{\langle \tilde{\sigma}^{a}_{\text{eff}} \rangle}{\sigma_c} \right)^2 - 1 \right\rangle \ . \tag{8.113}$$

The state function (8.113) models an isotropic failure surface with threshold in the space of principle effective stresses. Here σ_c is the critical fracture tensile stress. Note that this criterion cannot be deduced from a variational framework but is postulated based on the tensile stress which provides a sound physical motivation for crack driving.

8.5.4. Modified space-time-discrete formulations

Alternatively to the numerical schemes for the minimization and the saddle-point formulation we now want to make use of the modified Ginzburg-Landau-type form (8.107). Thus for the minimizer the necessary conditions (8.84) is rewritten as

$$\underline{\mathbf{R}}(\underline{\mathbf{d}}) := \int_{\mathcal{B}^h} \underline{\mathbf{B}}^T \cdot \check{\underline{\mathbf{S}}}\, dV - \int_{\partial\mathcal{B}^h_{\boldsymbol{T}}} \hat{\underline{\mathbf{N}}}^T_{\boldsymbol{\varphi}} \cdot \bar{\boldsymbol{T}}\, dA + \int_{\partial\mathcal{B}^h_{\mu}} \tau\bar{\mu}\hat{\underline{\mathbf{N}}}^T_{\mathbb{H}} \cdot \boldsymbol{N}\, dA = \boldsymbol{0} \tag{8.114}$$

and in analogy for the necessary condition (8.99) we obtain

$$\underline{\mathbf{R}}^*(\underline{\mathbf{d}}^*) := \int_{\mathcal{B}^h} \underline{\mathbf{B}}^T \cdot \check{\underline{\mathbf{S}}}^*\, dV - \int_{\partial\mathcal{B}^h_{\boldsymbol{T}}} \hat{\underline{\mathbf{N}}}^T_{\boldsymbol{\varphi}} \cdot \bar{\boldsymbol{T}}\, dA - \int_{\partial\mathcal{B}^h_{H}} \tau\hat{\underline{\mathbf{N}}}^T_{\mu}\bar{H}\, dA = \boldsymbol{0}\ . \tag{8.115}$$

In (8.114) and (8.115) we introduced the modified generalized stress vectors associated with the modified minimization formulation and the modified saddle-point formulation. By use of (8.107) together with an implicit Euler time-discretization scheme we get

$$\check{\underline{\mathbf{S}}} := \begin{bmatrix} \partial_{\boldsymbol{F}}\hat{\psi} \\ -\tau\partial_m\hat{\psi} \\ \tau\partial_{\mathbb{H}}\hat{\phi}_{\text{con}} \\ d + \tilde{\eta}(d-d_n)/\tau - (1-d)\mathcal{H} \\ l^2\nabla d \end{bmatrix}\ ,\ \check{\underline{\mathbf{S}}}^* := \begin{bmatrix} \partial_{\boldsymbol{F}}\hat{\psi} \\ -(m-m_n) \\ -\tau\partial_{\mathbb{B}}\hat{\phi}^*_{\text{con}} \\ d + \tilde{\eta}(d-d_n)/\tau - (1-d)\mathcal{H} \\ l^2\nabla d \end{bmatrix}\ . \tag{8.116}$$

The algebraic equations (8.114) and (8.115) are solved for $\underline{\mathbf{d}}$ and $\underline{\mathbf{d}}^*$ by a standard Newton-type iteration resulting in the update equations

$$\begin{aligned} \underline{\mathbf{d}} &\Leftarrow \underline{\mathbf{d}} - \underline{\mathbf{K}}^{-1}\underline{\mathbf{R}} \qquad \text{with} \quad \underline{\mathbf{K}} := \int_{\mathcal{B}^h} \underline{\mathbf{B}}^T\check{\underline{\mathbf{C}}}\underline{\mathbf{B}}\, dV\ , \\ \underline{\mathbf{d}}^* &\Leftarrow \underline{\mathbf{d}}^* - (\underline{\mathbf{K}}^*)^{-1}\underline{\mathbf{R}}^* \quad \text{with} \quad \underline{\mathbf{K}}^* := \int_{\mathcal{B}^h} \underline{\mathbf{B}}^T\check{\underline{\mathbf{C}}}^*\underline{\mathbf{B}}\, dV\ , \end{aligned} \tag{8.117}$$

with the modified monolithic tangent matrices $\check{\underline{\mathbf{C}}}$ and $\check{\underline{\mathbf{C}}}^*$. From (8.116) they can be identified explicitly as

$$\check{\underline{\mathbf{C}}} := \partial_{\mathbf{f}}\check{\underline{\mathbf{S}}} = \begin{bmatrix} \partial^2_{\boldsymbol{F}\boldsymbol{F}}\hat{\psi} & -\tau\partial^2_{\boldsymbol{F}m}\hat{\psi} & \cdot & \partial^2_{\boldsymbol{F}d}\hat{\psi} & \cdot \\ -\tau\partial^2_{m\boldsymbol{F}}\hat{\psi} & \tau^2\partial^2_{mm}\hat{\psi} & \cdot & \cdot & \cdot \\ \cdot & \cdot & \tau\partial^2_{\mathbb{H}\mathbb{H}}\hat{\phi}_{\text{con}} & \cdot & \cdot \\ -(1-d)\partial_{\boldsymbol{\varepsilon}}\mathcal{H} & \cdot & \cdot & 1 + \tilde{\eta}/\tau + \mathcal{H} & \cdot \\ \cdot & \cdot & \cdot & \cdot & l^2\boldsymbol{1} \end{bmatrix} \tag{8.118}$$

and by use of $\tilde{\underline{\mathbf{C}}}^*$ introduced in (8.98)

$$\check{\underline{\mathbf{C}}}^* := \partial_{\mathbf{f}^*}\check{\underline{\mathbf{S}}}^* = \left[\begin{array}{ccc|cc} & & & \partial^2_{\boldsymbol{F}d}\hat{\psi} & \cdot \\ & \tilde{\underline{\mathbf{C}}}^* & & \cdot & \cdot \\ & & & \cdot & \cdot \\ \hline -(1-d)\partial_{\boldsymbol{\varepsilon}}\mathcal{H} & \cdot & \cdot & 1 + \tilde{\eta}/\tau + \mathcal{H} & \cdot \\ \cdot & \cdot & \cdot & \cdot & l^2\boldsymbol{1} \end{array}\right]\ . \tag{8.119}$$

8.5.5. Staggered incremental minimization principles

Equation (8.117) provides monolithic update equations for the set of unknowns $\{\boldsymbol{\varphi}, \mathbb{H}, d\}$ in the modified minimization formulation and $\{\boldsymbol{\varphi}, \mu, d\}$ in the modified saddle-point formulation. Here the resulting tangent matrices $\underline{\check{\mathbf{C}}}$ and $\underline{\check{\mathbf{C}}}^*$ in (8.118) and (8.119) are non-smooth and non-symmetric. To this end, in analogy to Miehe et al. [182] we make use of a robust staggered solution scheme that divides the update into two steps. In particular the modified residuals $\underline{\mathbf{R}}$ and $\underline{\mathbf{R}}^*$ in (8.114) and (8.115) are split into two parts

$$\underline{\mathbf{R}} := \underline{\mathbf{R}}_{\boldsymbol{\varphi},\mathbb{H}} + \underline{\mathbf{R}}_d = \boldsymbol{0} \quad \text{and} \quad \underline{\mathbf{R}}^* := \underline{\mathbf{R}}_{\boldsymbol{\varphi},\mu} + \underline{\mathbf{R}}_d = \boldsymbol{0} \tag{8.120}$$

with their definitions

$$\begin{aligned}
\underline{\mathbf{R}}_{\boldsymbol{\varphi},\mathbb{H}} &:= \int_{\mathcal{B}^h} \underline{\mathbf{B}}^T \check{\underline{\mathbf{S}}}_{\boldsymbol{\varphi},\mathbb{H}}\, dV - \int_{\partial\mathcal{B}^h_{\boldsymbol{T}}} \hat{\underline{\mathbf{N}}}^T_{\boldsymbol{\varphi}} \cdot \bar{\boldsymbol{T}}\, dA + \int_{\partial\mathcal{B}^h_{\mu}} \tau\bar{\mu}\hat{\underline{\mathbf{N}}}^T_{\mathbb{H}} \cdot \boldsymbol{N}\, dA\,, \\
\underline{\mathbf{R}}_{\boldsymbol{\varphi},\mu} &:= \int_{\mathcal{B}^h} \underline{\mathbf{B}}^T \check{\underline{\mathbf{S}}}_{\boldsymbol{\varphi},\mu}\, dV - \int_{\partial\mathcal{B}^h_{\boldsymbol{T}}} \hat{\underline{\mathbf{N}}}^T_{\boldsymbol{\varphi}} \cdot \bar{\boldsymbol{T}}\, dA - \int_{\partial\mathcal{B}^h_{H}} \tau\hat{\underline{\mathbf{N}}}^T_{\mu}\bar{H}\, dA\,, \\
\underline{\mathbf{R}}_d &:= \int_{\mathcal{B}^h} \underline{\mathbf{B}}^T \check{\underline{\mathbf{S}}}_d\, dV\,.
\end{aligned} \tag{8.121}$$

Here we have introduced the modified generalized stress vectors associated to the minimization and saddle-point updates of the poro-hydro-mechanical unknowns given by

$$\check{\underline{\mathbf{S}}}_{\boldsymbol{\varphi},\mathbb{H}} := \begin{bmatrix} \partial_{\boldsymbol{F}}\hat{\psi} \\ -\tau\partial_m\hat{\psi} \\ \tau\partial_{\mathbb{H}}\hat{\phi}_{\text{con}} \\ 0 \\ \boldsymbol{0} \end{bmatrix}, \quad \check{\underline{\mathbf{S}}}_{\boldsymbol{\varphi},\mu} := \begin{bmatrix} \partial_{\boldsymbol{F}}\hat{\psi} \\ -(m-m_n) \\ -\tau\partial_{\mathbb{B}}\hat{\phi}^*_{\text{con}} \\ 0 \\ \boldsymbol{0} \end{bmatrix}, \tag{8.122}$$

together with the modified generalized stress vector associated to the time-discrete Ginzburg-Landau-type evolution equation for the update of the crack phase-field

$$\check{\underline{\mathbf{S}}}_d := \begin{bmatrix} \boldsymbol{0} \\ 0 \\ \boldsymbol{0} \\ d + \tilde{\eta}(d-d_n)/\tau - (1-d)\mathcal{H} \\ l^2\nabla d \end{bmatrix}. \tag{8.123}$$

With the splits (8.120) at hand, in a first solution step an update for the degrees of freedom related to the poro-hydro-mechanical fields is performed. These are for the modified minimization formulation the solid's deformation and the fluid mass flow vector $\{\boldsymbol{\varphi}, \mathbb{H}\}$ and for the modified saddle-point formulation the solid's deformation and the potential $\{\boldsymbol{\varphi}, \mu\}$. In this step the fracture phase-field d is hold constant. This results in a standard Newton-type iteration with symmetric stiffness. In a second solution step the poro-hydro-mechanical set of degrees of freedom is hold constant and $\underline{\boldsymbol{R}}_d = \boldsymbol{0}$ is solved for the phase-field d. Note that this results in a *linear* update equation for the fracture phase-field. This sequence of two-step algorithm can be repeated yielding a Gauss-Seidel iteration scheme until global convergence has been achieved. The staggered update procedure is summarized in Box 8.1. Here $\mathfrak{X}$ is a placeholder for either $\mathbb{H}$ if considering the modified minimization formulation or μ if considering the modified saddle-point formulation.

Box 8.1: Staggered Gauss-Seidel solution update procedure of poro-hydro-elasticity at fracture in $[t_n, t]$. $\mathfrak{X}$ is a placeholder for either $\mathcal{H}$ if considering the modified minimization formulation or μ if considering the modified saddle-point formulation.

1. Initialization
$$\{\boldsymbol{\varphi}^{(i=0)}, \mathfrak{X}^{(i=0)}, d^{(i=0)}\} = \{\boldsymbol{\varphi}_n, \mathfrak{X}_n, d_n\}$$

2. Solve the *poro-hydro-mechanical problem* $\{\boldsymbol{\varphi}^{(i+1)}, \mathfrak{X}^{(i+1)}\}$ with fixed phase-field $d^{(i)}$ such that
$$\underline{\boldsymbol{R}}_{\boldsymbol{\varphi},\mathfrak{X}} = \boldsymbol{0}$$

3. Solve for *fracture phase-field* $d^{(i+1)}$ with fixed poro-hydro-mechanical state $\{\boldsymbol{\varphi}^{(i+1)}, \mathfrak{X}^{(i+1)}\}$ such that
$$\underline{\boldsymbol{R}}_d = \boldsymbol{0}$$

4. Check for convergence
$$R = \|\underline{\mathbf{d}}_d^{(i+1)} - \underline{\mathbf{d}}_d^{(i)}\| \quad \begin{cases} \geq \epsilon & \text{go to 2. with } i = i+1 \\ < \epsilon & \text{go to 5.} \end{cases}$$

5. Update the solution
$$\{\boldsymbol{\varphi}, \mathfrak{X}, d\} = \{\boldsymbol{\varphi}^{(i+1)}, \mathfrak{X}^{(i+1)}, d^{(i+1)}\}$$

Table 8.2: Material parameters used for numerical simulations.

no.	par.	name	unit	value
1.	μ	shear modulus	[MN/m^2]	98.0
2.	ν	Poisson's ratio	[-]	0.3
3.	ρ_f	fluid density	[kg/m^3]	1000.0
4.	M	Biot's modulus	[MN/m^2]	100.0
5.	b	Biot's coefficient	[-]	1.0
6.	K	spatial permeability	[m^{3}s/kg]	$2.11 \cdot 10^{-13}$
7.	m_0	initial density of porous medium	[kg/m^3]	700.0
8.	η	dynamic viscosity of fluid	[Ns/m^2]	0.001
9.	ϵ	permeability transition exponent	[-]	50
10.	l	fracture length scale	[m]	
11.	$\tilde{\eta}$	dimensionless crack viscosity	[N/m^{2}s]	0
12.	σ_c	critical effective stress	[N/m^2]	0.005

8.6. Representative numerical examples

The performance of the continuum phase-field model for fracture in saturated porous media is now demonstrated by means of representative numerical examples. Goal of the model simulations is to highlight the fundamental phenomena of hydraulically driven fracture. The material parameters used for the numerical examples are given in Table 8.2. The length scale l is chosen such that $l \geq 2H^e$ where H^e is the mesh size.

8.6.1. Darcy-Poiseuille-type fluid flow through broken porous medium

The first boundary value problem demonstrates the capability to model the transition from Darcy's fluid flow at an unbroken material state to a Poiseuille-type fluid flow within a crack as proposed in (8.37). To this end, consider a two-dimensional square plate

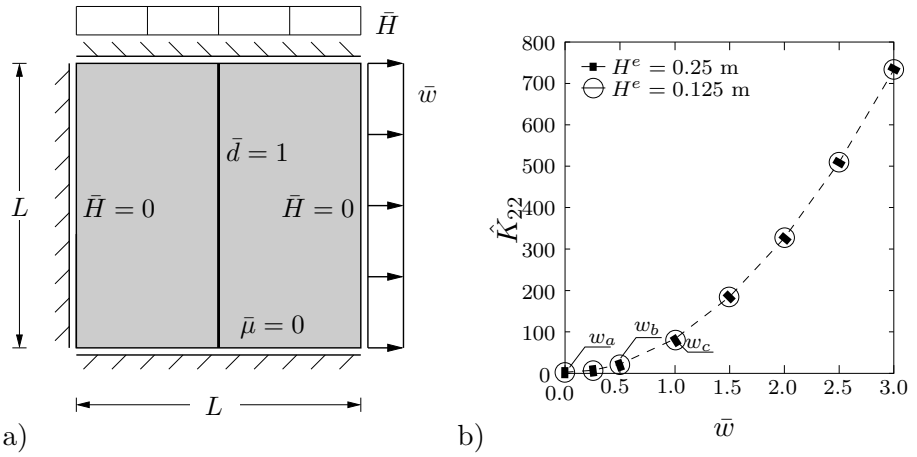

Figure 8.11: *Darcy-Poiseuille-type fluid flow through broken porous medium. Boundary value problem and results*: a) Square plate $\mathcal{B}$ that is fully broken in vertical direction at $x = 2.5$ m. The right part of the specimen is then deformed horizontally, creating a crack opening width $\bar{w}$. The broken mid-line of the specimen is prescribed by setting Dirichlet conditions $\bar{d} = 1$. b) Permeability $\widehat{K}_{22}$ for a fluid flow along the crack against $\bar{w}$ for different mesh sizes H^e.

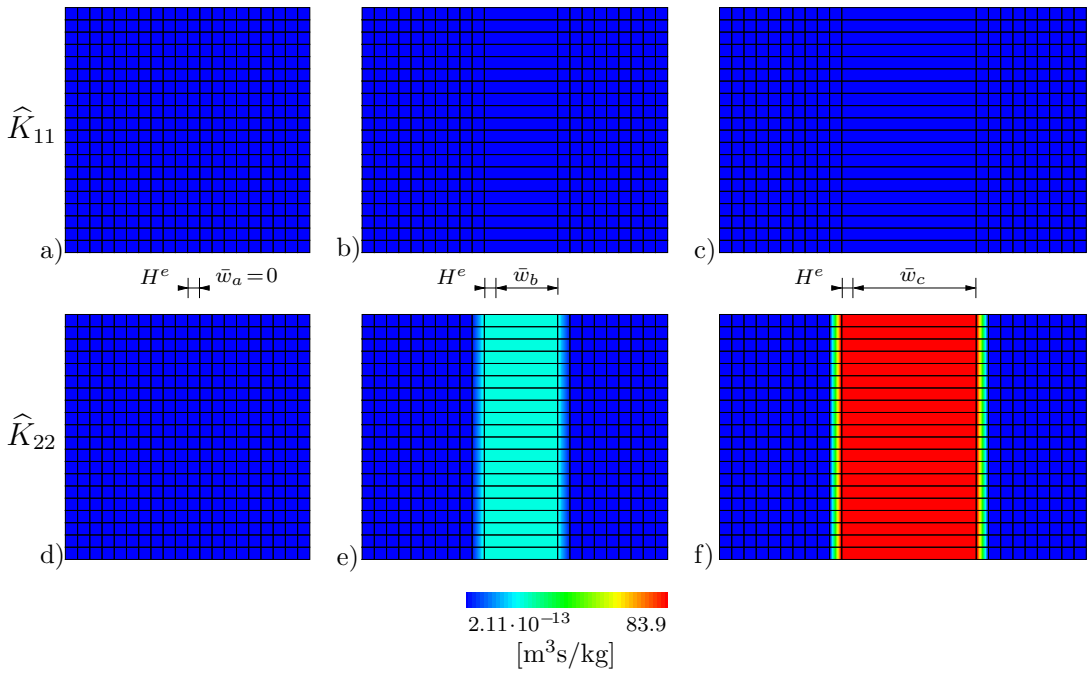

Figure 8.12: *Darcy-Poiseuille-type fluid flow through broken porous medium. Permeability*: Components of the permeability tensor $\widehat{\boldsymbol{K}}$ for different crack opening widths $\bar{w} = 0$ m, 0.5 m and 1.0 m. a,b,c) Permeability $\widehat{K}_{11}$ for a fluid flow in x-direction and d,e,f) permeability $\widehat{K}_{22}$ for a fluid flow in y-direction.

$\mathcal{B} = \{\boldsymbol{X} \in \mathcal{R}^2 | \boldsymbol{X} \in [0, L] \times [0, L]\}$ with $L = 5$ m that is fully broken in vertical direction at $x = L/2 = 2.5$ m. Within the numerical treatment the crack is realized by Dirichlet conditions $\bar{d} = 1$ at the nodes of the corresponding elements. The right part of the specimen is then moved horizontally in order to produce a crack opening width $\bar{w}$. Then a constant fluid mass flux of $\bar{H} = -16$ kg/m^{2}s is injected at the upper edge of the specimen. The bottom edge is assumed to be permeable by setting $\bar{\mu} = 0$ whereas the side edges are assumed to be impermeable, that is $\bar{H} = 0$. The geometric setup of the boundary value problem is visualized in Figure 8.11a). The presented results are obtained by use of the minimization formulation and where the specimen is discretized by 20×20 Q_1-RT_0-Q_1 finite elements. The saddle-point principle yields the same results which however is not shown here. The time step is chosen to be $\tau = 10.0$ s in the time range of the simulation $t \in [0, t_\infty]$ with $t_\infty = 12260$ s.

Figure 8.11b) shows the dependence of the permeability $\widehat{K}_{22}$ on the crack opening width $\bar{w}$. Consistent with Poiseuille's law, the permeability scales quadratically with the crack opening width $\bar{w}$. The deformation localizes in one vertical row of finite elements, that is the "cracked elements", see Figure 8.12. Again note that the definition of the crack opening must be scaled by the mesh size $L_\perp = H^e$ to obtain a mesh-independent formulation, see (8.43). Figure 8.11b) demonstrates this mesh-independency as the numerical results are plotted for two different mesh sizes H^e. In Figure 8.12 the contributions $\widehat{K}_{11}$ and $\widehat{K}_{22}$, that is the permeabilities for a flow in x and y direction for the observed scenario, are shown. In Figure 8.12a)–c) we observe a constant permeability in x direction, that is a fluid flow independent of $\bar{w}$. This result is expected as only the flow along the crack is scaled by the crack opening width, see (8.45). The permeability in y direction, that is in crack direction, changes proportional to $\bar{w}^2$ as expected, see Figure 8.12d)–f)

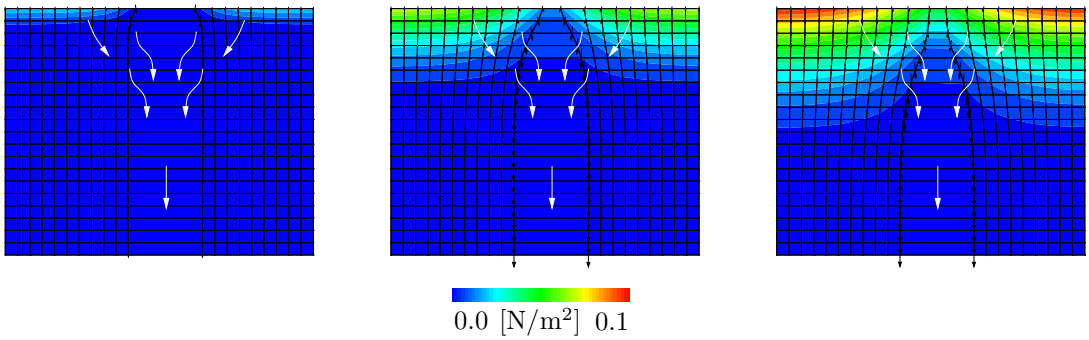

Figure 8.13: *Darcy-Poiseuille-type fluid flow through broken porous medium. Fluid flow.* Fluid pressure and fluid flow at different time steps a) $t = 504$ s, b) $t = 5504$ s and c) $t = 12260$ s.

and again Figure 8.11b). Note that only the permeability in the "cracked element" row changes, that is the choice of the transition rule (8.46) is appropriate. Figure 8.13 shows the fluid pressure p at three time steps of the simulation. Furthermore the true fluid mass flow $\mathbb{h}$ is visualized by arrows: white arrows depict the flow vector schematically whereas black arrows represent the quantitative nodal values of $\mathbb{h}$. We observe a flux from the unbroken bulk material into the crack and a rapid fluid flow within the crack. Due to the increased fluid pressure p at the top of the intact specimen the crack narrows. This shows the strong interaction between crack geometry, solid deformation and fluid flow. Note that the crack geometry is constant for this boundary value problem and thus no iterative Gauss-Seidel update has to be performed.

In order to demonstrate the capability in more complex geometric setups, Figure 8.14 depicts the results for a by $\alpha = 45°$ tilted crack and a prescribed displacement $\bar{\boldsymbol{u}}$ of the right edge that is tilted by $\alpha/2$. The left diagram shows the evaluated crack opening width w compared to the prescribed one $\bar{w} = \bar{\boldsymbol{u}} \cdot \boldsymbol{n}_\perp$ where $\boldsymbol{n}_\perp$ is the normal to the crack. For two different mesh sizes H^e the numerical evaluated crack opening width w equals the prescribed one $\bar{w}$. The right diagram visualizes the permeabilities along the crack $\hat{K}_{\boldsymbol{t}_\Gamma}$ and perpendicular to the crack $\hat{K}_{\boldsymbol{n}_\Gamma}$. Again the results fit the expected ones depicted by the dashed line for the two mesh sizes.

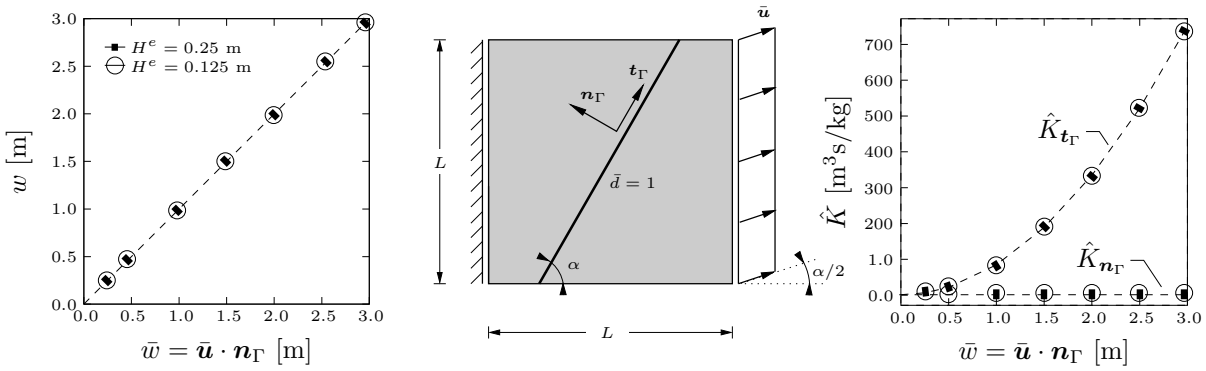

Figure 8.14: *Darcy-Poiseuille-type fluid flow through broken porous medium. Tilted crack*: numerical results for crack opening width w and the permeabilites for fluid flow along $\hat{K}_{\boldsymbol{t}_\Gamma}$ and perpendicular $\hat{K}_{\boldsymbol{n}_\Gamma}$ to the crack for a general geometric setup.

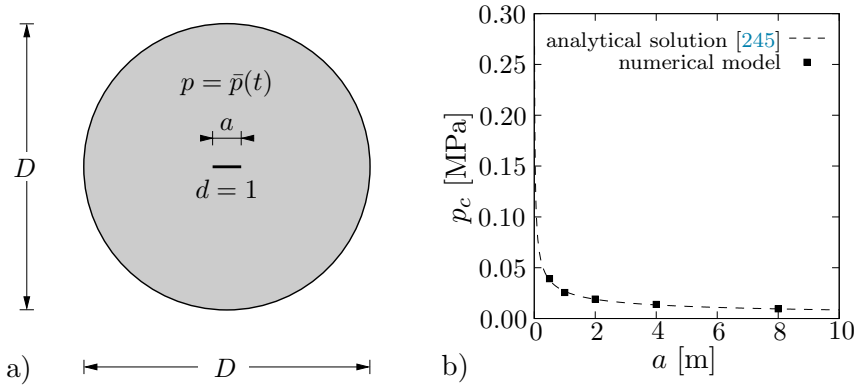

Figure 8.15: *Fluid pressure driven crack. Boundary value problem and results*: a) A circular plate of diameter $D = 80$ m is loaded by a fluid pressure $p = \bar{p}$ homogeneously in $\mathcal{B}$. A notch of length a is located in the center of the specimen by prescribed Dirichlet conditions $\bar{d} = 1$. b) Critical fluid pressure p_c when system gets unstable.

8.6.2. Fluid pressure driven crack

The goal of the next boundary value problem is to compare the crack propagation criterion to analytical solutions in linear elastic fracture mechanics of Sneddon & Lowengrub [245]. To this end, we perform numerical simulations by use of the Griffith-type energetic fracture criterion (8.20). Here we choose the critical energy release rate to $g_c = 8.06$ J/m^2. This boundary value problem is taken from Wilson & Landis [271]. Consider a circular specimen of diameter $D = 80$ m in the center of which a notch of length a is placed. The specimen is loaded by a fluid pressure $\bar{p}$ homogeneously within the whole body. The geometric setup is visualized in Figure 8.15a). $\bar{p}(t)$ is increased linearly up to the particular time step where the crack starts to propagate. This is the critical fluid pressure p_c that according to Sneddon & Lowengrub [245] can be evaluated analytically as

$$p_c = \sqrt{\frac{E' g_c}{\pi a}} \,. \tag{8.124}$$

Here we introduced $E' = E/(1-\nu^2)$ in terms of the Young's modulus E and the Poisson's ratio ν. The critical fluid pressure p_c of the numerical simulations obtained by use of the saddle-point principle and the Q_1-Q_1-Q_1 element design are shown in Figure 8.15b) for different lengths a of the notch. For the numerical simulations the Gauss-Seidel update introduced in Box 8.1 is performed until convergence is achieved. We observe agreement with the analytical solution (8.124). Hence the model formulation is able to capture linear elastic fracture mechanics solutions. The same results are obtained by the minimization formulation which is not shown here.

8.6.3. Hydraulically induced crack driven by fluid volume injection

Consider a square domain $\mathcal{B} = \{\boldsymbol{X} \in \mathcal{R}^2 | \boldsymbol{X} \in [0, L] \times [0, L]\}$ with $L = 80$ m. The domain has a notch of length $a = 8$ m in its center. A constant fluid mass of $M_{\text{injec.}} = \dot{m} A_{\text{injec.}} = 0.8$ kg/s is injected into the area $A_{\text{injec.}}$ around the notch. This is realized by introducing an additional mass source term $\dot{\bar{m}}$ in the fluid mass balance $(8.4)_1$, such that $\dot{m} = -\operatorname{Div}[\mathit{I\!H}] + \dot{\bar{m}}$. All edges of the specimen are assumed to be permeable, potential free and mechanically fixed, that is $\bar{\mu} = 0$ and $\bar{\boldsymbol{\varphi}} = \boldsymbol{X}$. The geometric setup is visualized

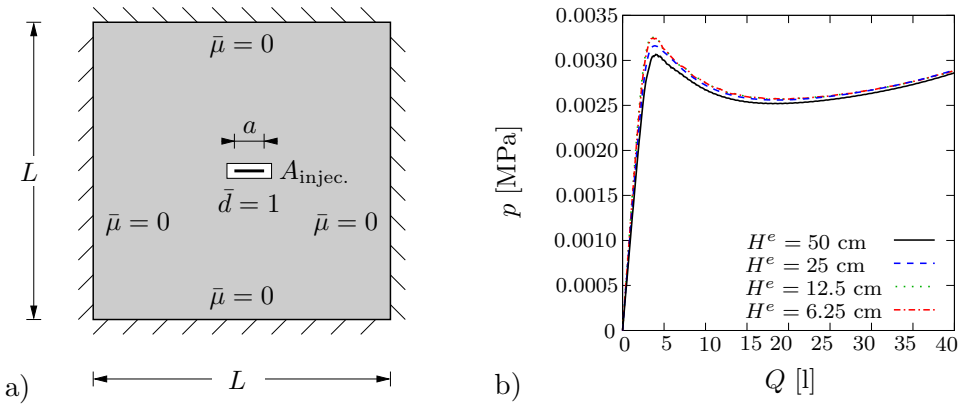

Figure 8.16: *Hydraulically induced crack driven by fluid volume injection. Boundary value problem and results*: a) A square specimen the boundaries of which are all mechanically fixed, permeable and potential free. A notch of length $a = 8$ m in the center is prescribed by Dirichlet conditions $\bar{d} = 1$. In the white shaded area $A_{\text{injec.}}$ around the notch fluid mass is injected. b) Fluid pressure p in the crack over the total injected fluid volume V for different mesh sizes H^e.

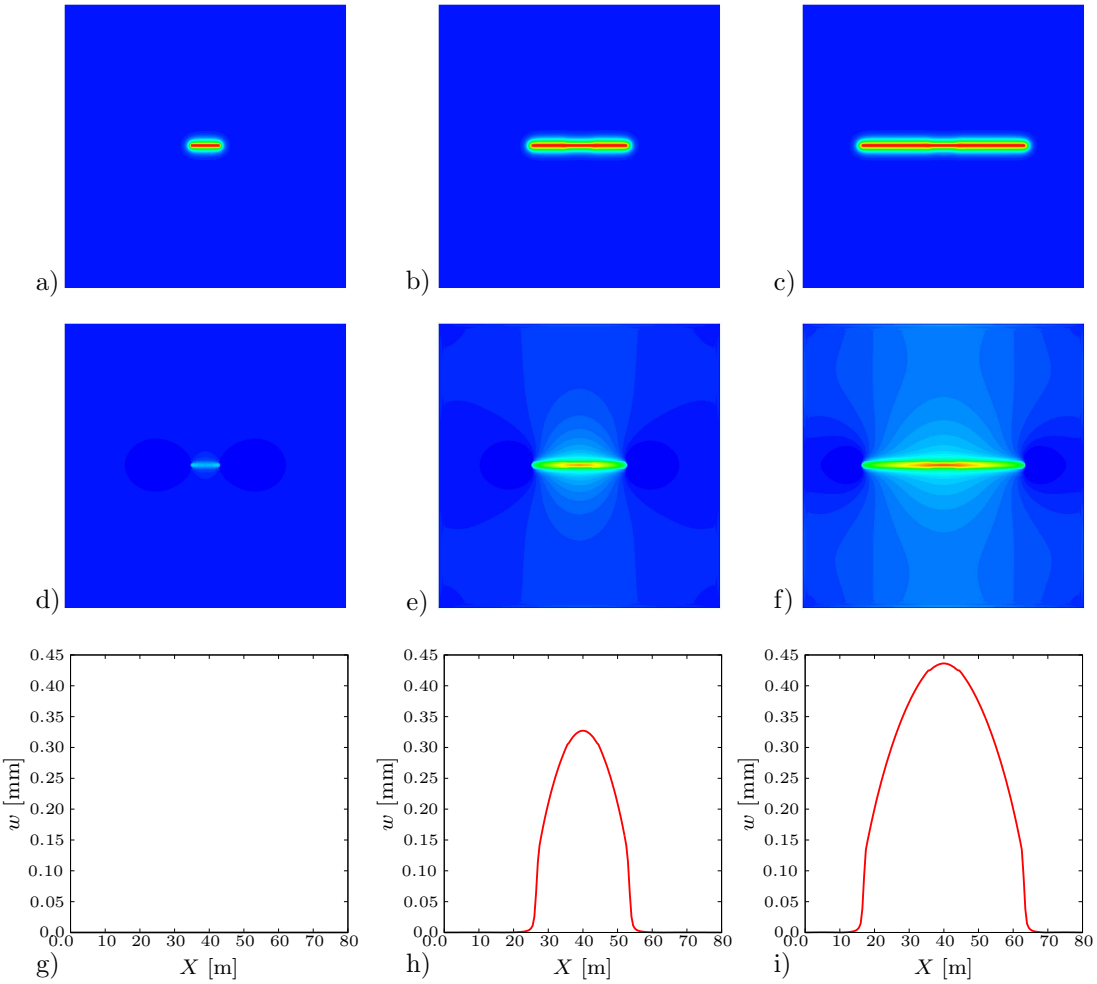

Figure 8.17: *Hydraulically induced crack driven by fluid volume injection. Results*: a)–c) Fracture phase-field d, d)–f) fluid pressure p and g)–i) crack opening width w at three different times $t = 1$ s, 5 s and 50 s.

in Figure 8.16a). For this and all subsequent boundary value problems the effective stress based crack driving force is used with $\sigma_c = 0.005$ N/m^2, as given in Table 8.2. The

presented results of the simulations are obtained by the minimization formulation and with the Q_1-RT_0-Q_1 element design. The numerical simulation is performed with different mesh sizes H^e and the time step is chosen to be $\tau = 0.1$ s. In order to save computational time only one Gauss-Seidel cycle is performed.

Figure 8.17 shows the fracture phase-field d, the fluid pressure p and the crack opening width w at three different times. The crack propagates in horizontal direction. Observe that the fluid pressure is high within the crack and the neighboring zone and very small in the rest of the specimen, see Figure 8.17d–f). This is due to the Poiseuille law inside the crack that results in a high fluid mass flow along the crack compared to the Darcy flow in the unbroken solid. The crack opening width in a horizontal cut through the specimen at the height of the crack is shown in Figure 8.17g)–i). Here we observe the typical ellipsoidal crack shape. In Figure 8.16b) the pressure inside the crack is plotted over the injected volume for different mesh sizes H^e. First observe that the pressure increases up to the point where the crack starts propagating. This is followed by a decreasing pressure due to the increasing crack length. This drop of pressure is well known in hydraulic fracturing, see for example the analytical solutions in Geertsma & de Klerk [113], Khristianovic & Zheltov [148], Detournay [82] or Hu & Garagash [136]. Analytical solutions do not show another increase in fluid pressure as observed here. This is due to the fact that analytical solutions consider an infinite half-space and thus consider the crack always being infinitely away from the drained and mechanically fixed boundary. For the numerical simulation, when the crack approaches the boundaries, the fluid pressure increases again. The results observed with the different mesh sizes H^e are in good agreement to each other, see Figure 8.16b).

8.6.4. Three-dimensional hydraulically induced crack

Now we turn the attention to a radial-symmetric three-dimensional boundary value problem. Consider a cylindrical domain with diameter $D = 40$ m and height $H = 20$ m. In its center a notch is placed by setting Dirichlet conditions $\bar{d} = 1$. In the notch a fluid mass of $M_{\text{injec.}} = 0.625$ kg/s is injected by prescribing a fluid mass source $\dot{m}$. The geometric setup is visualized in Figure 8.18. The numerical simulation is performed by use of the saddle-point formulation. The specimen is discretized by 61.440 Q_1-Q_1-Q_1 finite elements and a time step size of $\tau = 0.01$ s is chosen. In order to save computational time only one Gauss-Seidel cycle is performed.

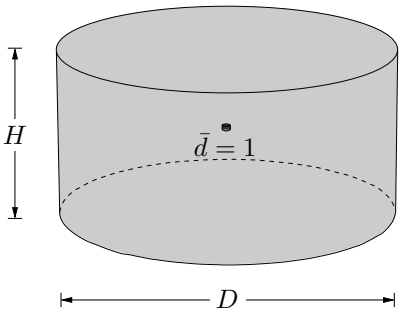

Figure 8.18: *Three-dimensional hydraulically induced crack. Boundary value problem*: Into a circular cylinder with a diameter D and height H fluid is injected into a notch placed in its center of volume.

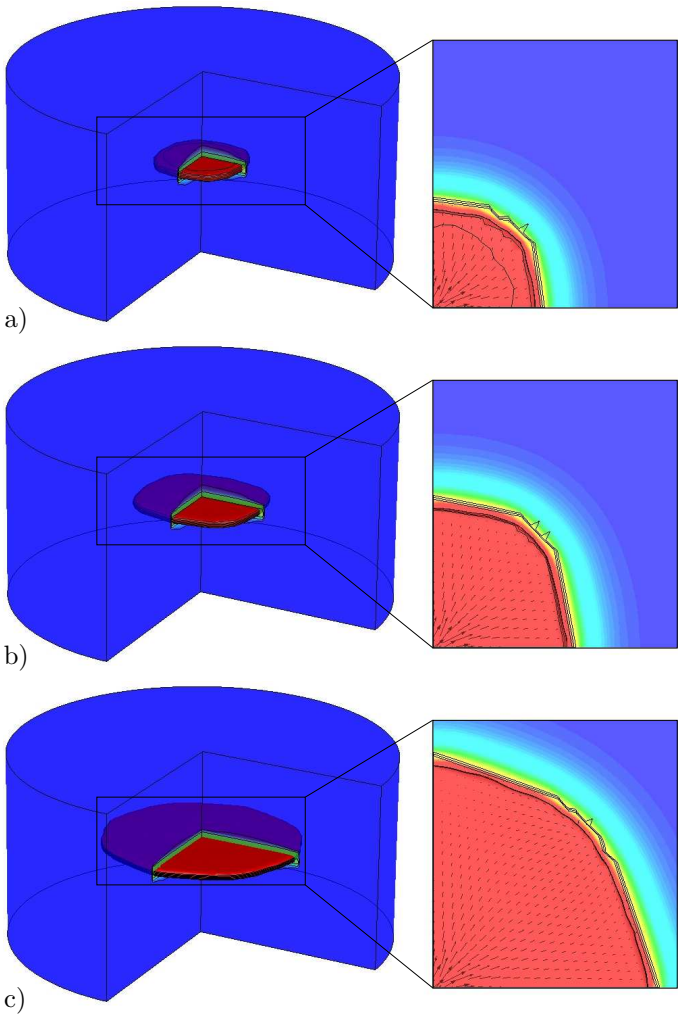

Figure 8.19: *Three-dimensional hydraulically induced crack. Results*: Fluid pressure field p and crack evolution at a) $t = 0$ s, b) $t = 2000$ s and c) $t = 50000$ s. Due to the low permeability of the porous bulk material the injected fluid stays primarily inside the crack yielding to high fluid pressure inside the crack and to nearly no increase of fluid pressure in the bulk. The arrows indicate the radial fluid flow $\mathbb{H}$ inside that crack.

Figure 8.19 shows the fluid pressure p and the evolution of the crack state at three different time steps in the numerical simulation. Due to the low permeability of the porous bulk material the injected fluid stays primarily inside the crack yielding to high fluid pressure p inside the crack and to nearly no increase of the fluid pressure in the bulk. On the right hand side of the figure the arrows indicate the fluid flow vector. We observe a fluid flow in radial direction that has the highest amount in the center of the crack at the point of injection.

8.6.5. Joining ensemble of 3D cracks driven by fluid volume injection

As a next three-dimensional boundary value problem consider a cubic domain $\mathcal{B} = \{\boldsymbol{X} \in \mathcal{R}^3 | \boldsymbol{X} \in [0, L] \times [0, L] \times [0, L]\}$ with $L = 50$ m. Inside the domain there are five rectangular initial notches with side lengths $a = 7$ m each. A constant fluid mass injection of $M_{\text{injec.}} = \dot{\bar{m}} V_{\text{injec.}} = 4.8$ kg/s is prescribed in the volumes $V_{\text{injec.}}$ around each notch based on the fluid mass source $\dot{\bar{m}}$ introduced above. All surfaces of the specimen are assumed to

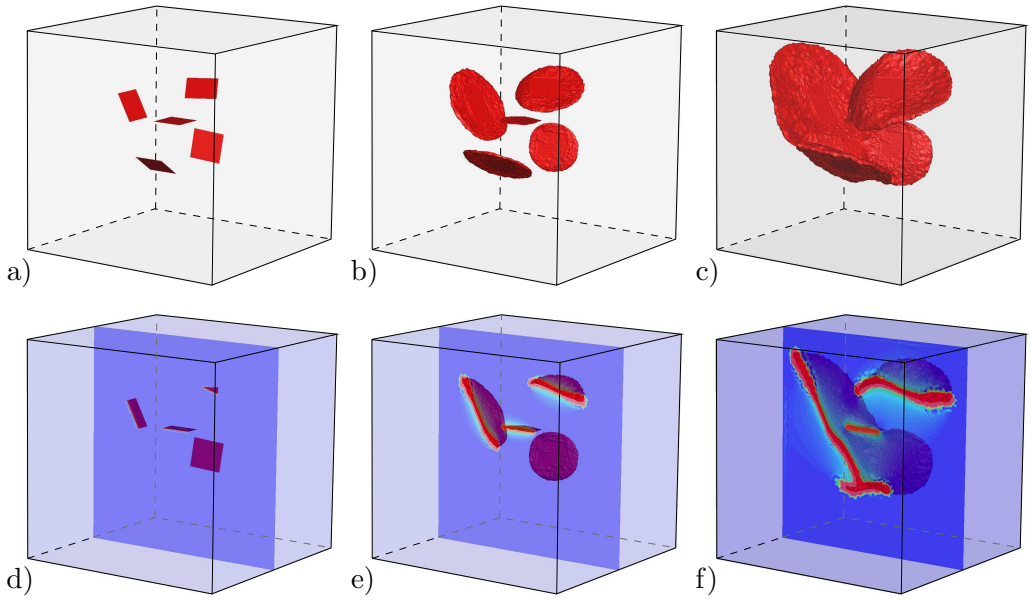

Figure 8.20: *Joining ensemble of 3D cracks driven by fluid volume injection. Results*: Contour plots of fracture phase-field d at a) $t = 0$ s, b) $t = 11$ s and c) $t = 20$ s, as well as fluid pressure field p at d) $t = 0$ s, e) $t = 11$ s and f) $t = 20$ s.

be mechanically fixed, permeable and potential free, that is $\bar{\mu} = 0$ and $\bar{\varphi} = \boldsymbol{X}$. The numerical results are obtained by the saddle-point formulation. Here the cubic domain is discretized by 4.278.041 P_1-P_1-P_1 tetrahedral elements. The time step is chosen to be $\tau = 0.1$ s during the whole simulation. The initial placement of the five notches can be seen in Figure 8.20a). In order to save computational time only one Gauss-Seidel cycle is performed.

Figure 8.20a)–c) shows contour plots of the fracture phase-field d at different time steps. As soon as the fluid pressure p inside the cracks reaches a critical value, crack propagation can be observed at each of the five notches. However the crack propagation is not in-plane and not all notches propagate by the same amount. In the observed setup the notch in the middle is shielded by the other notches and does not propagate very much. While propagating also coalescences of the individual cracks can be observed. Resultant contour plots of the fluid pressure p are visualized in Figure 8.20d)–f). We observe a nearly constant fluid pressure p inside of each crack due to the increased permeability inside the cracks due to the Poiseuille law. In the unbroken bulk solid the increase in fluid pressure p is negligible. These observations are in line with the two- and three-dimensional boundary value problems considered above.

8.6.6. Hydraulic fracturing starting from a three-dimensional borehole

As a last numerical boundary value problem consider a three-dimensional cubic domain $\mathcal{B} = \{\boldsymbol{X} \in \mathcal{R}^3 | \boldsymbol{X} \in [0, 2L] \times [0, 2L] \times [0, L]\}$ with side lengths $L = 50$ m and with a borehole of diameter $D = 2$ m. The borehole consists of one vertical branch that divides into four horizontal branches. Each of the horizontal branches has four notches around its curved surface. We prescribe a constant fluid mass of $M_{\text{injec.}} = 0.1$ kg/s from the borehole in each of the notches by prescribing a fluid mass source $\dot{m}$ as introduced above. All surfaces of the cubic specimen are assumed to be mechanically fixed, permeable and

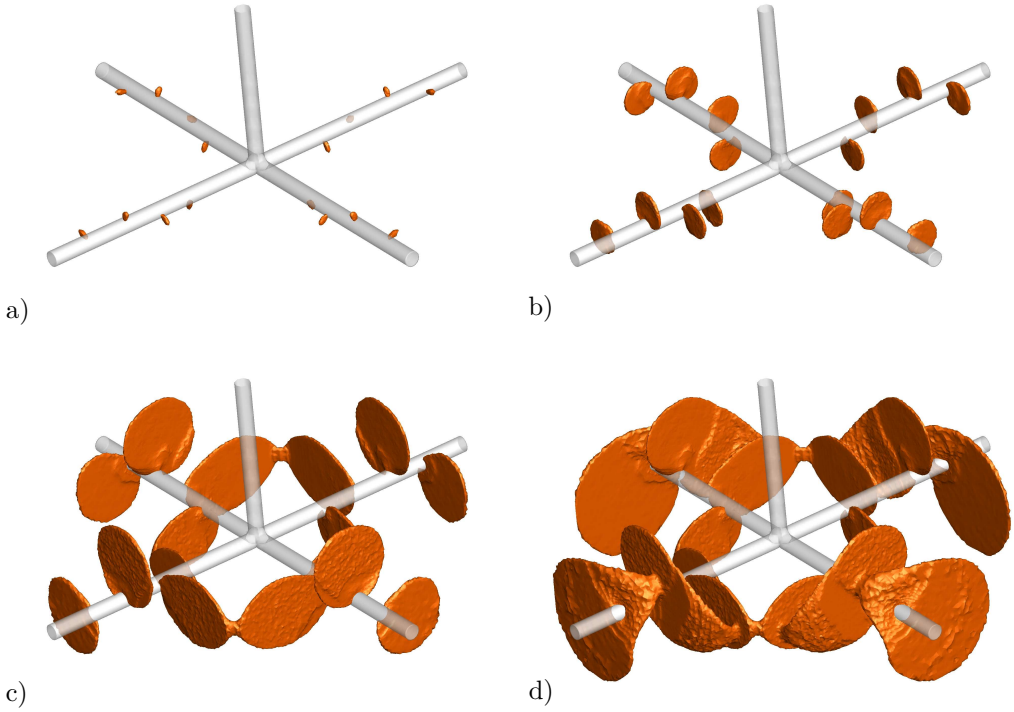

Figure 8.21: *Hydraulic fracturing starting from a three-dimensional borehole. Results*: Contour plots of fracture phase-field d at different times a) $t = 250$ s, b) $t = 2.250$ s, c) $t = 10.000$ s and d) $t = 28.750$ s.

potential free, that is $\bar{\mu} = 0$ and $\bar{\boldsymbol{\varphi}} = \boldsymbol{X}$. Furthermore, at all the curved surfaces of the borehole, the displacement normal to the curved surface is fixed. The numerical simulation is performed by use of the saddle-point formulation. Due to the symmetry of the boundary value problem only one fourth of the domain is discretized by 4.375.614 tetrahedral P_1-P_1-P_1 tetrahedral elements and the time step is chosen to $\tau = 5$ s during the whole simulation. Due to the high number of degrees of freedom for this boundary value problem, a parallel environment with 20 processors has been used. In order to save computational time only one Gauss-Seidel cycle is performed.

Figure 8.21a) shows the fracture phase-field d at $t = 0$, that is the 16 initial notches, where the borehole is perforated and the fluid escapes from the borehole and flows into the porous solid. The propagation of the cracks is then visualized in Figure 8.21b)–d). Again coalescences of the individual cracks can be observed during the propagation process. This example shows the conceptual application of the proposed formulation to the analysis of complex fracking problems.

Chapter 9

Conclusion

The main goal of this work is to develop a variational framework for finite strain multiphysics problems of multicomponent solids at fracture and its numerical treatment by use of the finite element method. The work is divided into two parts. The first part introduces the thermodynamical framework for multicomponent multiphysics problems of solids and develops variational formulations for two model problems related to porous media and diffusion processes in elastic solids. The second part of the work extends the framework by including crack propagation in order to model hydraulically driven fracture scenarios.

To this end, a review of *finite deformation kinematics* and *physical balance equations* for multiphysics problems in multicomponent solids is given. A consistent *modeling framework* is introduced by applying constitutive principles and thermodynamical restrictions. This framework is first applied to porous media without fracture. The purpose of this application is to compare different variational formulations and specifically to show the numerical efficiency of the new proposed minimization principle. To this end, first the modeling assumptions and the initial boundary value problem are summarized. This initial boundary value problem is expressed in the form of a *variational principle*. Due to the fluid flow within a porous solid being a dissipative mechanism this variational principle is expressed in *time-continuous rate form*. The focus here is on different forms of variational principles that are shown to be related by a partial *Legendre transformation*. In particular a *new canonical minimization formulation* is proposed which is then transformed into the classical $\{\boldsymbol{\varphi}, \mu\}$ *saddle-point formulation* widely used in the literature. These principles are then discretized in time yielding *incremental variational principles* for the initial boundary value problem. For the numerical treatment with the *finite element method* a space-discretization is conducted. By considering different numerical boundary value problems the space-time-discrete *canonical minimization* formulation and the *saddle-point* formulation are validated and compared to each other. The proposed minimization principle is shown to be advantageous over the classical saddle-point formulation as the interpolations of the fields are not restrained to an inf-sup (BBL) condition. Furthermore the computational efficiency of the minimization formulation is superior over the saddle-point formulation.

A second application related to diffusion processes in elastic solids puts the focus on the variational modeling of *gradient-enhanced Cahn-Hilliard-type* diffusion processes. After introducing the modeling assumptions the initial boundary value problem is reviewed and again expressed via a rate-type variational principle for both the minimization and the saddle-point formulation. A model reduction to Fickian-type diffusion is shown to yield the identical structure as for the porous media model. The interpolation space of the species flow vector in the minimization principle for the gradient-enhanced model under consideration requires finite element shape functions of higher-order continuity. To this end, time and space discretization is considered only for the saddle-point formulation, which is resulting in a *three-field problem* with the solid's deformation $\boldsymbol{\varphi}$, the species concentration c and the chemical potential $\tilde{\mu}$ as global degrees of freedom. For the reduced setting of Fickian-type diffusion the partial differential equation for c reduces to an ordinary differential equation and the *two-field* $\{\boldsymbol{\varphi}, \tilde{\mu}\}$ saddle-point formulation, as considered for the Darcy-type fluid flow, is regained.

The variational framework is then extended to include fracture processes. To this end, we make use of the *phase-field fracture* approach. This is a spatially smooth continuum approach that avoids the modeling of sharp discontinuities, which makes the numerical implementation straightforward. Furthermore this diffusive modeling allows the resolution of complex crack topologies including branching.

Besides the correct and efficient modeling of the poro-elastic bulk response in the intact soil as well as the modeling of crack initiation and propagation, a further key challenge for hydraulically induced fracture processes is the modeling of the additional fluid flow within the cracks. To this end, we make use of the classical *Poiseuille law* for laminar flow of a viscous fluids. For the modeling this results in a permeability in Darcy's law that is dependent on the crack opening width. We propose a continuum-based approximation for the evaluation of the crack opening width that suits the phase-field fracture approach. Starting with a rate-type variational principle for the problem of finite strain poro-hydro-elasticity at fracture, consistent time- and space-discretizations again yield a minimization and a saddle-point formulation for the problem under consideration. The capabilities of the proposed model is demonstrated by means of representative numerical examples. To sum up, the major contributions in this work are:

- *Rate-type potentials*: Construction of rate-type potentials for the evolution problem of multiphysics problems of solids both without and at fracture.
- *Time- and space-discretization*: Consistent time- and space-time-discrete counterparts of the potentials for implementation using the finite element method.
- *New stable minimization formulation*: The modeling in terms of a variational principle naturally leads to a canonical minimization formulation that is a priori stable and not constrained by a BBL condition.
- *Gradient-enhanced models*: The proposed potentials are shown to be able to model fluid flow with Darcy's law or Fickian-type diffusion as well as advanced Cahn-Hilliard-type diffusion.
- *Modeling of hydraulically driven fracture*: The model is extended in order to model the additional fluid flow along cracks.

Bibliography

[1] Abousleiman, Y.; Cheng, A.; Cui, L.; Detournay, E.; Roegiers, J.-C. [1996]: *Mandel's problem revisited.* Géotechnique, 46(2): 187–195.

[2] Adachi, J.; Siebrits, E.; Peirce, A.; Desroches, J. [2007]: *Computer simulation of hydraulic fractures.* International Journal of Rock Mechanics & Mining Sciences, 44: 739–757.

[3] Adler, P. M.; Thovert, J.-F.; Mourzenko, V. V. [2013]: *Fractured porous media.* Oxford University Press, Croydon.

[4] Advani, S. H.; Lee, T. S.; Lee, J. K.; Kim, C. S. [1993]: *Hygrothermomechanical evaluation of porous media under finite deformation. Part I–finite element formulation.* International Journal for Numerical Methods in Engineering, 36: 147–160.

[5] Aguilar, G.; Gaspar, F. J.; Lisbona, F.; Rodrigo, C. [2008]: *Numerical stabilization of Biot's consolidation model by a perturbation on the flow equation.* International Journal for Numerical Methods in Engineering, 75(11): 1282–1300.

[6] Anand, L. [2012]: *A Cahn-Hilliard-type theory for species diffusion coupled with large elastic-plastic deformations.* Journal of the Mechanics and Physics of Solids, 60: 1983–2002.

[7] Anderson, T. L. [1995]: *Fracture Mechanics: Fundamentals and Applications.* CRC Press, 2nd Edition.

[8] Anjam, I.; Valdman, J. [2015]: *Fast MATLAB assembly of FEM matrices in 2d and 3d: Edge elements.* Applied Mathematics and Computation, 267: 252–263.

[9] Armero, F. [1999]: *Formulation and finite element implementation of a multiplicative model of coupled poro-plasticity at finite strains under fully saturated conditions.* Computer Methods in Applied Mechanics and Engineering, 171(34): 205–241.

[10] Armero, F.; Linder, C. [2009]: *Numerical simulation of dynamic fracture using finite elements with embedded discontinuities.* International Journal of Fracture, 160: 119–141.

[11] Arnold, D. N.; Brezzi, F.; Fortin, M. [1984]: *A stable finite element for the Stokes equations.* Calcolo, 21: 337–344.

[12] Arnold, D. N.; Boffi, D.; Falk, R. S. [2005]: *Quadrilateral $H(\mathrm{div})$ finite elements.* SIAM Journal of Numerical Analysis, 42(6): 2429–2451.

[13] Avci, O. [2013]: *Coupled Deformation and Flow Processes of Partially Saturated Soil: Experiments, Model Validation and Numerical Investigations.* Ph.D. Thesis, University of Stuttgart, Institute for Applied Mechanics (CE).

[14] Babuška, I. [1973]: *The finite element method with Lagrangian multipliers.* Numerische Mathematik, 20: 179–192.

[15] Başar, Y.; Weichert, D. [2000]: *Nonlinear Continuum Mechanics of Solids.* Springer.
[16] Barenblatt, G. I. [1962]: *The mathematical theory of equilibrium cracks in brittle fracture.* Advances in Applied Mechanics, 7: 55–129.
[17] Batchelor, G. K. [1967]: *An Introduction to Fluid Dynamics.* Cambridge University Press.
[18] Bažant, Z. P.; Salviato, M.; Chau, V. T.; Viswanathan, H.; Zubelewicz, A. [2014]: *Why fracking works.* Journal of Applied Mechanics, 81(10): 1–10.
[19] Bedford, A.; Drumheller, D. [1983]: *Theories of immiscible and structured mixtures.* International Journal of Engineering Science, 21(8): 863–960.
[20] Belytschko, T.; Fish, J.; Engelmann, E. [1988]: *A finite element with embedded localization zones.* Computer Methods in Applied Mechanics and Engineering, 70: 59–89.
[21] Biot, M. A. [1941]: *General theory of three-dimensional consolidation.* Journal of Applied Physics, 12: 155–164.
[22] Biot, M. A. [1956]: *Thermoelasticity and irreversible thermodynamics.* Journal of Applied Physics, 27: 240–253.
[23] Biot, M. A. [1965]: *Mechanics of Incremental Deformations.* John Wiley & Sons Inc., New York.
[24] Biot, M. A. [1972]: *Theory of Finite Deformations of Porous Solids.* Indiana University Mathematics Journal, 21: 597–620.
[25] Biot, M. A. [1973]: *Nonlinear and semilinear rheology of porous solids.* Journal of Geophysical Research, 78(23): 4924–4937.
[26] Biot, M. A. [1975]: *A virtual dissipation principle and Lagrangian equations in non-linear irreversible thermodynamics.* Bulletin of Royal Academy of Belgium (Classe des Sciences), 61: 6–30.
[27] Biot, M. A. [1976]: *New chemical thermodynamics of open systems. Thermobaric potential, a new concept.* Bulletin of Royal Academy of Belgium (Classe des Sciences), 62: 239–258.
[28] Biot, M. A. [1977]: *Variational Lagrangian-thermodynamics of nonisothermal finite strain mechanics of porous solids and thermomolecular diffusion.* International Journal of Solids and Structures, 13: 579–597.
[29] Biot, M. A. [1977]: *New fundamental cconcept and results in themodynamics with chemical applications.* Chemical Physics, 22: 183–198.
[30] Biot, M. A. [1978]: *Variational irreversible thermodynamics of heat and mass transfer in porous solids: New cconcept and methods.* Quarterly of Applied Mathematics, 36: 19–38.
[31] Biot, M. A. [1979]: *New variational-Lagrangian thermodynamics of viscous fluid mixtures with thermomolecular diffusion.* Proceedings of the Royal Society London A, 365: 467–494.
[32] Biot, M. A. [1982]: *Thermodynamic principle of virtual dissipation and the dynamics of physical-chemical fluid mixtures including radiation pressure.* Quarterly of Applied Mathematics, 39: 517–540.
[33] Biot, M. A. [1984]: *New variational-Lagrangian irreversible thermodynamics with application to viscous flow, reaction-diffusion, and solid mechanics.* In Hutchinson, J.; Wu, T. (Editors), *Advances in Applied Mechanics*, Vol. 24, pp. 1–91. Elsevier.
[34] Biot, M. A.; Willis, D. [1957]: *The elastic coefficients of the theory of consoli-*

dation. Journal of Applied Mechanics, 79(594): 1–8.

[35] Bohn, E.; Eckl, T.; Kamlah, M.; McMeeking, R. [2013]: *A model for lithium diffusion and stress generation in an intercalation storage particle with phase change.* Journal of The Electrochemical Society, 160: A1638–A1652.

[36] Booker, J.; Small, J. [1975]: *An investigation of the stability of numerical solutions of Biot's equations of consolidation.* International Journal of Solids and Structures, 11: 907–917.

[37] Boone, T. J.; Ingraffea, A. R. [1990]: *A numerical procedure for simulation of hydraulically-driven fracture propagation in poroelastic media.* International Journal for Numerical and Analytical Methods in Geomechanics, 14: 27–47.

[38] Borden, M. J.; Verhoosel, C. V.; Scott, M. A.; Hughes, T. J. R.; Landis, C. M. [2012]: *A phase-field description of dynamic brittle fracture.* Computer Methods in Applied Mechanics and Engineering, 217-220: 77–95.

[39] Borja, R.; Alarcon, E. [1995]: *A mathematical framework for finite strain elastoplastic consolidation. Part I: Balance laws, variational formulation, and linearization.* Computer Methods in Applied Mechanics and Engineering, 122: 145–171.

[40] Bouklas, N.; Landis, C. M.; Huang, R. [2015]: *A nonlinear, transient finite element method for coupled solvent diffusion and large deformation of hydrogels.* Journal of the Mechanics and Physics of Solids, 79: 21–43.

[41] Bourdin, B.; Francfort, G.; Marigo, J.-J. [2008]: *The Variational Approach to Fracture.* Springer.

[42] Bowen, R. M. [1976]: *Theory of mixtures.* In Eringen, A. C. (Editor), *Continuum Physics Vol. III.* Academic Press, New York.

[43] Bowen, R. W. [1980]: *Incompressible porous media models by use of the theory of mixtures.* International Journal of Engineering Science, 18: 1129–1148.

[44] Bowen, R. W. [1982]: *Compressible porous media models by use of the theory of mixtures.* International Journal of Engineering Science, 20: 697–735.

[45] Braess, D. [2013]: *Finite Elemente.* Springer Spektrum, 5 Edition.

[46] Brezzi, F. [1974]: *On the existence, uniqueness and approximation of saddle-point problems arising from lagrangian multipliers.* Revue française d'automatique, informatique, recherche opérationnelle. Analyse numérique, 8: 129–151.

[47] Brezzi, F.; Fortin, M. [1991]: *Mixed and Hybrid Finite Element Methods.* Springer-Verlag.

[48] Brezzi, F.; Douglas, J.; Marini, L. [1985]: *Two families of mixed finite elements for second order elliptic problems.* Numerische Mathematik, 47: 217–235.

[49] Bunger, A. P.; Detournay, E.; Jeffrey, R. G. [2005]: *Crack tip behavior in near-surface fluid-driven fracture experiments.* Comptes Rendus Mechanique, 333: 299–304.

[50] Burch, D.; Singh, G.; Ceder, G.; Bazant, M. [2008]: *Phase-transformation wave dynamics in $LiFePO_4$.* Solid State Phenomena, 139: 95–100.

[51] Cahn, J. W. [1959]: *Free energy of a nonuniform system. ii. thermodynamic basis.* The Journal of Chemical Physics, 30: 1121–1124.

[52] Cahn, J. W.; Hilliard, J. E. [1957]: *Free energy of a nonuniform system. i. interfacial free energy.* The Journal of Chemical Physics, 28: 258–267.

[53] Cahn, J.; Hilliard, J. [1958]: *Free energy of a nonuniform system. I. interfacial free energy.* The Journal of Chemical Physics, 28: 258–267.

[54] Callari, C.; Armero, F. [2002]: *Finite element methods for the analysis of strong discontinuities in coupled poro-plastic media.* Computational Methods in Applied Mechanics and Engineering, 191: 4371–4400.

[55] Callari, C.; Armero, F.; Abati, A. [2010]: *Strong discontinuities in partially saturated poroplastic solids.* Computational Methods in Applied Mechanics and Engineering, 199: 1513–1535.

[56] Camacho, G. T.; Ortiz, M. [1996]: *Computational modelling of impact damage in brittle materials.* International Journal of Solids and Structures, 33: 2899–2938.

[57] Carter, J. P.; Booker, J. R.; Small, J. C. [1979]: *The analysis of finite elasto-plastic consolidation.* International Journal for Numerical and Analytical Methods in Geomechanics, 3(2): 107–129.

[58] Carter, J.; Small, J.; Booker, J. [1977]: *A theory of finite elastic consolidation.* International Journal of Solids and Structures, 13: 467–478.

[59] Chaboche, J. L. [1981]: *Continuous damage mechanics - a tool to describe phenomena before crack initiation.* Nuclear Engineering and Design, 64: 233–247.

[60] Chaboche, J. L. [1988]: *Continuum damage mechanics: Part 1 - general concepts.* Journal of Applied Mechanics, 55: 59–72.

[61] Chapelle, D.; Bathe, K. J. [1993]: *The inf-sup test.* Computers and Structures, 47: 537–545.

[62] Christian, J. [1977]: *Numerical methods in geotechnical engineering*, chapter Two- and three-dimensional consolidation, pp. 399–426. McGraw-Hill.

[63] Chukwudozie, C.; Bourdin, B.; Yoshioka, K. [2013]: *A variational approach to the modeling and numerical simulation of hydraulic fracturing under in-situ stresses.* In *Proceedings of the Thirty-Eighth Workshop on Geothermal Reservoir Engineering, Stanford University, Stanford, California.*

[64] Comi, C. [1999]: *Computational modelling of gradient-enhanced damage in quasi-brittle materials.* Mechanics of Cohesive-frictional Materials, 4(1): 17–36.

[65] Coussy, O. [1989]: *A general theory of thermoporoelastoplasticity for saturated porous materials.* Transport in Porous Media, 4(3): 281–293.

[66] Coussy, O. [1995]: *Mechanics of Porous Continua.* John Wiley & Sons, Chichester.

[67] Coussy, O. [2004]: *Poromechanics.* John Wiley & Sons, Chichester.

[68] Coussy, O.; Dormieux, L.; Detournay, E. [1998]: *From mixture theory to Biot's approach for porous media.* International Journal of Solids and Structures, 35(34–35): 4619–4635.

[69] Cryer, C. W. [1963]: *A comparison of the three-dimensional consolidation theories of Biot and Terzaghi.* Quarterly Journal of Mechanics and Applied Mathematics, 16: 401–412.

[70] Dal, H.; Miehe, C. [2015]: *Computational electro-chemo-mechanics of lithium-ion battery electrodes at finite strains.* Computational Mechanics, 55: 303–325.

[71] Darcy, H. [1856]: *Les fountaines publiques de la ville de Dijon.* Victor Dalmont, Paris.

[72] de Boer, R. [1996]: *Highlights in the historical development of porous media theory: Towards a consititent macroscopic theory.* Applied Mechanics Review, 49: 201–262.

[73] de Boer, R. [2000]: *Theory of Porous Media.* Springer, Berlin.

[74] De Boer, R.; Bluhm, J. [1999]: *The influence of compressibility on the stresses of elastic porous solids–semimicroscopic investigations.* International Journal of Solids

and Structures, 36: 4805–4819.

[75] de Boer, R.; Ehlers, W. [1988]: *A historical review of the formulation of porous media theories.* Acta Mechanica, 74: 1–8.

[76] de Boer, R.; Ehlers, W. [1990]: *The development of the concept of effective stresses.* Acta Mechanica, 83: 77–92.

[77] de Borst, R. [2016]: *Fluid flow in fractured and fracturing porous media: A unified view.* Mechanics Research Communications.

[78] de Borst, R.; Verhoosel, C. V. [2016]: *Gradient damage vs phase-field approaches for fracture: Similarities and differences.* Computer Methods in Applied Mechanics and Engineering.

[79] de Borst, R.; Réthoré, J.; Abellan, M.-A. [2006]: *A numerical approach for arbitrary cracks in a fluid-saturated medium.* Archive of Applied Mechanics, 75: 595–606.

[80] de Groot, S. R.; Mazur, P. [1984]: *Non-Equilibrium Thermodynamics.* Dover Books on Physics. Dover Publications, Inc., New York.

[81] Deshpande, R.; Cheng, Y. T.; Verbrugge, M. W. [2010]: *Modeling diffusion-induced stress in nanowire electrode structures.* Journal of Power Sources, 195: 5081–5088.

[82] Detournay, E. [2004]: *Propagation regimes of fluid-driven fractures in impermeable rocks.* International Journal of Geomechanics, 4(1): 35–45.

[83] Detournay, E.; Cheng, A. H.-D. [1993]: *Fundamentals of poroelasticity.* In Fairhurst, C. (Editor), *Comprehensive Rock Engineering: Principles, Practice and Projects, Vol. II, Analysis and Design Method*, chapter 5, pp. 113–171. Pergamon Press.

[84] Detournay, E.; Peirce, A. [2014]: *On the moving boundary conditions for a hydraulic fracture.* International Journal of Engineering Science, 84.

[85] Di Leo, C.; E., R.; Anand, L. [2014]: *A Cahn-Hilliard-type phase-field theory for species diffusion coupled with large elastic deformations: application to phase-separating Li-ion electrode materials.* Journal of the Mechanics and Physics of Solids, 70: 1–29.

[86] Dimitrijevic, B. J.; Hackl, K. [2006]: *A method for gradient enhancement of inelastic material models.* In Kojic, M.; Papadrakakis, M. (Editors), *Proceedings of First South-East European Conference on Computational Mechanics*, pp. 191–197.

[87] Dimitrijevic, B. J.; Hackl, K. [2008]: *A method for gradient enhancement of continuum damage models.* Technische Mechanik, 28(1): 43–52.

[88] Dimitrijevic, B. J.; Hackl, K. [2011]: *A regularization framework for damage-plasticity models via gradient enhancement of the free energy.* International Journal for Numerical Methods in Biomedical Engineering, 27: 1199–1210.

[89] Douglas, J.; Wang, J. [1989]: *An absolutely stabilized finite element method for the Stokes problem.* Mathematics of computation, 52(186): 495–508.

[90] Doyle, M.; Newman, J.; Gozdz, A. S.; Schmutz, C. N.; Tarascon, J. M. [1996]: *Comparison of modeling predictions with experimental data from plastic lithium ion cells.* Journal of Electrochemical Society, 143: 1890–1903.

[91] Dumstorff, P.; Meschke, G. [2007]: *Crack propagation criteria in the framework of X-FEM-based structural analyses.* International Journal for Numerical and Analytical Methods in Geomechanics, 31: 239–259.

[92] Ehlers, W. [2002]: *Foundations of multiphasic and porous materials.* In Ehlers,

W.; Bluhm, J. (Editors), *Porous Media: Theory, Experiments and Numerical Applications*, pp. 3–86. Springer-Verlag, Berlin.

[93] Ehlers, W. [2009]: *Challenges of porous media models in geo-and biomechanical engineering including electro-chemically active polymers and gels.* International Journal of Advances in Engineering Sciences and Applied Mathematics, 1(1): 1–14.

[94] Ehlers, W. [2012]: *Poröse Medien – ein kontinuummechanisches Modell auf Basis der Mischungstheorie.* Nachdruck der Habilitationsschrift aus dem Jahre 1989 (Forschungsbericht aus dem Fachbereich Bauwesen der Universität-GH-Essen, Heft 47, Essen).

[95] Ehlers, W.; Blome, P. [2003]: *A triphasic model for unsaturated soil based on the theory of porous media.* Mathematical and Computer Modelling, 37(5–6): 507–513.

[96] Ehlers, W.; Luo, C. [2017]: *A phase-field approach embedded in the theory of porous media for the description of dynamic hydraulic fracturing.* Computer Methods in Applied Mechanics and Engineering, 315(1): 348–368.

[97] Ehlers, W.; Wagner, A. [2015]: *Multi-component modelling of human brain tissue: A contribution to the constitutive and computational description of deformation, flow and diffusion processes with application to the invasive drug-delivery problem.* Computer Methods in Biomechanics and Biomedical Engineering, 18(8): 861–879.

[98] Ehlers, W.; Karajan, N.; Markert, B. [2009]: *An extended biphasic model for charged hydrated tissues with application to the intervertebral disc.* Biomechanics and Modeling in Mechanobiology, 8(3): 233–251.

[99] Ehlers, W.; Markert, B.; Röhrle, O. [2009]: *Computational continuum biomechanics with application to swelling media and growth phenomena.* GAMM-Mitteilungen, 32(2): 135–156.

[100] Eshelby, J. D. [1951]: *The force on an elastic singularity.* Philosophical Transactions of the Royal Society London A, 244: 87–112.

[101] Eshelby, J. D. [1970]: *Inelastic Behavior of Solids*, chapter Energy relations and the energy-momentum tensor in continuum mechanics, pp. 77–114. McGraw Hill, New York.

[102] Ferronato, M.; Castelletto, N.; Gambolati, G. [2010]: *A fully coupled 3-D mixed finite element model of Biot consolidation.* Journal of Computational Physics, 229: 4813–4830.

[103] Fick, A. [1855]: *Über Diffusion.* Annalen der Physik, 170(1): 59–86.

[104] Flory, P. J.; Rehner, J. [1943]: *Statistical mechanics of cross-linked polymer networks II. Swelling.* The Journal of Chemical Physics, 11(11): 521–526.

[105] Francfort, G. A.; Marigo, J. J. [1998]: *Revisiting brittle fracture as an energy minimization problem.* Journal of the Mechanics and Physics of Solids, 46: 1319–1342.

[106] Frémond, M. [2002]: *Non-Smooth Thermomechanics.* Springer.

[107] Frémond, M.; Nedjar, B. [1996]: *Damage, gradient of damage, and principle of virtual power.* International Journal of Solids and Structures, 33: 1083–1103.

[108] Freund, L. B. [1990]: *Dynamic Fracture Mechanics.* Cambridge University Press.

[109] Gajo, A. [2010]: *A general approach to isothermal hyperelastic modelling of saturated porous media at finite strains with compressible solid constituents.* Proceedings of the Royal Society London A, 466: 3061–3087.

[110] Gajo, A. [2011]: *Finite strain hyperelastoplastic modelling of saturated porous media with compressible constituents.* International Journal of Solids and Structures, 48: 1738–1753.

[111] Gajo, A.; Denzer, R. [2011]: *Finite element modelling of saturated porous media at finite strains under dynamic conditions with compressible constituents.* International Journal for Numerical Methods in Engineering, 85: 1705–1736.

[112] Garagash, D. I.; Detournay, E. [2005]: *Plane-strain propagation of a fluid-driven fracture: Small toughness solution.* Journal of Applied Mechanics, 72: 916–926.

[113] Geertsma, J.; de Klerk, F. [1969]: *A rapid method of predicting width and extent of hydraulic induces fractures.* Journal of Petroleum Technology, 21(12): 1571–1581.

[114] Ghadiani, S. R. [2005]: *A multiphasic continuum mechanical model for design investigations of an effusion-cooled rocket thrust chamber.* Ph.D. Thesis, University of Stuttgart, Institute for Applied Mechanics (CE).

[115] Gordeliy, E.; Detournay, E. [2011]: *A fixed grid algorithm for simulating the propagation of a shallow hydraulic fracture with a fluid lag.* International Journal for numerical and analytical methods in geomechanics, 35: 602–629.

[116] Graham, T. [1833]: *On the law of the diffusion of gases.* Philosophical Magazine, Series 3, 2(9): 175–190.

[117] Grassl, P.; Fahy, C.; Gallipoli, D.; Wheeler, S. J. [2015]: *On a 2d hydro-mechanical lattice approach for modelling hydraulic fracture.* Journal of the Mechanics and Physics of Solids, 75: 104–118.

[118] Gray, W. G.; Schrefler, B. [2001]: *Thermodynamic approach to effective stress in partially saturated porous media.* European Journal of Mechanics–A/Solids, 20: 521–538.

[119] Gresho, P. M.; Lee, R. L. [1981]: *Don't suppress the wiggles—they're telling you something.* Computers and Fluids, 9: 223–253.

[120] Griffith, A. A. [1920]: *The phenomena of rupture and flow in solids.* Philosophical Transactions of the Royal Society London A, 221: 163–198.

[121] Griffith, A. A. [1924]: *The theory of rupture.* In Biezeno, C. B.; Burgers, J. M. (Editors), *Proceedings of the First International Congress for Applied Mechanics, Delft*, pp. 55–63.

[122] Gross, D.; Seelig, T. [2006]: *Fracture Mechanics.* Springer-Verlag Berlin.

[123] Gürses, E.; Miehe, C. [2009]: *A computational framework of three dimensional configurational force driven brittle crack propagation.* Computer Methods in Applied Mechanics and Engineering, 198: 1413–1428.

[124] Gurtin, M. E.; Fried, E.; Anand, L. [2010]: *The Mechanics and Thermodynamics of Continua.* Cambridge University Press.

[125] Gurtin, M. [1996]: *Generalized Ginzburg-Landau and Cahn-Hilliard equations based on a microforce balance.* Physica D, 92(3-4): 178–192.

[126] Hackl, K.; Fischer, F. D. [2008]: *On the relation between the principle of maximum dissipation and inelastic evolution given by dissipation potentials.* Proceedings of the Royal Society A, 464: 117–132.

[127] Hackl, K.; Fischer, F. D.; Svoboda, J. [2010]: *A study on the principle of maximum dissipation for coupled and non-coupled non-isothermal processes in materials.* Proceedings of the Royal Society A, 467: 1186–1196.

[128] Haga, J. B.; Osnes, H.; Langtangen, H. P. [2012]: *On the causes of pressure oscillations in low-permeable and low-compressible porous media*. International Journal for Numerical and Analytical Methods in Geomechanics, 36(12): 1507–1522.

[129] Hakim, V.; Karma, A. [2009]: *Laws of crack motion and phase-field models of fracture*. Journal of the Mechanics and Physics of Solids, 57: 342–368.

[130] Hassanizadeh, S. M. [1990]: *Mechanics and thermodynamics of multiphase flow in porous media including interphase boundaries*. Advances in Water Resources, 13(4): 169–186.

[131] Helmig, R.; Class, H. [2005]: *Grundlagen der Hydromechanik*. Shaker Verlag, Aachen.

[132] Hildebrand, F. E. [2013]: *Variational multifield modeling of the formation and evolution of laminate microstructure*. Ph.D. Thesis, University of Stuttgart, Institute for Applied Mechanics (CE).

[133] Hildebrand, F. E.; Miehe, C. [2012]: *A phase field model for the formation and evolution of martensitic laminate microstructure at finite strains*. Philosophical Magazine, 92: 4250–4290.

[134] Holzapfel, G. A. [2000]: *Nonlinear solid mechanics*. John Wiley & Sons.

[135] Hong, W.; Zhao, X.; Zhou, J.; Suo, Z. [2008]: *A theory of coupled diffusion and large deformation in polymeric gels*. Journal of the Mechanics and Physics of Solids, 56(5): 1779 – 1793.

[136] Hu, J.; Garagash, D. I. [2010]: *Plane-strain propagation of a fluid-driven crack in a permeable rock with fracture toughness*. Journal of Engineering Mechanics, 136: 1152–1166.

[137] Huang, N. C.; Russell, S. G. [1985]: *Hydraulic fracturing of a saturated porous medium—I: General theory*. Theoretical and Applied Fracture Mechanics, 4: 201–213.

[138] Huang, N. C.; Russell, S. G. [1985]: *Hydraulic fracturing of a saturated porous medium—II: Special cases*. Theoretical and Applied Fracture Mechanics, 4: 215–222.

[139] Hughes, T. J. R. [1987]: *The Finite Element Method*. Prentice-Hall, Englewood Cliffs, N.J.

[140] Hughes, T. J. R.; Franca, L. P. [1987]: *A new finite element formulation for computational fluid dynamics: VII. The Stokes problem with various well-posed boundary conditions: symmetric formulations that converge for all velocity pressure spaces*. Computer Methods in Applied Mechanics and Engineering, 65: 85–96.

[141] Hughes, T. J. R.; Franca, L. P.; Balestra, M. [1986]: *A new finite element formulation for computational fluid dynamics: V. Circumventing the Babuška-Brezzi condition: A stable Petrov-Galerkin formulation of the Stokes problem accommodating equal-order interpolations*. Computer Methods in Applied Mechanics and Engineering, 59: 85–99.

[142] Irwin, G. R. [1957]: *Analysis of stresses and strains near the end of a crack traversing a plate*. Journal of Applied Mechanics, 24: 361–364.

[143] Irwin, G. R. [1958]: *Fracture*. In Flügge, S. (Editor), *Encyclopedia of Physics*, Vol. 6, Elasticity and Plasticity, pp. 551–590. Springer.

[144] Irzal, F.; Remmers, J. J. C.; Huyghe, J. M.; de Borst, R. [2013]: *A large deformation formulation for fluid flow in a progressively fracturing porous material*. Computer Methods in Applied Mechanics and Engineering, 256(0): 29–37.

[145] Jox, S.; Becker, C.; Meschke, G. [2007]: *Hygro-mechanical modeling of cracked concrete in the framework of X-FEM.* VI International Conference on Fracture Mechanics for Concrete and Concrete Structures, 6: 1–8.

[146] Kaliske, M.; Dal, H.; Fleischhauer, R.; Jenkel, C.; Netzker, C. [2012]: *Characterization of fracture processes by continuum and discrete modelling.* Computational Mechanics, 50: 303–320.

[147] Kanninen, M. F.; Popelar, C. H. [1985]: *Advanced Fracture Mechanics.* Oxford University Press, New York.

[148] Khristianovic, S.; Zheltov, Y. [1955]: *Formation of vertical fractures by means of highly viscous fluids.* Proceeding of the 4th World Petroleum Congress, Rome, II: 579–586.

[149] Klaas, O.; Schroeder, J.; Stein, E.; C., M. [1995]: *A regularized dual mixed element for plane elasticity implementation and performance of the BDM element.* Computer Methods in Applied Mechanics and Engineering, 121: 201–209.

[150] Knott, J. F. [1973]: *Fundamentals of Fracture Mechanics.* Butterworth, London.

[151] Korsawe, J.; Starke, G. [2006]: *A least-squares mixed finite element method for Biot's consolidation problem in porous media.* SIAM Journal on Numerical Analysis, 43(1): 318–339.

[152] Kovalyshen, Y. [2010]: *Fluid-driven fracture in poroelastic medium.* Ph.D. Thesis, University of Minnesota.

[153] Kowalski, S. J. [2000]: *Toward a thermodynamics and mechanics of drying processes.* Chemical Engineering Science, 55(7): 1289 – 1304.

[154] Kraaijeveld, F.; Huyghe, J. M.; Remmers, J. J. C.; de Borst, R. [2013]: *Two-dimensional mode I crack propagation in saturated ionized porous media using partition of unity finite elements.* Journal of Applied Mechanics, 80(2): 1–12.

[155] Krause, R. F. [2014]: *Growth, Modelling and Remodelling of Biological Tissue.* Ph.D. Thesis, University of Stuttgart, Institute for Applied Mechanics (CE).

[156] Krischok, A.; Linder, C. [2015]: *On the enhancement of low-order mixed finite element methods for the large deformation analysis of diffusion in solids.* International Journal for Numerical Methods in Engineering, 106(4): 278–297.

[157] Kuhn, C.; Müller, R. [2010]: *A continuum phase field model for fracture.* Engineering Fracture Machanics, 77: 3625–3634.

[158] Kuna, M. [2010]: *Numerische Beanspruchungsanalyse von Rissen. Finite Elemente in der Bruchmechanik.* Springer-Verlag, New York, 2nd Edition.

[159] Larsson, R.; Runesson, K.; Sture, S. [1996]: *Embedded localization band in undrained soil based on regularized strond discontinuity. Theory and FE-analyisis.* International Journal of Solids and Structures, 33(20–22): 3081–3101.

[160] Lawn, B. R. [1993]: *Fracture of Brittle Solids.* Cambridge University Press, 2nd Edition.

[161] Lee, S.; Wheeler, M.; Wick, T. [2016]: *Pressure and fluid-driven fracture propagation in porous media using an adaptive finite element phase field model.* Computational Methods in Applied Mechanics and Engineering, 305: 111–132.

[162] Lemaitre, J. [1996]: *A Course on Damage Mechanics.* Springer.

[163] Lemaitre, J.; Chaboche, J.-L. [1990]: *Mechanics of Solid Materials.* Cambridge University Press.

[164] Linder, C.; Armero, F. [2009]: *Finite elements with embedded branching.* Finite Elements in Analysis and Design, 45: 280–293.

[165] Lovadina, C.; Auricchio, F. [2003]: *On the enhanced strain technique for elasticity problems.* Computers and Structures, 81: 777–787.

[166] Lu, S.; Pister, K. [1975]: *Decomposition of the deformation and representation of the free energy function for isotropic thermoelastic solids.* International Journal of Solids and Structures, 11: 927–934.

[167] Mandel, J. [1953]: *Consolidation des sols.* Géotechnique, 7.

[168] Marsden, J. E.; Hughes, T. J. R. [1983]: *Mathematical foundations of elasticity.* Prentice-Hall.

[169] Mauthe, S.; Miehe, C. [2016]: *Hydraulic fracture in poro-hydro-elastic media.* Mechanics Research Communications, in press, doi: 10.1016/j.mechrescom.2016.09.009.

[170] Meguid, S. A. [1989]: *Engineering Fracture Mechanics.* Elsevier Science Publishers, England.

[171] Meschke, G.; Grasberger, S. [2003]: *Gekoppelte numerische Analysen trocknungs- und lastinduzierter Schädigung von Betonstrukturen.* Beton und Stahlbetonbau, 98(4): 226–235.

[172] Meschke, G.; Leonhart, D. [2015]: *A generalized finite element method for hydro-mechanically coupled analysis of hydraulic fracturing problems using space-time variant enrichment functions.* Computer Methods in Applied Mechanics and Engineering, 290: 438–465.

[173] Meschke, G.; Grasberger, S.; Becker, C.; Jox, S. [2011]: *Smeared crack and X-FEM models in the context of poromechanics.* In Hofstetter, G.; Meschke, G. (Editors), *Numerical Modeling of Concrete Cracking, CISM Courses and Lectures*, pp. 265–327. Springer Wien New York.

[174] Meschke, G.; Leonhart, D.; J., T. J.; Zhou, M.-M. [2011]: *Computational mechanics of multiphase materials–modeling strategies at different scales.* Computer Assisted Mechanics and Engineering Sciences, 18: 73–89.

[175] Miehe, C. [2002]: *Strain-driven homogenization of inelastic microstructures and composites based on an incremental variational formulation.* International Journal for Numerical Methods in Engineering, 55: 1285–1322.

[176] Miehe, C. [2011]: *A multi-field incremental variational framework for gradient-extended standard dissipative solids.* Journal of the Mechanics and Physics of Solids, 59: 898–923.

[177] Miehe, C. [2013]: *Geometrical methods of nonlinear continuum mechanics and continuum thermodynamics.* Lecture Notes.

[178] Miehe, C. [2014]: *Variational gradient plasticity at finite strains. Part I: Mixed potentials for the evolution and update problems of gradient-extended dissipative solids.* Computer Methods in Applied Mechanics and Engineering, 268: 677–703.

[179] Miehe, C. [2014]: *Theoretical and computer-oriented material theory.* Lecture Notes.

[180] Miehe, C.; Gürses, E. [2007]: *A robust algorithm for configurational-force-driven brittle crack propagation with r-adaptive mesh alignment.* International Journal for Numerical Methods in Engineering, 72: 127–155.

[181] Miehe, C.; Mauthe, S. [2015]: *Phase field modeling of fracture in multi-physics problems. Part III. Crack driving forces in hydro-poro-elasticity and hydraulic fracturing of fluid-saturated porous media.* Computer Methods in Applied Mechanics and Engineering.

[182] Miehe, C.; Hofacker, M.; Welschinger, F. [2010]: *A phase field model for rate-independent crack propagation: Robust algorithmic implementation based on operator splits.* Computer Methods in Applied Mechanics and Engineering, 199: 2765–2778.

[183] Miehe, C.; Welschinger, F.; Hofacker, M. [2010]: *Thermodynamically consistent phase-field models of fracture: Variational principles and multi-field FE implementations.* International Journal for Numerical Methods in Engineering, 83: 1273–1311.

[184] Miehe, C.; Aldakheel, F.; Mauthe, S. [2013]: *Mixed variational principles and robust finite element implementations of gradient plasticity at small strains.* International Journal for Numerical Methods in Engineering, 94: 1037–1074.

[185] Miehe, C.; Hildebrand, F. E.; Böger, L. [2014]: *Mixed variational potentials and inherent symmetries of the Cahn-Hilliard theory of diffusive phase separation.* Proceedings of the Royal Society A: Mathematical, Physical and Engineering Science, 470: 20130641 1–16.

[186] Miehe, C.; Mauthe, S.; Hildebrand, F. E. [2014]: *Variational gradient plasticity at finite strains. Part III: Local-global updates and regularization techniques in multiplicative plasticity for single crystals.* Computer Methods in Applied Mechanics and Engineering, 268: 735–762.

[187] Miehe, C.; Mauthe, S.; Ulmer, H. [2014]: *Formulation and numerical exploitation of mixed variational principles for coupled problems of Cahn-Hilliard-type and standard diffusion in elastic solids.* International Journal for Numerical Methods in Engineering, 99(10): 737–762.

[188] Miehe, C.; Dal, H.; Schänzel, L.-M.; Raina, A. [2015]: *A phase field model for chemo-mechanical induced fracture in lithium-ion battery electrode particles.* International Journal for Numerical Methods in Engineering.

[189] Miehe, C.; Hofacker, M.; Schänzel, L.-M.; Aldakheel, F. [2015]: *Phase field modeling of fracture in multi-physics problems. Part II. Brittle-to-ductile failure mode transition and crack propagation in thermo-elastic-plastic solids.* Computer Methods in Applied Mechanics and Engineering, 294: 486–522.

[190] Miehe, C.; Mauthe, S.; Teichtmeister, S. [2015]: *Minimization principles for the coupled problem of Darcy-Biot-type fluid transport in porous media linked to phase field modeling of fracture.* Journal of the Mechanics and Physics of Solids, 82: 186–217.

[191] Miehe, C.; Schänzel, L.; Ulmer, H. [2015]: *Phase field modeling of fracture in multi-physics problems. Part I. Balance of crack surface and failure criteria for brittle crack propagation in thermo-elastic solids.* Computer Methods in Applied Mechanics and Engineering, 294: 449–485.

[192] Mikelic, A.; Wheeler, M. F.; Wick, T. [2013]: *A quasistatic phase field approach to fluid filled fractures.* Technical report, ICES Report 13-22, The Institute for Computational Engineering and Science, The University of Texas at Austin.

[193] Mikelic, A.; Wheeler, M.; Wick, T. [2014]: *Phase-field modeling of pressurized fractures in a poroelastic medium.* Technical report, ICES Report 14-18, The Institute for Computational Engineering and Science, The University of Texas at Austin.

[194] Mikelic, A.; Wheeler, M. F.; Wick, T. [2015]: *Phase-field modeling of a fluid-driven fracture in a poroelastic medium.* Computational Geosciences, Springer

Verlag (Germany).

[195] Mikelic, A.; Wheeler, M.; Wick, T. [2015]: *A phase-field method for propagating fluid-filled fractures coupled to a surrounding porous medium.* SIAM Multiscale Modeling Simulation, 13(1): 367–398.

[196] Mira, P.; Pastor, M.; Li, T.; Liu, X. [2003]: *A new stabilized enhances strain element with equal order of interpolation for soil consolidation problems.* Computer Methods in Applied Mechanics and Engineering, 192: 4257–4277.

[197] Moës, N.; Belytschko, T. [2002]: *Extended finite element method for cohesive crack growth.* Engineering Fracture Mechanics, 69: 813–833.

[198] Moës, N.; Dolbow, J.; Belytschko, T. [1999]: *A finite element method for crack growth without remeshing.* International Journal for Numerical Methods in Engineering, 46: 131–150.

[199] Mohammadnejad, T.; Khoei, A. [2013]: *Hydro-mechanical modeling of cohesive propagation in multiphase porous media using the extended finite element method.* International Journal for Numerical and Analytical Methods in Geomechanics, 37: 1247–1279.

[200] Murad, M. A.; Loula, A. F. D. [1994]: *On stability and convergence of finite element aapproximation of Biot's consolidation problem.* International Journal for numerical methods in engineering, 37: 645–667.

[201] Murad, M. A.; Loula, A. F. [1992]: *Improved accuracy in finite element analysis of Biot's consolidation problem.* Computer Methods in Applied Mechanics and Engineering, 95(3): 359–382.

[202] Nguyen, Q. S. [2000]: *Stability and Nonlinear Solid Mechanics.* John Wiley & Sons, New York.

[203] Pandolfi, A.; Ortiz, M. [2002]: *An efficient adaptive procedure for three-dimensional fragmentation simulations.* Engineering with Computers, 18: 148–159.

[204] Pantuso, D.; Bathe, K. J. [1997]: *On the stability of mixed finite elements in large strain analysis of incompressible solids.* Finite Elements in Analysis and Design, 28: 83–104.

[205] Papastavrou, A.; Steinmann, P.; Stein, E. [1997]: *Enhanced finite element formulation for geometrically linear fluid saturated porous media.* Mechanics of Cohesive-Frictonal Materials, 2: 185–203.

[206] Peerlings, R. H. J.; de Borst, R.; Brekelmans, W. A. M.; de Vree, J. H. P. [1996]: *Gradient enhanced damage for quasi-brittle materials.* International Journal for Numerical Methods in Engineering, 39: 3391–3403.

[207] Peerlings, R. H. J.; Geers, M. G. D.; Borst, R. de ; Brekelmans, W. A. M. [2001]: *A critical comparison of nonlocal and gradient-enhanced softening continua.* International Journal of Solids and Structures, 38: 7723–7746.

[208] Peirce, A.; Detournay, E. [2008]: *An implicit level set method for modeling hydraulically driven fractures.* Computational Methods in Applied Mechanics and Engineering, 197: 2858–2885.

[209] Pham, K.; Amor, H.; Marigo, J. J.; Maurini, C. [2011]: *Gradient damage models and their use to approximate brittle fracture.* International Journal of Damage Mechanics, 20: 618–652.

[210] Philibert, J. [2006]: *One and a half century of diffusion: Fick, Einstein, before and beyond.* Diffusion Fundamentals, 4: 6.1–6.19.

[211] Phillips, P. J.; Wheeler, M. F. [2008]: *A coupling of mixed and discontinuous*

Galerkin finite-element methods for poroelasticity. Computers & Geosciences, 12: 417–435.

[212] Phoon, K. K.; Toh, K. C.; Chan, S. H.; Lee, F. H. [2002]: *An efficient diagonal preconditioner for finite element solution of Biot's consolidation equations.* International Journal for Numerical Methods in Engineering, 55(4): 377–400.

[213] Preisig, M.; Prévost, J. H. [2011]: *Stabilization procedure in coupled poromechanics problems: A critical assessment.* International Journal for Numerical and Analytical Methods in Geomechanics, 35: 1207–1225.

[214] Prévost, J. H. [1980]: *Mechanics of continuous porous media.* International Journal of Engineering Science, 18(6): 787–800.

[215] Prevost, J. H. [1982]: *Nonlinear tranisent phenomena in saturated porous media.* Computer Methods in Applied Mechanics and Engineering, 30: 3–18.

[216] Prévost, J. H. [1983]: *Implicit-explicit schemes for nonlinear consolidation.* Computer Methods in Applied Mechanics and Engineering, 39(2): 225–239.

[217] Prevost, J. H. [1985]: *Wave propagation in fluid-saturated porous media: An efficient finite element procedure.* Soil Dynamics and Earthquake Engineering, 4(4): 183–202.

[218] Raviart, P. A.; Thomas, J. M. [1977]: *Primal hybrid finite element methods for 2nd order elliptic equations.* Mathematics of computation, 31(138): 391–413.

[219] Reed, M. B. [1984]: *An investigation of numerical eerror in the analysis of consolidation by finite elements.* International Journal for Numerical and Analytical Methods in Geomechanics, 8(3): 243–257.

[220] Rempler, H.-U. [2012]: *Damage in multi-phasic materials computed with the extended finite-element method.* Ph.D. Thesis, University of Stuttgart, Institute for Applied Mechanics (CE).

[221] Rempler, H.-U.; Wieners, C.; Ehlers, W. [2011]: *Efficiency comparison of an augmented finite element formulation with standard return mapping algorithms for elastic-inelastic materials.* Computational Mechanics, 48: 551–562.

[222] Réthoré, J.; de Borst, R.; Abellan, M. [2007]: *A two-scale approach for fluid flow in fractured porous media.* International Journal for Numerical Methods in Engineering, 75: 780–800.

[223] Réthoré, J.; de Borst, R.; Abellan, M. [2008]: *A two-scale model for fluid flow in an unsaturated porous medium with cohesive cracks.* Computational Mechanics, 42: 227–238.

[224] Rice, J. R. [1968]: *A path independent integral and the approximate analysis of strain concentraction by notches and cracks.* Journal of Applied Mechanics, 35: 379–386.

[225] Rice, J. R.; Clearly, M. P. [1976]: *Some basic stress diffusion solutions for fluid-saturated elastic porous media with compressible constituents.* Reviews of geophysics and space physics, 14(2): 227–241.

[226] Ricken, T.; Schwarz, A.; Bluhm, J. [2007]: *A triphasic model of transversely isotropic biological tissue with application to stress and biologically induced growth.* Computational Materials Science, 39: 124–136.

[227] Rodrigo, C.; Gaspar, F. J.; Hu, X.; Zikatanov, L. T. [2016]: *Stability and monotonicity for some discretizations of the Biot's consolidation model.* Computer Methods in Applied Mechanics and Engineering, 298: 183–204.

[228] Rubin, A. M. [1995]: *Propagation of magma-filled cracks.* Annual Review of Earth

and Planetary Sciences, 23: 287–336.

[229] Saczuk, J.; Hackl, K.; Stumpf, H. [2003]: *Rate theory of nonlocal gradient damage-gradient viscoinelasticity.* International Journal of Plasticity, 19: 675–706.

[230] Sandhu, R.; Pister, K. [1970]: *A variational principle for linear, coupled field problems in continuum mechanics.* International Journal of Engineering Science, 8(12): 989–999.

[231] Sandhu, R.; Wilson, E. [1969]: *Finite-element analysis of seepage in elastic media.* Journal of the Engineering Mechanics Division, 95: 641–652.

[232] Savitski, A. A.; Detournay, E. [2002]: *Propagation of a penny-shaped fluid-driven fracture in an impermeable rock: asymptotic solutions.* International Journal of of Solids and Structures, 39: 6311–6337.

[233] Schrefler, B.; Secchi, S.; Simoni, L. [2006]: *On adaptive refinement techniques in multi-field problems including cohesive fracture.* Computer Methods in Applied Mechanics and Engineering, 195: 444 – 461.

[234] Schroeder, J.; Klaas, O.; Stein, E.; Miehe, C. [1997]: *A physically nonlinear dual mixed finite element formulation.* Computer Methods in Applied Mechanics and Engineering, 144: 77–92.

[235] Schwarz, A.; Schröder, J.; Starke, G. [2010]: *A modified least-square mixed finite element with improved momentum balance.* International Journal for Numerical Methods in Engineering, 81: 286–306.

[236] Secchi, S.; Schrefler, B. [2014]: *Hydraulic fracturing and its peculiarities.* Asia Pacific Journal on Computational Engineering, 1(8): 1–21.

[237] Secchi, S.; Schrefler, B. [2012]: *A method for 3-d hydraulic fracturing simulation.* International Journal of Fracture, 178: 245–258.

[238] Simo, J.; Armero, F. [1992]: *Geometrically nonlinear enhanced strain mixed methods and the method of incompatible modes.* International Journal for Numerical Methods in Engineering, 33: 1413–1449.

[239] Simo, J.; Rifai, M. S. [1990]: *A class of mixed assumed strain methods and the method of incompatible modes.* International Journal for Numerical Methods in Engineering, 29: 1595–1638.

[240] Simo, J. C.; Ju, J. W. [1987]: *Strain- and stress-based continuum damage models — I. Formulation.* International Journal of Solids and Structures, 23: 821–840.

[241] Simo, J. C.; Ju, J. W. [1987]: *Strain- and stress-based continuum damage models — II. Computational aspects.* International Journal of Solids and Structures, 23: 841–869.

[242] Simon, B. R.; Wu, J. S.-S.; Zienkiewicz, O. C.; Paul, D. K. [1986]: *Evaluation of $\boldsymbol{u}$-$\boldsymbol{w}$ and $\boldsymbol{u}$-π finite element methods for the dynamic response of saturated porous media using one-dimensional models.* International Journal for Numerical and Analytical Methods in Geomechanics, 10: 461–482.

[243] Simoni, L.; Schrefler, B. [2014]: *Multi field simulation of fracture.* Advances in Applied Mechanics, chapter 4, pp. 367–519. Elsevier.

[244] Singh, G. K.; Ceder, G.; Bazant, M. Z. [2008]: *Intercalation dynamics in rechargeable battery materials: General theory and phase-transformation waves in $LiFePO_4$.* Electrochimica Acta, 53: 7599–7613.

[245] Sneddon, I. N.; Lowengrub, M. [19697]: *Crack problems in the classical theory of elasticity.* John Wiley & Sons, Inc., New York.

[246] Spurk, J. H.; Aksel, N. [2008]: *Fluid Mechanics.* Springer Verlag Berlin Heidel-

berg, 2nd edition Edition.

[247] Steinmann, P. [1999]: *A finite element formulation for strong discontinuities in fluid-saturated porous media.* Mechanics of Cohesive-Frictional Materials, 4(2): 133–152.

[248] Sukumar, N.; Moës, N.; Moran, B.; Belytschko, T. [2000]: *Extended finite element method for three dimensional crack modelling.* International Journal for Numerical Methods in Engineering, 48: 1549–1570.

[249] Sukumar, N.; Chopp, D.; Moran, B. [2003]: *Extended finite element method and fast marching method for three-dimensional fatigue crack propagation.* Engineering Fracture Mechanics, 70(1): 29–48.

[250] Sun, W.; Ostien, J.; Salinger, A. [2013]: *A stabilized assumed deformation gradient finite element formulation for strongly coupled poromechanical simulations at finite strain.* International Journal for Numerical and Analytical Methods in Geomechanics, 37: 2755–2788.

[251] Svoboda, J.; Turek, I.; Fischer, F. D. [2005]: *Application of the thermodynamic extremal principle to the modeling of thermodynamic processes in material sciences.* Philosophical Magazine, 85: 3699–3707.

[252] Svoboda, J.; Fischer, F. D.; Frantzl, P. [2006]: *Diffusion and creep in multicomponent alloys with non-ideal sources and sinks for vacancies.* Acta Materialia, 54: 3043–3053.

[253] Taylor, C.; Hood, P. [1973]: *A numerical solution of the Navier-Stokes equations using the finite element technique.* Computers & Fluids, 1(1): 73–100.

[254] Tchonkova, M.; Peters, J.; Sture, S. [2008]: *A new mixed finite element method for poro-elasticity.* International Journal for Numerical and Analytical Methods in Geomechanics, 32: 579–606.

[255] Terzaghi, K. [1925]: *Erdbaumechanik auf bodenphysikalischer Grundlage.* F. Deuticke.

[256] Terzaghi, K. [1943]: *Theoretical Soil Mechanics.* Wiley, New York.

[257] Timothy, J. J.; Meschke, G. [2013]: *Modeling electrolyte diffusion in cracked cementitious materials using cascade continuum micromechanics and phase-field models.* VIII International Conference on Fracture Mechanics for Concrete and Concrete Structures, 8: 1–4.

[258] Toh, K.-C.; Phoon, K.-K. [2008]: *Comparison between iterative solution of symmetric and non-symmetric forms of Biot's FEM equations using the generalized Jacobi preconditioner.* International Journal for Numerical and Analytical Methods in Geomechanics, 32(9): 1131–1146.

[259] Truesdell, C. [1984]: *Rational Thermodynamics.* Springer, New York.

[260] Truesdell, C.; Noll, W. [1965]: *Handbuch der Physik Bd. III/3*, chapter The nonlinear field theories of mechanics. Springer, Berlin.

[261] Truesdell, C.; Toupin, R. [1960]: *The classical field theories.* In Flügge, S. (Editor), *Handbuch der Physik*, Vol. III/1, pp. 226–902. Springer-Verlag, Berlin-Göttingen-Heidelberg.

[262] Truty, A.; Zimmermann, T. [2006]: *Stabilized mixed finite element formulations for materially nonlinear partially saturated two-phase media.* Computer Methods in Applied Mechanics and Engineering, 195: 1517–1546.

[263] Vermeer, P. A.; Verruijt, A. [1981]: *An accuracy condition for consolidation by finite elements.* International Journal for Numerical and Analytical Methods in

Geomechanics, 5: 1–14.

[264] Verruijt, A. [2013]: *Theory and problems of poroelasticity*. Technical report, Delft University of Technology.

[265] Vinci, C.; Renner, J.; Steeb, H. [2014]: *A hybrid-dimensional approach for an efficient numerical modeling of the hydro-mechanics of fracture*. Water Resources Research, 50(2): 1616–1635.

[266] Šilhavý, M. [1997]: *The mechanics and thermodynamics of continuous media*. Texts and Monographs in Physics. Springer.

[267] Wagner, A. [2014]: *Extended Modelling of the Multiphasic Human Brain Tissue with Application to Drug-Infusion Processes*. Ph.D. Thesis, University of Stuttgart, Institute for Applied Mechanics (CE).

[268] Weitsman, Y. [1987]: *Stress assisted diffusion in elastic and viscoelastic materials*. Journal of Mechanics Physics Solids, 35: 73–93.

[269] Wheeler, M. F.; Wick, T.; Wollner, N. [2014]: *An augmented-Lagrangian method for the phase-field approach for pressurized fractures*. Computer Methods in Applied Mechanics and Engineering, 271: 69–85.

[270] White, J. A.; Borja, R. I. [2008]: *Stabilized low-order finite elements for coupled solid-deformation/fluid-diffusion and their application to fault zone transients*. Computer Methods in Applied Mechanics and Engineering, 197(49): 4353–4366.

[271] Wilson, Z. A.; Landis, C. M. [2016]: *Phase-field modeling of hydraulic fracture*. ICES Report, 16-10.

[272] Witherspoon, P. A.; Wang, J. S. Y.; Iwai, K.; Gale, J. E. [1980]: *Validity of cubic law for fluid flow in a deformable rock fracture*. Water Resources Research, 16(6): 1016–1024.

[273] Wriggers, P. [2001]: *Nichtlineare Finite Element-Methoden*. Springer-Verlag, Berlin Heidelberg, 1st Edition.

[274] Xu, X. P.; Needleman, A. [1994]: *Numerical simulations of fast crack growth in brittle solids*. Journal of the Mechanics and Physics of Solids, 42: 1397–1434.

[275] Zhang, X.; Detournay, E.; Jeffrey, R. [2002]: *Propagation of a penny-shaped hydraulic fracture parallel to the free-surface of an elastic half space*. International Journal of Fracture, 115: 126–158.

[276] Zhang, X.; Krischok, A.; Linder, C. [2016]: *A variational framework to model diffusion induced large plastic deformation and phase field fracture during initial two-phase lithiation of silicon electrodes*. Computer Methods in Applied Mechanics and Engineering, pp. –.

[277] Zhao, Y.; Stein, P.; Xu, B. X. [2015]: *Isogeometric analysis of mechanically coupled cahn-hilliard phase segregation in hyperelastic electrodes of Li-ion batteries*. Computer Methods in Applied Mechanics and Engineering, 00: 00.

[278] Zhou, X. X.; Chow, Y. K.; Leung, C. F. [2007]: *Hybrid and enhanced finite element methods for problems of soil consolidation*. International Journal for numerical methods in engineering, 69: 221–249.

[279] Ziegler, H.; Wehrli, C. [1987]: *The derivation of constitutive relations from the free energy and the dissipation function*. Advances in Applied Mechanics, 25: 183–238.

[280] Zienkiewicz, O. C.; Taylor, R.; Zhu, J. Z. [2005]: *The finite element method: Its basis and fundamentals*. Elsevier.

Curriculum Vitae

Personal data:

Name:	Steffen Alexander Mauthe
Date of birth:	July 6, 1987
Place of birth:	Balingen, Germany
Nationality:	German
Parents:	Gustav and Margit Mauthe
Siblings:	Thorsten and Eva Mauthe
Marital status:	married to Denise Nina Mauthe
Children:	Hannes David Mauthe

Education:

1993 – 1997	elementary school "Grund- und Hauptschule Obernheim", Obernheim, Germany
1997 – 2003	secondary school "Progymnasium Meßstetten", Meßstetten, Germany
2003 – 2006	secondary school "Philipp-Matthäus-Hahn-Schule", Balingen, Germany
06/2006	degree: "Allgemeine Hochschulreife" (high school diploma)
2006 – 2011	studies in civil engineering at the University of Stuttgart, Germany
10/2011	degree: "Diplom-Ingenieur (Dipl.-Ing.) Bauingenieurwesen"

Professional occupation:

12/2011 – 11/2016	teaching assistant and research associate at the Institute of Applied Mechanics (Civil Engineering) at the University of Stuttgart, Germany
12/2016	Simulation Engineer at Kärcher GmbH & Co. KG, Winnenden, Germany

Released Report Series

II-1 Gernot Eipper: *Theorie und Numerik finiter elastischer Deformationen in fluidgesättigten porösen Festkörpern*, 1998.

II-2 Wolfram Volk: *Untersuchung des Lokalisierungsverhaltens mikropolarer poröser Medien mit Hilfe der Cosserat-Theorie*, 1999.

II-3 Peter Ellsiepen: *Zeit- und ortsadaptive Verfahren angewandt auf Mehrphasenprobleme poröser Medien*, 1999.

II-4 Stefan Diebels: *Mikropolare Zweiphasenmodelle: Formulierung auf der Basis der Theorie Poröser Medien*, 2000.

II-5 Dirk Mahnkopf: *Lokalisierung fluidgesättigter poröser Festkörper bei finiten elastoplastischen Deformationen*, 2000.

II-6 Heiner Müllerschön: *Spannungs-Verformungsverhalten granularer Materialien am Beispiel von Berliner Sand*, 2000.

II-7 Stefan Diebels (Ed.): *Zur Beschreibung komplexen Materialverhaltens: Beiträge anläßlich des 50. Geburtstages von Herrn Prof. Dr.-Ing. Wolfgang Ehlers*, 2001.

II-8 Jack Widjajakusuma: *Quantitative Prediction of Effective Material Parameters of Heterogeneous Materials*, 2002.

II-9 Alexander Droste: *Beschreibung und Anwendung eines elastisch-plastischen Materialmodells mit Schädigung für hochporöse Metallschäume*, 2002.

II-10 Peter Blome: *Ein Mehrphasen-Stoffmodell für Böden mit Übergang auf Interface-Gesetze*, 2003.

II-11 Martin Ammann: *Parallel Finite Element Simulations of Localization Phenomena in Porous Media*, 2005.

II-12 Bernd Markert: *Porous Media Viscoelasticity with Application to Polymeric Foams*, 2005.

II-13 Saeed Reza Ghadiani: *A Multiphasic Continuum Mechanical Model for Design Investigations of an Effusion-Cooled Rocket Thrust Chamber*, 2005.

II-14 Wolfgang Ehlers & Bernd Markert (Eds.): *Proceedings of the 1st GAMM Seminar on Continuum Biomechanics*, 2005.

II-15 Bernd Scholz: *Application of a Micropolar Model to the Localization Phenomena in Granular Materials: General Model, Sensitivity Analysis and Parameter Optimization*, 2007.

II-16 Wolfgang Ehlers & Nils Karajan (Eds.): *Proceedings of the 2nd GAMM Seminar on Continuum Biomechanics*, 2007.

II-17 Tobias Graf: *Multiphasic Flow Processes in Deformable Porous Media under Consideration of Fluid Phase Transitions*, 2008.

II-18 Ayhan Acartürk: *Simulation of Charged Hydrated Porous Materials*, 2009.

II-19 Nils Karajan: *An Extended Biphasic Description of the Inhomogeneous and Anisotropic Intervertebral Disc*, 2009.

II-20 Bernd Markert: *Weak or Strong – On Coupled Problems In Continuum Mechanics*, 2010.

II-21 Wolfgang Ehlers & Bernd Markert (Eds.): *Proceedings of the 3rd GAMM Seminar on Continuum Biomechanics*, 2012.

II-22 Wolfgang Ehlers: *Poröse Medien – ein kontinuumsmechanisches Modell auf der Basis der Mischungstheorie*, 2012. Nachdruck der Habilitationsschrift aus dem Jahr 1989 (Forschungsberichte aus dem Fachbereich Bauwesen der Universität-GH-Essen **47**, Essen 1989).

II-23 Hans-Uwe Rempler: *Damage in multi-phasic Materials Computed with the Extended Finite-Element Method*, 2012.

II-24 Irina Komarova: *Carbon-Dioxide Storage in the Subsurface: A Fully Coupled Analysis of Transport Phenomena and Solid Deformation*, 2012.

II-25 Yousef Heider: *Saturated Porous Media Dynamics with Application to Earthquake Engineering*, 2012.

II-26 Okan Avci: *Coupled Deformation and Flow Processes of Partial Saturated Soil: Experiments, Model Validation and Numerical Investigations*, 2013.

II-27 Arndt Wagner: *Extended Modelling of the Multiphasic Human Brain Tissue with Application to Drug-Infusion Processes*, 2014.

II-28 Joffrey Mabuma: *Multi-Field Modelling and Simulation of the Human Hip Joint*, 2014.

II-29 Robert Krause: *Growth, Modelling and Remodelling of Biological Tissue*, 2014.

II-30 Seyedmohammad Zinatbakhsh: *Coupled Problems in the Mechanics of Multi-Physics and Multi-Phase Materials*, 2015.

II-31 David Koch: *Thermomechanical Modelling of Non-isothermal Porous Materials with Application to Enhanced Geothermal Systems*, 2016.

II-32 Maik Schenke: *Parallel Simulation of Volume-coupled Multi-field Problems with Special Application to Soil Dynamics*, 2017.